UNIVERSITY OF SOUTHAMPTON

FACULTY OF PHYSICAL SCIENCES AND ENGINEERING

School of Electronics and Computer Science

Thesis for degree of Doctor of Philosophy

A MEMS SENSOR FOR STRAIN SENSING IN DOWNHOLE PRESSURE APPLICATIONS BASED ON A DOUBLE MASS STRUCTURE

By

Nhan Truong Cong

(nct1g13@ecs.soton.ac.uk)

Supervisor: Prof. S.P. Beeby, Dr M.J. Tudor

October 2017

UNIVERSITY OF SOUTHAMPTON

ABSTRACT

FACULTY OF PHYSICAL SCIENCES AND ENGINEERING

SCHOOL OF ELECTRONICS AND CALCULATER SCIENCE

Thesis for degree of Doctor of Philosophy

By Nhan Truong Cong

Mircoelectromechanical (MEM) resonators have been widely used as sensors and accelerometers as the resonators' resonant frequencies shift when one of its properties, namely stiffness and mass change. The devices that employ stiffness sensing have been developed in many areas, including pressure sensors, accelerometers and force sensors. The double-mass resonator for pressure sensing has been the focus of many researches in recent year. By introducing the dual mass structure onto the traditional double-end tuning fork (DETF), it has been shown that this type of structural design has: 1) lower natural resonant frequency for easier detection mechanism; 2) improving the Quality factor (Q) due to lower total energy loss. However, the area of stress induction mechanism is under research.

This thesis introduces a novel stress induction mechanism to work with the double-mass structure, namely centrally located anchor points on diaphragm. The structure is intended to maximise the engagement of pressure induced stress in generating strain in the resonator while minimise the risk of structural failure in high pressure environment. In addition, I have investigated several practical aspects of double-mass resonator that have not been under intensively researched namely the sensor behaviour in high pressure environment (1000 Bar) and the risk of piezoresistor-on-chip detection mechanism.

I also investigated the disadvantage of traditional diaphragm structure. The diaphragm only engages shear stress in induction mechanism. To provide an alternative solution, the novel lateral stress induced structure (LSIS) is proposed. By using the LSIS, it was shown in simulation that the compressive stress can also be engaged in induction mechanism on the same level of magnitude with shear stress in diaphragm structure.

Finally, I have simulated the effect of high temperature condition have on resonator stiffness, hence its resonant frequency. Furthermore, based on these simulation result, I have proposed a novel dual double-mass structure, which is capable to be used as temperature compensation mechanism.

Contents

List of Figures

List of Tables

Chapter 1 Introduction

1.1 Motivation of research

Recent micro-electromechanical systems (MEMS) research has led to the development of various sensor applications. Mass, pressure, stress and acceleration can be measured by exploiting the mechanical properties of a micro-scale structure. One of the most researched areas of MEMS sensors is the pressure sensor with many successful devices demonstrated via the use of piezoresistive strain gauge, capacitive transducers. Pressure sensors are used for controlling and monitoring in a range of diverse applications in industries such as petrochemical, medical, aerospace, transportation and test and measurement. Measured pressure can also be used to indirectly calculate a range of other variables such as fluid or gas flow in pipes, volume of liquid inside an encapsulated space, altitude and speed. In precision pressure measurement application, resonant pressure sensors have been widely used because of their advantages of a high Q factor[1] as well as stability against temperature [2] and aging [3].

Oil reservoirs are typically located from 500 to 5000 metres underground, which is equivalent to 100 - 1000 bar pressure. Three types of measurement are taken, including for pressure build-up, long-term reservoir pressure surveillance and flow measurement. The first two measurements are used to measure the static pressure inside the well. The pressure build-up test is used to monitor the pressure at the bottom of the well after the well is shut. Long-term reservoir pressure surveillance constantly measures the pressure level inside the well for long period of time which can be up to several months. Both measurements require an absolute sensor that measures the static pressure against a reference pressure, usually a vacuum. The sensor has to have a sufficient range of operating pressure as well as a minimal long-term drift. The flow measurement is used to measure the productivity of an oil reservoir based on its flow rate. The number of barrels produced each day can be calculated from the flow rate and oil mass density. This type of measurement requires a differential pressure sensor, which must have high resolution or sensitivity to reduce the error in measured well production. This differential pressure sensor can also be realised by employing an absolute pressure sensors on each side of a Venturi or orifice plate[4]. The dominant product for downhole resonant pressure sensor application are manufactured by Quartzdyne ltd. Their product is made of quartz crystal, thus making their resonator several times larger than silicon counterpart. The incumbent Quartzdyne pressure sensor have following specification: accuracy of ±0.015% FS to 0.02% FS, resolution of 100 Pa, operating frequency from 0 to 1000 Bar and operating

temperature from 0 to 175ºC. The aim of this project is to achieve this specification while reducing the side of the sensor by employing MEMS resonator.

Most previous research into resonant pressure sensors have focused more on increasing the sensitivity in a range of operating pressures from 0 to 3 bar rather than maintaining a standard sensitivity over a long range of pressure up to 1000 bar [5]-[6]. Oil reservoirs are considered high pressure when its pressure is greater than 690 bar [7]. The requirement to sense pressure in extreme condition within a high pressure downhole oil well is beyond the operating range of current silicon resonant pressure sensors designs.

MEMS resonators have been developed for various applications such as atomic force microscopy (AFM) [9][10], accelerometers (inertial force sensing) [11][12], magnetic field sensing (Lorentz force sensing) [13][14] and strain sensing (stiffness changing sensing) [14][15]. In strain detection application, the geometry of the resonator has been proved to have significant effect on the sensitivity, damping ratio and operating range of the sensor. The majority of examples adopt single degree-of-freedom (DoF) resonator structures. This structure has been proved to be effective for aforementioned application. However, many single DoF structures have significant drawback of high energy loss during vibration, which lead to lower Q factor and fast aging problem [15]. A solution is to apply antiphase excitation forces onto two halves of the system, which will drive the structure onto balanced resonance. An alternative solution is to use 2 DoF structures, which are balanced structures. Coupled resonators (2DoF) have recently acquired more research interests in sensing application due to its sensitivity and stability [16]–[18]. In addition, 2 DoF structure provides the freedom to measure both pressure and temperature spontaneously. In this research, I am aiming to explore the usage of 2 DoF structure in pressure sensing application.

It is worth noting that the damping ratio can affect the sensitivity [19], resolution [20] and long term stability [21] of resonant sensors. A double-mass resonator structure fabricated from a Silicon on Insulator (SOI) wafer has been demonstrated to have excellent damping ratios in both vacuum and air medium [22]. Welham *et al*.[23] also showed that double mass structure experienced a reduction in sensitivity from 15%/bar to 3.8%/bar while increasing the range of pressure from 0-3 Bar to 0-10 bar by using a thicker diaphragm. However, this pressure range is much smaller than a standard high-pressure oil well.

This research focuses on the development of a silicon resonator structure for resonant pressure sensor on SOI wafer designed for the downhole oil application. The aim is to maximise the range of the applied stress while maintaining an acceptable level of sensitivity and resolution. To achieve this the use of coupled double-mass structure, which is illustrated by a two degree of freedom system (2DOF) has been explored. The theoretical model of the 2 DOF and the Finite Element Analysis (FEM) model of several double-mass structures are analysed. To verify the theoretical and simulation

result, a range of double-mass structure have been designed, fabricated and tested for resonant frequency and sensitivity against applied stress. In this work, much attention has been given to the resonator design, namely resonator structure, method for strain testing, actuating and detecting mechanism. The encapsulation method for packaging the device still hasn't been optimized. Future work should focus on the optimization of the packaging of the sensor for industrialization.

1.2 Research Objective

Considering the current status of research in this field, the major objectives of this research can be summarised as follows:

- Find an effective way to improve the sensitivity and operational range of a pressure coupled resonant sensor via simulation model.
- Develop a fabrication process and investigate the frequency response and Q factor of the fabricated resonators. Validate the simulation results.
- Analyse the pressure-coupling structures and find an alternative solution to the traditional diaphragm
- Investigate the frequency response and Q factor of the novel structure, then compare with the state-of-the-art devices
- Investigate a solution for high temperature compensation for a downhole resonant pressure sensor via simulation

1.3 Novelties

The novelties of this research are listed below:

- In this work, a novel structure for a resonant sensing device, which consists of a diaphragm-double-mass structure, are proposed. The two masses are coupled via mechanical coupling beams. The resonator is attached to the diaphragm via 2 anchor points, that can improve the strain sensitivity beyond the current state of the art.

- Despite the fact that diaphragm structure is widely used in strain sensing, optimal contact points between diaphragm and resonator structure has not been fully exploited. This motivates our research to consider the effect of applied pressure on the diaphragm structure theoretically. Better understanding of the diaphragm leads to the optimisation of diaphragm and anchor point, which ultimately improve the sensitivity of the sensor.

- In addition, diaphragm structure only employs the use of shear stress in generating tensile strain in the resonator structure. Novel structures called Lateral Stress Coupling Structure (LSCS) that take advantage of the compressive stress have been analysed. FEM has been used to simulate the device in a complete package to observe the effect of high pressure environment. The LSCS is shown to have the equivalent in sensitivity with diaphragm structure without the without the constraint of operational range that diaphragm possess.

- A state-of-the-art dual double-mass structure design is proposed and optimised. Dual double-mass structure is the solution for the harsh condition found in the downhole environment. The structure contains two silicon resonators: one exposed to pressure and temperature while the other are isolated from applied pressure. The measurement from the isolated resonator can be used to compensate for the frequency drift caused by thermal condition.

1.4 **Publications**

Since the research is fund by Senico Ltd, all publications, therefore, are restricted.

1.5 **Thesis Structure**

Chapter 2 presents a literature review on previous work in the field of MEMS pressure sensors, focusing on resonant devices. The effect of stress and damping on resonant frequency is also highlighted.

Chapter 3 describes the optimisation of coupled double-mass resonator structure with diaphragm. A mechanical model of coupled structure is presented and evaluated.

Chapter 4 presents simulation result and the fabrication plan for a coupled double-mass structure. The fabrication process developed for Silicon-on-Insulator (SOI) wafers at the University of Southampton is discussed and modified to suit the targeted design. The design of the photolithography mask sis also illustrated in this chapter. Test result of the fabricated structure are highlighted and discussed

Chapter 5 discusses the optimisation of the coupled double-mass resonator with the lateral stress-induced structure. The simulation results are compared with the resonator and diaphragm structure. Experimental result for resonant peak and Q factor are included. A state-of-the-art dual double-mass resonator is presented and simulated at the end of the chapter.

Chapter 6 concludes the thesis and provides an outlook on the future work for the research

Chapter 2 Literature review: MEMS pressure sensors

2.1 Introduction

This chapter presents an overview of technologies related to MEMS silicon pressure sensors and assesses their feasibility in measuring high pressure. The pressure sensing principle is introduced in section 2.2. The piezoresistive sensor is presented in section 2.3. Section 2.4 discusses the performance of capacitive sensors. In section 2.5, the resonant pressure sensor is presented in detail including the effect of stress and damping on a resonator, a summary of excitation and detection mechanisms and a review of previous resonant pressure sensors. Section 2.6 reviews the quartz technology that is used in down-hole application. Section 2.7 provides conclusions.

2.2 Pressure measurement

Pressure sensing is defined as a process of measuring the pressure of a medium, typically a gas or liquid. A pressure sensor acts as a transducer, which generates an electrical signal as a proportional function of the imposed pressure. The working principles for a pressure sensor are illustrated in fig. 2.1. The pressure is transferred into physical movement using a sensing element inside the sensor. This movement is converted into the electrical signal through a transduction mechanism.

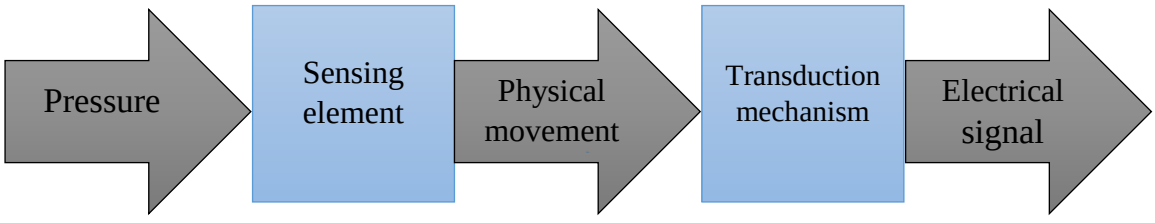

Figure 2.1 Block diagram of key pressure sensor components [24].

Pressure sensors can be classified in terms of the type of reference pressure they use in the measurement. Absolute pressure sensors measure pressure relative to a vacuum. Thus, these types of devices must contain an encapsulated vacuum within the sensor.

Gauge pressure sensors are devices that take measurement relative to atmospheric pressure. Therefore, the sensor either must contain a fixed reference pressure, which is the pressure at sea level or have a part vented to the ambient atmosphere. Differential pressure sensors measure the difference between two pressures, one connected to each side of the sensor. The design of this device offers many challenges since the mechanical structure is exposed to two different pressures [24].

Research into MEMS silicon pressure sensors began in the early 1960s [25] since silicon showed promising characteristics to become the dominant material in MEMS. Silicon is a pure, cheap, well-characterized material available in large quantities. Thanks to developments in semiconductor fabrication, a wide range of MEMS processing techniques for silicon are easily accessible. The use of silicon in MEMS also provides the potential for integration with electrical processing circuitry, which leads to a simplified user interface and a smaller chip size. Furthermore, the most significant advantage of silicon is its excellent mechanical properties and its inherent piezoresistivity, which is important for mechanical sensing [26]. The application of MEMS to pressure measurement has been developed for more than 30 years and undoubtedly is one of the most successful applications in the MEMS market. The MEMS technology capability of mass-produced miniature sensors at low cost has increased furthermore the range of applications. MEMS silicon pressure sensors can be classified in term of the mechanical sensing technique applied, which includes piezoresistive, capacitive and high-performance resonant frequency detection.

2.3 **Piezoresistive pressure sensor**

The discovery of the piezoresistance effect in silicon by Smith [27] inspired the development of piezoresistive sensor. In a piezoresistor, the resistance changes due to the strain in the silicon lattice caused by the applied force. Strain affects the mobility of charge carriers in silicon, thus either increasing or decreasing the resistance of silicon. Commercialised MEMS piezoresistive pressure sensors exploit the use of advanced fabrication processes such as anisotropic etching, fusion bonding and ion implanted strain gauges to achieve accuracy and reduce cost [24]. A typical piezoresistive pressure sensor contains two layers of fusion-bonded silicon as shown in fig. 2.2. Strain gauges are placed in the diaphragm layer via ion implantation[28].

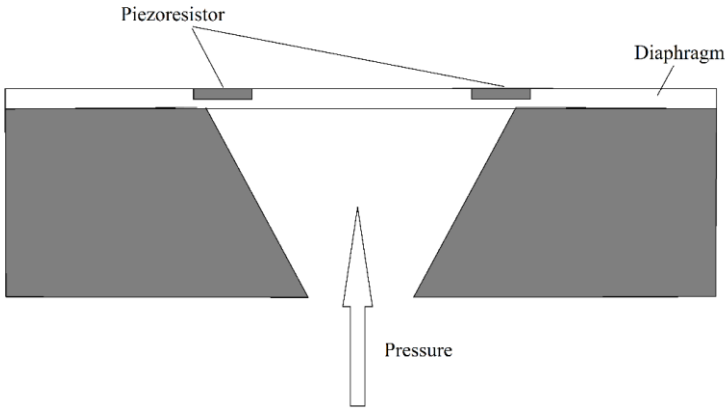

Figure 2.2 Fusion bonded silicon piezoresistive pressure sensor [24]

Silicon piezoresistive pressure sensor fabrication processes produce different output levels via controlling the ion-implanted strain gauges. The ratio of the relative change in resistance as a function of mechanical strain is called Gauge Factor. The Gauge factor of single crystalline silicon is 200, which means that a change in structure length is multiplied by 200 in the change in resistance. The piezoresistance change is adjusted via the doping concentration level of the strain gauges. However, increasing the resistance mean the power needed for operation will increase. In addition, the temperature cross-sensitivity is another major factor that prevents a silicon piezoresistor from achieving highly accurate measurement. The temperature coefficient of piezoresistive silicon is $-1600\times10^{-6}/^{o}C$ in compared with $4\times10^{-6}/^{o}C$ for capacitive method or $-30\times10^{-6}/^{o}C$ for resonant method and so piezoresistive based sensors require techniques to compensate for temperature sensitivity [29]. In addition, GE [30] have reported 0.1% per year long term drift in their piezoresistive commercial sensor. These drawbacks have limited the application of piezoresistors in high-pressure high temperature environments.

2.4 Capacitive pressure sensor

Capacitive pressure sensors were first developed in the early 1980s as an alternative method to low cost piezoresistive pressure sensors [31][32]. Capacitive sensors have a relatively simple structure but provide accurate measurement for pressure sensing. The device typically contains a fixed electrode and a flexible one in parallel as shown in fig.2.3 [33]. The capacitance, *C*, of a parallel plate capacitor is given by

$$C = \frac{\varepsilon A}{d} \tag{2.1}$$

Where ε, A and d are the permittivity of the medium inside the gap, the overlap area of two electrodes and the distance between the two electrodes, respectively. Under

applied pressure, the flexible electrode will deflect, decreasing the gap between electrodes and increase the capacitance.

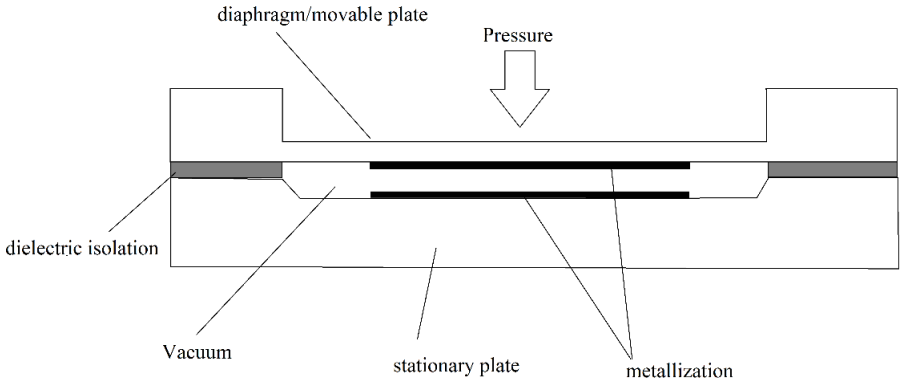

Figure 2.3 Anodic bonded capacitive pressure sensor contains a vacuum chamber for dielectric stability (similar to [33])

Unlike the piezoresistive pressure sensor, capacitive sensors suffer much lower temperature cross sensitivity, thus provide more temperature stability [24]. A typical capacitive sensor as shown in fig. 2.3, maintains vacuum or a reference pressure between the plates to avoid the change in dielectric constant, which affect the linearity of the output capacitance. However, the nonlinear output of the sensor is still the main drawback of the capacitive approach. The centre of the flexible diaphragm exhibits a higher deflection than the edge, which is bonded to the fixed electrode. As a result, the two electrodes will no longer be parallel to each other, which introduces nonlinearity to the output. A linearized approach is to measure only a particular part of the diaphragm with minimum non-linearity. By excluding the centre of the diaphragm from the capacitance sensing area, the nonlinearity is reduced. But studies also show significant reductions in sensitivity [34][35]. Despite the difficulty of nonlinearity, the capacitive sensor can be deployed to measure low stress levels, which generates a small deflection on the movable diaphragm and hence produces better linear output.

2.5 **Resonant pressure sensor**

Resonant pressure sensors are widely known for their high performance in sensing pressure change. A sensor typically comprises a resonator structure and a diaphragm. The resonator structure is designed to vibrate at a particular resonant frequency. As pressure applied to the diaphragm, the induced stress changes the mechanical stiffness of the resonator. Thus, the resonant frequency changes as a function of the applied pressure [21]. The advantage of a well-design resonant sensor compared with a piezoresistive and capacitive sensor are shown in table 2.1.

Table 2.1 Performance comparison of resonant, piezoresistive and capacitive pressure sensor [36]

Type	**Resonant**	**Piezoresistive**	**Capacitive**
Output form	Frequency	Voltage	Voltage
Resolution	1 part in 10^8	1 part in 10^5	1 part in 10^4-10^5
Accuracy	100-1000 ppm	500-10,000 ppm	100-10,000 ppm
Power consumption	0.1-10 mW	≈10mW	<0.1mW
Temperature cross-sensitivity	-30x10^{-6}/°C	-1600x10^{-6}/°C	4x10^{-6}/°C

2.5.1 Mechanical theory

The resonator structure is the part of the sensor that vibrates with higher amplitude at resonant frequencies. Each resonator design has several different resonant mode shapes, whose frequency, displacement and Q-factor are varied [21][37]. The cantilever beam, for example, can have different mode shapes as illustrated in fig. 2.4. The beam is fixed at one end, which allows the free movement at the other end. This free movement results in three fundamental mode shapes by vibrating in different direction. Each mode will also have several higher-order resonant frequencies called overtones. These overtones have shorter wavelengths, thus, higher frequencies than the fundamental mode. Complex structures such as the double ended tuning fork or horizontal plate with four anchor points have more complex mode shapes.

Flexural vibration (a) Torsional vibration (b) Longitudinal vibration (c)

Figure 2.4 Cantilever beams in fundamental (a) flexural, (b) torsional and (c) longitudinal vibration modes [21]

A cantilever beam vibration can be modelled as a simple harmonic oscillator.

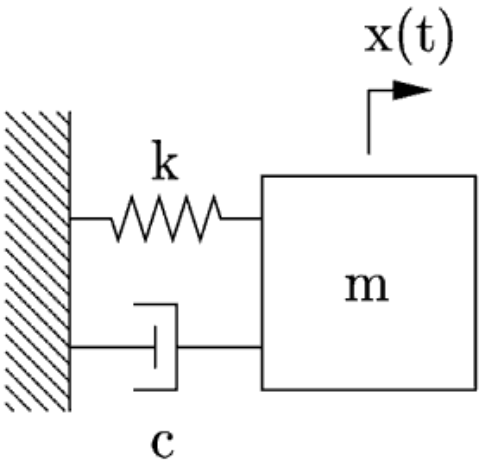

Figure 2.5 simple oscillator model for beam cantilever vibration (image from ocw.mit.edu)

The motion of the system can be described by

$$m\ddot{x} + c\dot{x} + kx = F_m \tag{2.2}$$

Where m, c, k, x and F_m are the effective mass, damping coefficient, spring constant, deflection and excitation force, respectively. Assuming that the oscillator operates in vacuum i.e. negligible damping coefficient. Solving Eq. (2.2) I obtain:

$$f_0 = \frac{1}{2\pi}\sqrt{\frac{k}{m}} \tag{2.3}$$

From Eq. (2.3), it can be clearly seen that changing the value of the effective mass and stiffness of the resonator will change its resonant frequency. Fundamentally, the resonant frequencies of a structure are determined by its stiffness, mass and damping coefficient [38][39]. If any of the two properties is changed, the resonant frequency will be altered.

2.5.2 Effect of stress on resonator

When an axial load is applied to a structure, a surface stress is generated. The surface stress will cause the structure to either stretch or compress. The deformation of the structure caused its resonant frequency to change. Applying a uniformly distributed axial load onto a beam structure, a constant surface stress, $\bar{\sigma} = dF_r/dL$ is produced. The equations of motion of a beam under axial loading have been presented previously [40][41][42], which predicts the *i*th-mode resonant frequency from the addition of a surface stress,

$$f_i^{+\bar{\sigma}} = \frac{1}{2\pi\sqrt{3}}\left[1 + \frac{2\bar{\sigma}L^3}{EI\pi^2}\right]^{1/2}\left(\frac{\alpha_i}{L}\right)^2\sqrt{\frac{EI}{\rho_b wt}} \tag{2.4}$$

Where *E, w and I* are the Young's modulus, width and moment of inertia of the object, and the α_i are determined from the frequency relation for a freely vibrating, cantilevered beam, the term inside the bracket of Eqn.(2.4) indicates that the introduced surface stress will affect the resonant frequency of the structure. If the stress is zero, the resonant frequency returns to the value of a stress-free structure. If the stress is tensile (i.e. $\bar{\sigma} > 0$), resonant frequency will tend to increase. On the other hand, if the stress is compressive (i.e. $\bar{\sigma} < 0$), resonant frequency will tend to decrease.

2.5.3 Effect of damping on resonator

Damping is one of three main factors that affect the resonant frequency of a microstructure, the other being mass and spring constant. A small damping coefficient means that most mechanical energy in the system is converted into vibration[43]. Thus, the amount of electrical energy required by the driving mechanism is reduced. Quality factor (Q-factor) can be used to quantify the mechanical effect of damping on a resonator system. It can be defined as the ratio of the total energy stored in the system to the energy lost per cycle due to damping effects. The Q-factor can also be calculated from the frequency spectrum of the system as shown from fig 2.6

$$Q = \frac{f_0}{\Delta f_0} \tag{2.5}$$

Where f_0 is resonant frequency and Δf_0 is the frequency bandwidth at 3dB point. A high Q-factor also means low unwanted coupling to the environment, thus increasing long term stability [21].

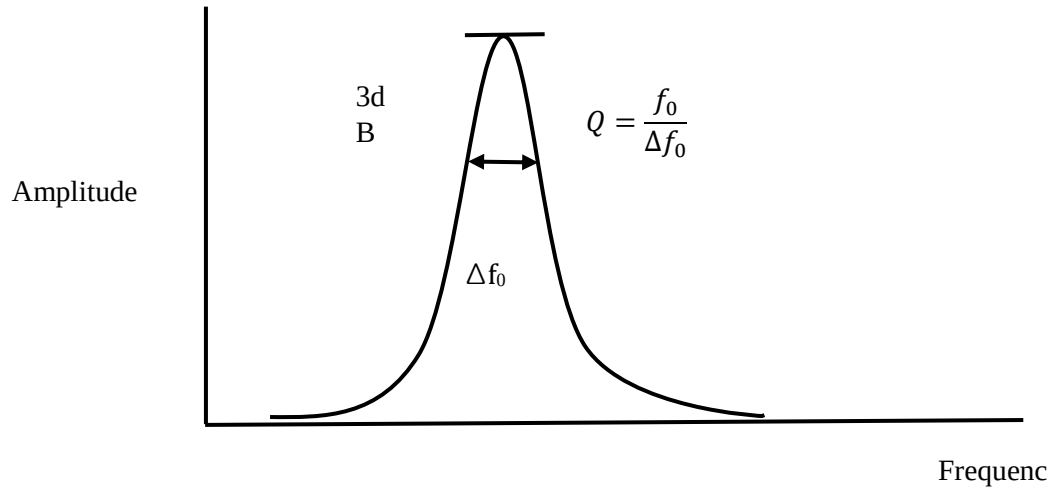

Figure 2.6 A typical frequency spectrum of a system at resonance.

The Q-factor depends on the mechanical properties of the resonator. Viscous drag and acoustic radiation, Q_a, radiation at the support, Q_s, and internal losses, Q_i, have been identified as the limiting mechanisms of the overall Q [44]. These Q-factors effect on the overall Q can be shown as[45]

$$\frac{1}{Q} = \frac{1}{Q_a} + \frac{1}{Q_s} + \frac{1}{Q_i} \tag{2.6}$$

If the resonator operates in fluid, mostly air, the energy loss due to Q_a is usually the largest of all the mechanisms. These losses are the result of mechanical energy transfer from the resonator surface to the fluid particles during vibration. As the result, the vibration of the resonator induces perpendicular and lateral movement in the surrounding fluid. Perpendicular vibration generates acoustic radiation while lateral movement leads to viscous drag losses. Acoustic radiation and viscous drag for different resonator design is shown in fig. 2.7. To reduce acoustic damping, I can either reduce the horizontal surface area[46] or lower the air pressure to vacuum [37][47].

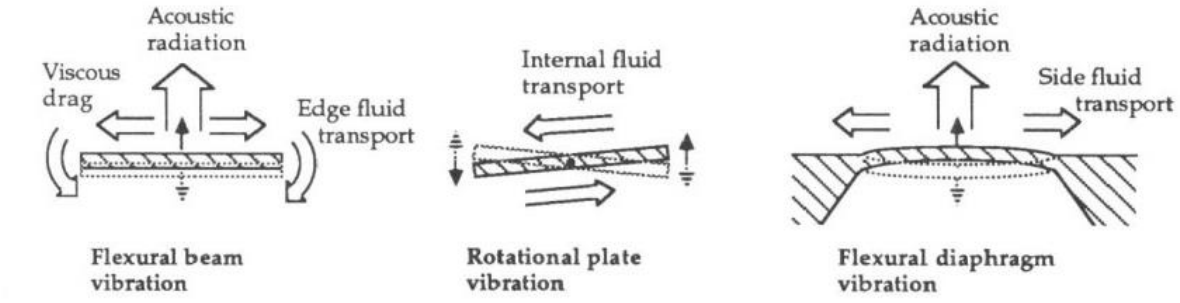

Figure 2.7 Damping effect of surrounding fluid have onto different vibrating structures.

Structural damping, $1/Q_s$, happens when the energy is lost at the support or end of resonator. To avoid this loss, the structure must be balanced during vibration. Following to Newton's second law, the structure has to have a fixed centre of gravity and its sum of force and moment has to equal to zero. Put another way, I am trying to minimise the motion of the support structure. The simple fixed-fixed beam structure damping coefficient can be increased by operating in an anti-phase mode of vibration [24]. In the anti-phase mode, the two-sides of the beam vibrate in opposite directions, thus cancelling out each other's moment. Multi-beam resonator design as shown in fig. 2.8 [48] has this dynamic moment cancellation by operating in different mode of operations.

Internal loss can be related to the resonator material, thus its properties. These losses can be caused by impurity, dislocations and thermoelastic loss of the material. However, single crystal silicon has shown high Q factors of 10^6 in vacuum [49] due to its high purity and is independent of dislocation below 673°C [44]. Heavily doped silicon structures have also shown Q-factors of the order 10^4 [50]. Most current

MEMS applications work with single crystal silicon as the main material, thus reducing the internal loss.

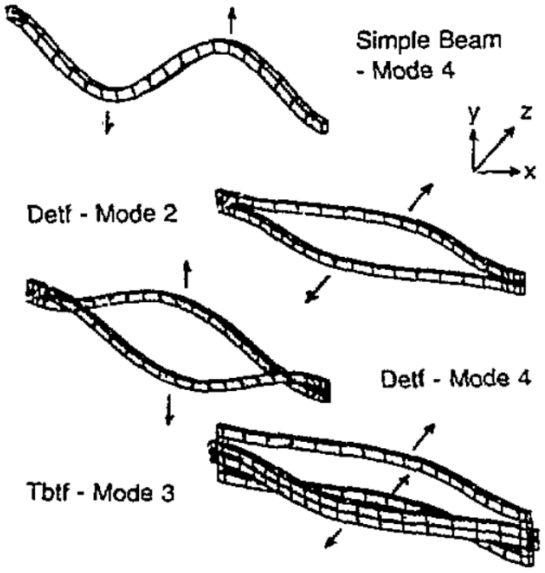

Figure 2.8 Balanced mode of vibration for single beam and multi-beam designs[48]

2.6 **Nonlinearities**

Nonlinearity alters the resonant frequency of a micro-resonator system. It exists in two forms, which are mechanical nonlinearity and electrostatic nonlinearity [51], which happens with capacitive detection. It is worth mentioning that nonlinearity also is classified into two groups of spring-hardening and spring-softening [52]. The nonlinearities in resonators can be modelled by including nonlinear springs k_1 and k_2 into the harmonic resonator:

$$m\ddot{x} + c\dot{x} + kx + k_1x^2 + k_2x^3 = F_m \quad (2.7)$$

Due to the nonlinear springs, the resonant frequency depends on vibration amplitude is

$$\omega_0^{'} = \omega_0 + \kappa x_0^2 \quad (2.8)$$

Where

$$\kappa = \frac{3k_2}{8k}\omega_0 - \frac{5k_1^2}{12k^2}\omega_0 \quad (2.9)$$

While mechanical nonlinear spring constants k_{m2} are typically positive, k_{m1} are negligible. Thus, κ_m are typically positive. As a result, spring hardening effect are typically from a mechanical nonlinearity. On the other hand, both electrostatic nonlinear spring constants k_{e1} and k_{e2} are typically negative, which results in a spring softening effect.

As shown in fig. 2.9, spring-hardening nonlinearity happens when the stiffness of the system increases, thus pushing the peak towards a higher frequency. Other the other hand, spring-softening nonlinearity has the stiffness of the system reducing, thus tilting the resonance peak to a lower frequency [52]. As the direct result, nonlinearity effect the maximum stable amplitude of the resonance peak. This is a significant factor since larger amplitude offers sharper output signal. It is therefore best to minimize the effect of nonlinearity in sensing applications.

Tocchio et al [52] proposes 2 different approaches to solve the spring hardening problem. The first method is to employ a cross-section "L-shaped" beam instead of conventional "I-shaped" one. It has been demonstrated that the former type of beam has better capacity of stress release as well as more flexibility at the supports, hence improving the maximum linear amplitude compared to the latter type of beam. The second viable method is to employ a bias DC voltage. The DC voltage introduces a spring-softening nonlinearity into the system, which cancels out the spring-hardening nonlinearity effect. Linearity is improved as the result.

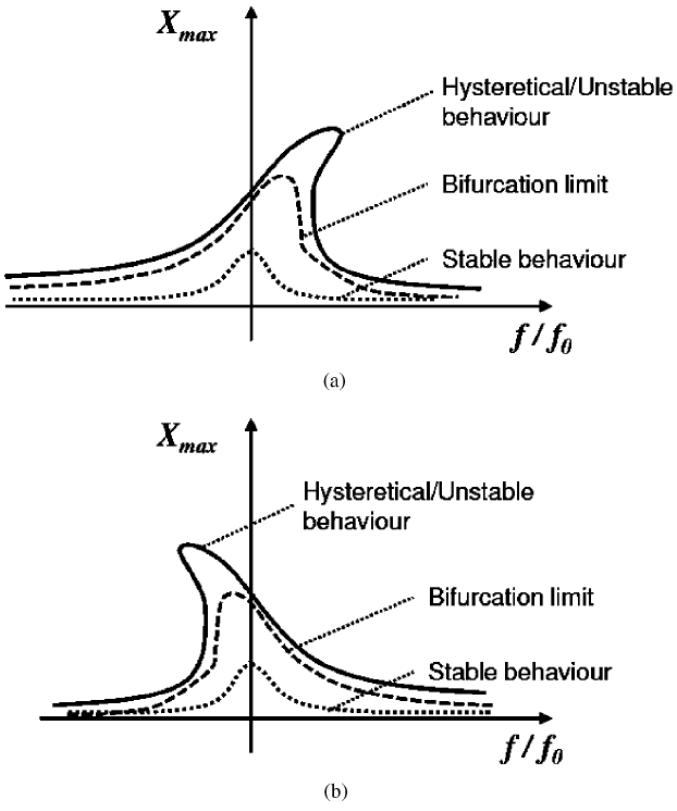

Figure 2.9: Nonlinearities of MEMS resonators: (a) spring-hardening nonlinearity and (b) spring-softening nonlinearity [51]

2.7 Excitation and detection mechanisms for a resonant sensor

In order to measure the resonant frequency of a mechanical resonator, it has to be actuated into vibration and the vibrations will then need to be detected as shown in fig. 2.10. When the applied pressure alters the resonant frequency of the resonator, the detection unit senses the change and produces the correct driving frequency. An amplifying feedback loop sends the sensed frequency back to the excitation unit, which adjust its driving frequency to the modified signal. The most common mechanisms include following effects: piezoresistivity, piezoelectricity, capacitance, optical and electromagnetic. This section will review these mechanisms.

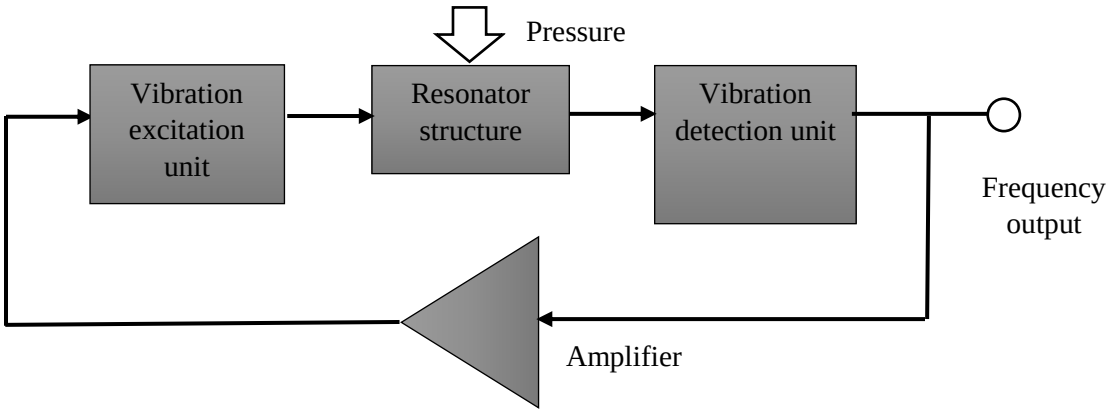

Figure 2.10 Block diagram of resonant pressure sensor

2.7.1 Electrostatic excitation and capacitive detection

In mechanical sensing applications, the most commonly used mechanism is electrostatic. The fundamental principle is applied two opposite charges onto two parallel planes, one being a part of the resonator while the other is a fixed electrode. Ignoring the fringing effects, the electrostatic force between the resonator and the electrode is given as:

$$F = \frac{\varepsilon_0 \varepsilon_r A V^2}{2g^2} \tag{2.10}$$

Where V is the applied potential, ε_0 is free space permittivity, ε_r is the permittivity of dielectric material, g is the gap between two plates and A is the overlap area of two plates. When an AC signal is applied, the charge polarity on the structure change periodically. Therefore, the resonator is attracted and repelled by the changing force, and hence will vibrate at the excitation frequency. The capacitive detection

mechanism shares the same principle as electrostatic driving. The capacitance between two plates varies periodically as the resonator oscillates. Thus, the change of capacitance can be used to determine the resonant frequency of the structure.

In MEMS application, parallel moving plates known as a comb drive or lateral comb are widely used for both electrostatic excitation and capacitive detection. The typical design can be seen in fig. 2.11. The motion of comb drive is assumed to be in the lateral direction (x) only. The comb design contains movable fingers and stationary fingers overlapped symmetrically. Thus, the electrostatic forces in the y-axis apply onto the finger in an equal and opposite direction, which cancel out and provide the stability in y direction.

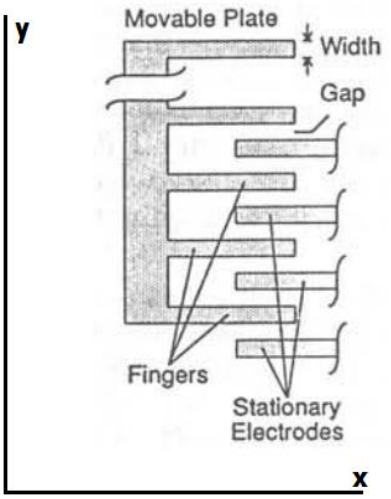

Figure 2.11 lateral comb schematic with moveable plate and stationary plate [53]

An application of lateral comb in a double-ended tuning fork resonator can be seen in fig. 2.12. The two outer combs drive the resonator into an anti-phase mode while the two inner combs detect the change in capacitance due to the motion. The total capacitance of the comb drive can be calculated by

$$C(x) = 2N\frac{\varepsilon_0(x_0+x)z_0}{y_0} \tag{2.11}$$

Where x_0 is the finger overlap length, y_0 is the gap between two fingers, z_0 is the finger thickness and N is the number of fingers in a single lateral comb.

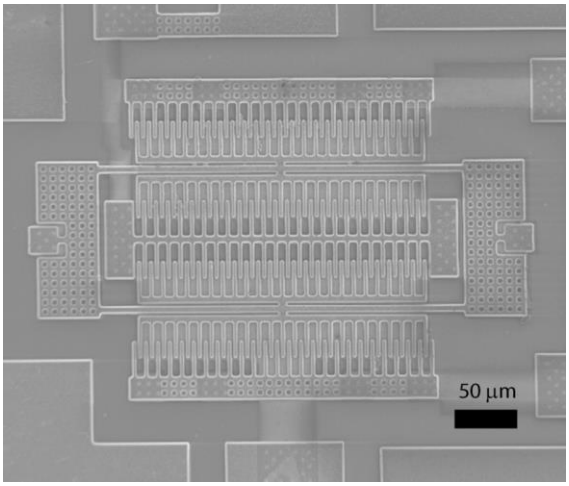

Figure 2.12 SEM picture of the comb drive design for DETF resonator [14]

Pull-in effect in electrostatic MEMS devices, especially lateral electrostatic excitation and detection mechanism, are common. When voltage is applied over the capacitance, electrostatic force works to reduce the gap between plates. At small voltages, the electrostatic voltage is countered by the spring force but as voltage increased the plates will eventually snap together. The force acting on the movable plate is obtained by [54]:

$$F = \frac{1}{2}\frac{\varepsilon A_{el}}{(d-x)^2}U^2 - kx \qquad (2.12)$$

Where $d - x$ is the gap between plates, U is the applied voltage, k is the stiffness of the movable plates, A_{el} is the overlapping area of two plates and x is the initial distance between plates.

2.7.2 Piezoelectric excitation and piezoelectric detection

Some crystal materials such as quartz have a built in dipole, which produce a change in electrical voltage when subjected to deformation [21]. This type of material also deforms in response to an applied voltage source. This property is called piezoelectricity and is the result of asymmetrical distribution of charge inside the material. The equation for charge generation from an applied force is given as

$$Q = d_{ij} \times F \qquad (2.12)$$

Where d_{ij} is charge coefficient. Hence, the resultant voltage is

$$V = \frac{Q}{C} = \frac{d_{ij}Ft}{\varepsilon A} \qquad (2.13)$$

Where ε is the material permittivity, A is the area, t is the thickness. As silicon has a symmetrical structure, it, hence, is not piezoelectric material. Several other materials such as PZT or Zinc oxide (ZnO) have a high piezoelectric constant and can be deposited onto a silicon wafer. However, the introduction of a layer of polycrystalline

thin-films reduces the Q-factor as well as increases the temperature coefficient. Fig. 2.13 provides a visual representation of the piezoelectric detection mechanism.

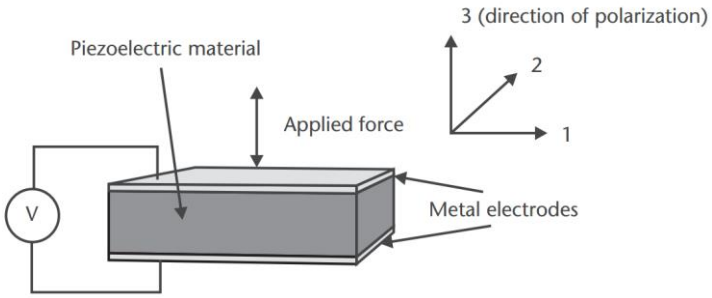

Figure 2.13 Piezoelectric effect. Applied force generate a voltage between two electrodes [24]

Based on their mode of vibration, the resonators which employ piezoelectric drive and sensing can be classified into flexural and width-extensional vibrations [55]. Flexural vibration is commonly used in a beam shaped resonator that is formed by a stack of piezoelectric material or a layer of piezoelectric material on top on a structural layer. The piezoelectric material is excited then deforms which causes the structural layer goes into vibration in a flexural mode. An example of a beam resonator with ZnO film on top is shown in fig. 2.14.

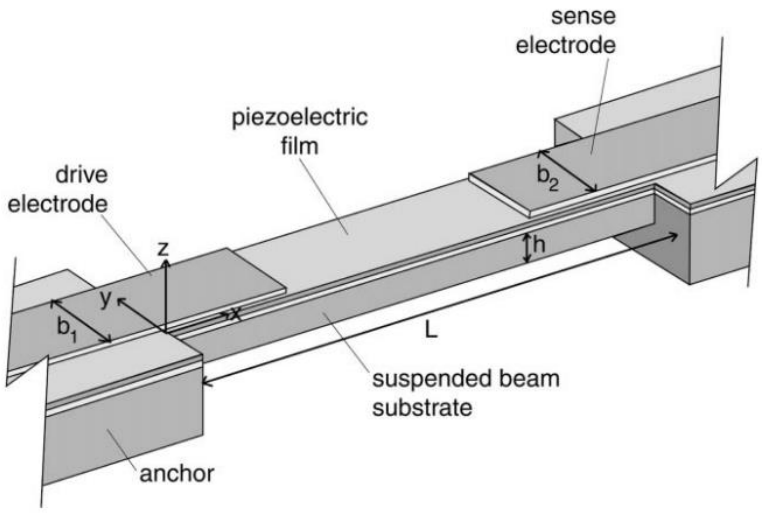

Figure 2.14 Cross-section model of the piezoelectric doubly-clamped beam resonator [56]

Width-extensional vibrations are widely used with thin film plate resonators. The simplest form of width-extensional vibration is the fundamental resonant frequency. In this form, opposite voltages are applied to electrodes on the top and bottom of the plate resonator. The electric field then excites the piezoelectric material in the vertical direction as shown in fig. 2.15. The number of electrode pairs can be increased to excite the resonator into a higher mode of operation for high frequency application.

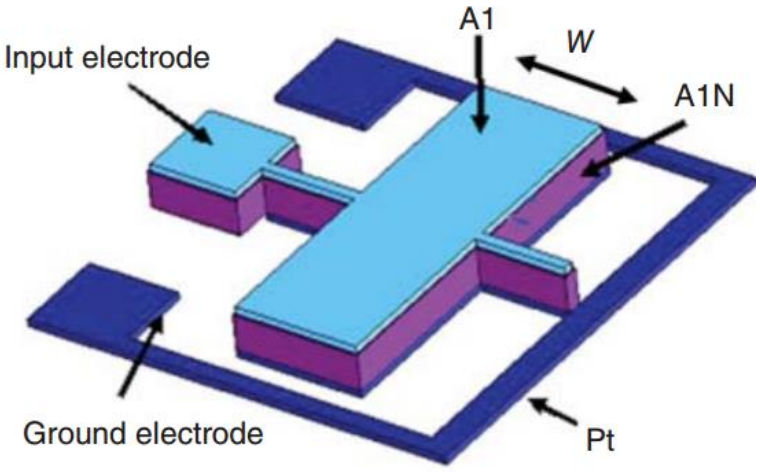

Figure 2.15 Schematic model of a resonator plate vibrating in its fundamental mode

2.7.3 Optical thermal excitation and optical detection

Thermal excitation is the method that takes advantage of laser beam power. A laser beam is aligned to cover part of the resonator and the intensity of the incident light is varied periodically. The absorbed light energy will generate a thermal stress, which share the same frequency with excitation laser. This thermal stress, then, will lead to vibration in the resonator.

Optical methods can also be used to detect the vibration. There are several schemes available including intensity modulation and phase detection. Intensity modulation provides a simple solution by employing optical detectors to measure the intensity variation. The main drawback is low signal-to-noise-ratio, since there are many noise-related issues such as change in temperature and the performance of detectors. On the contrary, phase detection devices such as interferometers are not affected by the variation of the intensity; hence provide much more accurate results. Two or more optical beams, which have the same frequency, are used to interact with the resonator. The reflective lights then undergo interference to produce the difference between two phases. This system can resolve sub-wavelength variation, which lead to the measurement of submicron displacement of the resonator.

2.7.4 Piezoresistive detection

For piezoresistive pressure sensor, piezoresistive effect is defined as the change in resistance of the material due to applied strain. Gauge factor (G) is the fractional change in resistance per unit strain.

$$G = \frac{dR/R}{\varepsilon} \tag{2.14}$$

Where δR is the change resistance, R is total resistance and ε is the applied strain. Since $\varepsilon = dl/l$ and$R = \rho l/wt$, I can derive

$$G = \frac{dp/p}{\varepsilon} + (1 + 2v) \tag{2.15}$$

Where v is Poisson's ratio and p is resistivity of the material. The second term, which is due to geometric effect, is significantly smaller than the piezoresistive effect in contribution to the total gauge factor in silicon, especially in the case of single crystal silicon.

To enhance the piezoresistive effect, n-type or p-type dopant can be implanted into the silicon wafer. Resistance can be increased or decreased depending on the type of strain and direction of strain relative to crystal orientation and current flow. The microstructure at resonance usually has a displacement in the micron range, which leads to periodic strain cycle across the resonator. By optimising the amount of implantation, the accuracy in resonant frequency detection is increased.

To increase the output signal, four piezoresistors are usually employed in a Wheatstone bridge. By arranging the resistors' location on the resonator structure, both the longitudinal and transverse coefficient are exploited to boost the output signal for the desired vibrating mode while supressing unwanted resonant modes. Brand, *et al* [55] simulated two different bridge layouts using FEM to find the uniaxial stress with their desirable vibrating mode as shown in fig. 2.16 (a),(b) . The frequency response of the model in fig. 2.16(c) shows a clear peak for desired in-phase mode while suppressing other modes.

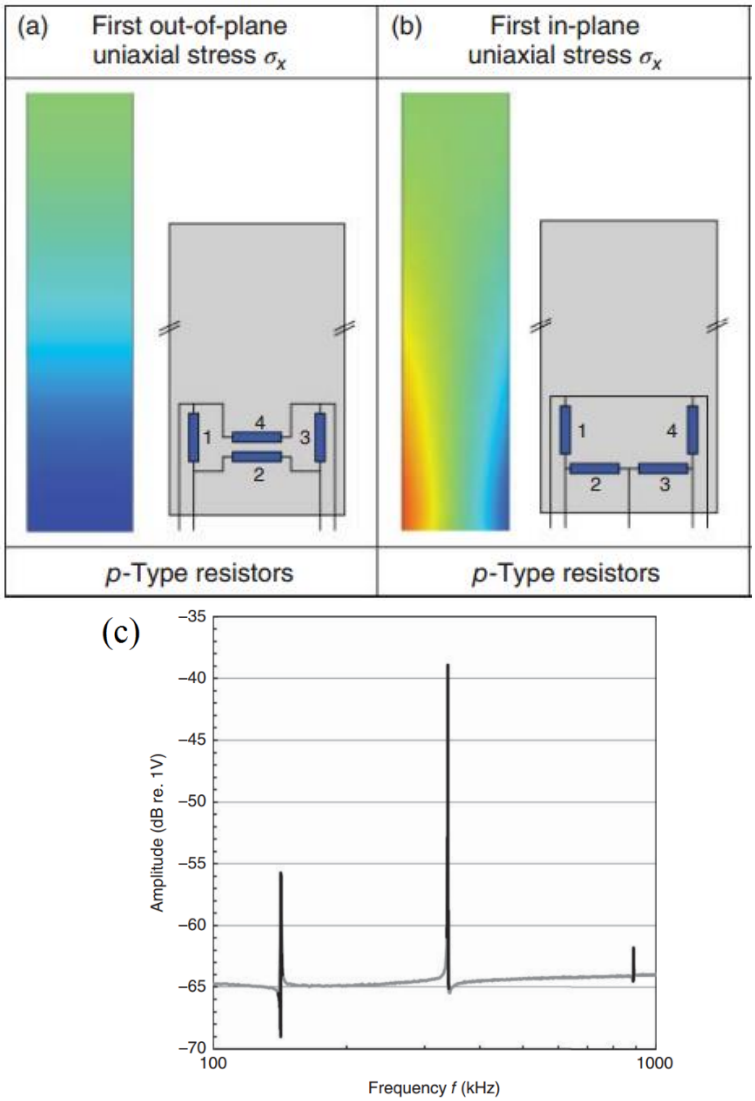

Figure 2.16 (a) out of plane, (b) in plane uniaxial stress response in two Wheatstone bridge layouts and (c) in-plane frequency response of the resonator

2.7.5 Magnetic excitation and magnetic detection

The principle of magnetic excitation is the use of electromagnetic force (Lorentz force). As the current-carrying resonator is placed inside a magnetic field, Lorentz force is produced in the direction perpendicular to both the current and the magnetic field. The force magnitude will be proportional to both current and magnetic field. The equation of the force is given

$$\boldsymbol{F} = \boldsymbol{I}\boldsymbol{l} \times \boldsymbol{B} \tag{2.3}$$

Where $\boldsymbol{I}$ is the vector of current, $\boldsymbol{B}$ is the vector of magnetic field and $\boldsymbol{l}$ is the vector whose magnitude is the length of the conducting element. The magnetic actuators are commonly placed outside the silicon chip frame as shown in fig. 2.17 since compatible permanent magnetic materials are very limited. In addition, the vibration of the resonator inside the magnetic field generates electromagnetic induction, which

creates an induced voltage. This voltage can be connected to a circuit to detect the vibration.

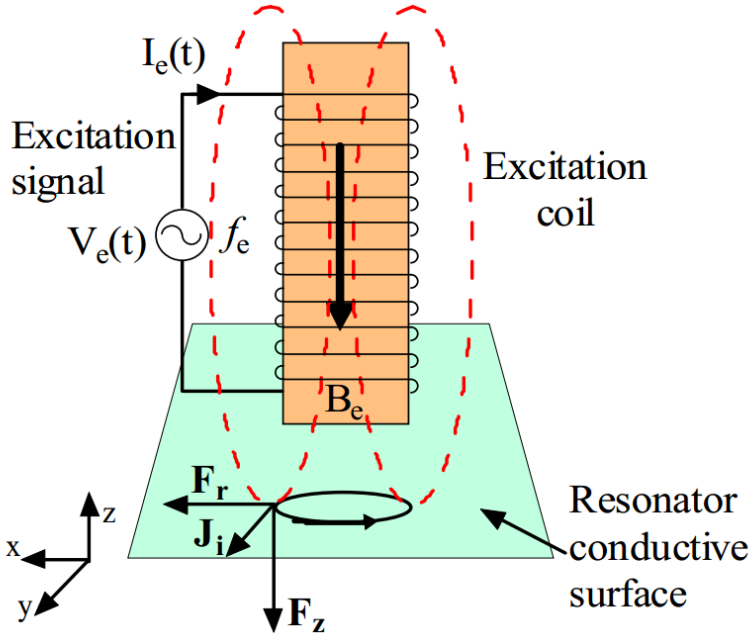

Figure 2.17 Schematic diagram of the magnetic excitation principle[57]

2.7.6 Discussion

Table 2.1 summaries all the widely used excitation and detection mechanism. The suitability of these mechanisms for a resonator driving or sensing depends mostly on the magnitude of the driving force and practical consideration regarding the sensor fabrication process and operating environment. Methods such as optical thermal/optical and magnetic/magnetic cannot be integrated into the sensor structure. Thus, these methods are preferable for testing devices before designing an integrated circuit for driving and sensing. The piezoelectric/piezoelectric method is suitable for low Q device such as thin-film polysilicon resonators. Electrostatic/ capacitive mechanism is widely used in commercial products due to its low cost and simplicity in implementation. It is worth mentioning that piezoresistive detection offers a simple and accurate method for sensing. In addition, piezoresistive detection can also be combined with electrostatic drive and be integrated into small size sensor design.

Table 2.2 Summary of excitation and detection mechanism

Excitation mechanism	**Detection mechanism**
Electrostatic	Capacitive
Magnetic	Magnetic
Piezoelectric	Piezoelectric
Optical thermal	Optical
Electrostatic/ Optical thermal	Piezoresistive

2.8 **Previous MEMS silicon resonant pressure sensors**

Despite having different application objective, most research groups investigating silicon resonant pressure sensor have similar conclusions on the key parameters. The resonator structures are designed to have sufficient input parameter selectivity i.e. diaphragm deflection under pressure and sensitivity of the resonant frequency [21]. These structures also need high Q-factor, which results in high stability and sensitivity. For high-pressure application, it is important that the sensor can operate in a wide range of pressure while maintaining the long-term stability. These factors are under consideration while reviewing the literature.

Burns, *et al.* [58] presented the feasibility of using simple polysilicon micro-beam structure in a resonant pressure sensor. Different excitation and detection mechanisms including electrostatic drive/piezoresistive sensing, optical drive/optical sensing, piezoelectric drive/optical sensing and electrostatic drive/laser sensing were tested. In order to apply the piezoresistive sensing method, a strain gauge resistor was fabricated onto the structure as shown in fig. 2.18(a). Operating at fundamental frequency of 223 kHz, the sensor showed a sensitivity of 3880 Hz psi $^{-1}$ for a range of 5 psi. The Polysilicon beam design employs the lateral mode, which are unsymmetrical for this structure. Thus, the Q factor is reduced significantly. Optical sensing can be done in experimental environment but can’t be used in commercialised product, thus limiting the application of the device.

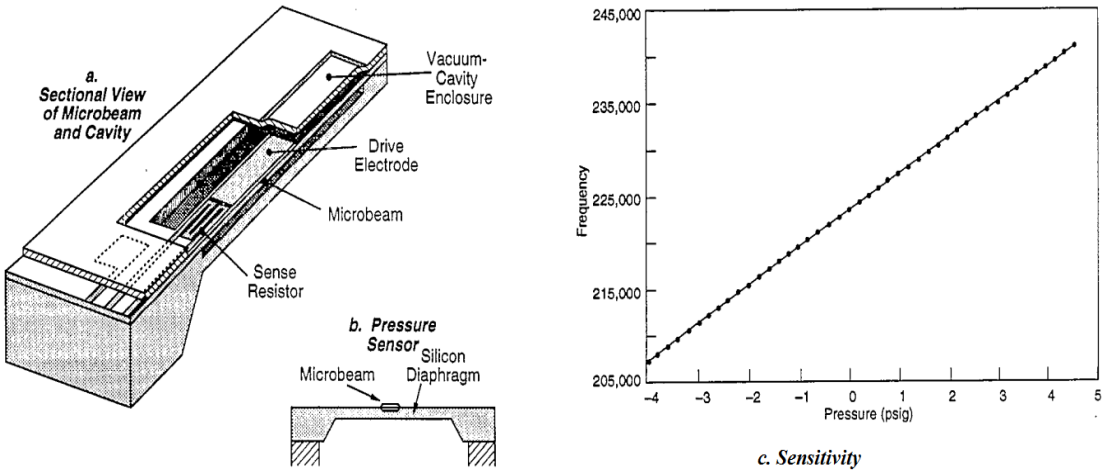

Figure 2.18 (a) (b) sectional view of the microbeam resonator and (c) its sensitivity performance.[47]

Bianco, *et al* [59] presented a silicon microcantilever resonator for absolute pressure measurement. The cantilever is fabricated from single crystal silicon and is 800 µm long, 100 µm wide and 5 µm thick as shown fig. 2.19 (a). The resonator is electrostatic-excited and capacitively-detected using the side electrodes. The recorded unstrained resonant frequency and Q factor are 7690 Hz and 10000 respectively. Under applied pressure, both the Q factor and resonant frequency reduce as seen in fig. 2.19 (b). The sensitivity level of 60 Hz/bar for pressure range from 0 to 500 mbar was recorded. Since cantilever is an unsymmetrical structure, the obtained Q factor is reduced. Thus, the sensor need to address its long-term stability prior to any commercialized attempt.

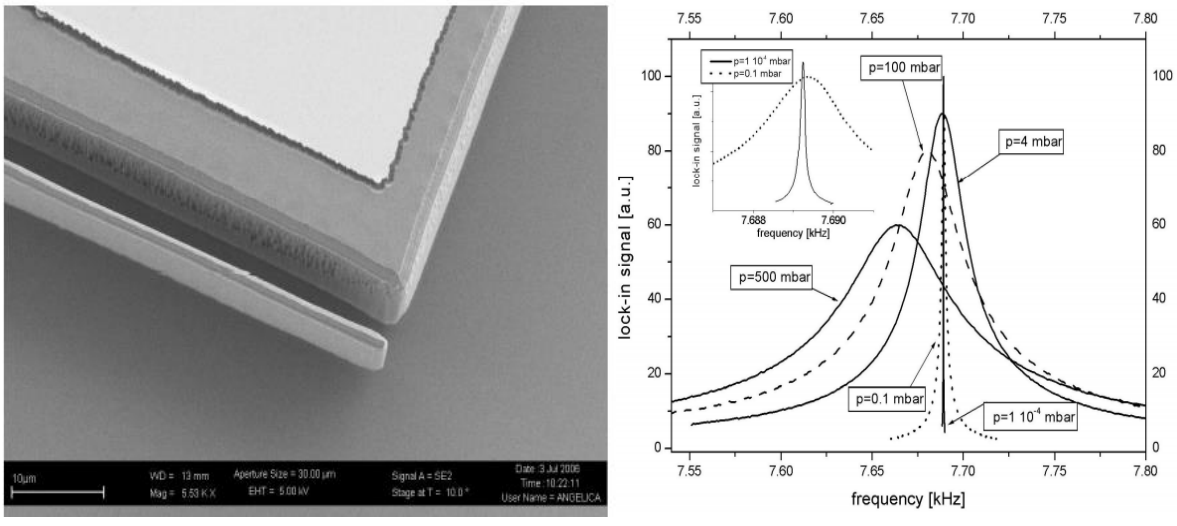

(a) (b)

Figure 2.19 (a) SEM picture of the resonating cantilever and (b) its performance against applied pressure [59]

Fonseca, *et al* [60] have developed a ceramic passive LC resonator design for pressure sensing. The design consists of two diaphragms which are separated by an evacuated

cavity in the middle as shown in fig. 2.20 (a). The two diaphragms are in close proximity with two electrodes to form two capacitors. This circuit is connected to an inductor coil and become an LC passive resonator. When pressure is applied, the two diaphragms deform, hence change the value of the capacitor. The resonant frequency of the system changes as a result. Under unstrained condition, the resonator obtains 16.99 MHz and 62 for its resonant frequency and Q factor respectively. Three samples with an unstrained resonant frequency of 16.99 MHz, 19.49 MHz and 22.68 MHz were tested against applied pressured from 0 to 7 Bar as shown in fig. 2.20 (c). The measured sensitivities are 105 kHz/bar, 154 kHz/bar and 164 kHz/bar respectively. The sensitivities level reduces when the applied pressure exceeds 3 bar. Low Q in combination with thin diaphragm design has prevented dual diaphragm structure from being used in harsh environment such as high pressure high temperature reservoir.

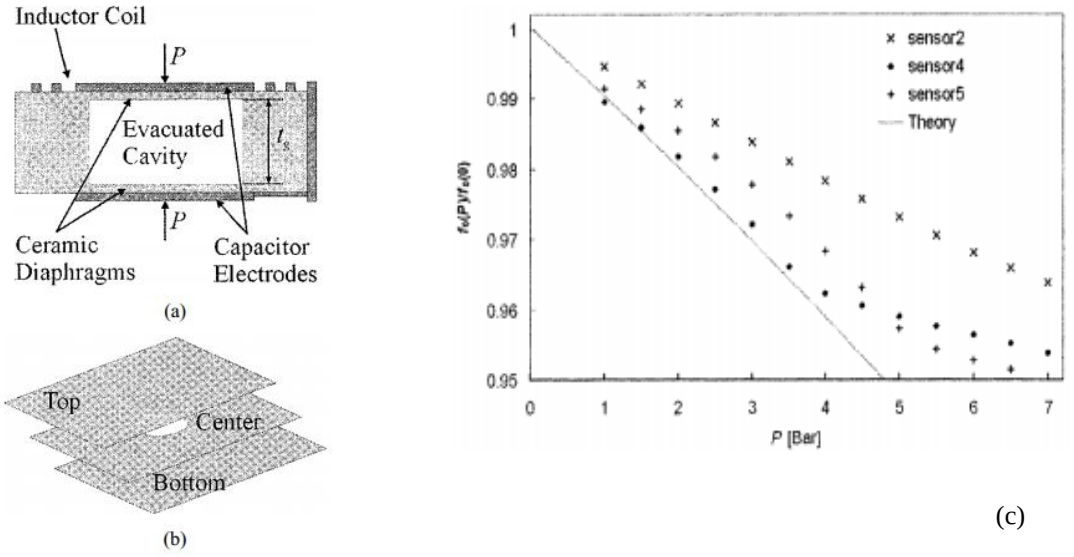

Figure 2.20 (a) cross sectional view, (b) 3D layer construction of the ceramic resonator and (c) samples' performances against pressure[60]

Baldi, et al [61] introduce another micro-machined passive pressure sensor design. The micromechanical part contains a planar coil and a flexible membrane attached to a piece of ferrite as seen in fig 2.21 (a). An applied pressure will deflect the membrane, which in turn pushes the ferrite to the coil, hence increasing the inductance of the system. The increasing inductance results in a reduced self-resonant frequency. This design produces an unstrained resonant frequency of 31.8MHz and Q factor of 5.4. The measured sensitivity is 9.6 kHz/kPa for the pressure range from -20 kPa to 60 kPa. This is another example of low Q, low operational range pressure sensor.

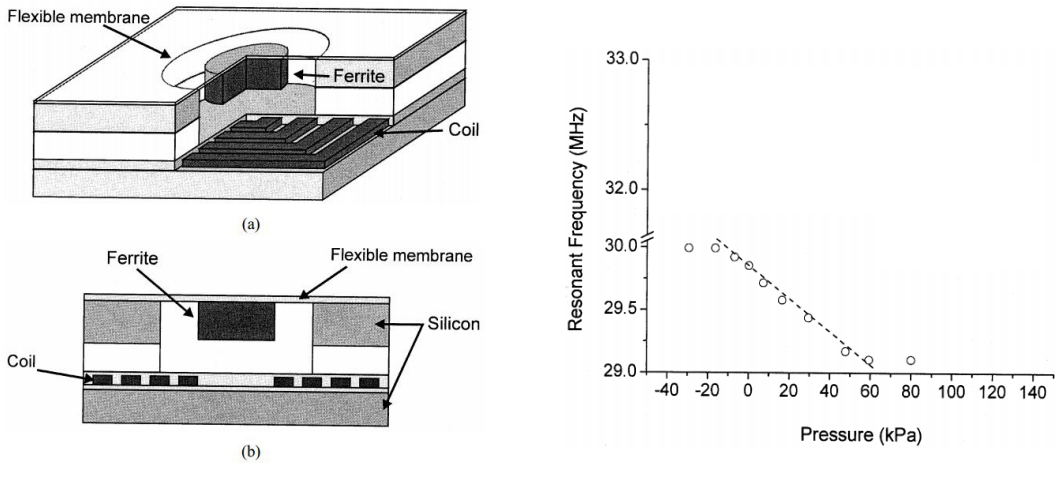

Figure 2.21 Inductive passive resonator: (a) three-dimension model (b) cross sectional display and (c) resonant frequency against applied pressure

Welham, et al. [62] presented a laterally driven mechanism on a single-mass resonator structure. The resonator uses electrostatic comb finger as the driving and sensing structure for in-plane flexural vibration. This approach reduces the sensitivity of the Q-factor to the cavity gas; hence reducing viscous drag and the overall damping coefficient. However, the resonator testing experienced a dramatic drop in Q-factor from 50 000 in vacuum to 50 in air. The resonator structure comprised an inertial mass supported by four beams fabricated from polysilicon as shown in fig. 2.22(a). In operation, the whole structure moves to one side before returning to its original position. Thus, its central of gravity is always in constant movement. As a result, most of its energy disperses quickly to the external world, hence, the Q-factor reduction occurs. The sensor still produced a sensitivity of 8.8 kHz bar $^{-1}$ with a resonant frequency of 52 ± 15 kHz. The operating range is limited to 3.5 bar as a result of small distance between the resonator and the diaphragm.

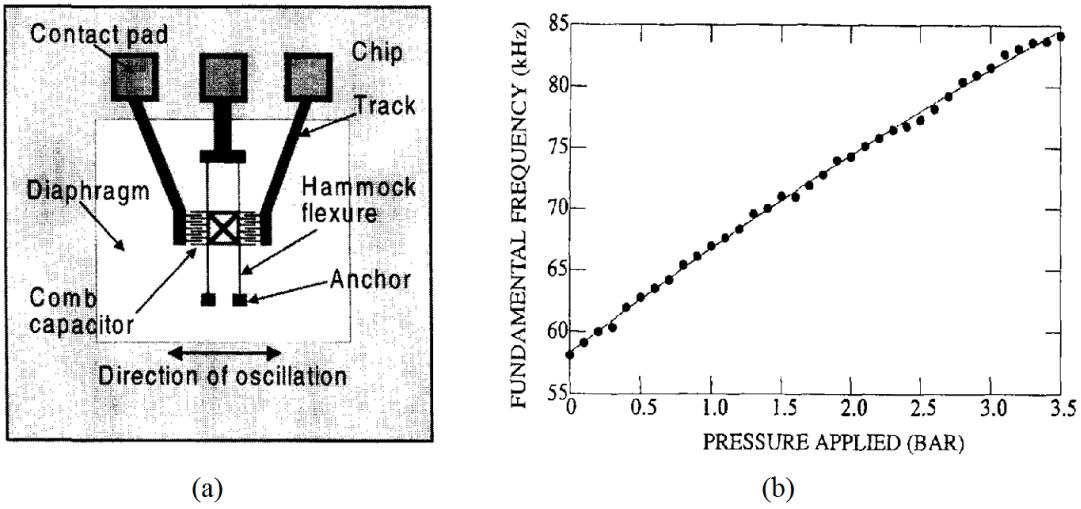

(a) (b)

Figure 2.22 (a) Structure of lateral resonant pressure sensor and (b) its frequency shift under applied pressure at 19.5 ^{0}C [62]

Corman, et al. [63] presented a planar double-loop structure as a resonator for pressure sensing. The resonator consists of two symmetrical rectangular loops bound to a fixed centre axis as shown in fig. 2.23 (a). The structure is encapsulated by two bonded glass lids with integrated electrode for excitation and detection. The encapsulation is used to increase the Q factor of the resonator. The measured Q factor is 20 000 for 0.1 mBar pressure and is reduced to approximate 5000 for 1000 mBar. The recorded unstrained resonant frequency is 8848 kHz. The sensitivity is 8 Hz/Bar for pressure ranges from 0.1 mbar to 1000 mbar with a high level of non-linearity. The detail can be seen in fig. 2.23 (b).

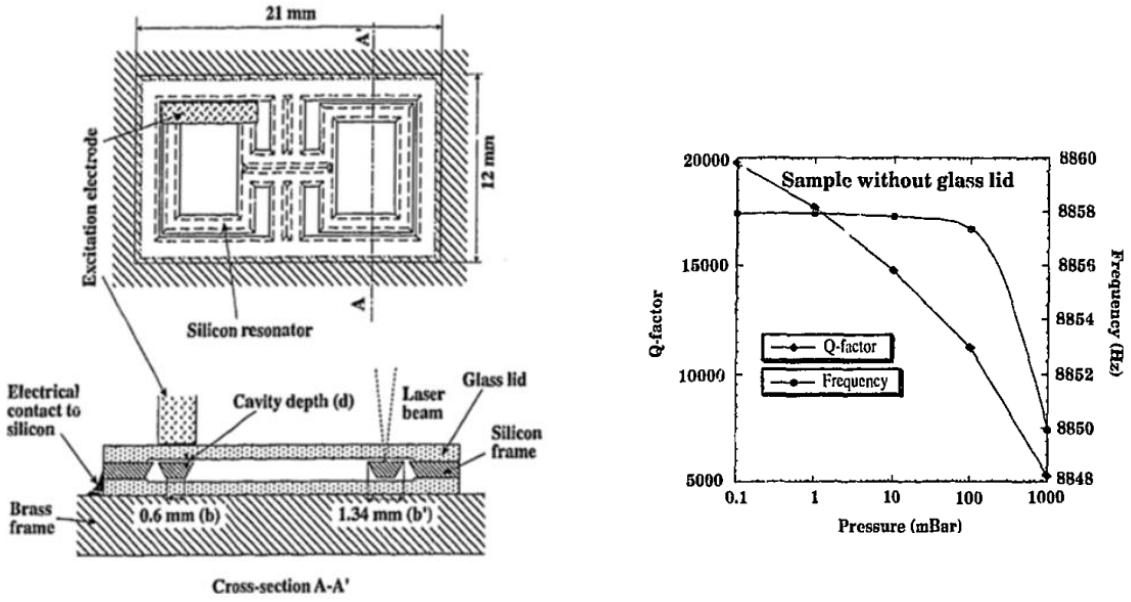

(a) (b)

Figure 2.23 (a) top view and cross-sectional view of the sensor and (b) Q factor and resonant frequency against pressure

Southworth, et al [64] introduced a drumhead resonator design fabricated from a silicon on insulator wafer. The resonator is a circular-shaped membrane as shown in fig 2.24 (a). When air is compressed underneath the membrane, it induces a change in the spring constant of the membrane. As a result, the resonator shows a linear relationship with applied pressure. The device is excited and detected optically. Three variations of the resonator with differing air gaps between the resonator and the handle wafer were tested for resonant frequency and its quality factor. The result showed similar fundamental resonant frequencies of 9.38 ± 0.15 MHz and Q factor of approximately 1.4×10^4. However, the change in resonant frequency under pressure showed different level of sensitivity for different variation of the air gap as shown in fig. 2.24 (b).

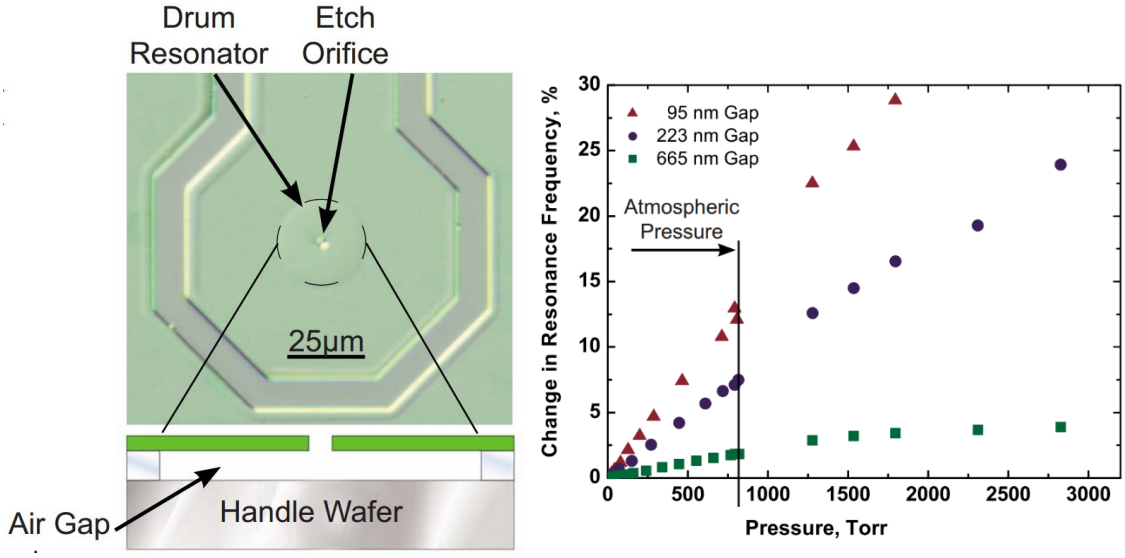

(a) (b)

Figure 2.24 (a) Drum resonator top view and (b) variation of the sensor performances against pressure

Defay, et al [65] presented a vibrating membrane that yield a high sensitivity. The membrane is composed of a $Pb(Zr,Ti)O_3$ (PZT) laying on top a Si layer as shown in fig.2.25. Under zero pressure, the resonant frequency was measured to be 18.6 kHz. The device is excited electrostatically while being detected by laser vibrometer. The change of resonant frequency while applying different pressures shows the sensitivity of 115 Hz/mbar and high level of linearity for pressure from 15 mbar to 140 mbar. No record of Q factor was provided.

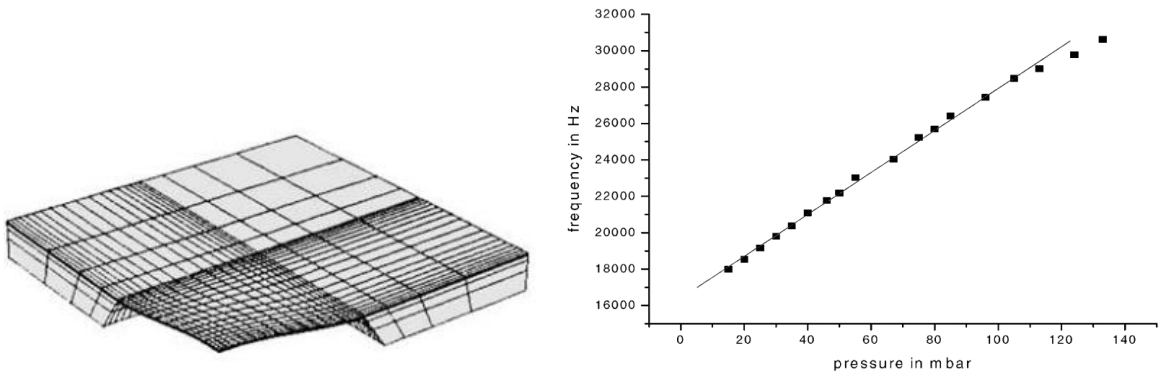

(a) (b)

Figure 2.25 (a) FEM model of the membrane and (b) its performance against pressure [65]

Stemme, et al. [6] proposed a balanced resonant pressure sensor that can operate both in air and vacuum with a high Q-factor. The resonator was made from single crystal silicon, comprised of two parallel diaphragms bonded together. This structure was fixed to the chip frame via four supporting beams as shown in fig. 2.26(a). The device operates in torsional mode. The cavity trapped between two diaphragms acted as the reference pressure. As a result, the two diaphragms deflected outwards or inwards according to the ambient pressure. This mode of operation removed most of the viscous drag while maintaining a fixed centre of gravity, therefore, yielded a Q of 2400 in air and of 80 000 in vacuum. The device produced a sensitivity result of 14% bar $^{-1}$ with resonant frequency about 17 kHz in vacuum reference pressure via electrostatic drive and optical detection. The pressure range in their experiment was 1 bar, which is suitable for barometric pressure devices.

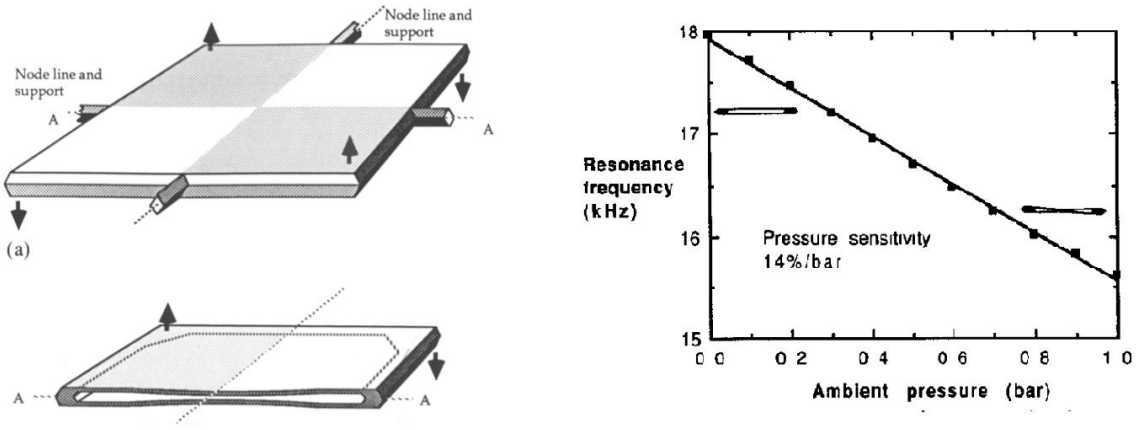

(a) (b)

Figure 2.26 (a) Dual-diaphragm cavity structure cross section view and (b) its sensitivity to ambient pressure [6]

Another resonant barometric pressure sensor structure has been reported to achieve a low long term stability error of 0.05% F.S over period of 3 months as shown in fig. 2.27 [66]. This is a promising result for pressure sensing in a hostile environment such

as downhole. However, the resonator design has a limited maximum pressure input to only 11.8 MPa. The resonator as shown in fig. 2.28(a) consists of four "H" type doubly clamped micro beams connecting via three-anchor point. The whole structure is fabricated from the top single-crystal silicon of a silicon on insulator (SOI) wafer, which results in Q-factor of 6000 in vacuum and 1200 in air. The diaphragm deflection under pressure induces an axial tensile tress on the central beams while causing an axial compression stress on the two side beams. All four beams operate in lateral vibration via electromagnetic excitation. The sensitivity was recorded to be 5.2 kHz bar $^{-1}$ and 5.3 kHz bar $^{-1}$ for the side beams and centre beam, respectively.

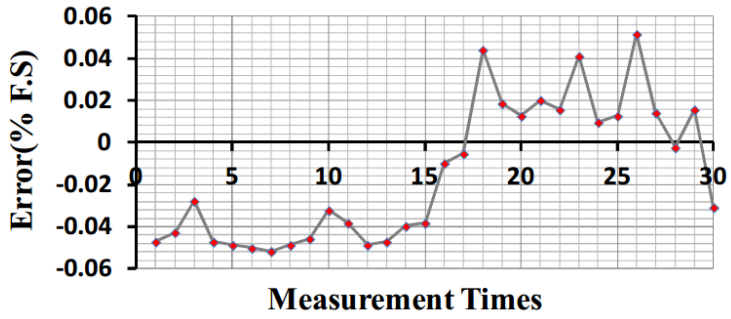

Figure 2.27 Long term stability of "H" type doubly-clamped beam pressure sensor at 20°C, 1atm over 3 months period [66]

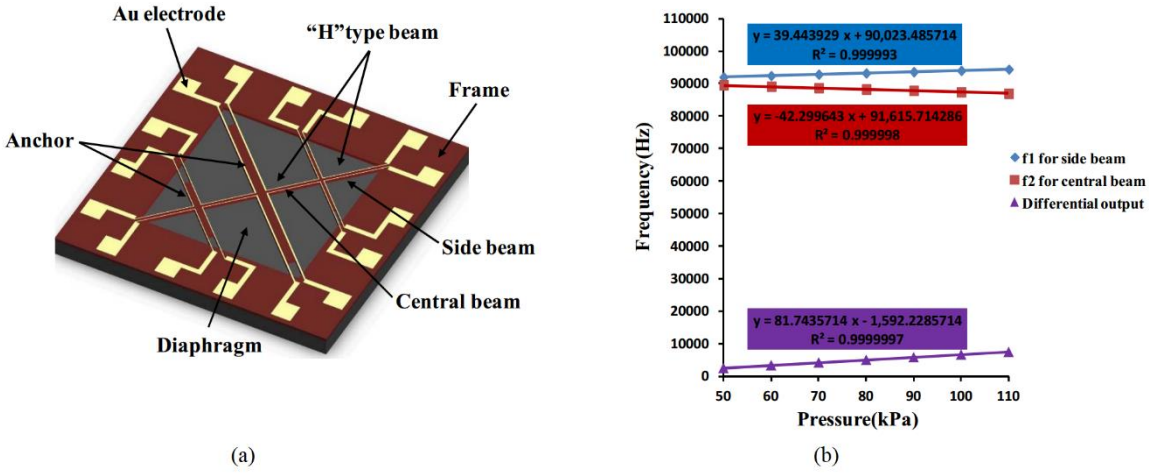

Figure 2.28 (a) the schematic of "H" type doubly-clamped beam pressure sensor and (b) its sensitivity performance at 20°C[66]

Further research on "H" type doubly clamped resonator encapsulation has shown a long-term stability of the structure to 0.01% F.S/year [67]. A layer of polysilicon was grown on top the resonator, entrapping it inside the cavity formed from the newly

developed layer and the diaphragm as shown in fig.2.29 (a). A 10 µm thickness cavity wall was able to withstand a high pressure of 100 MPa. Inside the vacuum cavity, the resonator achieved a Q factor of above 50 000. The vibration was supported by an external magnetic field via an AC feedback loop. The sensitivity was presented in terms of a gauge factor of about 3000.

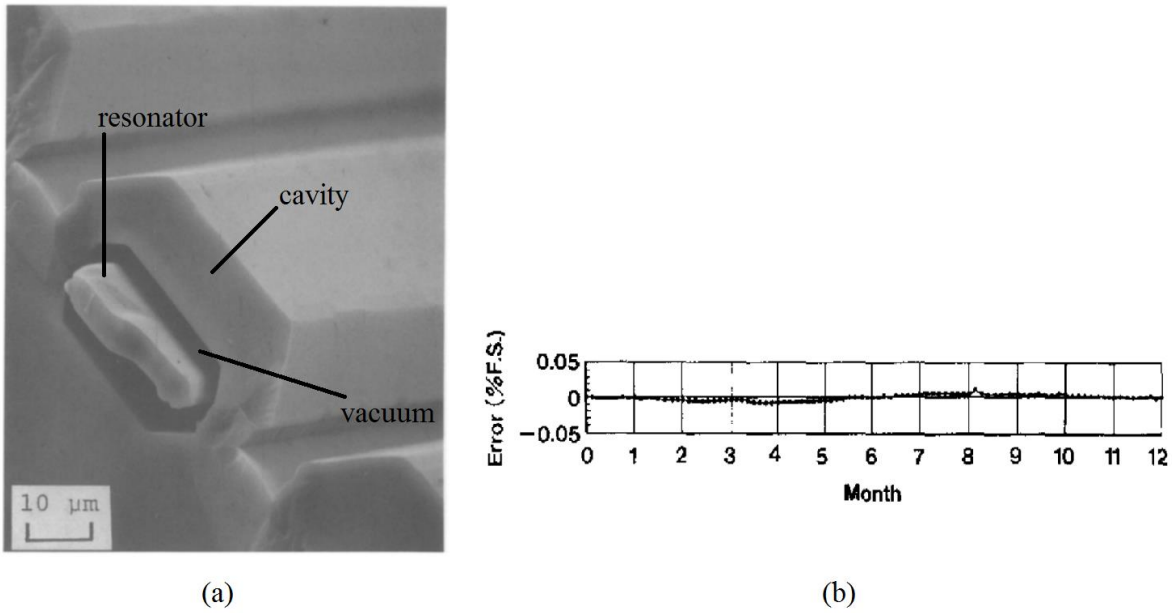

Figure 2.29 (a) cross-sectional SEM view in one beam of the "H" shaped resonator and (b) its performance in long term stability at room temperature [67]

Beeby, et al. [5] presented a double-ended tuning-fork (DETF) resonator structure for pressure sensing. The resonator consisted of two identical beams, joined at fixed ends to the surroundings as shown in fig. 2.30 (a). Operated in lateral anti-phase mode, the structure experienced a fixed centre of gravity and a minimum amount of coupling energy, which increased the Q-factor to 40 000 in vacuum. Under applied pressure, the diaphragm moves perpendicular to the vibration and increase the stiffness of the resonator, hence, cause the resonant frequency to shift. Piezoresistors were deposited at the edges of the beam, where displacement is the largest, as the detection mechanism for frequency measurement. Finite element analysis indicated a shift of 21.56 kHz for eight bar pressures in anti-phase mode with a resonant frequency of 169.54 kHz. However, the structure exhibited a hard spring effect due to the long and thin design of the two beams, as shown in the amplitude against frequency graph in fig. 2.31. This lead to amplitude stiffening of the resonator and hence affects the linearity of the output signal. The test device was fabricated from a silicon-on-insulator (SOI) wafer, which enabled the use of crystal silicon for resonator structure.

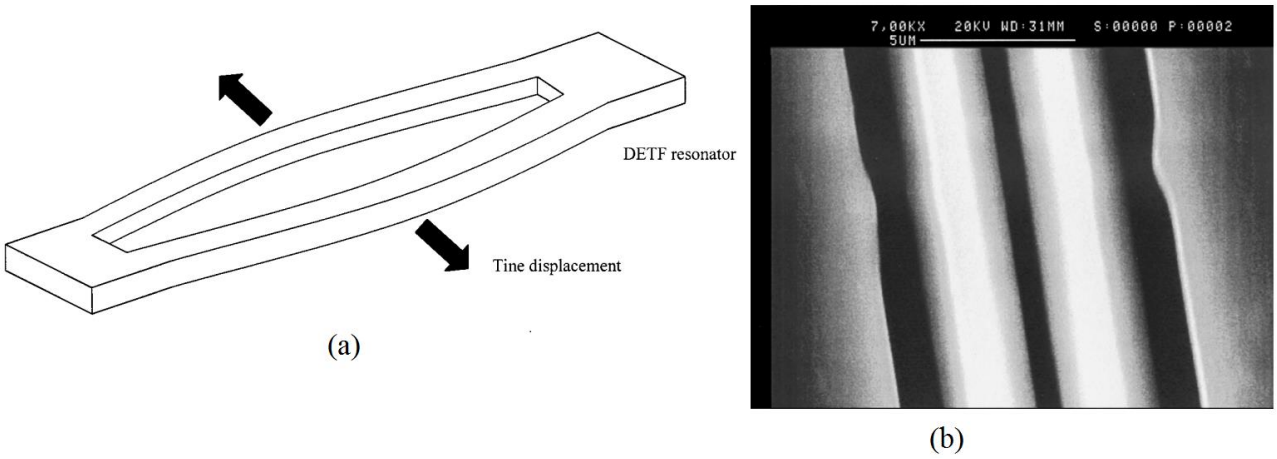

Figure 2.30 (a) Antiphase mode operation of DETF resonator and (b) SEM view of the beams at resonant frequency [5]

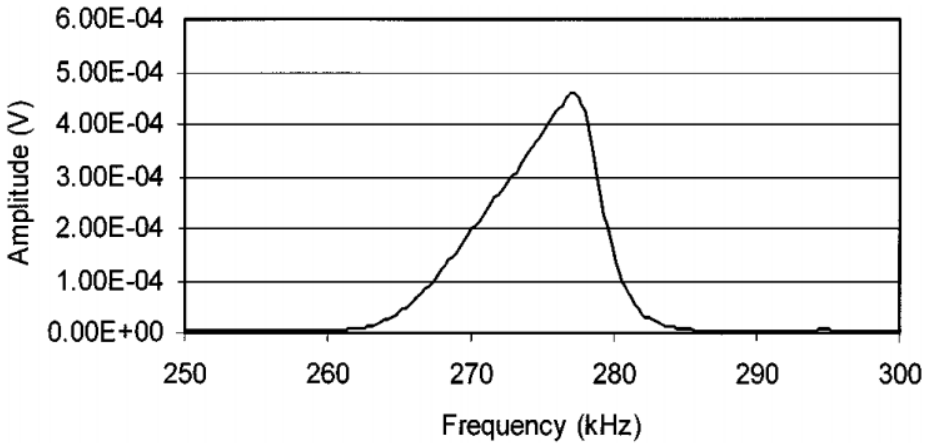

Figure 2.31 amplitude against frequency plot of DETF resonator [5]

Wojciechowski [68] also published research on a DETF resonator as a strain sensor as shown in fig 2.32 (a). The resonator is fabricated from polysilicon, so the Q factor is much lower than Beeby's single crystal design. Measured value of Q is 370 at atmospheric pressure. The sensor deploys separate comb drives as the excitation and detection mechanism. A resonant frequency of 217 kHz was measured. An axial strain actuator is connected to the design to measure the strain sensitivity of the resonator. The measured sensitivity shown in fig. 2.32 (b) is 39 Hz/με for the range of applied strain from 0 to 25με with a high level of linearity.

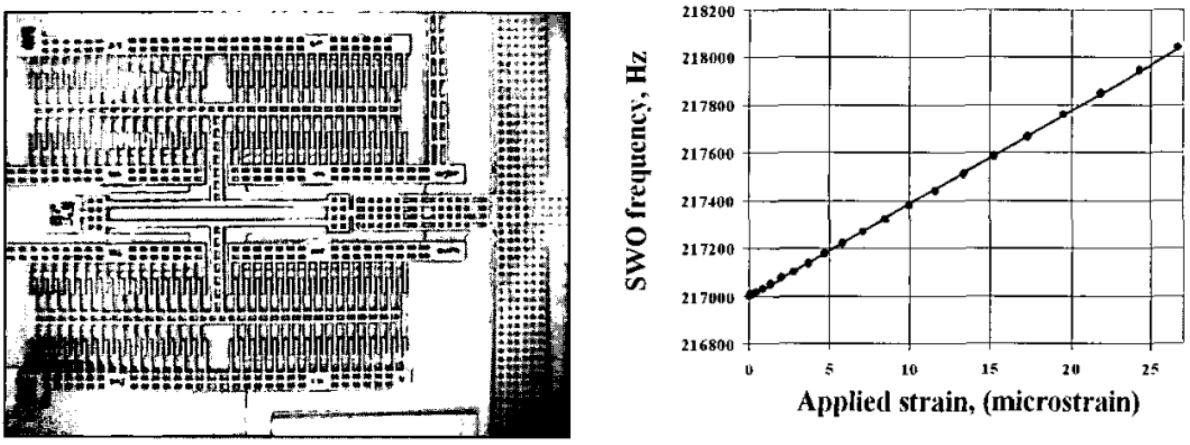

(a) (b)

Figure 2.32 (a) top view of polysilicon DETF and (b) applied strain against resonant frequency [68]

Welham, et al. [23] presented a modified DETF structure called ‘ double-shuttle’ lateral resonator. Instead of two simple parallel beams, this device comprised two inertial masses supported by eight parallel flexures as shown in fig. 2.33(a). A pair of piezoresistors is used to couple to two masses. In vibration, the piezoresistors also act as a linkage structure that separate the anti-phase mode from adjacent modes, hence increasing the range of operating frequency. The lateral oscillation mode triggered via electrostatic comb-drive provides a balanced vibration in the system. It also means that the Q-factor was less affected from residual gas and energy loss through the supporting structure. In electrical operation, inverse driving signals were fed to the opposing comb-drives, which resulted in zero voltage at the piezoresistive pickup. Another electrical connection connected the piezoresistor to a Wheatstone bridge circuit for resistance measurement. The amplitude of the output signal is amplified before being fed back to the drive circuit. The sensor achieved a Q-factor of 50 000 in vacuum while maintaining a value of 1000 in air. Two different diaphragm thicknesses were used for sensitivity measurement. A 120 µm thick diaphragm showed a performance of 3.8% bar $^{-1}$ over a pressure range from 0 to 10 bar. A 25 µm thick diaphragm increase the sensitivity to 15% bar $^{-1}$ but dramatically reduce the range of pressure from 0-10 bar to 0-2 bar. The diaphragm thickness is inversely proportional to the deflection caused by applied pressure. Thus, a high-pressure range sensor has to make a trade-off between sensitivity and pressure range.

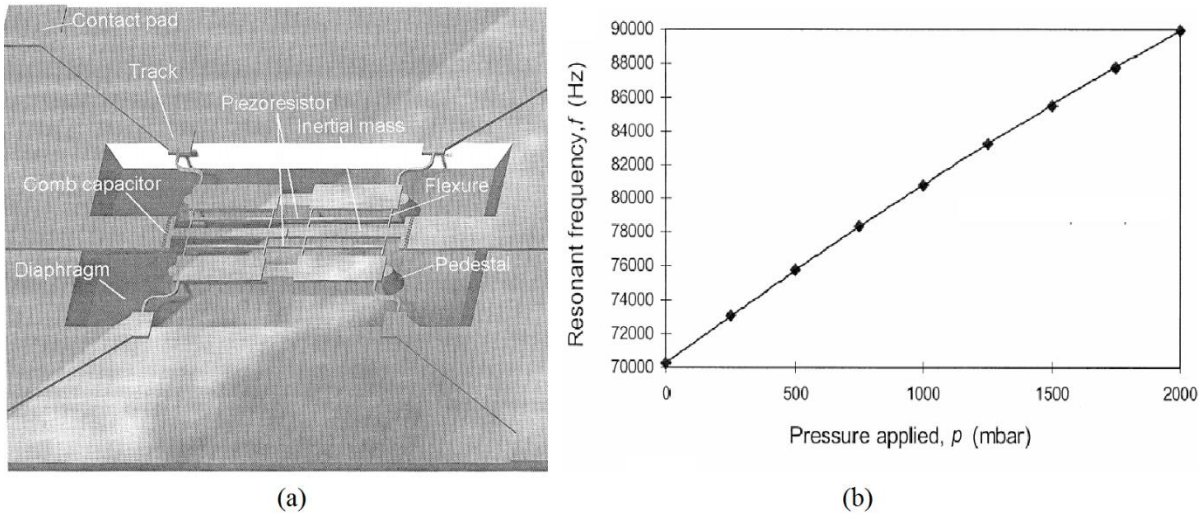

Figure 2.33 (a) 3D schematic of the lateral resonant pressure sensor and (b) its sensitivity performance for 120 μm thick diaphragm [23]

Greenwood [69] indicated that the previously described 'double-shuttle' having heat dissipation problem related to the location of piezoresistive strain gauge. He proposed a solution by relocating the coupling piezoresistor to a newly added overhead linkage as shown in fig. 2.34. This device used the same operating mode, driving and detecting technique, differs only by the position of electrical contact between stationary and moving parts. It was claimed to increase the strain gauge output in compared to the 'double-shuttle' design. However, both devices still operate in pressure range under 10 bar. It is suggested that the size of the sensor limiting its performance. By reducing the size of the resonator, I can use the same diaphragm thickness, hence the same pressure range, while significantly improving its sensitivity.

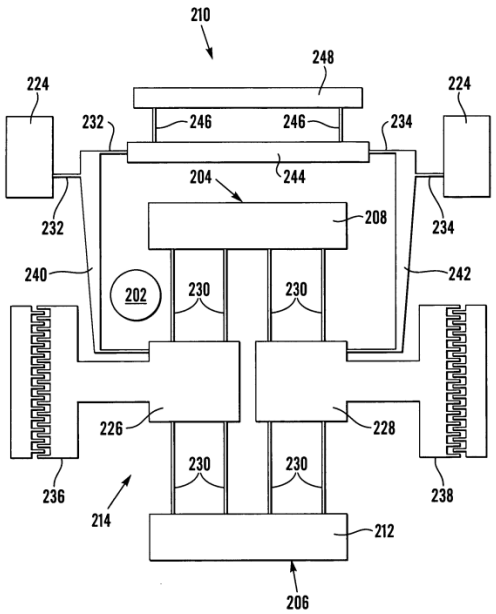

Figure 2.34 Modified 'double-shuttle' design including overhead linkage (244), piezoresistor (232,234) and electrical contact (248,224) [69]

Ren, et al [22] proposed another modification for the 'double-shuttle' resonator packaged in dry air without vacuum encapsulation. The structure consists of two inertial masses and eight flexures coupling via a suspended flexural spring as shown in fig. 2.35. The flexures connect the resonator to two anchor masses, which sit on top of the dielectric buried oxide (BOX) layer. This design employed a pair of static comb-finger electrode for capacitive sensing. As the resonator operates at atmospheric pressure, a large signal to noise ratio (SNR) is crucial and can obtained from optimising the mechanical design. To improve the SNR, a thick resonator layer of 60 µm and large comb-fingers increase the signal amplitude while applying electromechanical amplitude modulation for capacitive detection reduce the noise disturbance. The additional spring attaches to the two inertial masses and increases the spring constant as well as the effective mass of the system. As a result, the mechanical coupling between the flexural anti-phase mode and the in-phase mode is reduced. The two mode frequencies are separated; thus, frequency crossover can be avoided. The device was tested in a pressure range of 100-400 kPa giving a Q-factor as high as 1772. Measurement shows that the sensor has a pressure sensitivity of 20 Hz/kPa with a resonant frequency of 34.55 kHz. At full pressure scale of 120 MPa with a frequency shift percentage of 18.40% were predicted from finite element analysis.

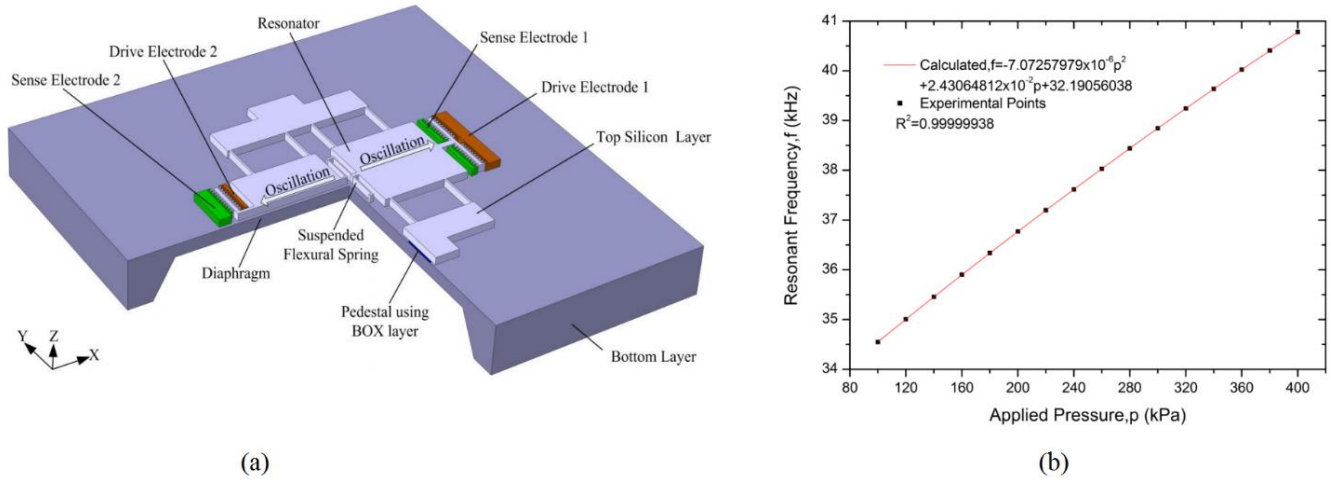

Figure 2.35 (a) 3D schematic of modified DETF resonator and (b) its sensitivity performance at 20ºC [22]

Kinnell, et al [70] from GE Sensing and Inspection Technologies presented the 8000 series sensor based on MEMS silicon resonant chip technology. The GE website [71] indicated that the resonator is a version of a double-ended tuning fork (DETF) as

shown in fig 2.36(a). The two parallel beams are moved further away from each other, leaving a space in the middle for the anchor. The newly located anchor is closer to the centre of the diaphragm; hence, its deflection magnitude is greater than conventional location of diaphragm-edge-oriented. The large deflection induces a much larger shift in resonant frequency, which in turn increases the resolution of the sensor. The device, hence, achieved a sensitivity of approximately 3Hz/mbar with a natural frequency of 26 kHz. The anchor positions have been optimised to ensure the mechanical reaction forces, which are generated by the resonator in lateral anti-phase mode, are balanced and minimize the energy transfer to the diaphragm. As a result, the balanced design obtained a Q factor of 38 000 in both air and vacuum. The paper also stated that packaging is the key consideration for long-term stability. The resonator, fabricated from SOI wafer, was first fusion bonded to the diaphragm layer, then a cap layer. As a result, the resonator was sealed in vacuum by this hermetic encapsulation. Three sensor prototypes were fabricated; differing by the content for hermetic package filling. The performance over two years showed less than 100 ppm drift of F.S as shown in fig. 2.36(b). The long-term stability and predicted range of pressure from 1 to 700 bar is a promising result for high pressure sensing application.

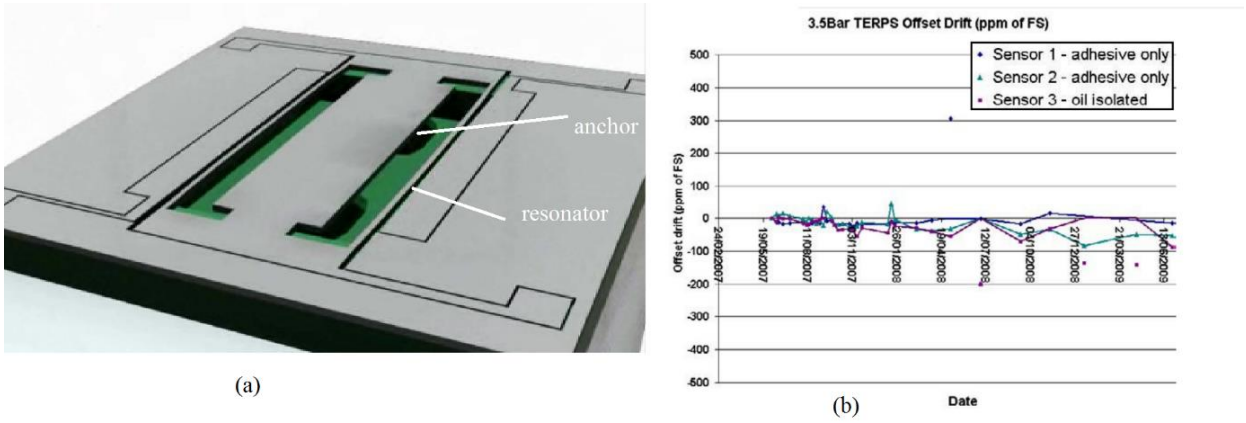

Figure 2.36 (a) GE design of DETF [72] and (b) its record of long term stability [70]

The same author [73] then patterned a modified version of DETF as shown in fig. 2.37, which improved the Q factor even further. The pressure induced vibration of the two beams causes distortion in the anchor energy, which in turn reflects the distortion back to the beams and reduce the precision of measurement. The new design replaces the single contact point between anchor and the end of each beam by several branches. By attaching each end to more than one support points, the moment and reaction forces at the support is balanced, hence reduce the distortion transfer into anchor, diaphragm, and increase Q factor. As a result, measurement that is more accurate.

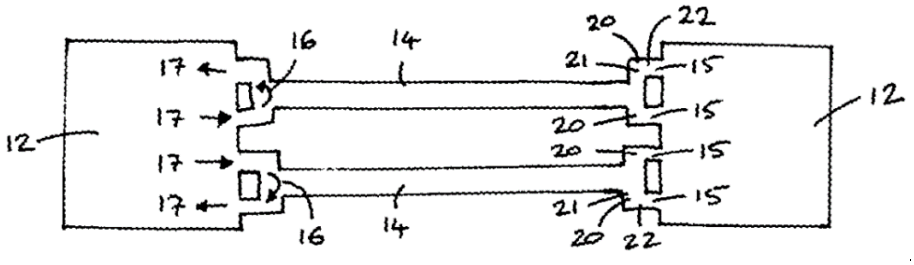

Figure 2.37 Sketch of the DETF resonator with (15) indicated the modified supports [73]

2.8.1 Discussion

In this section, previous work in pressure resonant sensor is discussed. Table 2.3 compares the performance of the device that has been featured. Long-term stability is a key factor for high-pressure sensor performance. It is shown that vacuum encapsulation minimise the effect of long-term drift on resonant frequency [70]. However, the optimised fabrication method for vacuum encapsulation is far from fully understood. Furthermore, balanced structure and balanced operating mode are preferable in most devices. Balance structures minimise the energy loss during vibration to the external world via the supporting structure, resulting in a higher Q-factor. High Q factor devices when operating in vacuum can be exited with driving signal of a few millivolts, thus, reducing the power consumption. Ultimately, there are four types of resonator based on their structural designs namely cantilever, dual diaphragm, doubly ended single beam and doubly ended tuning fork (DETF).

Cantilever is simple structure, that offers simple fabrication technique, driving and detecting mechanism. Thus, early researches preferred to employ cantilever to test silicon structure viability in pressure sensing. However, since cantilever is asymmetrical structure with only one fixed anchor point, its Q factor is heavily reduced. Low Q factor affects measurement precision, long-term stability and operational range. Thus, cantilever application is limited to low range, low precision sensor.

Dual diaphragm structure offers more balance vibration mode, hence theoretically improve the Q factor. Experimentally, poor encapsulation technique left air in the supposedly vacuum gap between the two diaphragms significantly reduced the Q factor. A thicker diaphragm design will limit the air diffusion but sacrifice its sensitivity performance.

Doubly ended single beam structure is a more stable solution. The structure can be encapsulated without sacrificing its sensitivity, but it lacks a balanced mode of operation.

DETF [70], achieved relatively high sensitivities with the without expense of lower Q factor. Several main factors affect the pressure range of a sensors including material and fabrication process. Single crystal silicon offers very high strength and elasticity,

which can maintain the performance of the sensor in high-pressure environment. SOI am available and have intensively been employed in MEMS resonant sensor application.

Greenwood's design [69] provides a standard framework DETF to work upon. The design has been modified to increase the operating pressure range to 1000 Bar as well as maintaining the required sensitivity of at least 35 Hz/Bar. Greenwood resonator has its anchors fixed to the edge of the diaphragm, which doesn't employ the majorities of the axial stress from applied pressure. In addition, Greenwood had the overhead structure attached to the resonator, which ultimately reduce its Q factor. The proposed design will make two critical changes from Greenwood's design including changing the anchor position and removing the overhead structure from the design.

Table 2.3 Summary of resonant pressure silicon sensor performance

Ref. & Year	**Resonator type**	**Mode**	**Excitation/detection principle**	**Sensitivity**	**Operating range**	**Q**
[58] 1995	Polysilicon beam	Fundamental, flexural	Electrostatic/ Optical, Piezoresistive	3880 Hz/psi	5 psi	N/A
[59] 2008	Microcantilever – single crystal silicon	Flexural	Electrostatic/Capacitive	60 Hz/bar	500 mbar	10000 in vacuum
[60] 2002	Double sided diaphragm - Ceramic	N/A	Electrostatic/Capacitive	164 kHz/bar	3 bar	62 in air
[61] 2003	Two-layer single membrane - Silicon rubber and Ferrite	N/A	Electrostatic/ Inductive	9.6 kHz/kPa	-20kPa to 60 kPa	5.4 in air
[62] 1996	Single mass suspended on four beam – single crystal silicon	Fundamental, flexural	Electrostatic/ Piezoresistive	8.8 kHz/bar	3.5 bar	50 000 in vacuum 50 in air
[63] 1997	Planar double loop structure – single crystal silicon	Antiphase torsional	Electrostatic/Optical	8 Hz/bar	1000 mBar	20 000 in vacuum
[64] 2009	Single drumhead diaphragm – single crystal silicon	N/A	Optical/Optical	200 Hz/Torr	3000 Torr	14 000 in vacuum
[65] 2002	Single vibrating membrane – PZT thin film	Fundamental	Electrostatic/ Optical	115 Hz/mbar	140 mbar	N/A
[6] 1990	Dual-diaphragm suspended on four beam – single	Torsional	Electrostatic/ Optical	2.4 kHz/bar	1 bar	80 000 in vacuum

	crystal silicon					2400 in air
[66] 2013	Four "H" type doubly clamped micro beams – single crystal silicon	Anti-phase lateral	Electromagnetic / Electromagnetic	5.2 kHz/bar	11.8 MPa (theoretically)	6000 in vacuum 1200 in air
[67] 1990	H" type doubly clamped micro beams – single crystal silicon	Fundamental, flexural	Electromagnetic / Electromagnetic	Gauge factor of 3000	N/A	50 000 in vacuum
[5] 2000	Double-ended tuning fork (DETF) – single crystal silicon	Anti-phase lateral	Electrostatic/ Piezoresistive	2.7 kHz/bar	N/A	40 000 in vacuum
[68] 2004	Double-ended tuning fork – polysilicon	Anti-phase lateral	Electrostatic/ Capacitive	39 Hz/με	25με	370 in air
[23], [69] 2003	'double-shuttle' suspended on eight beam – single crystal silicon	Anti-phase lateral	Electrostatic/ Piezoresistive	15% /bar for 25 μm diaphragm	10 bar	50 000 in vacuum 1000 in air
[22] 2013	Modified 'double-shuttle' with centre coupling	Anti-phase lateral	Electrostatic/ capacitive	20 Hz/kPa	Tested: 400kPa	1772 in air
[70], [73] 2009	DETF	Anti-phase lateral	Electrostatic/ N/A	3 Hz/mbar	700 bar	38 000 in vacuum 38 000 in air

2.9 **Quartz crystal Oscillator**

Many current applications in pressure measurement are using the quartz crystal oscillator [45], [74]. Quartz is an attractive material for resonant pressure sensor as it is a single crystal material. The main advantage of quartz resonator is high Q factor due to its high-purity property [75] . Another advantage is that the piezoelectric nature of Quartz allows the use of piezoelectric excitation and detection mechanism in driving and sensing the quartz crystal oscillator. Stressing or compressing the quartz resonating structure deforms the crystal, which lead to the change in its resonant frequency. The developed technology in quartz resonator packaging, metallization and mounting technique made quartz ideal for pressure sensor research [70].

Quartz resonators are typically classified based on the resonance mode shape, namely single-end flexural, double-ended flexural, torsional and thickness shear. In this

section, thickness shear and double-ended flexure mode are discussed as they are the dominant design in pressure sensing application [76].

2.9.1 Double-ended flexural mode operation

A number of quartz sensors employ one or multiple long, slender beams, which is sensitive to longitudinal force. When the beams are under lateral stress, the structure produced a restoration force, which is equal force but in opposite direction. The restoration force affects the rigidity of the structure, hence, increase the resonant frequency [76]. Both structural ends are converged in order to apply tension. In order to increase the Q factor or minimise energy losses during vibration, the beam design need to have total moment equal to zero. There are two frequently used structures namely double and triple beam as shown in fig2.38. Double-ended tuning fork has each two tines move in opposite direction, resulting in the cancellation of opposite moments. Thus, the structure obtains a high Q factor. The triple beam design accommodates the out-of-plate vibration. The middle beam, which is twice the mass of two outside beams, move in opposite direction with the outside beams. All three beams vibrate horizontally. The net mass movement is zero, thus high Q factor is obtained.

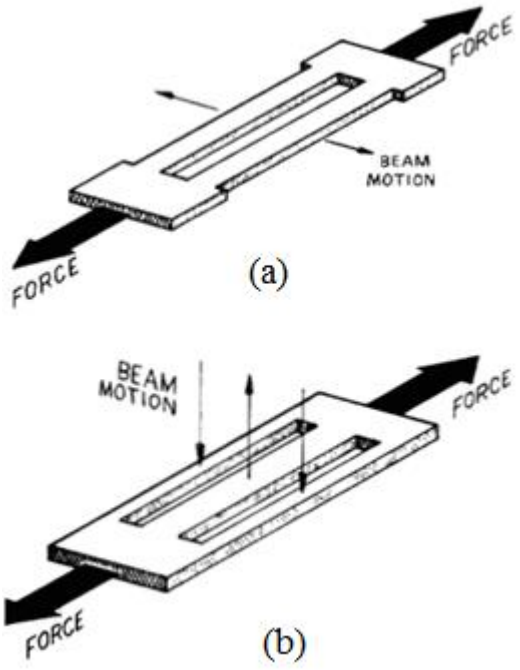

Figure 2.38: symmetrical balanced designs for quartz double-end resonator (a) double beam and (b) triple beam [76]

Paros [77][78] has developed an all quartz double-end tuning fork that allows large frequency shift in the range of operation. The crystal cut was chosen for a low temperature coefficient as well as in-plane shear resonance mode. Four electrodes are deposit onto the resonator, two on top and two at the bottom surface as shown in

fig.2.39 (a). The resonator is piezo-electrically driven into resonance via out-of-phase mode. In this mode, the momentum of two beam cancel each other out to reduce the loss energy, hence increasing Q factor. A bellows tube is used to couple the pressure onto the resonator. The sensor was designed for a ± 1.1 Bar range. The operational frequency range is ± 4000 Hz for the unstressed frequency of 40 kHz. The sensor is hermetically sealed in vacuum. The sensor achieved high stability with static error is under 0.02 hPa for its range of operation as shown in fig.2.39(b).

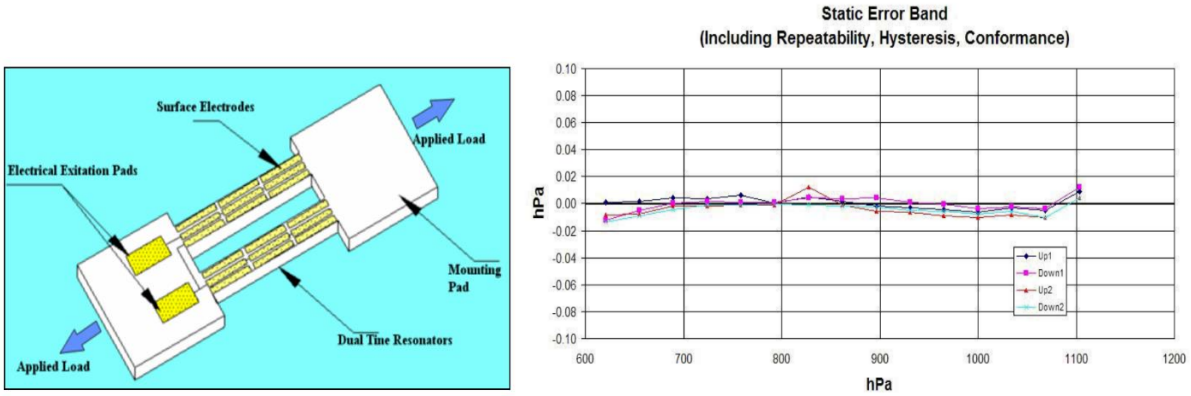

(a) (b)

Figure 2.39: Paros's double-end tuning fork: (a) design and (b) stability performance [78]

Ueda, *et al.* [79] employed quartz double end tuning fork for force sensing. The development of photolithography technology allows quartz resonator to be manufactured in a large scale with low cost, making quartz attractive than other alternatives such as elinvar alloy. Since mechanical property of quartz crystal depends on the cut angle. In this work, the quartz is cut so that the temperature coefficient is zero at room temperature. The Q factor is 7000 at close to vacuum condition. The Q is measured against ambient pressure and shows a decay value with increased pressure as shown in fig 2.41(a). Structural aging is measured as well. Fig 2.41(b) shows long-term drift of the resonator against time. The temperature is set at 50^{o}C for experimental acceleration. The natural frequency shifts 25 ppm after 1000 working hours.

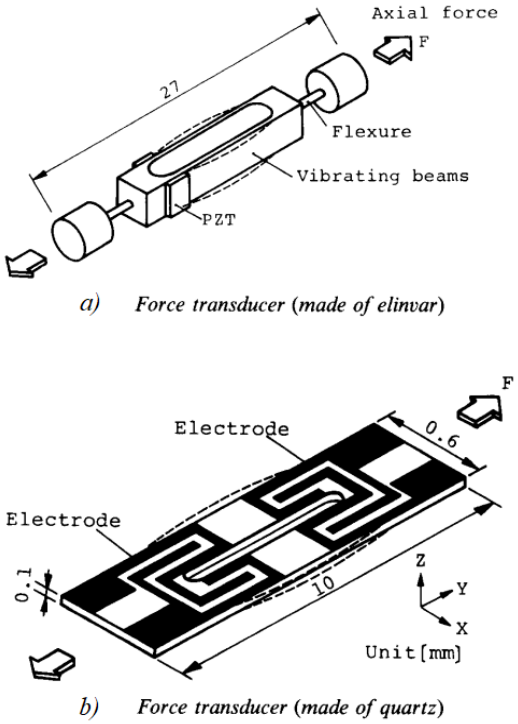

Figure 2.40 Double-ended tuning fork design made of (a) elinvar and (b) quartz [79]

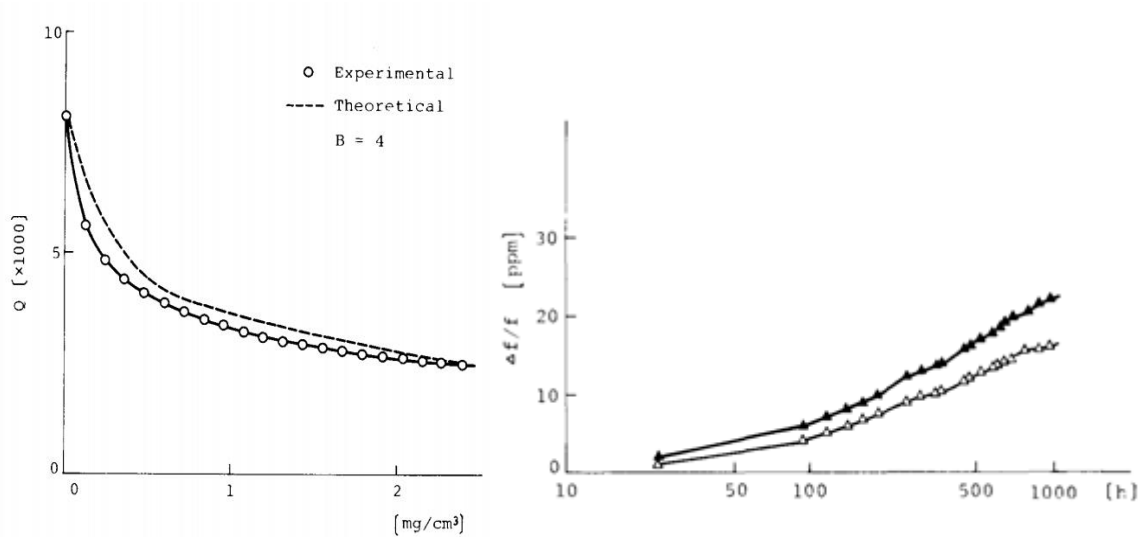

(a) (b)

Figure 2.41 Quartz DETF performance: (a) Q factor against surrounding air density and (b) frequency drift against operating time [79]

2.9.2 Thickness shear mode operation

Resonator that employs thickness shear mode, typically consists of a plate (rectangular or circular) of crystalline quartz. The thin-film electrodes are deposited on top of the

faces. The applied voltage triggers the plate to vibrate as the result of inverse piezoelectric effect. The crystal orientation needed to be select so that the shear stress is created with applied voltage. The plate is designed to be thicker in the middle, which caused most of the vibration energy to concentrate into this area. This energy trapping mechanism and Quartz high purity property contribute to high mechanical Q factor.

The two types of cut that make quartz crystal sensitive to applied stress are AT- and BT-cut [75].While AT-cut resonator increases resonant frequency in response to compressive stress, BT-cut resonator frequency reduces [80][81][82].

Karrer and Leach [83] constructed an all-quartz structure to measure pressure. In this work, the resonator and cylinder are made from a single piece of crystalline quartz for uniformly distribution of external pressure. Then, the end caps are adhered to the structure via joints made from elastic cement thin film as shown in fig 2.42(a)-(b). The crystal is BT-cut to operate on the third overtone thickness shear mode with the unstressed frequency of 5 MHz Karrer stated that the dimension of the cylinder affects the sensitivity of the resonator structure. The transfer function (σ/P) over the dimension of the cylinder is shown in fig 2.42(c). Ultimately, the sensor sensitivity is at 22 Hz/Bar and range of operation is 0 to 700 Bar.

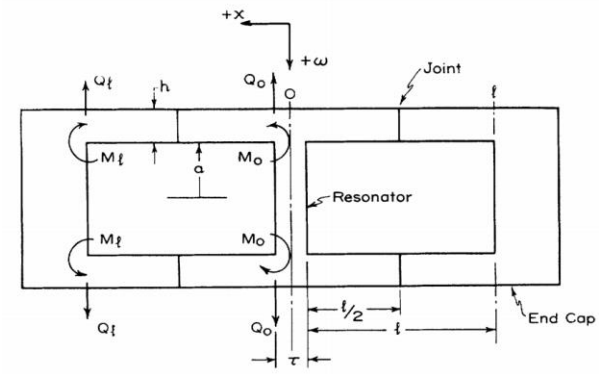

(a)

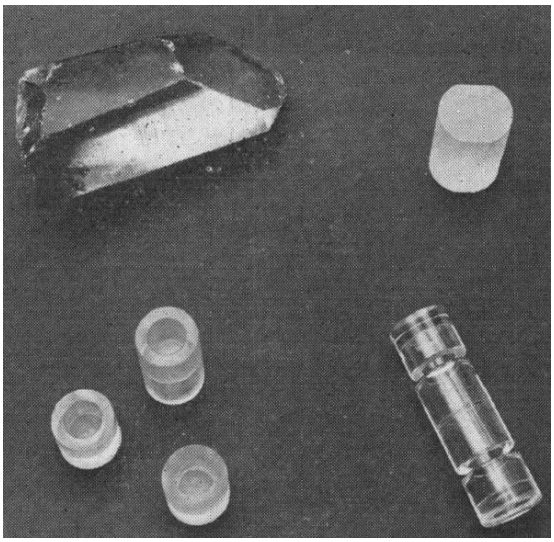

(b)

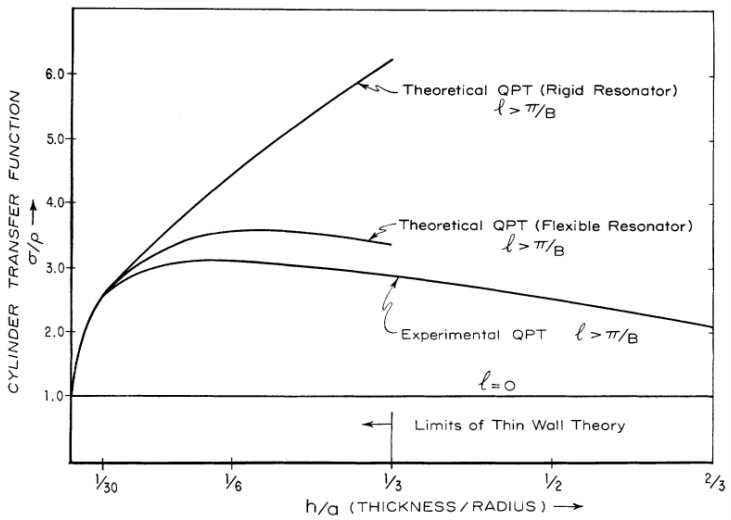

(c)

Figure 2.42 Karren and Leach's Resonator (a) structural design, (b) Fabrication flow and (c) transfer function against design dimension [83]

Besson *et al*. developed [84] a dual mode thickness-shear resonator for pressure sensing application. The crystal was cut to employ the piezoelectric coupling to both of the thickness-shear (B- and C-) modes of resonance. The cut is called stress compensated for B-mode and temperature compensated for the C-mode (SBTC). Its purpose is to employ the B-mode oscillator for temperature sensing while engage the temperature compensated C-mode in measuring applied pressure. The crystal is rectangular shape and is an integral part of a cylindrical structure as shown in fig 2.43(a). The other cylindrical layer converted the applied pressure into a uniaxial compressive stress in the resonator crystal. The electrodes are deposited far away from the centre of the crystal plate to ensure high spectral purity and Q factor. The resonator is driven into dual mode oscillation simultaneously. The B-mode oscillation is significantly independent of the applied pressure up to 100 Mpa as shown in fig 2.43(b). On the contrary, C-mode vibration is largely depended on the pressure while the effect of temperature on frequency shift is minimal. A sensitivity of 145 Hz/Mpa at 175 deg C is recorded.

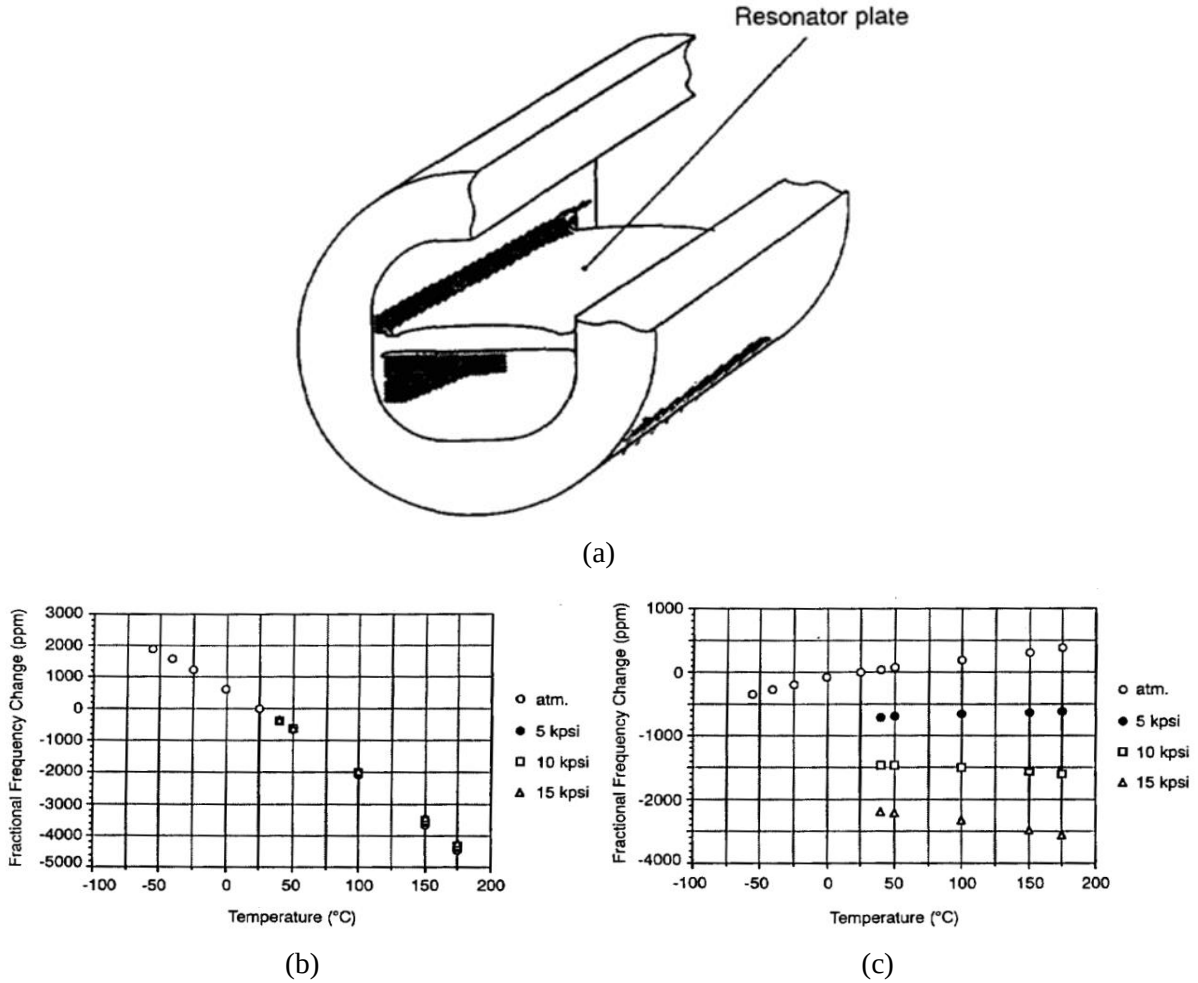

Figure 2.43 Besson's quartz resonator (a) design, (b) B-mode performance and (c) C-mode performance [84]

Eernisse *et al*. [85] developed a non-cylindrical, integral shell structure that transmit non-uniform force to the resonator device. The shell design is purposely flat on two side walls to generate maximum stress in this area. The minor stress on the thicker wall still contribute to the total stress in the resonator. By adjusting the dimension of the flat wall, an additional degree of freedom for maximizing the sensitivity is introduced. The cut angle of the flat wall is simulated against force sensitivity coefficient for sensitivity optimisation as shown in fig 2.44(b). Ultimately, the fabricated sensor showed a sensitivity of 3.5 ppm/kPa with the range of 110 MPa. In addition, Earnisse employs a torsional tuning fork quartz resonator as temperature sensor for temperature compensation.

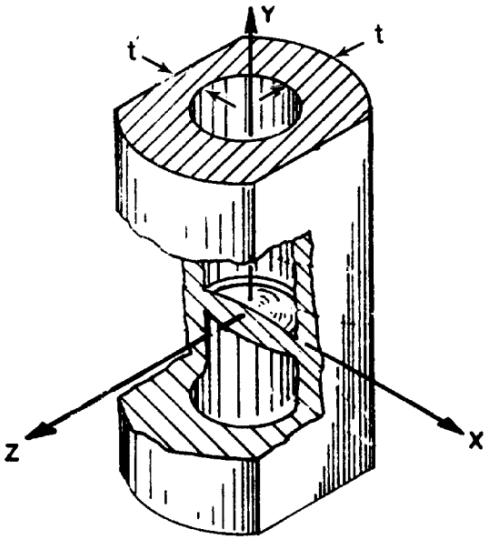

(a)

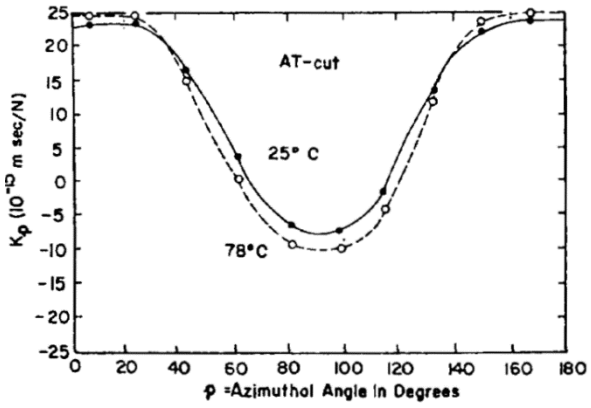

(b)

Figure 2.44 (a) Structural design of Eernisse's Quartz pressure sensor and (b) sensor sensitivity against the cut angle of the flat wall design.[85]

Quartzdyne [86] presented an advanced quartz crystal oscillator design that can operate in a high pressure environment up to 1300 bar. The device has three quartz crystals: a pressure-sensing crystal, a temperature sensing crystal and a reference frequency crystal. The temperature sensing crystal works independently from the other two crystals and measures the temperature in the well, which is used to compensate the error caused by temperature in pressure measurement. The reference crystal provides a constant frequency independent from applied pressure and temperature. This frequency is used to digitalize the pressure-induced frequency. The product that aims for the 1000 bar market delivers a sensitivity of 35 Hz/Bar and an offset drift of 0.06 bar in 3 days as shown in fig 2.45 However, quartz sensor element is generally large compared with silicon-based element that has advantages in more state-of-the-art MEMS fabrication technology. Furthermore, bigger size required more complex packaging technique as well as largest cost in order to deliver to deep measuring area.

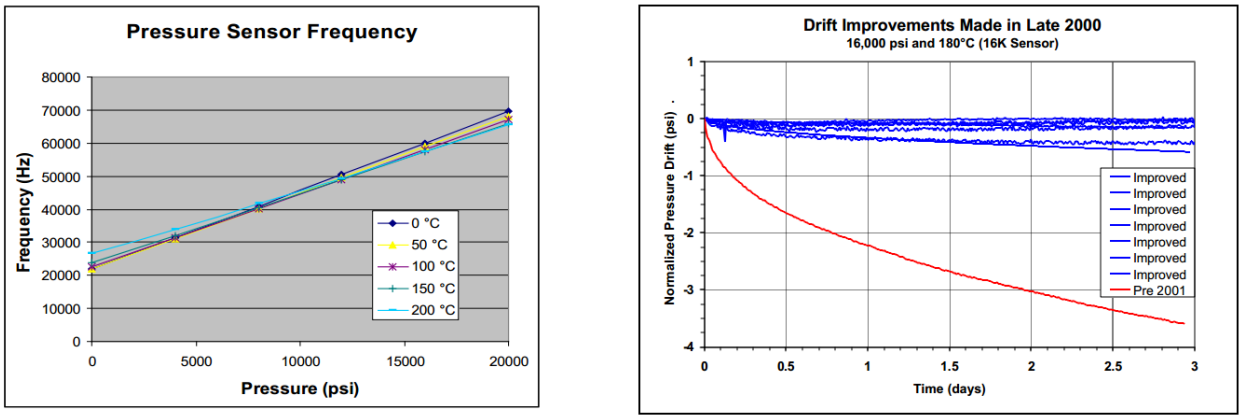

(a) (b)

Figure 2.45 (a) Sensitivity and (b) long-term stability performance of Quartzdyne sensor for 16 000 psi [86]

2.9.3 Discussion

Quartz fabrication technique has limited the application of double-end flexural mode to low range pressure sensing application. Thickness shear mode sensors have shown more potentials in term of fabrication, sensitivity and stability, which are essential for downhole application. The summary of different thickness shear mode resonators is shown in table 2.4.

Table 2.4: Different thickness shear mode resonators' performance

Author	Refs	Crystal cut	Full scale (MPa)	Temperature compensation	Sensitivity (ppm/kPa)	Frequency (MHz) and Overtone
Karren and Leach	[81]	BT	0.7	Crystal cut	2	5 3rd
Besson et al	[82]	SBTC	110	Crystal cut	1.6	5.15 3rd
Eernisse et al	[83]	AT	110	Dual resonator	3.5	3.6 5th
Quartzdyne	[84]	AT	110	Dual resonator	2	7.2 3rd

Quartzdyne and Eernisse et al. employs the benefit of quartz reference crystal in counter system to add a third quartz resonator fore temperature compensation. This is a simple way to provide a high temperature sensing mechanism. This system has been commercialised successfully for downhole application. In addition, Quartzdyne resonator design is relatively simple, hence reducing its size compared with its

competitors. The smaller sensors are less expensive to deliver and install in deep reservoir, making Quartzdyne attractive for downhole measurement.

2.10 **Conclusions**

Piezoresistive, capacitive and resonant methods have all been used in pressure measurement. Piezoresistive sensors are based on the piezoresistive properties of silicon. This method provides a simple solution that directly measures the pressure as the result of change in resistance. The expense for the simplicity is lower accuracy and high temperature cross sensitivity. A state-of-the-art low temperature-dependent pressure sensor achieved 2000 ppm/^{o}C in signal response of temperature [87]. The drawback limited the use of piezoresistive method in high-pressure application. High pressure sensor that employs piezoresistive mechanism is commercialised for pressure range of 3000 Bar and lower [88]. The second type of sensor reviewed applied capacitive method. This type of sensors provides similar resolution with piezoresistive type. Although it has smaller temperature cross sensitivity, capacitive sensor output is non-linear due to its membrane deflection. Thus, the electronic circuit for signal processing become more complex.

Resonant pressure sensor measurement is based on a change in resonant frequency under applied pressure. The change in Quartz sensor frequency is due to the deformation of the Quartz crystal while the main factor that affects the frequency in a silicon sensor is the strain gauge effect. Quartz devices are several magnitudes larger than the silicon counterpart. Thus, Quartz is currently dominating the down-hole pressure measurement market; silicon resonant devices, offering the advantages of smaller size and by using state-of-the-art MEMS technologies have the potential to be reduced the cost of producing and integrating into downhole surveillance system.

Current silicon resonant sensor technologies focus on the development of high sensitivity devices that operate in a low-pressure environment. GE have commercialised a range of silicon resonant pressure sensor that operate from 70mbar to 700 bar [89]. Through this extensive literature review, double-mass structure has shown a high level of sensitivity in the magnitude of 3~5kHz/Bar as well as a balanced operating mode with Q factor of 10~40000, at least 10 times higher than presented devices. Further research on this structure and the encapsulation method have shown to increase its range of operating pressure from air pressure to 100Mpa reservoir.

In the literature, Silicon on insulator (SOI) is frequently used for MEMS sensor. It offers crystalline silicon, which achieved high Q factor in magnitude of 10^4, as the material for device structure. In addition, by using SOI wafer, the complicated process of silicon-to-silicon bonding in traditional fabrication has been removed.

Chapter 3 Coupled double-mass resonator analysis

3.1 Introduction

In this chapter, the coupled double mass resonator structure is investigated and characterised. The mechanical model of the double ended beam is analysed and the stiffness and mechanical non-linearity of three different type of beams are compared. A model of coupled double-mass structure is presented to analyse in-phase and out-of-phase modes. In order to understand the mechanism of pressure-induced structures, an investigation of the diaphragm structure is conducted. Finally, the electrostatic excitation and capacitive detection technique are discussed in detail.

3.2 MEMS resonator mechanical theory

In order to understand the mechanics and working dynamic of the double-mass structure, I will investigate the physic properties of its most fundamental element, the double ended beam as shown in fig.3.1. The uniform rectangular bending beam has appeared as an integrating part in most of the resonator structures reviewed in chapter 2.

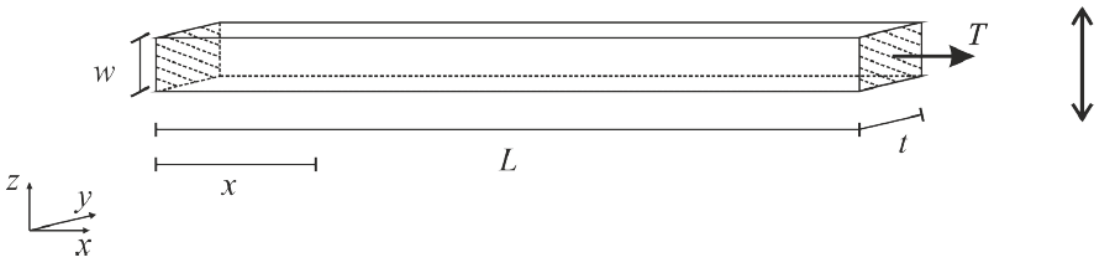

Figure 3.1: Double ended beam model with dimension and axial stress

The differential equation for transversally oscillating motion of a uniform beam (motion in x direction), given no external force, is illustrated by [90]:

$$\frac{\partial^2}{\partial x^2}\left[EI\frac{\partial^2 g(x,t)}{\partial x^2}\right] + c\frac{\partial g(x,t)}{\partial t} - \frac{\partial}{\partial x}\left[T\frac{\partial g(x,t)}{\partial x}\right] + \mu\frac{\partial^2 g(x,t)}{\partial t^2} = 0 \quad (3.1)$$

Where, $g(x,t)$ is the bending in z axis of the double ended beam at the x position $(0 < x < L)$, E is the young's modulus, I is the moment of inertia of the beam, c is

the damping coefficient, T is the applied axial tension, μ is mass per unit length of the beam, $\mu = \rho wt$,where ρ is the density of the material. It is worth mentioning that I is dependent on the direction of motion. In fig.3.1, the beam is designed to vibrate in z direction, $I = w^3t/12$.

Transforming eqn.(3.1) in term of function of time-motion $g(t)$ and function of mode shape $g(x)$, I arrive with an equation of an unforced spring-damper-mass system in z axis

$$M\frac{\partial^2 g(t)}{\partial x^2} + C\frac{\partial g(t)}{\partial t} + Kz(t) = 0 \quad (3.2)$$

Where effective mass and stiffness constant of the beam is given by [15]:

$$M = \int_0^L \rho wt g^2(x)dx \quad (3.3)$$

$$K = \int_0^L EI\left(\frac{\partial^2 g(x)}{\partial x^2}\right)^2 dx + \int_0^L T\left(\frac{\partial g(x)}{\partial x}\right)^2 dx \quad (3.4)$$

For different given boundary conditions for the two ends of the beam, I obtain different mode shape function $g(x)$ [91]. For double-mass resonator, the suspension beam is a cantilever with one fixed end and one end that allows movement in vertical direction as seen in fig.3.2. The movement is directional limited as the free end is mechanically coupled with the mass, which prevent z-direction movement.

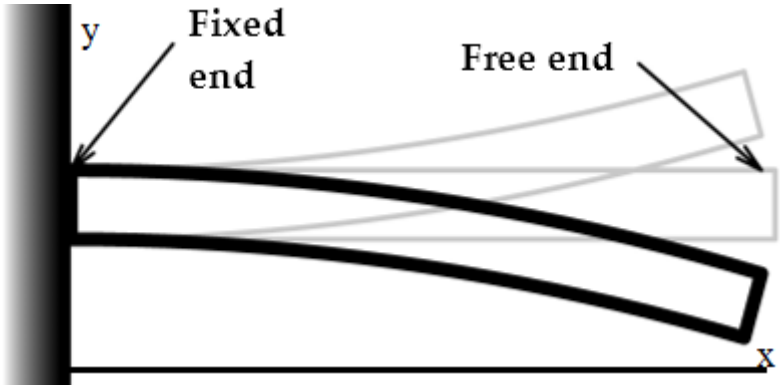

Figure 3.2 One fixed end beam with vertical movement on the other end

The fundamental mode shape function for aforementioned beam type is given by [91].

$$g(x) = \frac{3x^2}{L^2} - \frac{2x^3}{L^3}, 0 < x < L \quad (3.5)$$

Substituting eqn.(3.5) into eqn.(3.3) and eqn.(3.4), I will obtain the effective mass and effective stiffness of this type of beam for its fundamental mode.

$$M_e = 0.371\rho wtL \quad (3.6)$$

$$K_e = {Ew^3t}/{L^3} + {1.2T}/{L} \quad (3.7)$$

As mentioned in literature review, mechanical spring stiffening exists in beam structure. Taking nonlinearity into consideration, the third nonlinear stiffness constant is given [90]:

$$K_{e,3} = {Ewt}/{2L}\left(\int_0^L \left(\frac{\partial g(x)}{\partial x}\right)^2 dx\right)^2 \quad (3.8)$$

Substituting eq.3.5 into eq.3.8, I obtain the spring stiffening of the suspended beam with one fixed end and one end that moves in vertical direction.

$$K_{e,3} = {0.72Ewt}/{L^3} \quad (3.9)$$

Given the fundamental mode shapes function [92] and effective stiffness constant, effect of axial tension on stiffness and spring stiffening constant [93] of cantilever, double ended beam and suspension beam, I am able to calculate the ratio of stiffness change due to axial tension and proportion of nonlinear term in the stiffness of three given type of beams, as seen in table.3.1.

Table 3.1: Coefficients for the fundamental mode of resonance for three different types of beams

Parameter	**Double ended beam**	**Cantilever beam**	**Suspension beam for double-mass resonator**
Stiffness without tension ($\times \boldsymbol{Ew^3t/L^3}$)	198	3	12
Stiffness change due to axial tension ($\times \boldsymbol{T/L}$)	4.9	1.2	1.2
Ratio of stiffness change due to tension ($\times \boldsymbol{TL^2/Ew^3t}$)	0.02	0.4	0.1
Spring stiffening ($\times \boldsymbol{Ew^3t/L^3}$)	11.9	0.68	0.72
Ratio of **spring stiffening** over total stiffness	0.06	0.18	0.06

Given the same dimensions of the beam, I can see that the double ended beam has the highest stiffness without tension. As the result, its stiffness change due to tension is lowest. In contrast, cantilever stiffness and ratio of stiffness change due to tension are the lowest and highest respectively. Thus, given the same applied tensile force, cantilever beam outperforms double end beam in term of conversing the force into stiffness change.

Regarding the spring stiffening coefficients, while both the double ended beam and suspension beam have relative low ratio over the total stiffness, cantilever beam

nonlinearity ratio is three times larger than its counterpart. Hence, despite showing a promising response to tensile stress, cantilever beam nonlinearity makes it less attractive for high precision instrument. The suspension beam, which ranked second and first in tensile stress response and nonlinearity respectively, is becoming a suitable option.

3.3 Mechanical model of coupled double-mass structure

To understand the linear response of the double-mass structure, it is useful to neglect the nonlinearity and model the MEMS resonator with a simple mode. A two degree-of-freedom (DOF) system can be used to represent a coupled double-mass structure as shown in fig.3.3. Each resonator is represented by a mass, m_1 or m_2. Assuming that the inertial masses act as a mass point, hence, k_1 or k_2 represents the total stiffness of four suspended beams for each mass. The coupling element is represented by a string k_c. Corresponding damping coefficients are c_1, c_2 and c_c. The displacement and excitation force for each mass is given by x_1 or x_2 and F_1 or F_2, respectively.

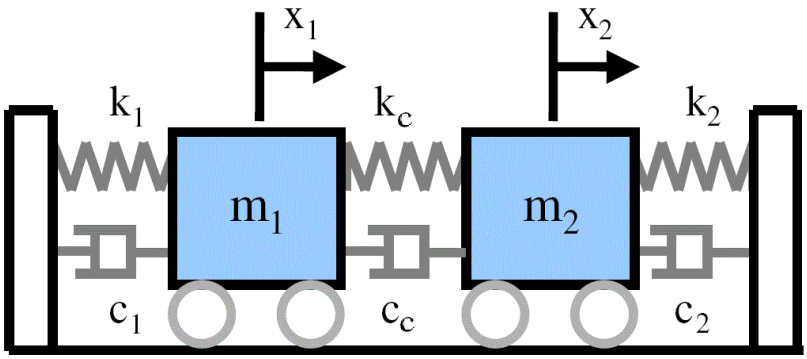

Figure 3.3 DOF representation for double-mass resonator structure

The equations of motion of the 2DOF system can be found using Newton second law of motion [94].

$$m_1\ddot{x}_1 - c_c\dot{x}_2 + (c_c + c_1)\dot{x}_1 - k_c x_2 + (k_c + k_1)x_1 = F_1 \quad (3.10)$$

$$m_2\ddot{x}_2 - c_c\dot{x}_1 + (c_c + c_2)\dot{x}_2 - k_c x_1 + (k_c + k_2)x_2 = F_2 \quad (3.11)$$

Where $m_1 = m_2 = m$, $k_1 = k_2 = k$ and $c_1 = c_2 = c$ for ideal double-mass structure. The equations can be rewritten in matrix format

$$\begin{bmatrix} m & 0 \\ 0 & m \end{bmatrix}\begin{bmatrix} \ddot{x}_1 \\ \ddot{x}_2 \end{bmatrix} + \begin{bmatrix} c_c + c_1 & -c_c \\ -c_c & c_c + c_2 \end{bmatrix}\begin{bmatrix} \dot{x}_1 \\ \dot{x}_2 \end{bmatrix} + \begin{bmatrix} k_c + k_1 & -k_c \\ -k_c & k_c + k_2 \end{bmatrix}\begin{bmatrix} x_1 \\ x_2 \end{bmatrix} = \begin{bmatrix} F_1 \\ F_2 \end{bmatrix} \quad (3.12)$$

Eqn. (3.12) can be expressed in form that is more compact

$$[M]\{\ddot{X}\} + [C]\{\dot{X}\} + [K]\{X\} = \{F\} \quad (3.13)$$

where [*M*], [*C*] and [*K*] are mass, damping and stiffness matrices, respectively. Which is given by

$$[M] = \begin{bmatrix} m & 0 \\ 0 & m \end{bmatrix} \qquad [C] = \begin{bmatrix} c_c + c_1 & -c_c \\ -c_c & c_c + c_2 \end{bmatrix} \qquad [K] = \begin{bmatrix} k_c + k_1 & -k_c \\ -k_c & k_c + k_2 \end{bmatrix} \quad (3.14)$$

In order to obtain stable vibration in a resonator system, the excitation forces are supposed to cancel out all the damping effects, i.e. $[C]\{\dot{x}\} = \{F\}$. Eqn. (3.4) can be rearranged as

$$[M]\{\ddot{X}\} + [K]\{X\} = 0 \quad (3.15)$$

The equation need to be transformed into an eigenvalue problem to find the eigenfrequencies and corresponding shapes. Therefore, eqn. (3.6) has been rearranged and expressed into frequency domain as follows

$$[-\omega^2[M] + [K]]\{X\} = 0 \quad (3.16)$$

Solving the eigenvalue problem, I obtain two sets of value for eigenvalue and eigenfrequency

$$\lambda_1 = \frac{k}{m}, X_1 = \begin{bmatrix} 1 \\ 1 \end{bmatrix} \qquad \lambda_2 = \frac{k+2k_c}{m}, X_2 \begin{bmatrix} 1 \\ -1 \end{bmatrix} \quad (3.17)$$

From eqn. (3.10), it can be seen that the 2-DOF system produces two fundamental mode frequencies. While one has the resonator mass move in-phase with each other, the other present an out-of-phase vibration as shown in fig. 3.4.

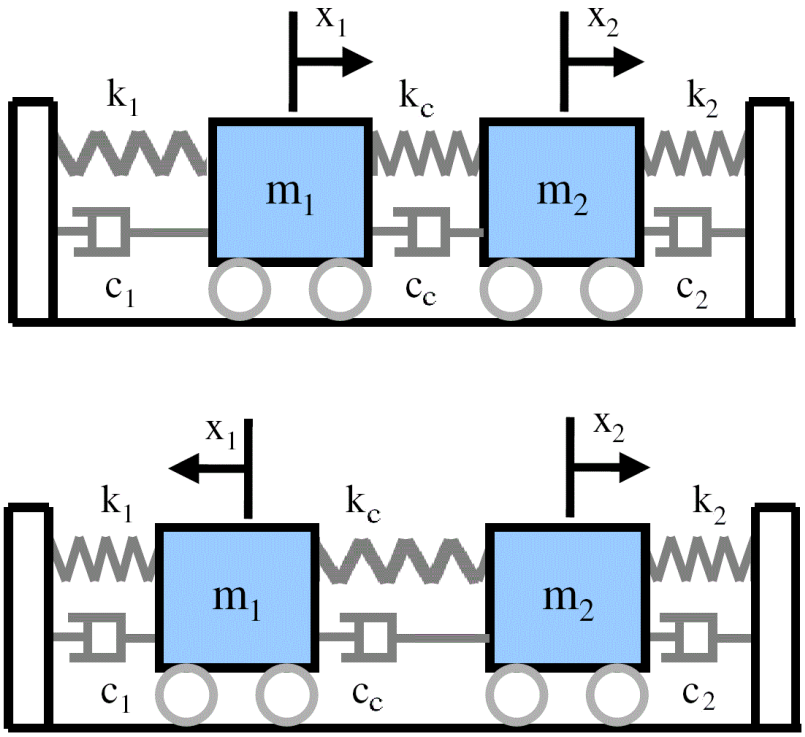

Figure 3.4 In-phase and out-of phase oscillating mode shapes of 2-DOF system

In uncoupled systems, the two mass oscillate independently. Thus, there is no difference between in-phase and out-of-phase resonant frequency. By adding the coupling element, I introduce k_c into the system, hence; increase the gap between two resonant frequencies. From Eqn. (3.10) result, I select the nominal value of $k = 1$ and $m = 1$, while varying the value of k_c, producing the plot in fig. 3.5. The plot illustrates how two eigenvalues of 2-DOF change with the coupling stiffness. This result can be used to separate the two adjacent modes in design state.

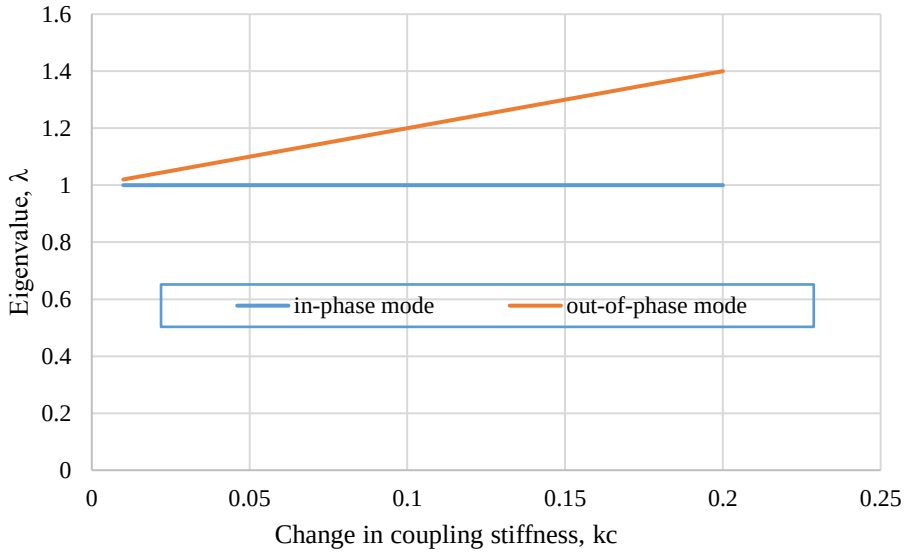

Figure 3.5 In-phase and out-of-phase eigenvalues for 2-DOF system under effect of coupling stiffness

Greenwood's design [69] employed an overhead structure to introduce the coupling stiffness k_c into the resonator mechanical system. However, the overhead structure is only attached to one end of the double-mass structure, which ultimately made the system mechanically unbalanced. As the result, the intrinsic Q factor is significantly reduced. In addition, Greenwood attached a piezoresistor structure onto the resonator, which introduced two more coupling stiffness into the system. Thus, by changing the coupling stiffness structure to a more balanced design and removing the piezoresistor structure, the resonator can be mathematically modelled more accurately as well as achieve a higher Q factor.

3.4 Pressure-induced structure dynamics

In understanding of working principles of the resonant pressure sensor, it is important to analyse the dynamic pressure-induced structure. Most aforementioned sensor devices discussed in literature review employed the rectangular diaphragm structure as shown in fig.3.6.

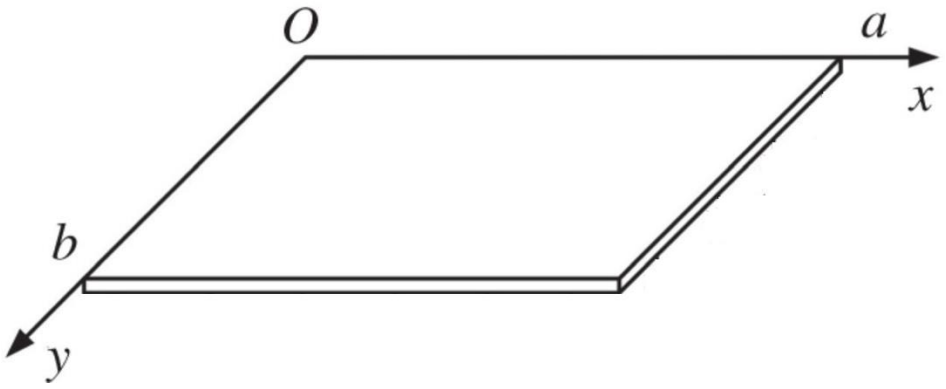

Figure 3.6: Rectangular diaphragm with parameters with O as origin and a,b as lengths

The bending moment balance equation of the diaphragm with applied transverse force are given by [95]:

$$\frac{\partial^2 M_{xx}}{\partial x^2} + 2\frac{\partial^2 M_{xy}}{\partial x \partial y} + \frac{\partial^2 M_{yy}}{\partial y^2} = q(x,y) \qquad (3.18)$$

Where $q(x,y)$ is an applied transverse load per unit area, bending moment M_{xx} , M_{xy} and M_{yy} are stress resultants with dimensions of moment per unit length. It is worth noting that these bending moment can be presented in term of the Young's modulus matrix of the material E , the height of the diaphragm h and second derivative of deflection is given directions k_{xx} , k_{xy} and k_{yy}[96]:

$$\begin{bmatrix} M_{xx} \\ M_{yy} \\ M_{xy} \end{bmatrix} = \frac{h^3}{12}\begin{bmatrix} E_{11} & E_{12} & E_{13} \\ E_{12} & E_{22} & E_{23} \\ E_{13} & E_{23} & E_{33} \end{bmatrix}\begin{pmatrix} k_{xx} \\ k_{yy} \\ 2k_{xy} \end{pmatrix} \qquad (3.19)$$

The general applied load is considered uniform load in pressure sensor, thus

$$q(x,y) = q_0 \quad (3.20)$$

It is worth noting that the diaphragm is simply supported from all four edges as appeared in many of the reviewed resonant sensors papers. Thus, I have the boundary condition that $M_{xx} = 0$ when $x = 0$ and $x = a$ and $M_{yy} = 0$ when $y = 0$ and $y = a$

Substituting Eqn. (3.19) and Eqn. (3.20) into Eqn. (3.18) and applying the aforementioned boundary condition, I am able to obtain the matrix of deflection for given dimension (x, y):

$$w(x,y) = \sum_{m=1}^{\infty}\sum_{n=1}^{\infty}\frac{16q_0}{(2m-1)(2n-1)\pi^6 D}\left(\frac{(2m-1)^2}{a^2}+\frac{(2n-1)^2}{b^2}\right)^{-2} \times \sin\frac{(2m-1)\pi x}{a}\sin\frac{(2n-1)\pi y}{b} \quad (3.21)$$

Where $D = Eh^3/12(1-v^2)$ and v is the Poisson's ratio of the given material.

The bending moments as well as the stresses in the plate can be derived from the deflection.

$$M_{xx} = -D\left(\frac{\partial^2 w}{\partial x^2} + v\frac{\partial^2 w}{\partial y^2}\right) \quad (3.22)$$

$$M_{yy} = -D\left(\frac{\partial^2 w}{\partial y^2} + v\frac{\partial^2 w}{\partial x^2}\right) \quad (3.23)$$

$$\sigma_{xx} = \frac{3z}{2h^3}M_{xx}, (-h < z < h) \quad (3.24)$$

$$\sigma_{yy} = \frac{3z}{2h^3}M_{yy}, (-h < z < h) \quad (3.25)$$

From obtained formulas, I am able to use MATLAB to theoretically calculate the deflection and stresses along $x = a/2$ for a rectangular diaphragm. For example, fig.3.7 shows the deflection and stresses of a typical square silicon diaphragm structure, which has $a = b = 800\mu m$ and $h = 100\mu m$ under applied pressure $q_0 = 20MPa$. The pressure is applied to the bottom surface of the diaphragm. The blue line represents the bottom of the diaphragm, while the green line and red line represent the middle and the top of the diaphragm respectively.

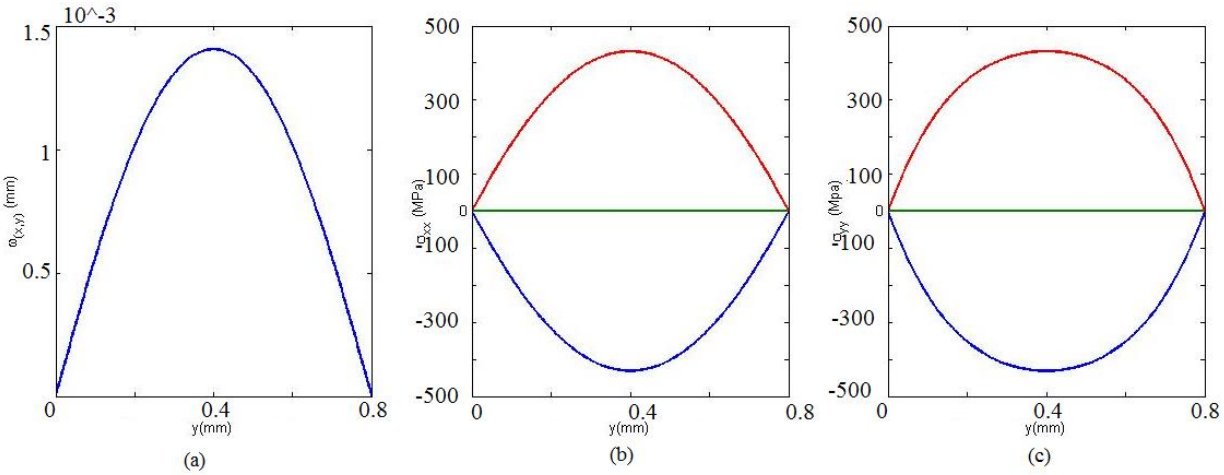

Figure 3.7: An example of square diaphragm's (a): deflection, (b) stress in x direction and (c) stress in y direction

Even under a uniform applied load, the deflection of the diaphragm shows a curved shape with $y = b/2$ as the highest point. As a result, the in-plane stress is zero at the edge and gradually increase until reaching the maximum value in the centre area. Thus, the contact point/points of diaphragm and resonator need to be located in proximity of the centre point $(x, y) = (\frac{a}{2}, \frac{b}{2})$ of the diaphragm to maximize the tensile strain across the resonator and therefore change in resonant frequency.

3.5 Capacitive comb-arm structure analysis

In chapter 2, I have discussed and compared several types of driving and sensing mechanism. Due to the low power consumption, simplicity in implementation as well as flexibility in term of employment, capacitive comb-arm transduction as shown in fig.3.8 is chosen as the driven and detection methods for the works in this thesis and is given an in-depth analysis in this section. Electrostatic actuation force as well as capacitive motional sensing current will be discussed. I will also analysis the different effects that lateral and vertical comb-arm have on the sensing signal.

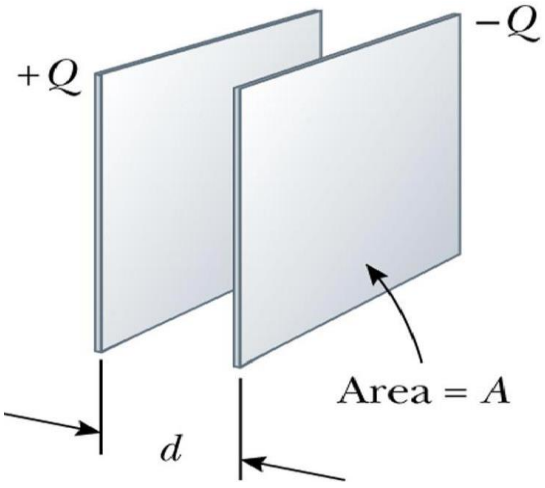

Figure 3.8: Parallel plate capacitive transducer

3.5.1 Electrostatic actuator

For electrostatic excitation, the excitation force is naturally an electrostatic force as mentioned in chapter 2. The formula is given by [92]:

$$F = \frac{1}{2}V^2\frac{dC}{dx} \quad (3.26)$$

Where V, C, d, x are the potential difference between two opposite plates, capacitance, distance between those plate and displacement, respectively. Given that the voltage comprises of a DC voltage applied on movable plate and AC voltage on the stationary plate, then $V = V_{ac}sin\omega t - V_{dc}$. Eqn. (3.26) can be transformed into:

$$F = \frac{1}{2}(V_{ac}sin\omega t - V_{dc})^2\frac{dC}{dx}$$

$$= \frac{1}{2}\left[\left(V_{dc}^2 + \frac{1}{2}V_{ac}^2\right) - 2V_{dc}V_{ac}sin\omega t + \frac{1}{2}V_{ac}^2 cos2\omega t\right]\frac{dC}{dx} \quad (3.27)$$

It can be seen clearly that the resulting force comprises of 3 components, which are the desired driving frequency of ω component, a DC component and a driving component at double the driving frequency of 2ω. To mininise the undesirable effect of the double frequency component which might excite resonant modes at twice the driving frequency, the applied DC need to be much larger than its AC counterpart ($V_{dc} \gg V_{ac}$). Thus, the magnitude of 2ω component can be neglected in comparison with the force component at ω. Under this assumption, the force equation can be rewritten as:

$$F \approx \left(\frac{1}{2}V_{dc}^2 - 2V_{dc}V_{ac}sin\omega t\right)\frac{dC}{dx}, V_{dc} \gg V_{ac} \quad (3.28)$$

Suppose parallel capacitive actuator have cross-sectional area of *A*, distance between plate of *d*, dielectric constant of ε_0 and the displacement of the movable part of *x* in *x*-axis, the capacitance is:

$$C = \frac{\varepsilon_0 A}{d+x} \quad (3.29)$$

Thus

$$\frac{dC}{dx} = -\frac{\varepsilon_0 A}{(d+x)^2} \quad (3.30)$$

Substituting Eqn. (3.30) into Eqn. (3.28), I obtain the excitation force:

$$F \approx \left(2V_{dc}V_{ac}sin\omega t - \frac{1}{2}V_{dc}^2\right)\frac{\varepsilon_0 A}{(d+x)^2}, V_{dc} \gg V_{ac} \quad (3.31)$$

Eqn. (3.31) clearly shows that the excitation is a periodical AC force overlaid by a DC force, which is affected by the displacement *x*. This displacement dependent force is

acting like a spring. As the displacement is typically much smaller than the distance between two plate $x \ll d$ [92], it is safe to assume that the spring system is linear and can be formulated by [97]:

$$F_e = -K_e x \tag{3.32}$$

The linear spring constant is:

$$K_e = -\frac{V_{dc}^2 \varepsilon_0 A}{d^3} \tag{3.33}$$

From Eqn. (3.33), I can see that the electrostatic actuator has a negative spring constant. Thus, it is worth remembering that by using the electrostatic actuator, I am reducing the spring constant of the resonator system.

The aforementioned AC force component equals to:

$$F_{ac} = -V_{dc}\frac{\varepsilon_0 A}{d^2}V_{ac}sin\omega t = \eta_{A,P}V_{ac}sin\omega t \tag{3.34}$$

Where $\eta_{A,P}$ is defined as the actuation transduction factor [92], which fundamentally is the coefficient representing the transformation from electrical to mechanical energy.

3.5.2 Capacitive detection

For a parallel plate detection mechanism as shown in fig. 3.9, when there is a constant DC potential difference of *V* on the opposite plates, the displacement *x* of movable plate will incite an alteration in capacitance. Therefore, the charge of Q across the plate changes, which in turn lead to current production. Thus, motional current *i* of micro-resonator is defined as a resulted current from motion of the movable plate. The current can be expressed as:

$$i = -\frac{\partial Q}{\partial t} = -\frac{\partial (CV)}{\partial t} = -V\frac{\partial C}{\partial t} \tag{3.35}$$

The equation can be rearranged as:

$$i = -V\frac{\partial C}{\partial x}\frac{\partial x}{\partial t} = \eta_{S,P}\dot{x} \tag{3.36}$$

Where $\eta_{S,P}$ is defined as the sensing transduction factor, which is essentially the coefficient of transformation from mechanical energy to electrical energy.

$$\eta_{S,P} = V\frac{\varepsilon_0 A}{d^2} \tag{3.37}$$

In lateral comb-arm base as shown in fig.3.9, I employed the change in area of *A* to trigger the change in motional current. $A = w(l \pm x)$ where *w*,*l* and *x* is the thickness, length and displacement of the lateral comb finger. The addition of *x* essentially alters the magnitude in linearity, resulting the change in motional current.

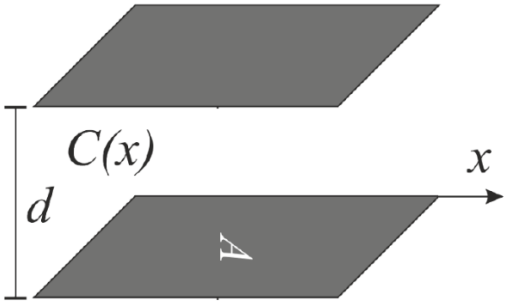

Figure 3.9: Demonstration of lateral comb-arm detection mechanism

On the other hand, the vertical comb-arm as shown in fig.3.10 use the change of the distance d between the opposite plates to incite the motional current. As $d = d_0 \pm x$ and $\eta_{S,P} \sim 1/d^2$. The change in distance trigger an exponential change in motional current, which is one order of magnitude larger than lateral counterpart.

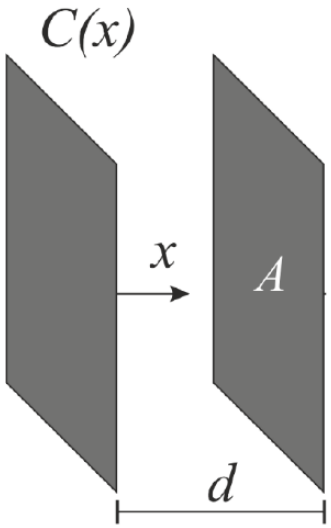

Figure 3.10: Demonstration of vertical comb-arm detection mechanism

3.6 **Conclusion**

In this chapter, fundamental theories of coupled double-mass resonator, including resonator dynamics, pressure-induced technique as well as further discuss on excitation and detection mechanism are covered. I have laid the foundation for coupled resonator sensor for future analysis and simulation. I have also analysed the differences between three types of beams, comparing their properties such as stiffness and nonlinearity, for which is suitable for our cause.

The suspension beam for double-mass structure's stiffness without tension is one order in magnitude higher than cantilever beam, hence increase the Q factor in vibration. In addition, the suspension beam's nonlinear stiffness obtains one order in

magnitude lower than double-ended beam, thus, reducing the noise in output signal during vibration. Both mentioned advantages make suspension beam ideal for resonant strain gauge sensor development.

The double-mass structure's in-plane and out-of-plane resonant mode operate at the same frequency. Out-of-phase mode is a symmetrical one, which minimise the energy loss during vibration, hence obtaining high Q factor. In order to excite only the out-of-phase mode, the coupling mechanism is added to the structure. Eqn (3.17) indicated that the larger the stiffness of the coupling structure, the larger the gap between two resonant modes. Therefore, the coupling structure is necessary for the development of double-mass resonator.

Square diaphragm stress distribution is also analysed. The stress distribution pattern can be described as low in the edge and increasing when move inward. The maximum stress point is at the centre of the diaphragm, where the displacement is also highest. This analysis is critical for the locations of contact points between diaphragm and resonator. The optimal location will increase the pressure-induced strain in the resonator structure.

In addition, capacitive detection and electrostatic excitation are discussed in detail. I also have proved the advantages of vertical comb-arm base such as enhancing the motional current of the resonator system.

Chapter 4 **Coupled double-mass with diaphragm**

4.1 **Introduction**

In this chapter, the previously discussed double-mass structure is first investigated via simulation then fabricated. The theory states that the double-mass resonator need a coupling structure to separate the in-phase mode from the out-of-phase mode. Hence, the uncoupled structure is simulated first to verify this. Then, several coupled structures are proposed, and the resonant frequency tested. The first structure is solely based on Greenwood's design [69], whose piezoresistor coupling structures on the design are removed to achieve a 2DOF mechanical system. Then, second spring coupling structure is introduced. The newly introduced coupling structure differs from Greenwood's design in size and location. The spring coupling is located in-between the two masses and its size is significantly smaller than Greenwood's design. This alternation is proposed to reduce in mechanical imbalance caused by Greenwood's coupling structure. The final coupling structure introduces a balance coupling design in order to obtain a high Q factor. This final design also changes the location of the contact anchor between the diaphragm and the resonator to maximise the induced stress, which lead to enhanced frequency shift due to applied pressure. In addition, the in-plane stress on the plate-shaped diaphragm is revisited and verify by simulation. Combining both analytical and numerical modelling, the location of contact points between diaphragm and resonator are optimised.

In the later part of this chapter, the fabrication process is discussed in detail. Since the resonator device need to be suspended, the process requires at least 3 layers; device structure, insulator and block handle layer. Hence, a silicon on insulator (SOI) wafer is required. When using an SOI wafer, one of the recurring challenges is double-sided alignment, which is required to accurately position features in the device and handle layers. The double-sided alignment masks, therefore, is introduced to the project in anticipation of the problem. The process flow then is presented in separate steps with the support of process tables to summarise all key points.

Finally, the double-mass resonators are tested for resonant frequency and Quality factor (Q factor). The measured resonant frequency is compared with the theoretical and simulated results. The observed Q-factors are discussed at the end of the chapter.

Novelties of the coupling double-mass resonator in this chapter are

- Introduce a double-linkage coupling structure that is mechanically balance, which aim to obtain a high intrinsic Q factor for the resonator.
- Relocate the contacted anchor between diaphragm and resonator to the area where the induced stress is concentrated.

4.2 Finite-element simulation of double-mass resonator with diaphragm

In this section, finite-element method (FEM) simulations on uncoupled and coupled double-mass resonator design have been performed with ANSYS and COMSOL, two multi-physic simulation software packages. The effect of pressure on the resonant frequency of the coupled double-mass resonators has been simulated.

4.2.1 Mode shape simulations of uncoupled double mass resonator

Initial FEM simulations in ANSYS have been performed using a simple the model of double-mass resonator. The structure is comprised of two inertial masses and four supporting beams for each mass. The eight beams then connected to two fixed anchors. The masses are not linked directly other than through the anchors and therefore this structure is defined as uncoupled. The interested mode of operation is inplane out-of-phase. The full model for simulation can be seen in fig. 4.1.

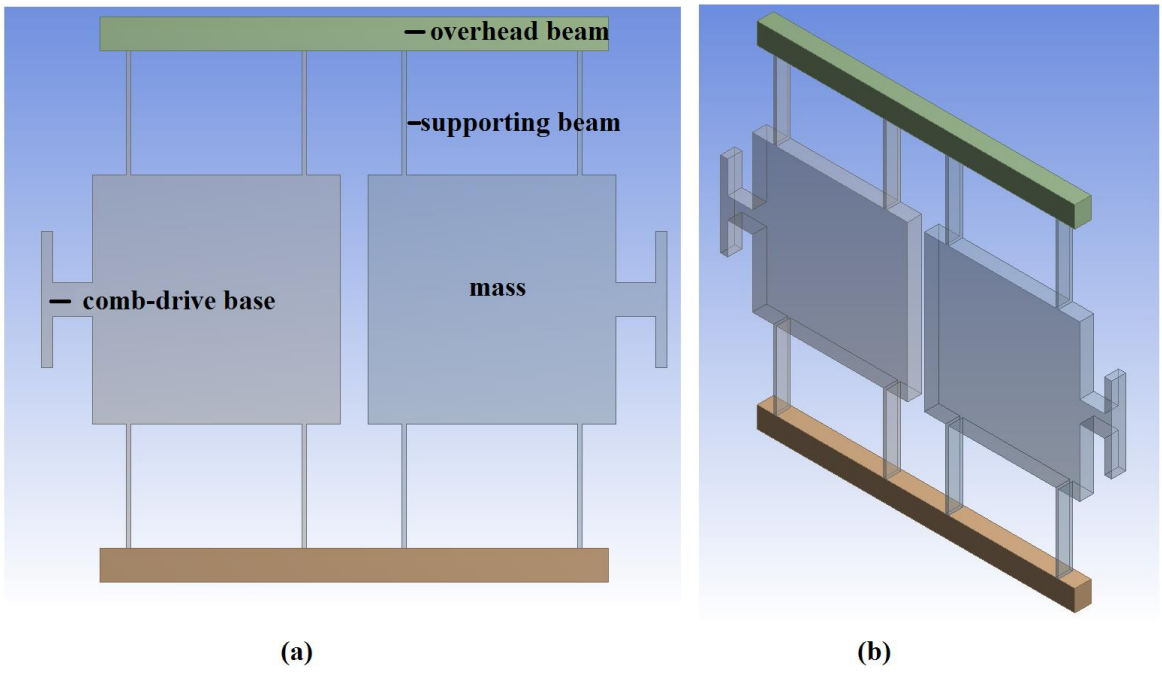

Figure 4.1 (a) Top view and (b) 3D view of double-mass resonator geometry

For fabrication purpose, the choice of design is limited by the photo-lithography process in the Southampton nano fabrication centre and the specification of the SOI wafer. The photo-lithography only provides high resolution for feather of size 4μm and above. The SOI wafer top silicon layer's thickness are 20μm. The parameter of the resonator is listed in table 4.1.

Table 4.1 Dimensions of the device

Parameter	**Design value**	**Unit**
Device layer thickness	20	μm
Suspension beam length	110	μm
Suspension beam width	4	μm
Proof mass	220x220	$(\mu m)^2$
Gap between masses	12	μm

Using Eqn.(3.7), I can easily calculate the spring constant of the suspension beam:

$$K_e = {Ew^3t}/{L^3} \approx 174.3(N/m) \quad (4.1)$$

As the masses of the beam is negligible compared to the proof mass, the mass of the system can be calculated as

$$M_e = tAd \approx 1.86 \times 10^{-9}(kg) \quad (4.2)$$

Thus, I can calculate the estimated resonant frequency from spring constant and effective mass of the system

$$f = \frac{1}{2\pi}\sqrt{\frac{K_e}{M_e}} \approx 48.2\ (kHz) \quad (4.3)$$

The FEM model is generated to test the performance of double-mass resonator without the coupling element. Two overhead beams are assigned to be the fixed support. Using a standard ANYS mesh, the model is broken into 10 500 elements with over 57 000 physical nodes. A modal analysis is used to study the different mode shapes and mode frequencies of the resonator. Fig. 4.2 shows the analysis result with the first 4 mode shapes and mode frequencies. The first two resonant frequencies are the in-phase and out-of-phase mode. The two modes share the same frequency of 48.7 kHz. This result concurs with the theory that without coupling structure, the in-phase and out-of-phase modes cannot be separated. It is worth mentioning that the simulation result is 1% different from the theoretical calculation of resonant frequency. Thus, using Eqn. (4.3), I am able to estimate the fundamental frequency of the system quite precisely. Two masses without coupling will vibrate independently from each other. The first fundamental in-plane frequency mode of single mass structure transforms into the first two in-plane modes of the double-mass structure. By introducing the coupling element, a coupling stiffness, k_c, is added to the equation of

the anti-phase frequency, hence, separating it from the in-phase frequency. Several coupling techniques are proposed.

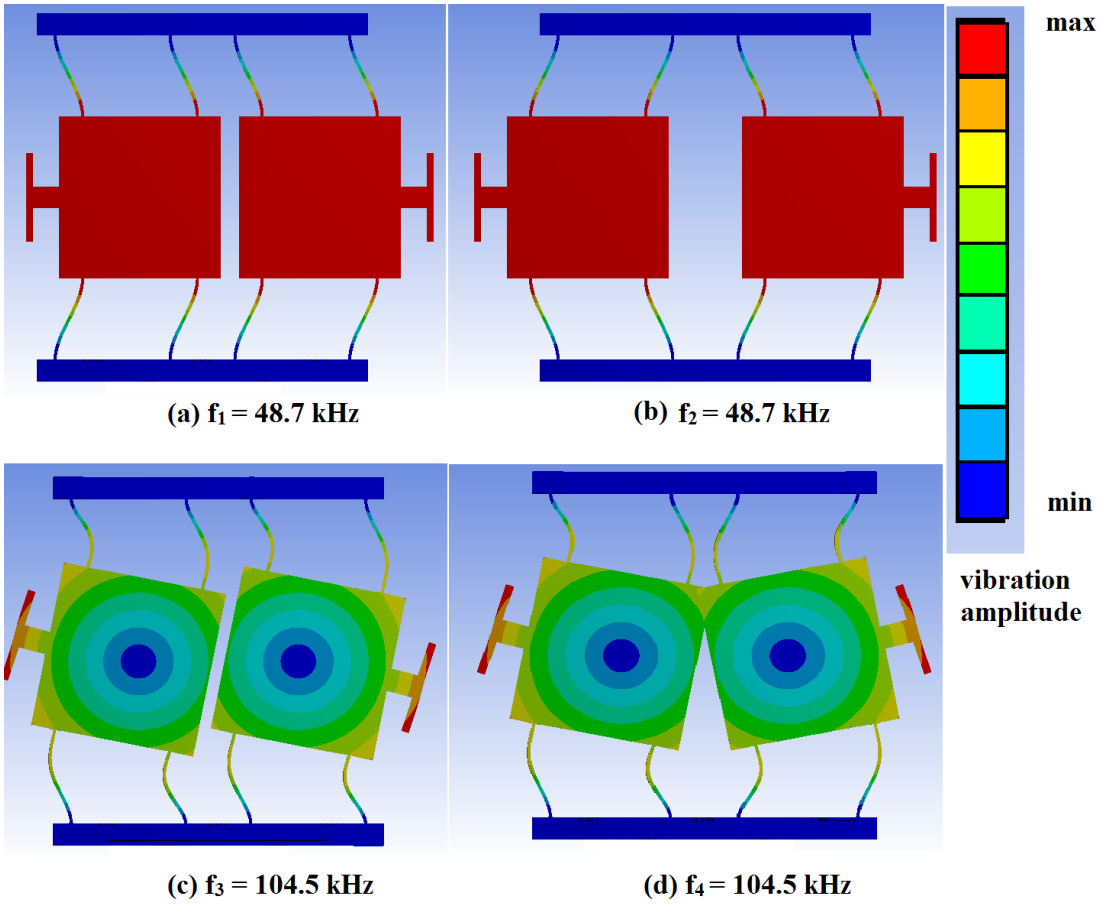

Figure 4.2 Top view for the first 3 mode shape of resonator design: (a) flexural in-phase mode, (b) flexural anti-phase mode, (c) torsional in-phase mode and (d) torsional anti-phase mode

4.2.2 Mode shape simulations of coupled double mass resonator

First, coupling structures similar to the one proposed by Greenwood [69] can be used to directly couple the two masses. The design, as seen in fig.4.3, is similar in structure but with modified dimension to fit the SOI wafer. The chip size is reduced from millimetre to hundred micro scale. The freestanding overhead linkage consists of two vertical beams and one horizontal beam. The two vertical beams are connected to the masses and the horizontal beam via four flexible joins. The vertical beams have a length of 200 µm, width of 30 µm and a thickness of 20 µm. The horizontal beam is 450 µm long; other dimension is the same with vertical beams. The joins only have 4 µm width, which reduces its stiffness significantly. Therefore, the stiffness of the overhead structure depends much on the stiffness of the joins. In addition, the structure is integrated with a pair of piezoresistors for frequency detection. Introduction of these piezoresistor allows us to evaluate their effect on the stiffness of

the resonator, which in turn changes the resonant frequency. A pair of piezoresistor is coupled into the supporting beam.

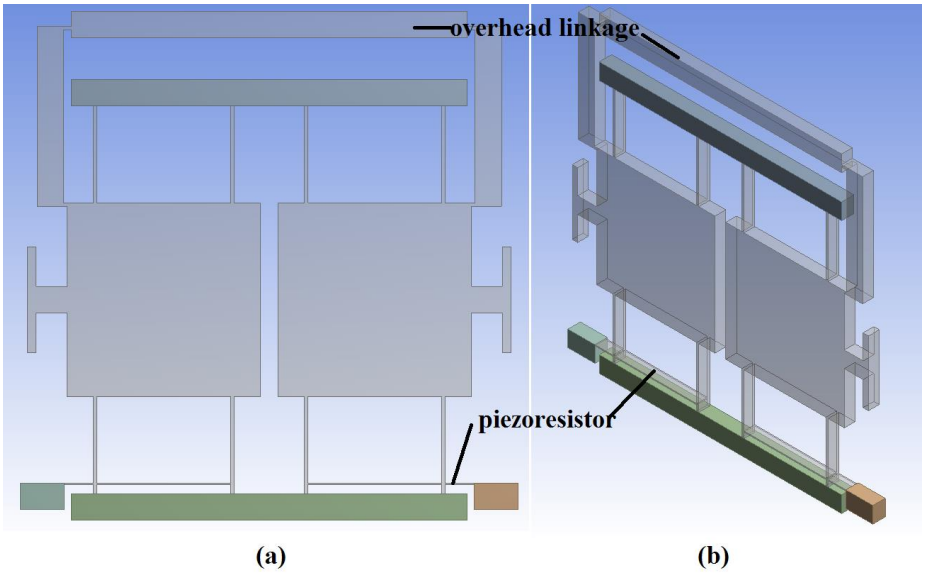

Figure 4.3 Overview of double-mass structure with overhead linkage: (a) top view and (b) 3D view

It is worth mentioning that the overhead linkage also introduces additional mass of M_c into the spring system. The formula for in-phase frequency becomes

$$f_{ip} = \frac{1}{2\pi}\sqrt{\frac{K_e}{M_e+M_c}} \quad (4.4)$$

While the formula for out-of-phase frequency is

$$f_{op} = \frac{1}{2\pi}\sqrt{\frac{K_e+K_c}{M_e+M_c}} \quad (4.5)$$

Where $K_c = Ew^3t/L^3$ for the join part of the linkage and additional mass is the sum of all its component's mass $M_c = \sum t_i A_i d$. From eqn. (4.4) and (4.5), I found that the theoretical out-of-phase and in-phase frequency are equal to 53.3 kHz and 39.7 kHz, respectively. The in-phase frequency has reduced due to the introduction of the mass of the coupling structure.

The FEM simulation result shows an increase in the out-of-phase frequency from 48.7 kHz to 53.8 kHz. In the case of without the piezoresistor, out-of-phase frequency is equal to 53.6 kHz. Thus, the piezoresistor mechanical effect is negligible compared to the coupling structure one. The in-phase vibration mode is separated from out-of-phase mode with resonant frequency at 39 kHz. Other adjacent modes are all over 300 kHz. This result once again agrees well with the theoretical calculation with a

difference of less than 2% for the mode frequency, indicating that the theoretical estimations are accurate.

A second approach involved investigating a flexural spring structure to couple the masses. The structure is shown in fig.4.4. The spring structure is located in the gap between the two masses. The two vertical beams are coupled via a join on top and coupled to the masses via two joins on the side. The spring stiffness was optimised by increasing its beams' width to produce a significant gap between out-of-phase mode and adjacent mode while maintaining the frequency value under 100 kHz. The optimised beams are 70 µm long, 7 µm wide and 20 µm thick. When vibrating in the out-of-phase frequency, the spring is compressed for half the period. The two masses move inwards and squeeze the two beams together. Thus, the gap of 3 µm between two beams is used at a buffer zone, which prevents them from colliding into each other.

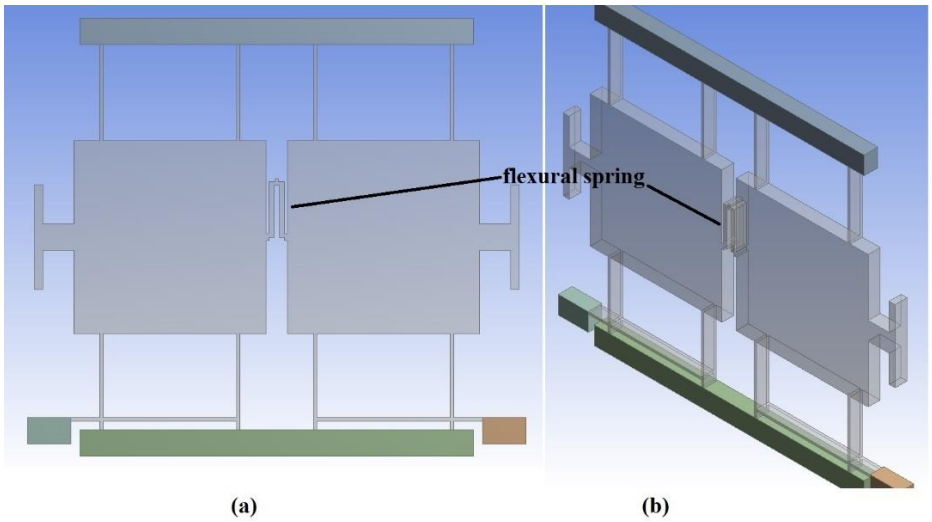

Figure 4.4 Overview of double-mass structure with flexural-coupled spring: (a) top view and (b) 3D view

The simulation shows a gap of 37 kHz between out-of-phase and in-phase mode. While the out-of-phase frequency experienced an increase of 40 kHz to a value of 88 kHz, in-phase mode slightly reduces to 46.8 kHz. The coupling structure stiffness and mass are equal to 385 N/m and 68×10^{-12} kg, respectively. Using eqn. (4.4) and (4.5), the theoretical inphase and out-of-phase frequency are equal to 46.4 kHz and 87.3 kHz respectively. The relative difference of mode frequency is less than 1%.

The third proposed design is shown in fig. 4.5. Instead of directly coupling two masses, the supporting beam is connected together via two horizontal linkages. The anchors are moved further away and linked to the coupling linkages via two thin beams. These linkages are 450 µm long, 30 µm wide and 20 µm thick. The anchor acts at the fixed support as well as the electrical contact. Thus, the piezoresistor now can be located onto the supporting beams. When the resonator vibrates, these beams

are under strain, hence, produce change in resistance. This design seems to reduce the stiffness for in-phase oscillation, as its in-phase frequency is 41.1 kHz in compared to 48.7 kHz of the original design. The result for out-of-phase frequency is 49.1 kHz. Thus, I create a gap of 8 kHz between the two adjacent modes. Using eqn. (4.1) and (4.2), the calculated effective stiffness and mass of the coupling linkage are equal to 72.9 N/m and 0.78×10^{-9} kg respectively. Thus, the theoretical in-phase and out-of-phase frequency are 40.9 kHz and 48.7 kHz respectively. The relative difference is less than 2% in this computation.

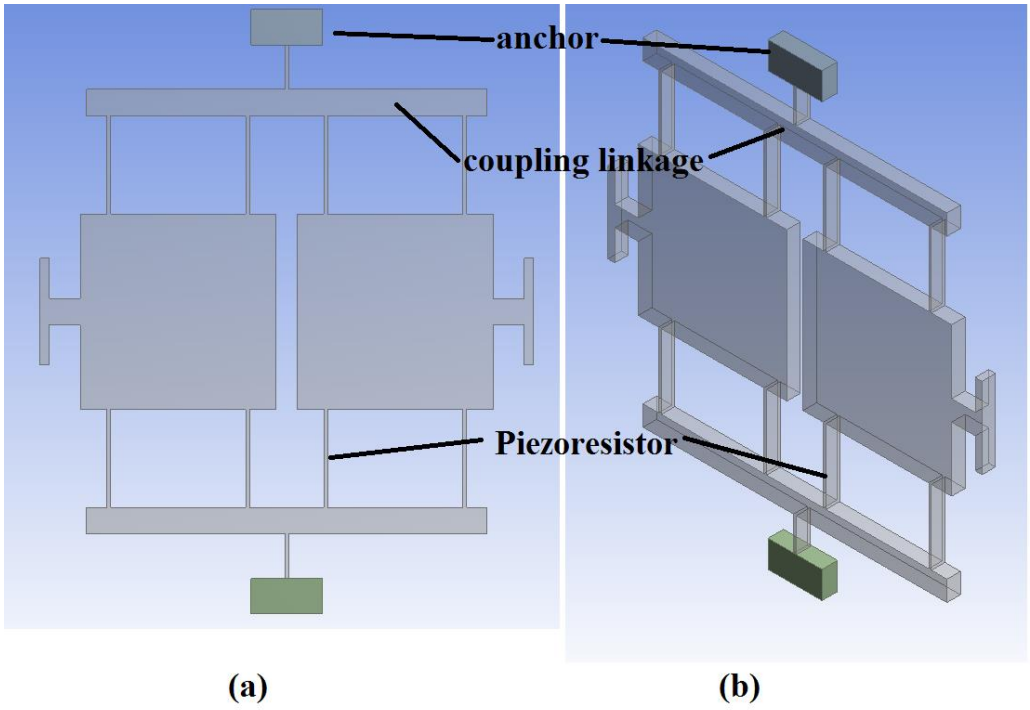

Figure 4.5 Overview of double-mass structure with modified anchor: (a) top view and (b) 3D view

The three coupling structures all produce a significant gap between two flexural in-plane modes as shown in table 4.2. Quartz sensor's resonant frequency is under ten kHz, while typical silicon resonant frequency is in order of 10^2 kHz [24]. Low resonant frequency allows the resonant peak to be detected with simple detection circuit. Next step is to investigate the frequency shift of each structure due to applied strains and optimise the design for maximum sensitivity. In addition, frequency cross-over is another factor to consider. The two adjacent frequencies show different shifts under applied pressure. Thus, it is possible that the two modes meet and cross-over, which results in difficulty for detecting the correct mode afterwards.

Table 4.2 Out-of-phase mode and adjacent frequency for three different coupling structure

Coupling design	In-phase theoretical	In-phase simulation	Out-of-phase theoretical	Out-of-phase simulation
Over-head linkage	39.7 kHz	39 kHz	53.3 kHz	53.8 kHz
Flexural spring	46.4 kHz	46.8 kHz	87.3 kHz	88 kHz
Beam coupled linkages	40.9 kHz	41.1 kHz	48.7 kHz	49.1 kHz

4.2.3 Pressure induced deflection simulation of diaphragms

The diaphragm is the part of the sensor in direct contact with applied pressure. Then, the pressure induces the deflection in the diaphragm, which in turn causes stress and mode frequency shift in the resonator structure. Thus, the diaphragm has to have sufficient strength and elasticity to survive the high pressure in down-hole application. A solution is to use single crystal silicon as material for the diaphragm. Single crystal silicon is not only strong and elastic [98] but also is compatible with many fabrication processes as well as electronic circuit integration. In the previous chapter, I have investigated the theoretical deflection and in-plane stress of thin plane diaphragm structure. Hence, I am able to verify the theoretical calculation with simulation result. The square diaphragm model was built in ANSYS as shown in fig.4.6.

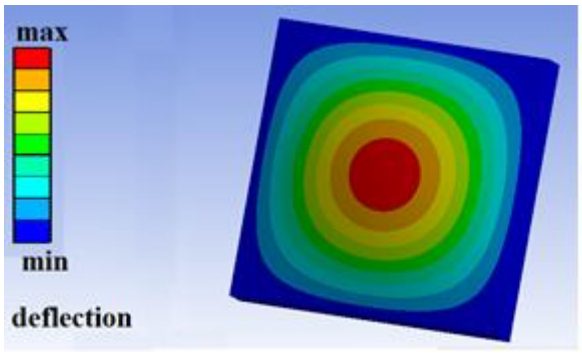

Figure 4.6: Square diaphragm structure used in FEM simulation. Colour contour represent the relative displacement caused by arbitrary pressure applied from the backside

For verification purpose, the choice of design parameters of the device was arbitrary. It is worth noting that the smaller the size of the sensor will lead to lower cost in installing and oil well monitoring. Three different thicknesses are select to for analysis. The device's parameter is listed in table 4.3:

Table 4.3: Dimension of the diaphragm

Dimension	Design value	Unit
Width	800	µm
Length	800	µm
Thickness	60/90/120	µm

Three different thicknesses for each type of diaphragm are simulated for maximum deflection and in-plane tensile stress as the result of pressure from 100 to 1000 bar. The theoretical maximum deflection and in-plane tensile stress were calculated using Eqn. (3.21) and Eqn. (3.25), respectively. The result for both simulation and theoretical calculation deflection are shown in fig. 4.7.

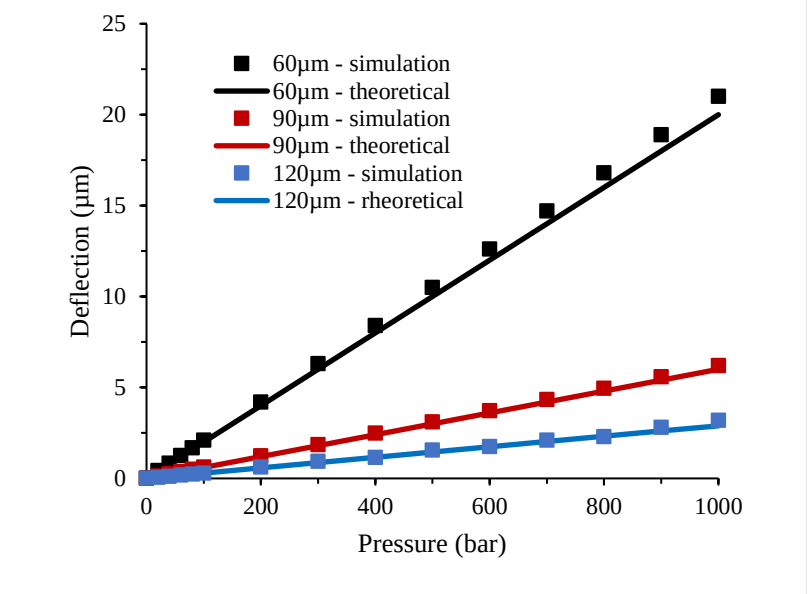

Figure 4.7 Theoretical and simulated diaphragm maximum deflection (measured at the centre) plotted vs applied pressure for different types and thicknesses

Silicon on insulator (SOI) wafer is preferable to fabricate the sensor as it provides an alternative for complicated silicon-to-silicon bonding process. The top layer is patterned into resonator while bottom silicon layer is used as the diaphragm. The insulator layer between two silicon layers can have maximum thickness of 4 µm due to fabrication constraints. Thus, the 120 µm thick square diaphragm, whose maximum deflection under 1000 bar pressure is less than 3 µm, is preferable.

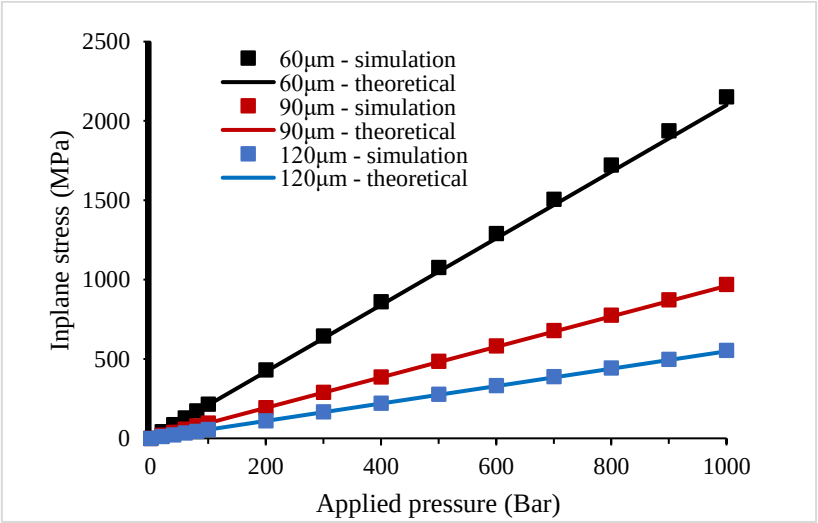

Figure 4.8 Maximum theoretical and simulated inplane stress (measured at the centre) in *y* direction vs applied pressure for square diaphragm

It is important to consider the inplane stress to understand the mechanism of the diaphragm. Inplane stress directly induces tensile stress onto the resonator, hence is the key factor for pressure induced technique. The goal is to maintain the induced stress while reduce the deflection caused by applied pressure. Fig.4.8 shows the calculated and simulated in-plane stress. The relative difference is less than 2% for three different thicknesses. It is worth mentioning that the loss in deflection is directly proportional to the reduction in in-plane stress when increasing thickness of the diaphragm. Table 4.4 shows the ratio of simulated inplane stress over deflection at 1000 Bar for all three diaphragms' thickness. The higher the ratio, the more efficient a diaphragm operates. The result shows an increase in the ratio with the two thicker diaphragms, almost double the value of 60µm diaphragm. However, as the mentioned ratio of 120 µm diaphragm is lower than one of 90µm counterpart, 120 µm is considered fairly optimal but not the most optimized thickness for the application.

Table 4.4 Ratio of simulated deflection over inplane stress at 1000 Bar

Diaphragm thickness (µm)	**Deflection at 1000 Bar (µm)**	**Inplane stress at 1000 Bar (Mpa)**	**Inplane stress - deflection ratio (Mpa/ µm)**
60	19.8	2150	108.5
90	4.9	960	196
120	2.6	485	186

4.2.4 Simulation on the combined diaphragm double-mass resonator design for selectivity

Greenwood's design [69], which is used to measure lower range of pressure, has been redesigned to increase the pressure range from 0-5 bar to 0-1000 bar. The resonator design can fit on top of an 800 µm side-length square diaphragm as shown in fig. 4.9. To investigate the shift in resonant frequency in ANSYS, a Static Structural module can be used to analyse the pressure effect on the device's stiffness before applying a second modal module to track the change in mode frequency. The desired mode of operation (Out-of-phase mode) and two adjacent modes are simulated to assess their response to a range of applied pressure up 1000 Bar.

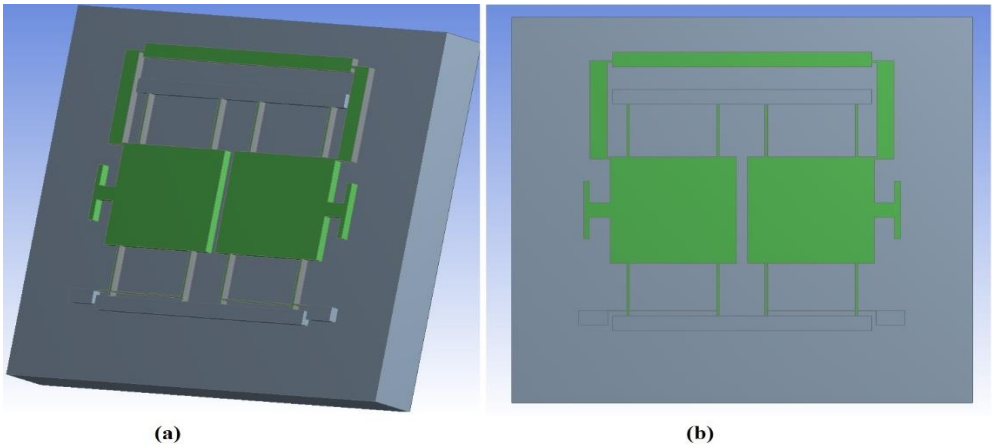

Figure 4.9 (a) 3D and (b) top view of overhead coupling double mass resonator integrated into diaphragm.

Using Eqn. (3.25), I am able to calculate the pressure-induce tensile stress on *y* axis. Then by applying Eqn. (3.7), I can calculate the additional spring constant imposed upon the resonator by the applied stress. Hence, the resulted resonant frequency can be theoretical calculated.

The frequency for both theoretical analysis and simulation is illustrated in fig. 4.10. The simulation shows no cross-over between adjacent modes up 1000 Bar. The closest observed gap is approximately 2.5 kHz between inphase and out-of-phase mode at 1000 bar pressure. The overall sensitivity is 38 Hz/Bar with unstressed out-of-phase frequency of 53.3 kHz. The simulated results agreed well with the theoretical frequency shift, with relative difference less than 3%.

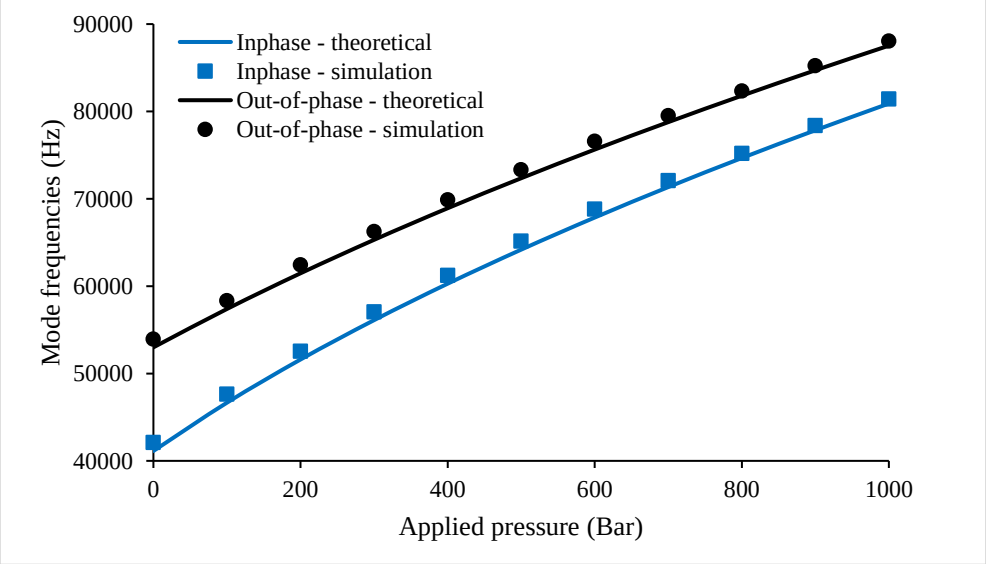

Figure 4.10 Fundamental mode frequencies of overhead coupling structure against applied pressure

The flexural coupling spring structure as shown in fig.4.11 has also been optimised to produce the highest sensitivity. The two masses are 24 µm away, leaving the gap for spring design. As 1000 bar is applied to the diaphragm, the in-phase mode (mode 1) and out-of-phase mode (mode 2) start to shift with similar rate and maintain the gap of approximately 18 kHz as shown in fig. 4.12. The simulated sensitivity is 18 kHz/Bar with fundamental out-of-phase frequency of 88 kHz. The gap between two modes can be increased by increasing the stiffness of the coupled structure. This change also increases the resonant frequency of the resonator.

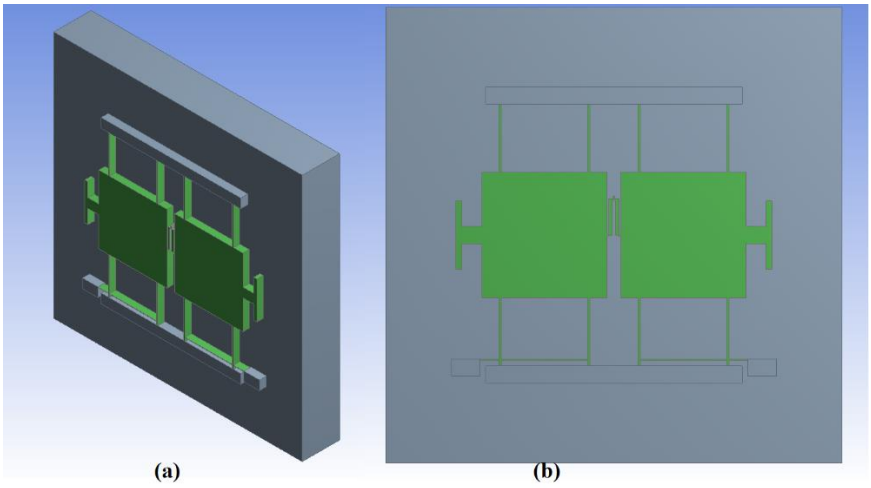

Figure 4.11 (a) 3D and (b) top view of flexural spring coupling double mass resonator integrated into diaphragm.

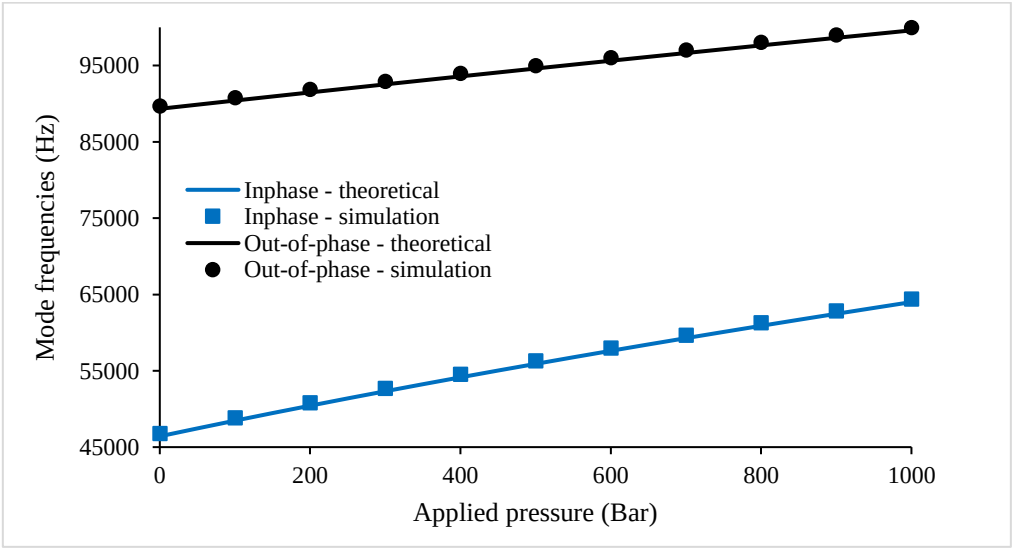

Figure 4.12 Fundamental mode frequencies of flexural spring coupling structure against applied pressure

The supporting beam coupling structure optimisation was carried on several parameters including the linkage-to-anchor dimensions, anchor dimensions and position as well as the supporting beam length and width. It is found that by relocating the anchors position between the linkages and the masses, the sensitivity of the device

increases significantly. The electrical contacts remain but use a smaller and longer connecting track to minimise its effect on the resonant frequency. The final design shape is shown in fig 4.13. The gap between the underneath diaphragm and resonator is 3 µm in vertical direction. Under increasing applied pressure, mode 1 and mode 2 start to separate as their induced stiffnesses change differently. No cross-over during the course of 1000 bar pressure is observed. The overall sensitivity is approximately 48 Hz/Bar with the unstressed out-of-phase resonant frequency of 49.6 kHz

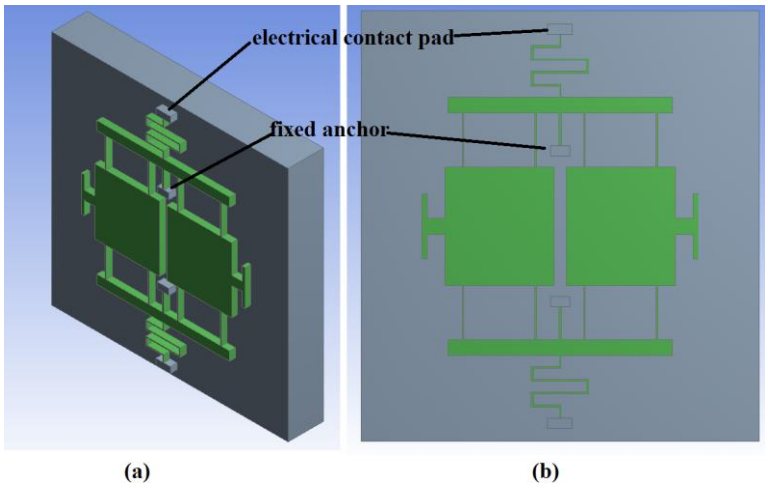

Figure 4.13 (a) 3D and (b) top view of supporting beam coupling double mass resonator integrated into diaphragm

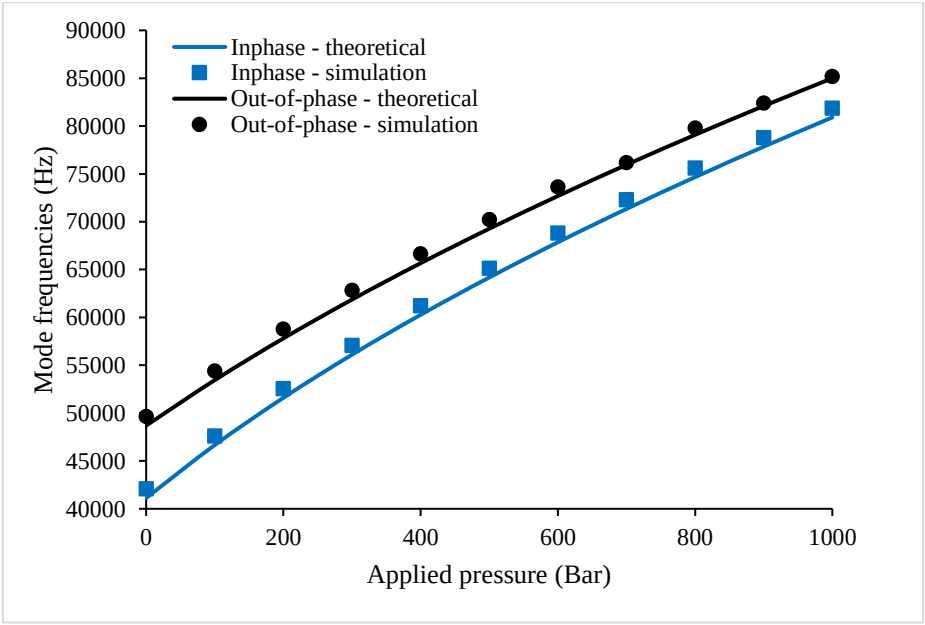

Figure 4.14 Fundamental mode frequencies of supporting beam coupling structure against applied pressure

The supporting beam coupling structure has performed well with a sensitivity of 48 Hz/bar over 1000 bar range. The location of the anchor is identified as the main

contribution to the rise in sensitivity. Moving the anchor toward the centre of the diaphragm increase the axial strain, which in turn increase the sensitivity of the resonator.

4.2.5 Discussion

The unstrained frequency target is lower than 100 kHz in order to obtain a high resolution for the final design. During the simulation, the flexure beam dimensions have been identified as the main factor that effects the resonant frequency. As the double mass provides a fixed mass constraint, the dimensions of the flexure beam decide the stiffness of the resonator. A wider beam is associated with higher stiffness level, which results in higher resonant frequency. Thus, the beam width is optimised to 4µm, which is the minimum feature dimension in fabrication process to minimise the unstrained resonant frequency.

The optimised coupled double-mass has shown a sensitivity level of 48 Hz/bar over 1000 bar range with the unstrained frequency of 49.6 kHz. This simulated result concurs with the theoretical result, giving the relative difference of less than 3%. However, the design need to be modified in order to overcome fabrication challenges such as separating resonator layer from the diaphragm using Hydrofluoric acid (HF) vapour and the potential stiction between the two layers. The fabrication process is presented in the next section.

4.3 Fabrication Process flow

In this section, the fabrication process is discussed in detail. A brief section on previously successful fabrication flow for MEMS suspended structure at University of Southampton is included. The process then is modified to accommodate the coupled double-mass resonator and its piezoresistive detection mechanism.

4.3.1 State-of-the art fabrication process for MEMS suspended structure

Southampton nano fabrication centre have the facility to support a wide range of MEMS device fabrication. Previously, there has been process that is developed for suspended structure for SOI wafer [99]. This process allows the release of large feature size without the problem of stiction caused during wet processing. The wafer used in this research has a diameter of 150 mm with backside layer thickness of 560 µm. The top silicon layer with thickness of 50 µm is separated from backside layer by a 3 µm thick buried oxide layer (BOX). The technologies used in the process include deep reactive ion etching (DRIE), plasma-enhanced chemical vapour deposition (PECVD), inductive coupled plasma (ICP), Hydrofluoric acid (HF) vapour and photolithography.

The first step of the process is to deposit thin layers of silicon dioxide (SiO_2) on top of device layer as well as handle wafer using PECVD. Next, two layer of positive resist

is deposited on top of silicon dioxide layer by spin-coating. These resist layers are patterned and developed using standard photolithography. Next, ICP is used to remove the oxide that is not protected by the remaining resist. Then, all resists are removed and the oxide layers act as the mask for a subsequent etching step. DRIE is used to the trench in backside wafer and device layer as seen in fig.4.17 (a) and (b). Next, the wafer is processed inside an HF vapour etcher (VPE) to remove the BOX layer as shown in fig. 4.17 (c). The oxide removal releases the device from the handle block as well as the wafer grid in fig. 4.17 (d). Thus, the device is removed without using dicing step. The flow is shown in table.4.6.

Table 4.5 Southampton fabrication process flow for device suspension on SOI wafer

No	Step	Material	Method	Thickness
1	Deposit	SiO_2	PECVD	1 um
2	Deposit	Positive resist S1813	Spin-coating	1um
3	Removal	Positive resist S1813	- Expose to UV light under the photo-mask in a mask aligner - Develop in developer MF319	1um
4	Etching	SiO_2	ICP	1um
5	Etching	Front side	Dry etch with DRIE	50um
6	Etching	Back side	Dry etch with DRIE	600 um
7	Removal	BOX	HF vapour	2 um

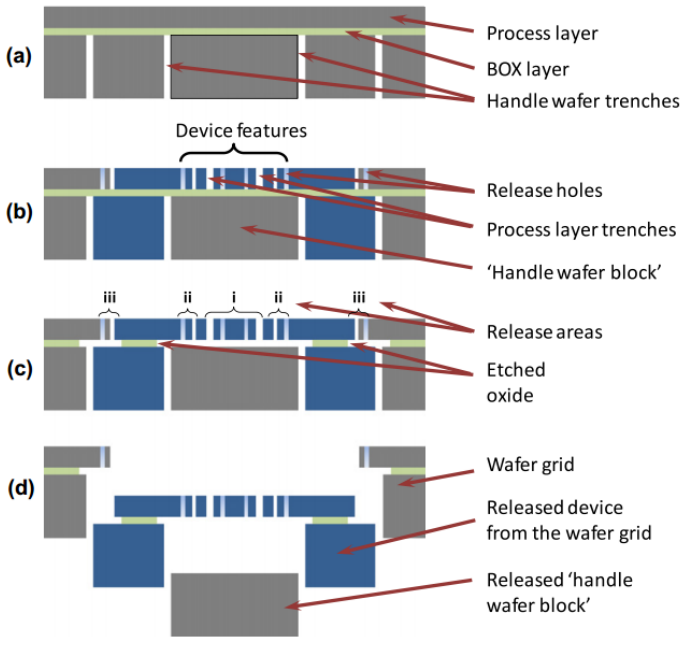

Figure 4.15 Fabrication flow of Southampton process for SOI wafer

Since suspended structures are susceptible to stiction with the handle wafer layer when using the HF released step. To avoid the risk of stiction, any part of the

resonator, that has a large area, is fabricated with released holes. These release holes allow HF vapour to access the BOX layer underneath and remove it completely. The size and spacing of the holes is optimised so that the resonator is the first feature to be released. Then, the device is released from the wafer grid. However, this process removes the handle block underneath the resonator, which would form part of the diaphragm for a pressure sensor application. Hence, the process is suitable to in other types of MEMS device such as accelerometer and gyroscope and prototype resonator. Different approach to retain the diaphragm structure is needed.

This process is used for wafer with very low resistivity i.e. 0.1-0.001 Ω/m^2. Since proposed coupled double-mass resonator employs piezoresistive detection mechanism, the wafer's resistivity is of 20 Ω/m^2. Thus, the process need to be modified to include the dopant diffusion step to reduce the resistance on conductive pad, which is used to wire-bonded to chip-carrier. The conductive pad resistance requirement is 0.5 Ω/m^2. An additional alignment marking etching step is also introduced to produce a reference mark for future steps.

4.3.2 Photomask design with variation of the functional area

In this section, the design of the photomask is briefly discussed. Then, the device design variation is described in detail. The device designs are adjusted based on their flexure beam thickness, mass side-length, length of comb drive base and the overhead linkage width.

The first step of MEMS resonator fabrication is to design a series of photo-masks. Each mask contains a pattern for depositing or removing material for a specific step. Optical lithography is the standard method used to transfer the design on the photo-mask onto the wafer. The mask is aligned to the photoresist-coated wafer and exposed by UV radiation inside a mask-aligner/exposer tool. The masks for double-mass resonator structure are 7 x7 inches to accommodate 6 inches SOI wafer size. The design contains 4 layers that are alignment, contact, device layer and backside mask.

In fabrication process flow, the alignment is used first to etch a visible mark onto front side of the wafer. This mark is subsequently used in aligning other layers. Then, a contact mark is used for implantation process, which reduces the resistivity of the electrical contact pad in resonator structure. The device layer and backside mask can then be used to pattern the resonator structure and backside trench for release process. While the first three marks are used to expose the SOI layer, backside mark apply to the backside wafer. Therefore, double-sided alignment mask is used and is aligned to the front side using the double-sided features etched on to the front of the wafer. Device, contact and alignment layer share the same mask, while the backside has a slightly larger feature as shown in figure 4.15. The four alignment marks are located on the centre diameter of the masks.

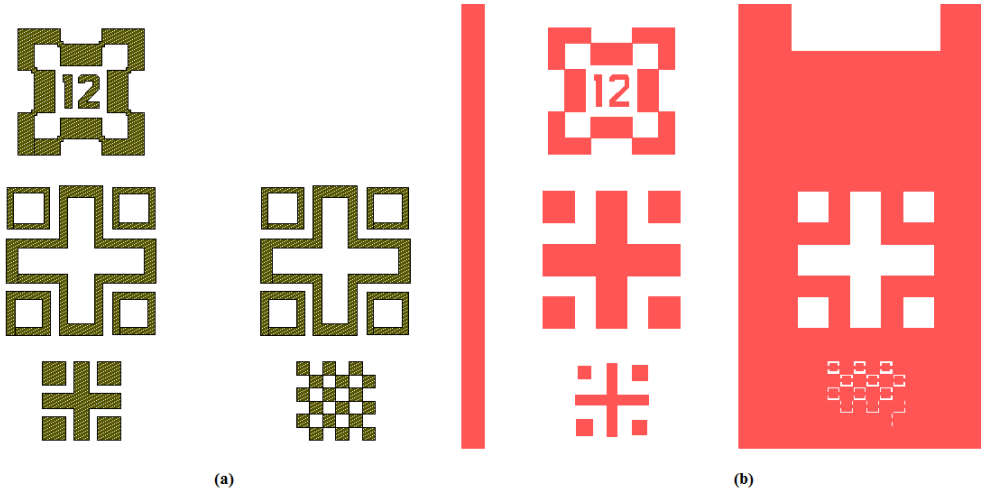

Figure 4.16 Double sided alignment mark (a) back side; (b) front side

4.3.2.1 Device variations

Chip design variation are implemented in the device layer mask. In this mask, resonator designs are distinguished based on four parameters: flexure beam width, mass side-length, length of comb drive base and the overhead linkage width. Different beam widths theoretically lead to different spring constant while mass side-length adjustment alter the mass of the resonator. These two parameters are the deciding factor for the resonant frequency of the device. Four different versions of the resonator are shown in table 4.5. The comb-base length is also considered due to its effect on the excitation force. A large comb-base increases the excitation force. To find the optimal force, three different comb-base lengths is used. In addition, the gap between in-phase and out-of-phase mode is dependent on the coupling spring constant, hence, the linkage width. Thus, 4 different widths have been included in the mask design: 30 µm, 50 µm, 70 µm and 90 µm. These designs will be tested for the in-phase and out-of-phase resonant frequency. In addition, the device is filled with released holes in order to increase the released speed of resonator structure during HF vapour process.

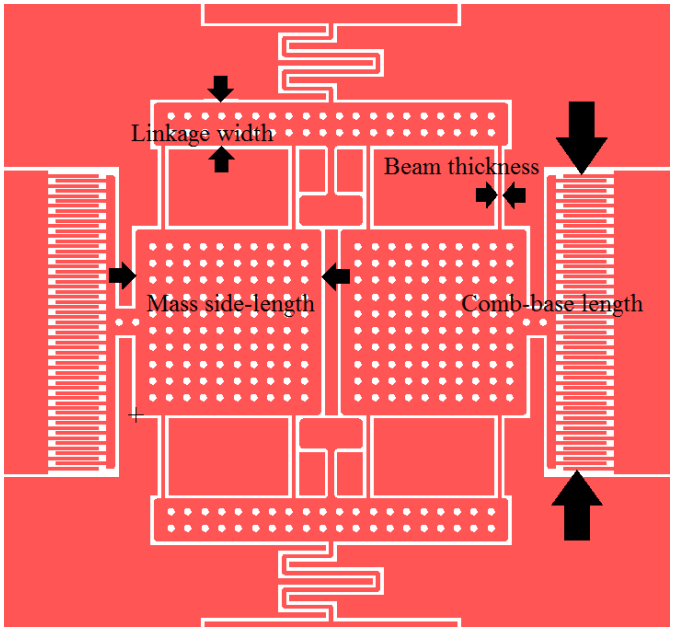

Figure 4.17 Photolithography mask layout for coupled double-masses resonator design. Red: device layer

Table 4.6 Example of coupled double-masses resonator design with different supporting beam thickness, mass side-length and comb-base length

Device	Beam thickness (µm)	Mass side-length (µm)	Comb-base length (µm)
1	4	220	200
2	4	220	350
3	4	240	200
4	4	240	350
5	6	220	350
6	6	220	200
7	6	240	200
8	6	240	350

4.3.3 Alignment marking

Alignment marking is the first step in fabrication process after which a permanent alignment marks will be etched into the device layer. First, the SOI wafer is cleaned using the RCA process to remove organic, ionic contaminants as well as any native oxide, leaving a pure silicon surface. Then, a 1µm layer of positive resist (S1813) is deposited onto the device layer by spin-coating at 5000 rpm. The wafer, then, is baked in hot-plate for 60s at 115 ºC to harden the resist. This photo resist layer is the light sensitive material used for photolithography process. Next, the wafer is exposed to UV light in the mask aligner for 2.5s. The exposed resist is developed in the developer solution (MF319) for 45s. Then the wafer is rinsed in wafer for 180s and dried for 60s using the spinner. Next, the device layer is etched for 2 minutes using RIE. Finally,

oxygen plasma is used to remove the resist completely from wafer surface. The detail steps are shown in table 4.7.

Table 4.7 Processing steps to etch the alignment mark into wafer

No	Step	Material	Method	Thick -ness	Time	Mask
1	Clean	Wafer	RCA clean		20 min	
2	Deposit	Positive resist S1813	Spin-coating at 5000 rpm	1um	60s	
3	Removal	Positive resist S1813	- Expose to UV light under the photo-mask in a mask aligner - Develop in developer MF319	1um	2s 45s	Alignment
4	Rinsing & Drying	Wafer	-Rinsing using water -Drying using spinner		180s 60s	
5	Etching	SOI layer	Dry etch with RIE	1um	120s	
6	Removal	Positive resist S1813	Use oxygen plasma to remove the resist completely	1um	15 min	

The etch depth was measured to be 945 to 1020 nm and the features are shown under the microscope as seen in fig. 4.18. Since the flexural beam's width are 4 µm, obtaining high resolution for dimension of 2 µm is critical.

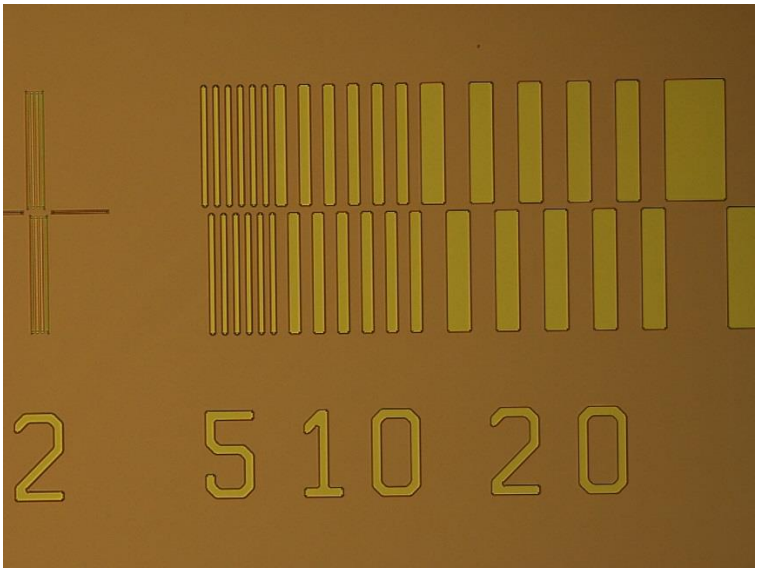

Figure 4.18 Alignment mask on SOI wafer before removing the resist.

4.3.4 Dopant diffusion

The purpose of implantation step is to increase the doping concentration in the contact area. As the result, the resistivity at these areas is lowered for electrical signal to be

delivered and read without noise. Other parts of device layer still have high resistivity as I employed piezoresistive detection. First, a 1µm oxide layer is deposited on top of the front side wafer by using PECVD. Next, a 6µm layer of positive resist (AZ9260) is deposited on top of the oxide layer using spin-coating. This resist is baked in hot-plate for 120s at 120 ºC to be hardened. Then, the wafer is positioned in the mask aligner along with the 'Contact' mask to expose the photoresist under UV light. The exposed resist, then, is developed in AZ400K solution for 6 to 7 minutes. Next, exposed oxide layer is etched using ICP for 4:30 minutes. The remaining resist is then removed completely by using oxygen plasma. The top layer silicon is revealed after oxide-etching and resists-stripping process. Boron dopant B153, then, is spin-coated at 5000rpm on top of the wafer before being annealed at 1000ºC for 12 hours. After being removed from the furnace, the wafer is left to cool down. Next, the wafer is dip etched in HF for 10 minutes to remove surface oxide layer.

Fig.4.19 shows the function of 'contact' photo-mask layer on fabrication process. The mask pattern covers most of the wafer, leaving only the where electrical signal is contacted. Implantation process reduces the resistance of these areas, hence, increase power efficiency of overall circuit. The complete process is summarised in table 4.8.

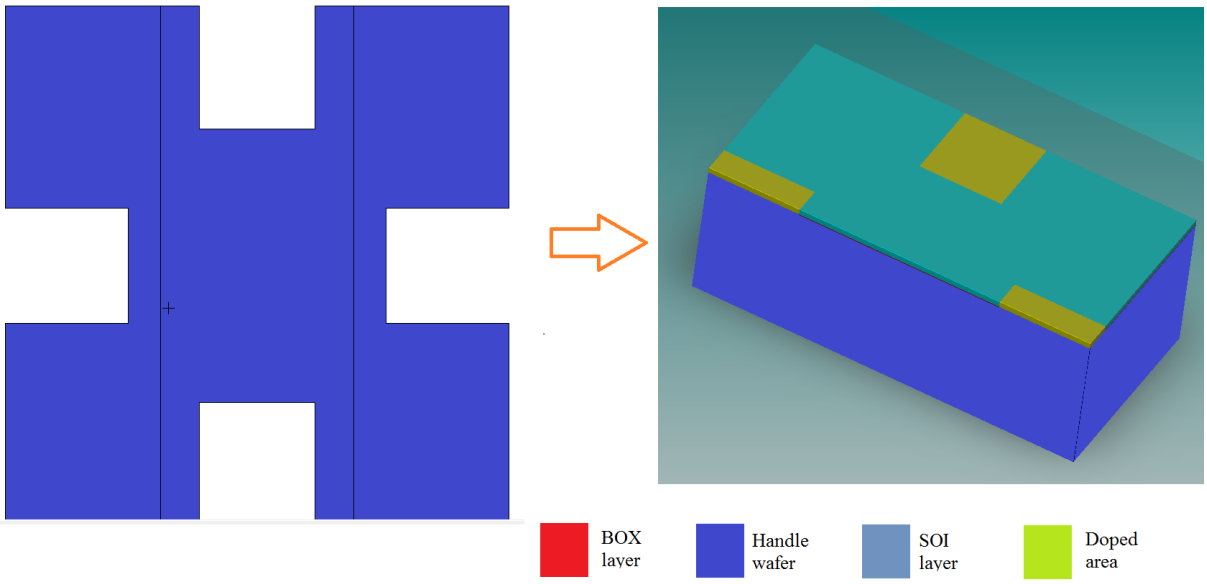

Figure 4.19 Photo-mask used for doping process and cross-sectional view of animated wafer

Table 4.8 Processing steps to dope the contact area

No	Step	Material	Method	Thickness	Time	Mask
1	Deposit	Oxide (SiO_2)	Use PECVD (SiH_4, N_2, N_20)	1um	15 min	
2	Deposit	Positive resist AZ9260	Spin-coating at 3500 rpm	6um	2 min	
3	Removal	Positive resist	- Expose to UV light under the	6um	10s	Contact

		AZ9260	photo-mask in a mask aligner - Develop in developer AZ400K		6 min
4	Removal	Oxide (SiO_2)	Etch using ICP (C_4F_8/O_2)	1um	5 min
5	Removal	Positive resist AZ9260	Use oxygen plasma to remove the resist completely	6um	15 min
6	Doping (deposit)	Boron (B)	Spin coat boron dopant and anneal at 1200^oC Remove dopant in HF 7:1		10 min 10 min
7	Removal	Oxide	Dip etch by HF bench	1um	10 min

The standard 15 minutes PECVD recipe results in 1100 µm of silicon dioxide due to slight variation of processed gas during the deposition process. Thus, the ICP time is adjusted to 5 minutes. The etch rate in the centre area is faster than at the edge of the wafer. Thus, to remove completely the oxide in the edge area, centre area is over-etched a few hundred nanometres.

4.3.5 Patterning the resonator and backside layer

Patterning the resonator and backside layer is the photolithography process that prepares the wafer for dry etching. Front side mark is patterned with 'device' mask, which contains the detail of every part of the resonator. The process is as follows. First, a 1µm oxide layer is deposited on top of the front side wafer by using PECVD. Next, a 1.5 µm layer of positive resist (S1813) is deposited on top of the oxide layer using spin-coating. This resist is baked in hot-plate for 60s at 110 ^oC to be hardened. Then, the wafer is positioned in the mask aligner along with the 'Device Layer' mask to expose the photoresist under UV light. Only the contact area not protected by the mask is exposed. The exposed resist, then, is developed in MF319 solution for 45 seconds. Next, exposed oxide layer is etched using ICP for 4 minutes. The remaining resist, then, is removed completely using oxygen plasma. After careful examination, the front side is coated with 1 µm of S1813 to protect the delicate feature of the device. The summary of the process is shown in table 4.9.

Table 4.9 Processing steps for patterning top layer

No	**Step**	**Material**	**Method**	**Thickness**	**Time**	**Mask**
1	Deposit	Oxide	Use PECVD (SiH_4, N_2, N_20)	1um	15 min	
2	Deposit	Positive resist S1813	Spin-coating at 5000 rpm	1.5 um	1 min	
3	Removal	Positive resist S1813	- Expose to UV light under the photo-mask in a mask aligner - Develop in developer MF-319	1.5um	2s 45s	Device layer
4	Removal	Oxide	Etch using ICP (C_4F_8/O_2)	1um	5 min	
5	Removal	Positive resist	Use oxygen plasma	1.5um	10 min	

		S1813			
6	Deposit	Positive resist S1813	Spin-coating at 5000 rpm	1um	60 s

The comb-drive areas have the densest concentration of feature with critical dimension. Visual examination was performed on 100 devices per wafer. I obtained an average successful patterning rate of 97%. The failed devices were mostly located on the edge of the wafer. This could be the result of combining factors including thick resist on the edge, exposure time and developing time.

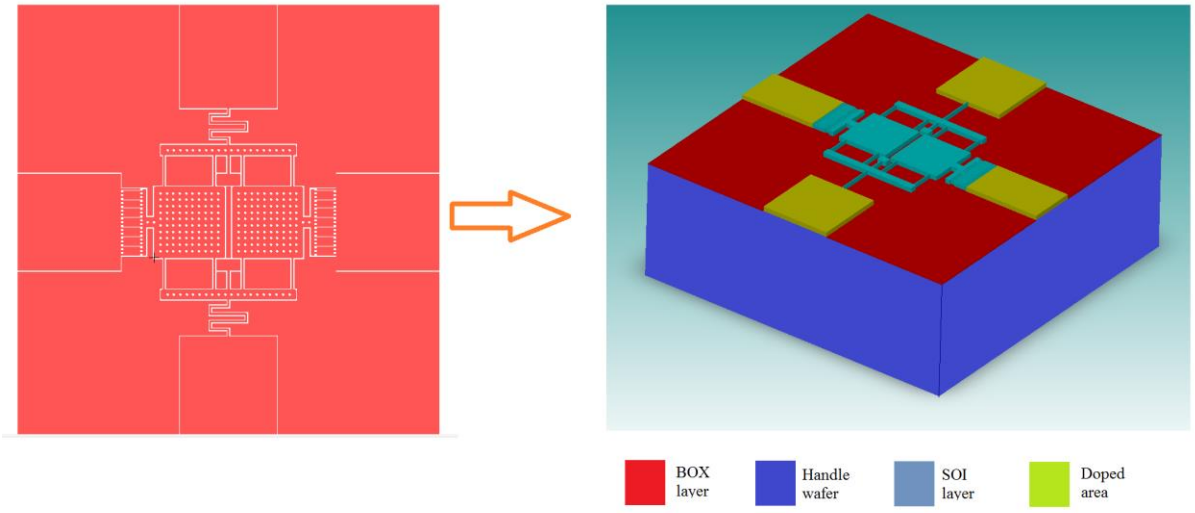

Figure 4.20 Photomask used for patterning the SOI layer and 3D view of animated wafer

Backside layer is patterned with 'backside' mask. The backside mask target is to etch a deep trench across the border of the device frame to release it from wafer grip. The process is similar to resonator patterning, only differing by the thickness of surface oxide layer. This oxide layer acts as a protective layer during dry etching. As the thickness of the handle wafer is 600 µm in compared to 25 µm of the resonator layer, the etch time is longer. By increasing oxide thickness, I ensure that the wafer is not damaged during etching. The selectivity of DRIE process is around 160. Thus, I need a 4.2 µm of oxide to cover the backside silicon layer. The detail of the processed is shown in table 4.10.

Table 4.10 Processing steps for patterning the back-side layer

No	Step	Material	Method	Thickness	Time	Mask
1	Deposit	Oxide	Use PECVD (SiH_4, N_2, N_20)	4.5um	60 min	
2	Deposit	Positive resist AZ9260	Spin-coating at 3500 rpm	6um	2 min	

3	Removal	Positive resist AZ9260	- Expose to UV light under the photo-mask in a mask aligner - Develop in developer AZ400K	6um	10s 6 min	Backside
4	Removal	Oxide	Etched using ICP (C_4F_8/O_2)	4.5um	23 min	
5	Removal	Positive resist AZ9260	Use oxygen plasma	6um	15 min	

This step requires double side alignment. Crosshair mode in aligner is used to ensure two side of the wafer align correctly. Small part of the resist is removed during aligning process as the result of contact between mask and the wafer. Several different gap lengths between mask and wafer is tried to minimise the damage to the resist. The thickness of backside oxide deposition varies from 4300 nm to 4500 nm. Thus, the ICP time is slightly adjusted to adapt to different thickness.

4.3.6 DRIE and HF release

The final step is to etch the wafer to create the resonator and then remove it from the wafer grip. First, the front side wafer is etched by using DRIE. Next, a layer of oxide is deposited on top of the recently etched resonator layer to protect its details. This is done by using PECVD. Then, the backside wafer is etched by using DRIE. Finally, the wafer is located inside HF vapour etcher to strip the BOX layer, hence release the device from the wafer.

Table 4.11 Processing steps for etching and releasing device structure

No	Step	Material	Method	Thickness	Mask
1	Etching (removal)	SOI layer	DRIE with DSE	25um	
2	Deposit	Oxide	PECVD	1um	
3	Etching (removal)	Backside layer	DRIE with DSE	625um	
4	Removal	Surface Oxide and BOX	Wet etch by using HF vapour	1um 3um	

In order to check the aspect ratio and estimated etch rate for the standard recipe, the process was first performed on dummy wafers for both front side and backside mask. The front-side was etched for 5 minutes while backside-etching process was performed in 50 minutes. Both vertical walls are observed to be slightly curved at the bottom of the trench as shown in figure.4.21. However, high aspect ratio trenches have been realised for defining and releasing the device. The etch rate is lower for deeper trenches with 5 µm/min and 4.5 µm/min for 25 µm and 230 µm trenches

respectively as shown in fig.4.21. The same recipe, then, is implemented onto the SOI wafer. The device layer is finished after 7 minutes front-side etching. The comb-drive base with critical dimension of 4 µm was the last feature to be completely etched as smaller feature take longer to etch. However, the backside trenches are only able to reach 340 µm and then silicon grass were formed at the bottom of the trenches as shown in fig. 4.22. The bias voltage of the polymer etch was identified to be the source of the issue. The bias voltage used was not high enough to penetrate deep silicon trenches. The etch rate slows down while the polymer deposition rate is constant. As a result, a thick polymer layer is deposited on the bottom of the trenches. This polymer layer prevents the ICP power from etching the silicon. By increasing the bias voltage, the etch can overcome the accumulation of charge at the bottom of the trench to reach the BOX layer.

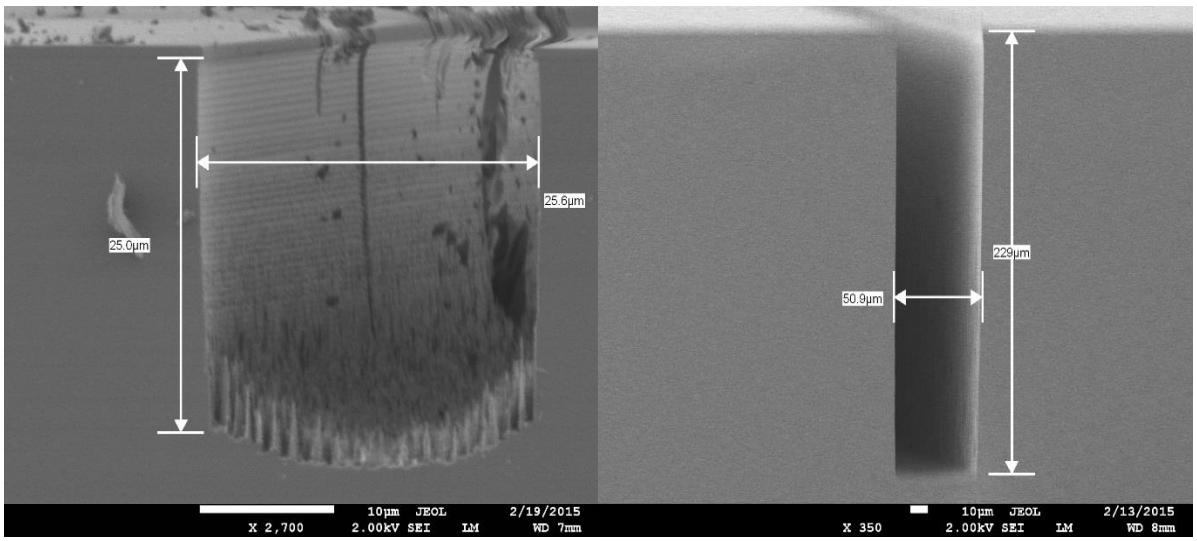

(a) (b)

Figure 4.21 (a) front side 5 minutes etch test and (b) back side 50 minutes etch test on dummy wafer

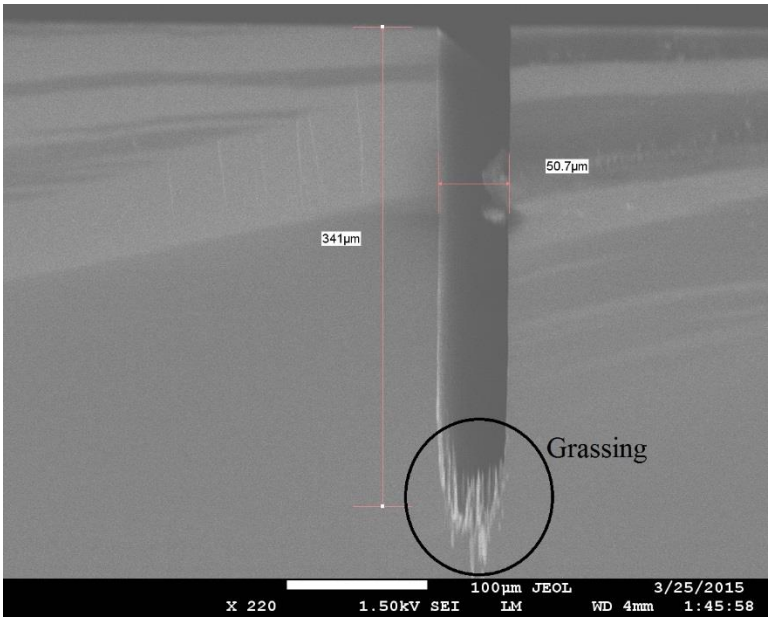

Figure 4.22 Grassing occurred at the bottom of the trenches for 400V bias voltage

A customised recipe that increases the bias voltage from 400 to 600V for 120 minutes etch was tested. After 114 minutes, the trenches reached the backside of the test wafer and the processes automatically stopped due to the rise in the backside helium cooling pressure. The result of the test etch is shown in table 4.12. The etch was stopped every 30 minutes in order to inspect the wafer and obtain the etch rate.

Table 4.12 Backside test etch with bias voltage increasing from 400 to 600 V

Time	Bias Voltage	Centre trenches	Edge trenches
30 min	400 - 426V	230 µm	222 µm
60 min	426 - 457 V	410 µm	407 µm
90 min	457 - 499 V	567 µm	567 µm
114 min	500 – 562 V	652 µm	652 µm

The SOI wafers have a slightly lower etch rate in comparison with the plain wafer. After 120 minutes, the trenches in the centre part reach the BOX layer while in the edge part is still approximate 20µm short. Due to the faster etch in the centre of the wafer, the helium cooling pressure raise the warning level, thus the trenches around the edge part cannot be completely etched. The resulted etch rate is presented in table 4.13.

Table 4.13 Backside etch for SOI wafer using the customised recipe with bias voltage ramping from 400 to 600 V

Time	Voltage	Centre trenches	Edge trenches
30 min	400 - 426V	221 µm	215 µm
60 min	426 - 457 V	390 µm	365 µm
90 min	457 - 499 V	530 µm	500 µm
114 min	500 – 562 V	600 µm	580 µm

The final stage of HF vapour is designed to release the resonator and the chips from the wafer frame. The wafer is placed upside down inside the HF chamber. HF vapour reaches the BOX layer via the released hole from front-side silicon layer and remove the oxide from below. The oxide mask on top of the front side silicon also reduce the etch rate of the BOX layer. Both oxide layers are removed at the end of the process. When the BOX layer was removed, the devices were suspended via 2 anchor located both side of the resonator. Due to different etch rate across the wafer, the observed release times are varied. Few devices are released after 80 minutes. Most of them were released after 100 and 110 minutes. Overall, more than 200 chips have been released from the wafer grid. A typical resonator structure can be seen in fig.4.23.

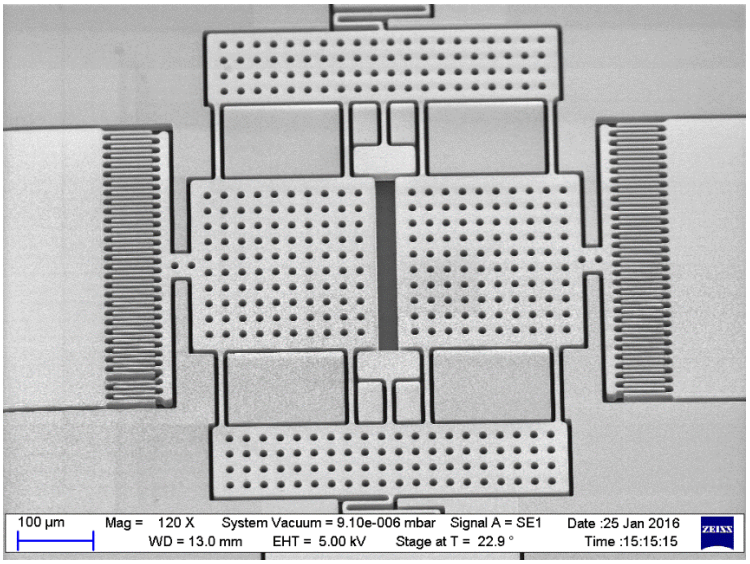

Figure 4.23: SEM image of a double-mass resonator

4.3.7 Discussion

In this section, the dicing free fabrication process on SOI wafer for MEMS resonant pressure sensor has been presented. Consecutive deep reactive etching (DRIE) for both front and backside of the wafer step increase the device resolution as well as provide an alternative solution for dicing. In the release step, HF vapour is crucial as it prevent any surface stiction from binding resonator and diaphragm layer together. As a result, this process provides a complete solution for fabricating resonator device on SOI wafer.

Photo-mask and its integration into cleanroom fabrication are also illustrated. Several variations of optimal coupled double-mass structure are included into mask design in order to be examined in testing phase. The alignment mark is located in along the centre diameter of mask design.

The fabrication flow is discussed in detail. Two more steps, which are alignment mark etching and dopant diffusion, are added to the Southampton fabrication process. These steps are used ensure the resonator to have high resistivity, which is used in detection mechanism. While some steps such as photolithography and PECVD have standard recipe that is available to use, others such as DRIE and HF vapour require experiences and intuitions for optimal solution. Test on dummy wafer is implemented before applying the recipe onto the wafer to reduce failure and cost. The fabrication process has successfully released more than 200 chips, which will be tested for resonant frequency as well as Q factor.

4.4 Verification of simulation by testing

This section presents the electrical test setup, test circuit as well as the resonant frequency result. The first section explains the use of different test equipment and the

overall set up of the test. Second section illustrates the process of designing the test circuit. The circuit diagram is illustrated and then simulated to obtain the required output amplitude before the PCB is designed.

4.4.1 Electrical test configuration

For testing, the resonator was mounted onto a device carrier using double sided adhesive tape, then wire-bonded to the conductive pads. The device carrier was connected to a printed circuit board (PCB), which was located inside a custom-made vacuum chamber. The PCB was connected to electrical drive signal and oscilloscope via electrical feedthroughs. The chamber was evacuated to a pressure of 10^{-5} mTorr to minimise the air damping losses and enhance the quality factor. The test set-up can be seen in fig. 4.24.

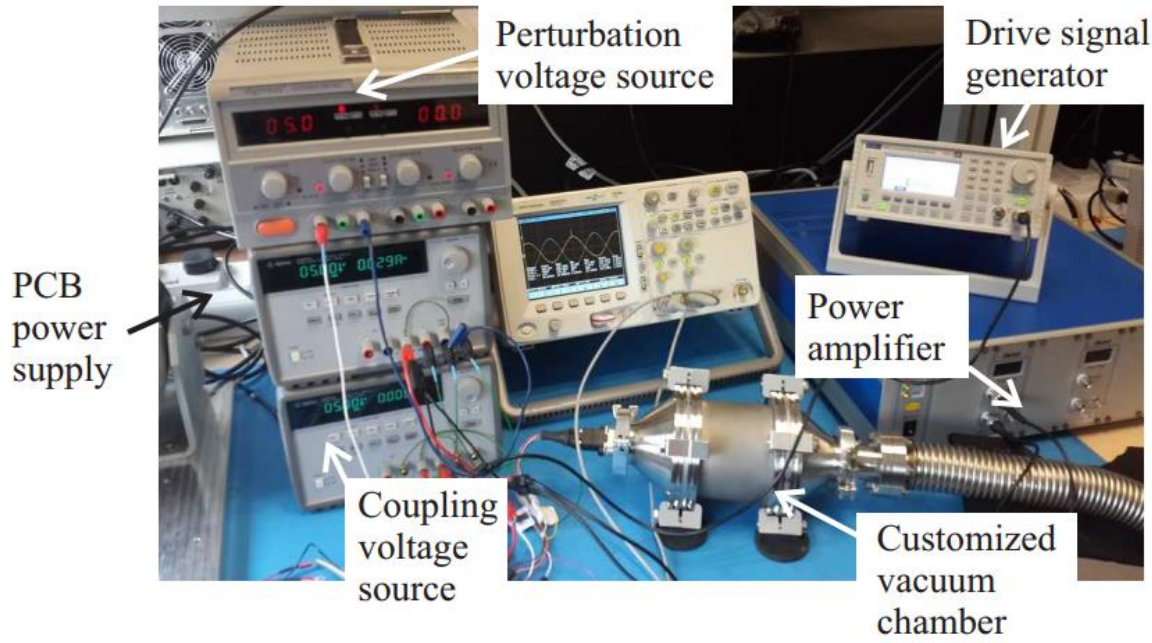

Figure 4.24 Experimental configuration for resonator resonance testing

The resonator was excited using a sinusoidal AC voltage with a frequency generated from the signal generator. The DC source is used to power the PCB as well as provide a DC offset voltage for the resonator. The offset voltage ensures the resonator resonating at the same frequency with excitation voltage as described in section 3.5.

4.4.2 Test circuit board design

The circuit board was developed to perform two tasks: resonator excitation and detection. A high level of sensitivity and high output gain was required to detect the low amplitude voltage and amplify the signal to an observable level.

The resistance of resonator is from 2.2 Mohm to 2.7 Mohm. This resistance oscillates when the resonator is resonating, a constant voltage can be applied across the resonator, which produces oscillating current corresponding to the resistance. Then the

motional current can be magnified via the use of an amplifying circuit. To put this into context, the resonator is connected in parallel with a diode to keep its voltage constant at 5V. The outgoing current is fed into an inverting amplifier with gain *Av* = 2. It is worth mentioning that the circuit operates at 5V and the output DC offset is 2.5V. Thus, I employ a differentiator as 2nd stage amplifier in order to eliminate any DC bias on the 1st stage output and further amplify the signal before releasing the output voltage with 2.5 swing DC offset. The differentiator uses an input capacitor of 1 nF and feedback resistor of 910 Ω, hence produce a gain of 60 for 100 kHz. Lower frequencies expect slightly smaller gain. The circuit diaphragm is shown in fig.4.25.

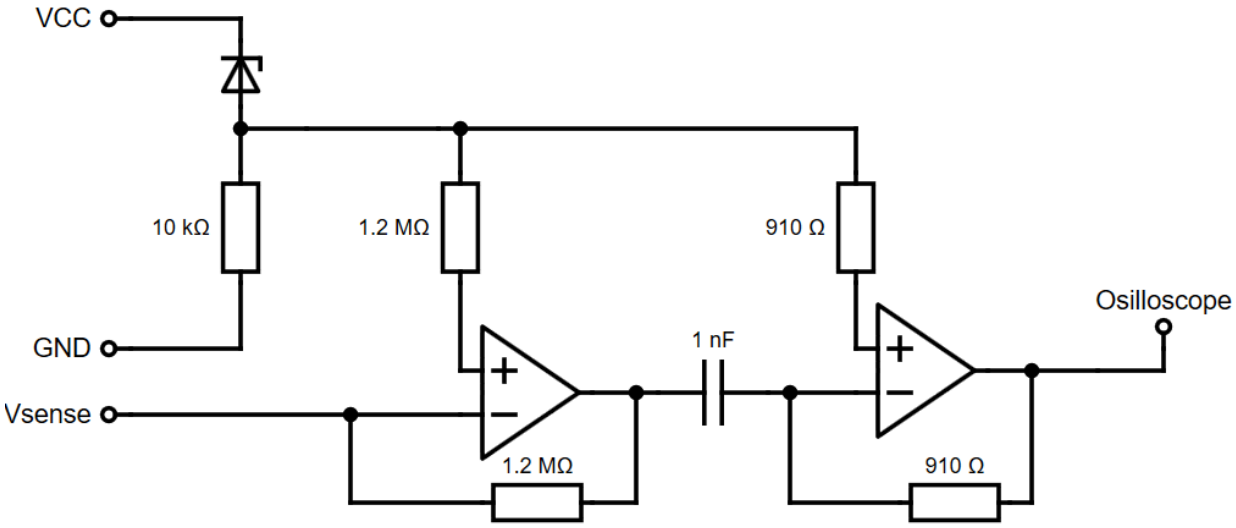

Figure 4.25: Schematic overview of current amplifying circuit for one signal

The PCB I/O electrical interface was a 9 ports D sub connector.

4.4.3 Experimental methodology

In this experiment, I employed real-time measurement approach. Dual-channel of amplifiers were connected to two detecting contact pad to pick up the motional current. With both parts of the resonator vibrating at the same frequency and were set up to detect in the same phase, the detecting signal is the constructive interference of the two output signals.

The amplified signal then was detected by a dual-channel oscilloscope (Agilent technologies DSO6032A). The second channel is to observe the excitation signal simultaneously with the output signal. The purpose is to compute the mechanical phase-shift during resonance. The phase-shift happens as the direct result of rapidly changing amplitude. The signal generator then can sweep through the frequency in the range of interest to find the resonance peak. The Quality factor can be found using the half-power point method, whose formula is given as.

$$Q = \frac{f_p}{\Delta f} \quad (4.6)$$

where f_p is the peak frequency and Δf is the half-power bandwidth. The excitation voltage then can be change in order to test the effect of excitation force on the vibration amplitude. Typical results for different level of damping can be seen in fig.4.26.

$$Q = \frac{f_p}{\Delta f} \quad (4.7)$$

where f_p is the peak frequency and Δf is the half-power bandwidth. The excitation voltage then can be change in order to test the effect of excitation force on the vibration amplitude. Typical results for different level of damping can be seen in fig.4.26.

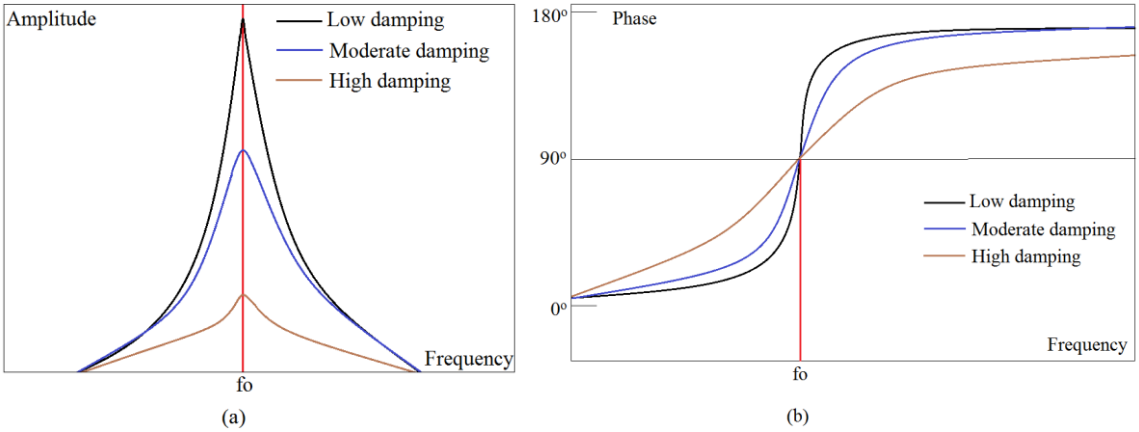

Figure 4.26: (a) amplitude and (b) phase response for typical mechanical resonance with different damping coefficient

4.5 Experimental results

In this section, the experimental results of 4 testing samples are presented. The samples are named from 1 to 4 due to their testing time.

4.5.1 Device 1 frequency and phase response

Device 1's test on resonant frequency is to investigate the amplitude and phase response of the resonator in the spectrum of interested frequency. Frequency sweeps were implemented to identify the dynamic range and Q factor of the device. The phase difference between the device's signal and the drive signal is measured to provide the detail of phase changes inside the dynamic range. An example for frequency response can be found in fig.4.27.

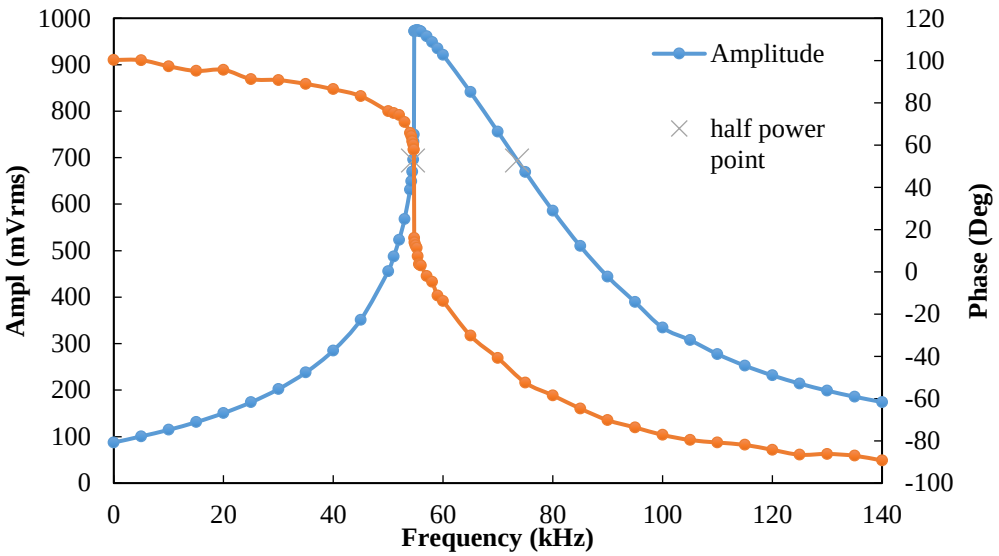

Figure 4.27: Frequency response of device 1 with 5V bias on resonator, drive voltage of 800 mVpp, measured Q factor of 5.9 using half-power point technique. The result suggests a strong out-of-phase mode with no in-phase mode to be seen

It can be seen that the result is a typical mechanical resonant peak with clear phase change in coherent with the highest observed amplitude. The frequency of out-of-phase mode were found to be 58.92 kHz while in-phase mode cannot be detected. The observed resonant frequency is 16 kHz larger than theoretical and simulation result. In fabrication, the mass of the resonator is reduced because the release holes were added for structural released step which meant the resonator structure lost 19.6% of the total mass. The readjusted theoretical unstressed resonant frequency is 53.54 kHz, which is 6.42 kHz away from the measured frequency. However, the observed bandwidth is 11.2 kHz, resulting in very low Q of 5.3. This result will be explained in discussion section in more detail.

To observe the resonance performance in detail, different drive voltages were applied. Examples of frequency and phase response is shown in fig.4.28. The increase in drive voltage lead to a nonlinear response in peak frequency. The resonant frequency drops twice when drive voltage is raised from 400mV to 600mv and 800mV respectively. this behaviour is identified as softening effect, which is typically associated with increasing in electrostatic force. Detail of the change of resonant frequency, bandwidth and Q factor is shown in table 4.14.

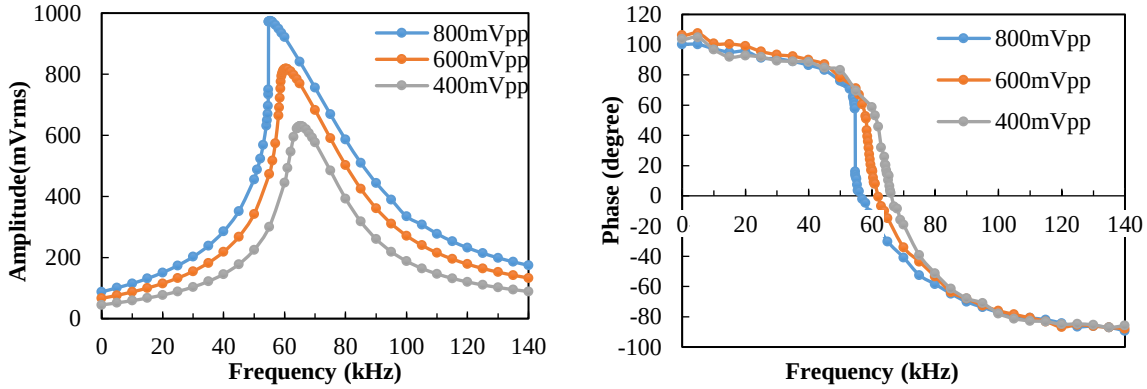

(a) Amplitude vs frequency (b) Phase vs frequency

Figure 4.28: Measured responses of device 1 at resonance for multiple excitation voltage. (a) amplitude response to frequency and (b) phase response to frequency

Table 4.14 excitation voltage vs unstressed resonant frequency of double-mass structure

V_{drive} (mV)	400	600	800
f_0 (kHz)	63.14	60.45	58.92
Bandwidth (kHz)	18.5	17	11.2
Q factor	3.2	3.7	5.3

Further tests on a different device 1, device 3 and device 4 demonstrated resonant frequencies in the range of interest. The dynamic ranges are shown in fig.4.29 while the resonant peak and Q factor is represented in table 4.15. The Q factor is consistently low for all working samples. The highest recorded Q factor is only 8 while expected value is larger than 1000.

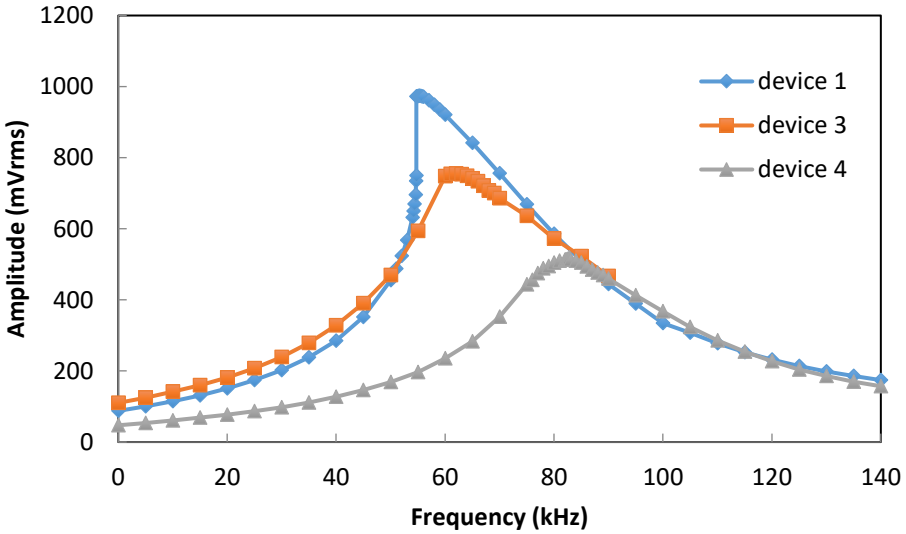

Figure 4.29: Dynamic ranges of three working samples. The excitation voltage (V_{drive}) is 800 mV and DC bias (V_{bias}) is 5V.

Table 4.15 Resonant frequencies and Q factors for multiple tested devices, V_{drive}= 800mV, V_{bias}=5V

Device	1	2	3	4	5
f_0 (kHz)	58.92	n/a	60.31	81.82	n/a
Q factor	5.3	n/a	8	4.1	n/a

4.6 **Analysis on low Q factor and observed mode**

In the experiment, it was observed that three out of five devices have low Q factor value. The test has proved that the fabrication has successfully release the resonator from the backside wafer. The low Q factor can be explained by the high bias DC voltage. As explained in Eqn.(3.55), the motional current is proportional with the voltage difference between the static comb and the movable resonator. When the DC bias (V_{bias}) is much larger than detected voltage (v) i.e. $V_{bias} >> v$, the motional current (*i)* is largely depended on the DC bias amplitude and the Q factor of the samples are subdued. Unfortunately, the samples are spent after experiments, thus more experiments with lower DC bias have been postponed for the experiment in the next chapter.

In addition, I only observe out-of-phase mode in the experiment. The driving signal in the stationary comb drive is in-phase in order to attract or repel the resonator simultaneously. Thus, the resonator has strong tendency to move into out-of-phase mode during the experiment.

4.7 **Conclusion**

In this chapter, the doublemass resonator structure fabricated on SOI was investigated as a prototype resonator for downhole pressure sensor. SOI wafer provided a single platform, in which the fabrication for single crystal silicon structure with 2 layers can be implemented efficiently. Three designs of doublemass structure were simulated to test their response in high pressure environment and the sensitivity of each individual structure against the increasing pressure. The supporting beam coupling doublemass resonator (SBCDR) response to high pressure was identified as the most promising design in term of sensitivity. The SBCDR also shows no sign of cross-over between out-of-phase and in-phase mode.

Four stages fabrication flow has been developed to obtain the desired resonator structure. The DRIE step is crucial for the devices release from the handle wafer. Insufficient forward ICP power led to lower etching speeds and etching stopping midway through the etch. An exponential increase in ICP power keeps the etching speed at a constant rate and successfully removed the trenches completely to prepare the wafer for release step. The released devices were tested for resonant frequency and Q factor. The resonant frequency is slightly different from the theoretical computation

due to the different resonator mass while the Q factor is significantly affected from the internal friction generated by the resistance heat.

The experiment has been partially successful in showing the resonant frequency of the double-mass resonator structure. The coupled double mass resonator has been proved theoretically to be cable of producing high sensitivity with the change in pressure and measuring high pressure data. The setback of overbiasing has led to a very low Q measurement. Another alternative is to replace the piezoresistive detection with capacitive detection. This approach only changes the initial resistance of the material without overcomplicating the fabrication process. Further discussion on capacitive detection and change in double-mass resonator is introduced and discussed in the next chapter.

.

Chapter 5 Lateral stress-induced resonator

5.1 Introduction

In this chapter, the disadvantages of diaphragm structure for pressure measurement are first analysed. These disadvantages are large displacement required for high sensitivity as well as the non-employment of compressive stress in frequency shifting mechanism. Compressive stress is the primary component induced by applied pressure. However, conventional diaphragm structure is designed to transduce shear stress without employing the compressive stress. From an understanding these factors, alternative designs to replace the traditional diaphragm structure for novel approaches to best utilize the compressive stress are produced.

The goal of an inductive mechanism in resonant pressure sensor is to transduce applied pressure into tensile stress in the resonator. Traditional diaphragm employs two fixed anchors on its structure to transduce the shear stress into tensile stress. Thus, I need to find a method to transduce compressive stress into tensile stress. Compressive stress, by definition, is in inward direction, i.e. heading toward the centre of the object while tensile stress is in outward direction. A spring is the structure that has been proven to experience both compressive stress and tensile stress simultaneously as seen in fig. 5.1. When 2 ends of the spring are compressed, the 2 remaining ends will stretch. The stretching leads to the generation of tensile stress. I can employ this mechanism to develop a new type of pressure transduction as an alternative for traditional diaphragm structure.

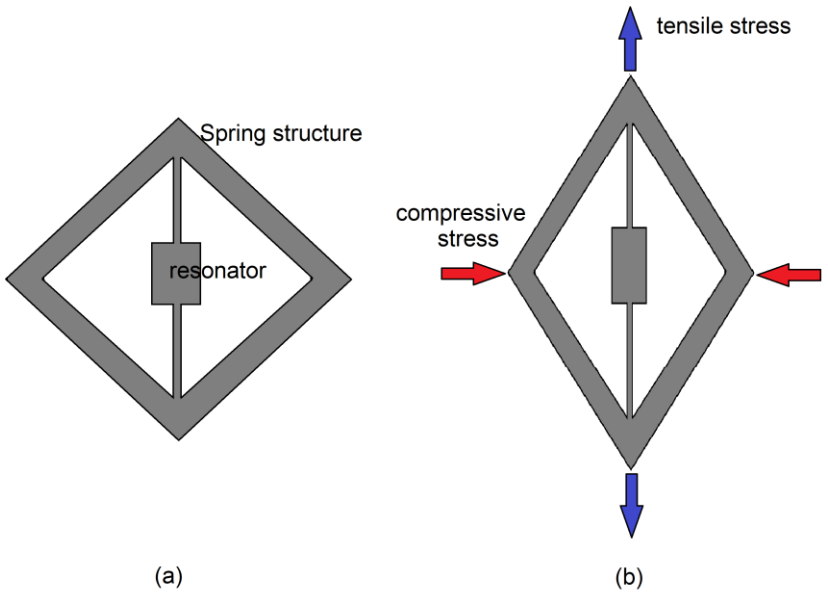

Figure 5.1 Spring system (a) unstressed and (b) under stress

Therefore, two lateral stress-induced structures are introduced, these being the transmission spring and the transmission bar design. By employing the spring system, the compressive stress on the surface layer can directly induce the tensile stress on the resonator, which eliminates the need for diaphragm structure. The coupled double-mass resonator is intact. Instead of using the diaphragm for pressure induction as shown in figure 4.13, side-wall with strong compressive stress has been used. A spring system is used to transduce the compressive stress from the side-wall into tensile stress in the resonator. Due to the diaphragm removal, the contact anchor positions are changing from central of diaphragm to 2 stretched ends of the spring structure. By relocating to this new location, the resonator will experience large tensile stress when the sensor is under pressure.

The resonator with spring transduction system is first simulated for feasibility study. It is worth noting that the packaging solution for vacuum encapsulation introduce additional pressure on the structure. Further analysis onto the packaging solution is therefore then presented.

The second fabrication process for the spring transduction system is a slight variation from the first one. The section, therefore, focuses on the alternations and provides a summary of the process flows. A significant change is the switch from high resistance silicon to very low resistance one due to the overheating issue discussed in section 4.6. A further notable detail is that the trenches in backside layer have been widened from 50 to 60 μm. Therefore, the required penetrated power for DRIE is reduced slightly. Overall, the deep etching on the backside layer process is 10 minutes faster.

Then, testing on the resonator sample's resonant peak and Q factor are discussed. The measured resonant frequencies range from 23.034 to 25.966 kHz on 5 working devices while the simulated peak frequency is 22.568 kHz. In addition, the measured Q factor is in range from 100k to 170k. The agreement in peak resonant frequency and high-quality factor prove that the capacitive detection can be used to eliminate the risk of overheating in resonator structure.

A potential issue with downhole application is the high temperature drift. The high temperature condition causes the resonator structure to expand, hence changing its resonant frequency. Simulation of the bar-transmission structure to measure the frequency drift is undertaken. A state-of-the-art dual double-mass resonator for temperature compensation is proposed and simulated. The structure includes two resonators, one exposed to both temperature and pressure while the other is isolated from the applied pressure. The response of the dual double-mass structure to applied pressure and temperature are discussed in detail.

In summary, the difference from the design in chapter 5 in compared with chapter 4 are:

- Using spring system instead of diaphragm structure as the mean to transduce pressure onto resonator
- Employ compressive force instead of shear force as the primary source for induce the tensile stress in resonator structure
- Change the contact anchor position from centre of the diaphragm onto the 2 stretched ends of the spring system

5.2 Lateral stress induction dynamic in diaphragm structure

A diaphragm is the standard stress-generating structure for a resonant pressure sensor. The advantage of a diaphragm is that it is relatively easy to fabricate. The structure bends under pressure, thus, inducing stress onto the resonator. The more the contraction is, the larger induced-stress is generated. Thus, the gap between the diaphragm and resonator structure is crucial for the range of operation for sensor design. For a SOI wafer, the thickness of buried silicon oxide (BOX) between two crystal silicon layers is limited to 5μm. Thus, the need to find a new stress-generating structure that circumvents the limit of the gap between the silicon layers is crucial for the employment of SOI wafer in fabricating a resonant pressure sensor.

In addition, in contradiction to the concept that a standard diaphragm employs most of the induced-stress, only in-plane shear stress is used to create the tensile stress in the resonator structure [100][101]. A large portion of the compressed stress generated from applied pressure is wasted. Hence, it is needed to compare the magnitude of this unused stress with the magnitude of the in-plane shear stress. The diaphragm can be treated as an edge simply supported rectangular flat plate as seen in fig.5.2[100].

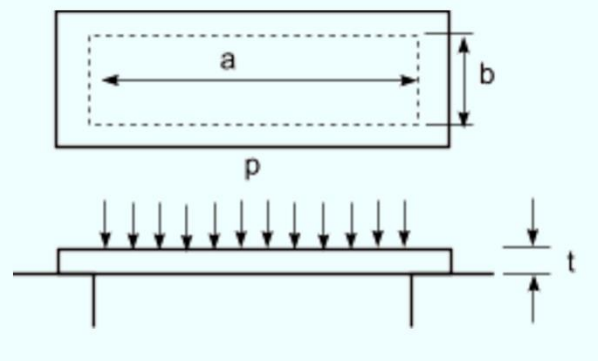

Figure 5.2 Rectangular flat plate, simply supported edge, under uniform load – *a, b*: plate's length and width, *t*: plate's thickness, p: uniform load

Given the uniform applied pressure *p*, the maximum induced compressive stress at the centre of the [102] diaphragm can be calculated by;

$$\sigma_m = \frac{0.75pb^2}{t^2[1.61{}^{b}/_{a}{}^{3}+1]} \quad (5.1)$$

Where σ_m is the maximum compressive stress, *p,a,b* and *t* are given in fig. 5.1. Eqn. (3.24) and (3.25), previously mentioned in section 3.4, formulated the in-plane shear stress in the *x* and *y* directions. By recycling the parameter used in Fig.3.7, the maximum compressive stress for the same diaphragm design can be calculated. By substituting *p* = 20 MPa, *a* = *b* = 800 µm and *t* = *100* µm, the maximum compressive stress of 367 MPa is obtained. This result is in the same order of magnitude with the in-plane stress. As a result, the induced compressive stress theoretically could have the same effect on the resonator structure as the predominantly used shear stress. This discovery inspires the design of several stress induced structures, which entirely remove the diaphragm structure from the sensor. Due to the fact that the compressive stress is employed, the pressure-induced structure can be in-plane with the resonator device. Therefore, the out-of-plane silicon blocks can be thickened to withstand higher pressure environment.

5.3 In-plane stress induced structure as an alternative to a diaphragm

To find an alternative to the diaphragm structure, two different designs of pressure-induced compressive stress structure are proposed and simulated. The first part of this section presents the design and summarise the result of the transmission spring structure. The packaging concept for proposed structure is investigated. The second section shows the proposed transmission bar design and its simulation results.

5.3.1 Transmission spring structure

The overall system structure consists of a double-mass coupled to an in-plane hollow rectangular structure via four stress-transmission spring arms as shown in fig.5.2. The hollow rectangular structure mechanically acts as four doubly ended beams, each of which deflects independently under applied pressure. As discussed in section 3.4, the central part of a beam or plate is the most concentrated stress and largest displacement area. Thus, the spring system deployed in this area will take advantage of the displacement and impose the tensile stress onto the double-mass structure. The spring has its thickness much larger than then flexural beam in the double-mass. Thus, stiffness of the spring is much higher than the stiffness of the flexure beam. As a result, most of the mechanical energy is transmitted onto the double-mass structure, increasing the efficiency of the mechanism. The two ends of the spring which connect to the hollow rectangular structure and the double-mass structure respectively, have lower stiffness than the mid part of the spring. Thus, they are flexible and are able to move in the y direction. The springs, hence, are able to transduce the mechanical movement of the side beam into tensile stress of the double-mass structure. Since the models were for proof-of concept purposes, they were not intended to match the

unstressed frequency of the previously discussed resonator. Therefore, the selection of design parameters for the devices was arbitrary and only optimized for the fabrication process. However, some design considerations in the device design may be helpful for future optimization.

5.3.1.1 Resonator structure frequency response

In this simulation, 4 structural variations are made in the original design shown in fig.5.3. The 4 indicated changes are the top beam thickness (d1),the side beam thickness (d2),the spring contact length (d3) and the mass to beam distance (d4). These changes are not expected to alter the unstressed frequency of the structure but provide better understanding on pressure response of the resonator.

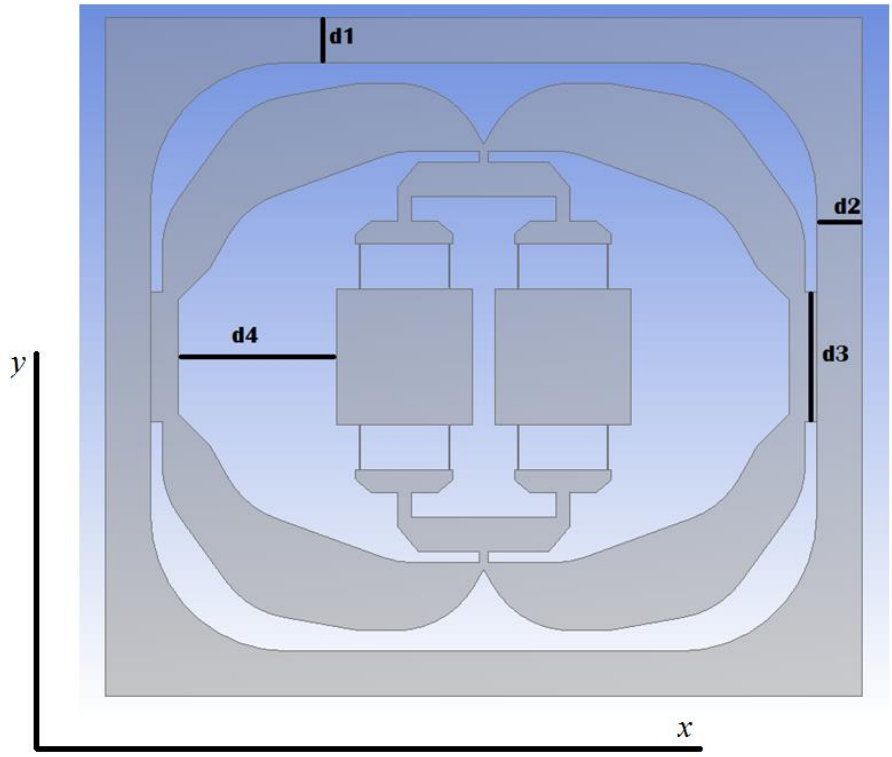

Figure 5.3: Top view of transmission spring model including the double-mass structure

Table 5.1 Altered dimension of simulated transmission spring designs

Design	Top beam -d1 (µm)	Side beam -d2 (µm)	Spring contact length-d3 (µm)
1	200	200	570
2	200	200	***670***
3	200	***150***	570
4	***150***	200	570

Each design is simulated under a range of applied pressure to check for the frequency change. The results are shown in below fig. 5.4.

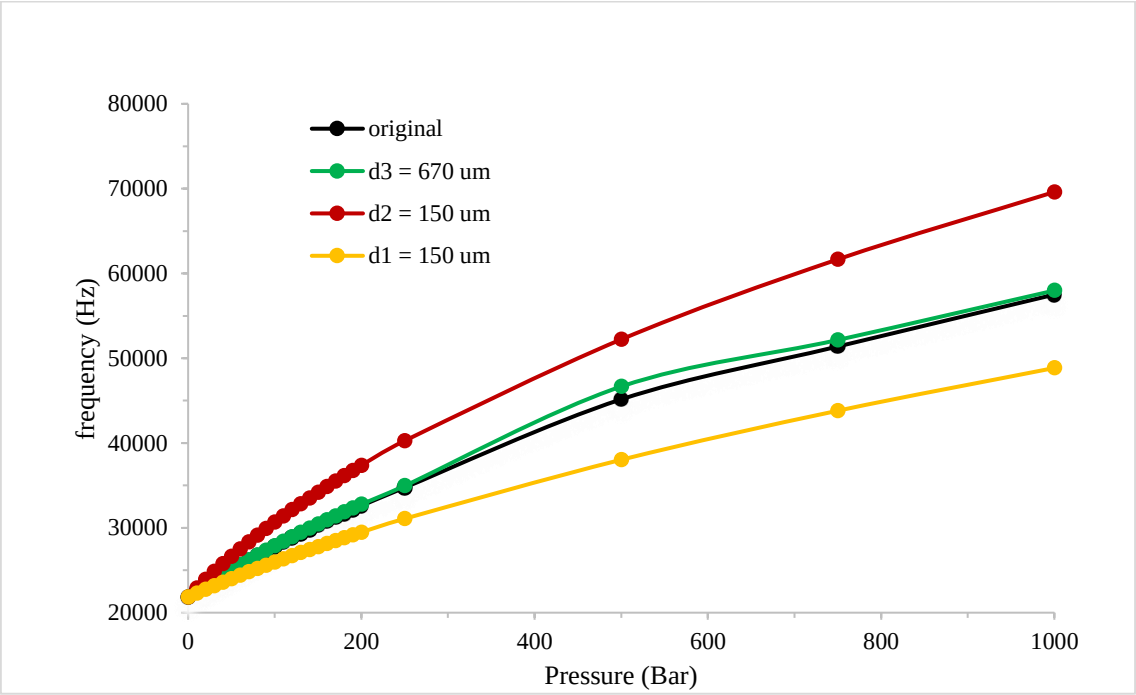

Figure 5.4 Frequency vs pressure for various parameter alteration

From the result, it can be seen that the length of the transmission spring contact (d3) has tiny effect on the frequency. The modified version has a slight shift of 250 Hz from the resonant frequency of the original at 1000 bar. By increasing the contact area, the transmission spring incorporate more displacement and transduces it into more tensile tress. However, as the displacement magnitude in the central part of the beam is much larger than elsewhere, the additional induced tensile stress is insignificant when compared to the original value.

On the other hand, the reduction in side beam thickness (d2) implies a larger tensile stress in the double-mass structure. A thinner beam leads to larger deflection under applied pressure. Therefore, the tensile stress and its derivative the sensitivity increases by 25% from the original design. In contrast, the top beam thickness (d1) reduction leads to a lower sensitivity. Due to the thinner thickness of the top beam, the join where side and top beam meet, is under a larger compression force. This force increases the stiffness of the side beam, hence reducing its displacement under applied pressure. The sensitivity reduces as a direct result.

5.3.1.2 Packaging solution and high-pressure environment constraint

The typical packaging solution for resonant pressure sensor includes the bottom silicon part of SOI wafer and a silicon cap. These two layers encapsulate the resonator inside a vacuum environment. Therefore, the sensor will maintain a high Q and aging effect caused by air contact is removed. The fabrication of the packaging is intended to be developed after the project. However, the full model of the device with

packaging solution should be analysed at this stage to discover potential problems in the design. Four variations are implemented in the structure to test its stress response a high-pressure environment. Cap thickness (t1) and backside thickness (t2) are two newly introduced parameters. Along with the previously mention parameter of side/top beam thickness (d1 and d2), three parameters are used to alter the structural design of the packaging solution. The parameters of the packages and design changes are shown in table 5.2.

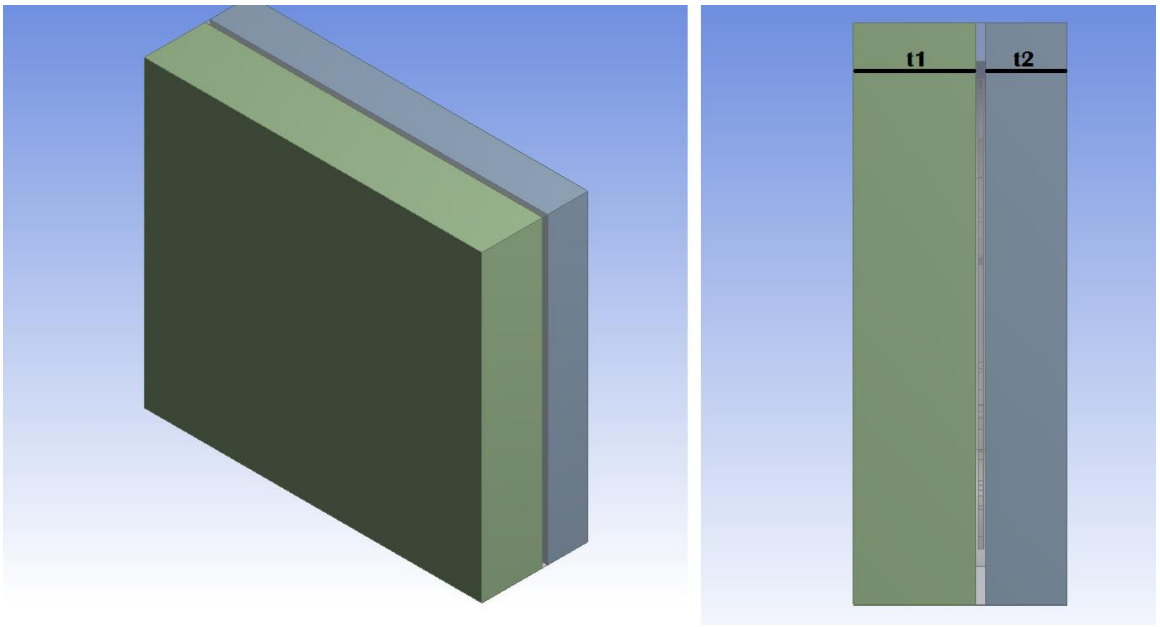

Figure 5.5: Side view of the packaging solution model

Table 5.2: Variation of parameters for packaging design optimization

Design	**top thickness (t1)**	**bottom thickness (t2)**	**side-top beam (d1=d2)**
1	400	400	200
2	***600***	400	200
3	***600***	***600***	200
4	600	600	***400***

In this simulation, the focus is on the maximum deformation of the backside layer deformation and the induced-stress on the double-mass structure. The result is showed in fig.5.6 and 5.7.

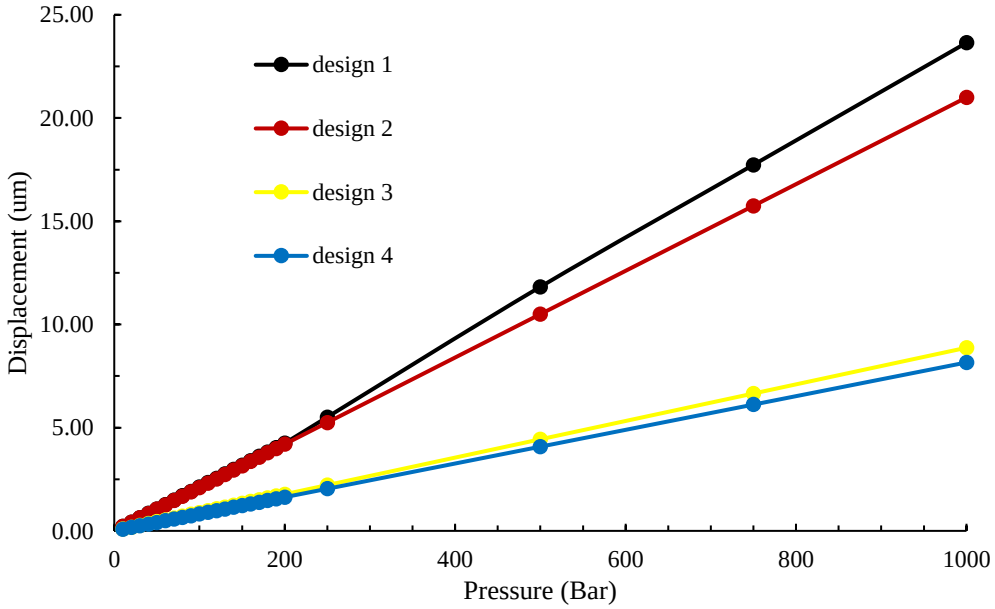

Figure 5.6: Simulated cap/backside maximum displacement against applied pressure

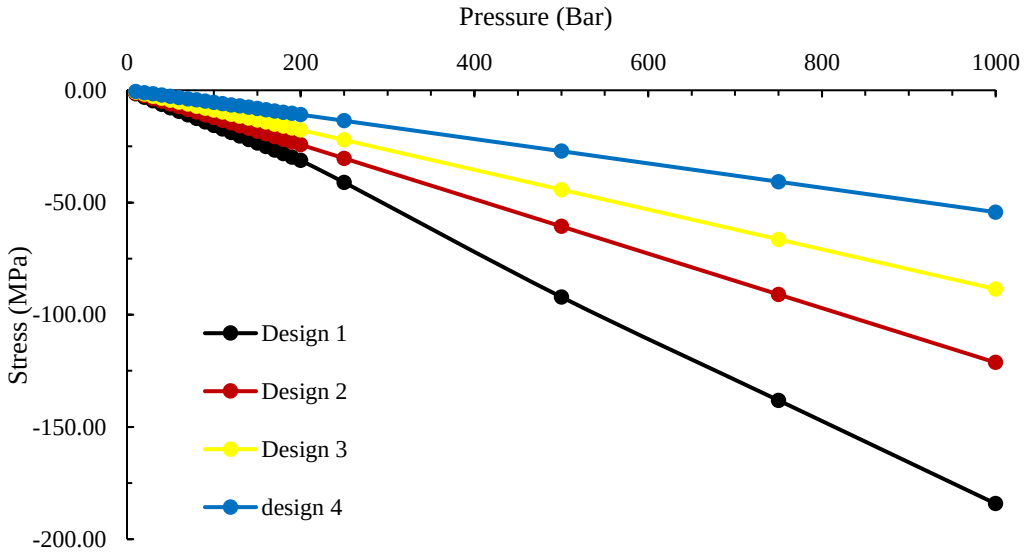

Figure 5.7: Double-mass structural stress against applied pressure

Since the SOI wafer oxide layer is typically from 1 to 4 µm, the backside displacement is required to be less than 4 µm at 1000 Bar pressure. The increase in cap layer thickness has small effect on the displacement of backside layer as seen in fig.5.6. On the other hand, by increasing the backside layer thickness, undesirable backside displacement is significantly reduced. As thickness is increased, the stiffness of the layer increases proportionally. Therefore, displacement reduction is the outcome.

It is worth mentioning that the backside layer is placed under compressive as seen in fig.5.7. The larger inward deformation of the bottom layer has not only cancelled the inward motion of the side ring but also generate an outward stress on this part of the structure. The consequence is that compressive stress is generated onto the double-mass structure. Theoretically speaking, compressive stress also alters the stiffness of the double-mass, hence, shifting the resonant frequency. However, fatigue crack in silicon grows under compressive loading [103], which lead to structural failure.

In order to understand the effect that high-pressure environment has on the packaging solution, the top cap silicon layer is analysed separately. The cap layer has a total of 6 surfaces, of which only 5 are under applied pressure. The 4 vertical walls consist of two pairs of identical area surfaces but under load from opposite directions as seen in fig.5.8. Hence, the loads on these surfaces neutralise each other out. As a result, the only external load p_t applied to the cap layer is on the top horizontal surface. The bottom layer also is under a similar load. The complete design, therefore, comprises 2 packaging surface under vertical compression and a resonator structure under lateral compression. Due to the fact that the surface is of the 2 packaging layers is significantly larger than the one of the resonator structure, the lateral compression is, therefore, negligible in inducing stress onto the resonator. Both packaging layers deform inward under pressure, which in turn induce compress stress onto resonator structure. Thus, an alternative solution, which replace the compressive stress on the double-mass structure with tensile stress is required.

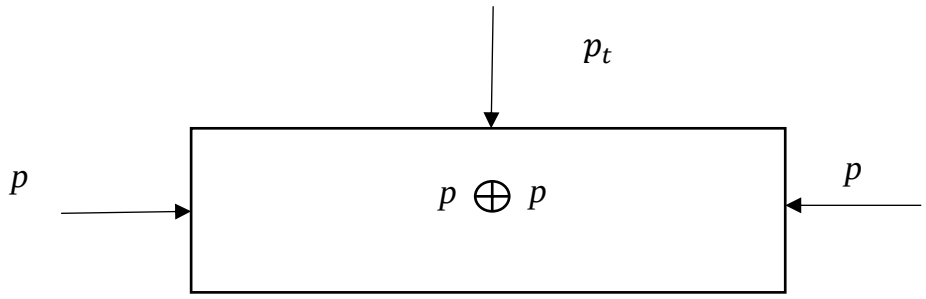

Figure 5.8 Resultant pressure onto cap layer under high pressure environment

5.3.2 Transmission bar structure

Motivated by the outward deformation of the beam structure, the model is redesigned to translate this deformation into tensile stress. In this design, the double-mass structure is linked with the side ring via two transmission bars as shown in fig.5.9.

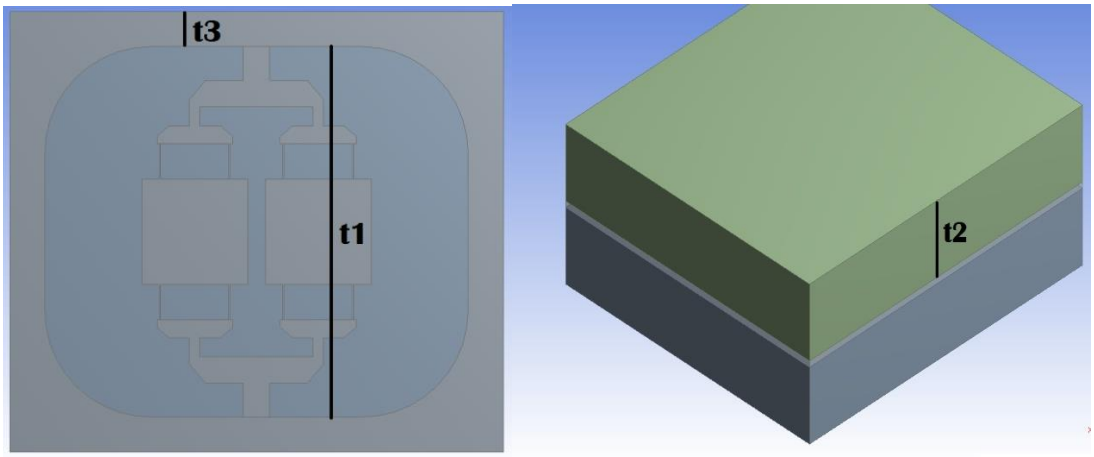

Figure 5.9: Top view of transmission bar model including the double-mass structure

As the top beam moves in an outward direction, the bar induces a tensile stress onto the double-mass resonator. Five different designs were simulated to verify this. The designs differ in the encapsulation length (t1), cap/backside thickness (t2) (they have the same thickness) and side ring thickness (t3). All design variations are presented in table below.

Table 5.3: Variation of parameter for transmission bar design optimization

Design	**Encapsulation length (t1) (µm)**	**Cap/backside thickness (t2) (µm)**	**Side ring thickness (t3) (µm)**
1	2400	400	200
2	**2200**	400	200
3	2400	**600**	200
4	2400	**600**	**100**

In the simulation result, the deformation of the cap and backside layer and the tensile stress of the double-mass structure vs applied pressure is investigated. The result is presented in fig.5.9 and 5.10.

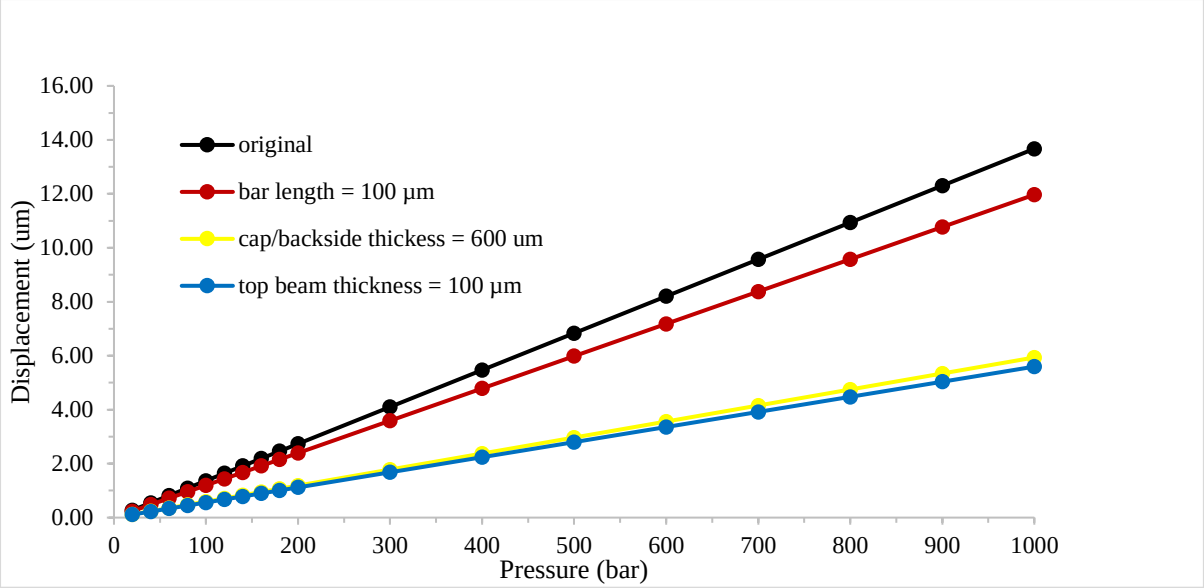

Figure 5.10: backside deformation against applied pressure for transmission bar structure

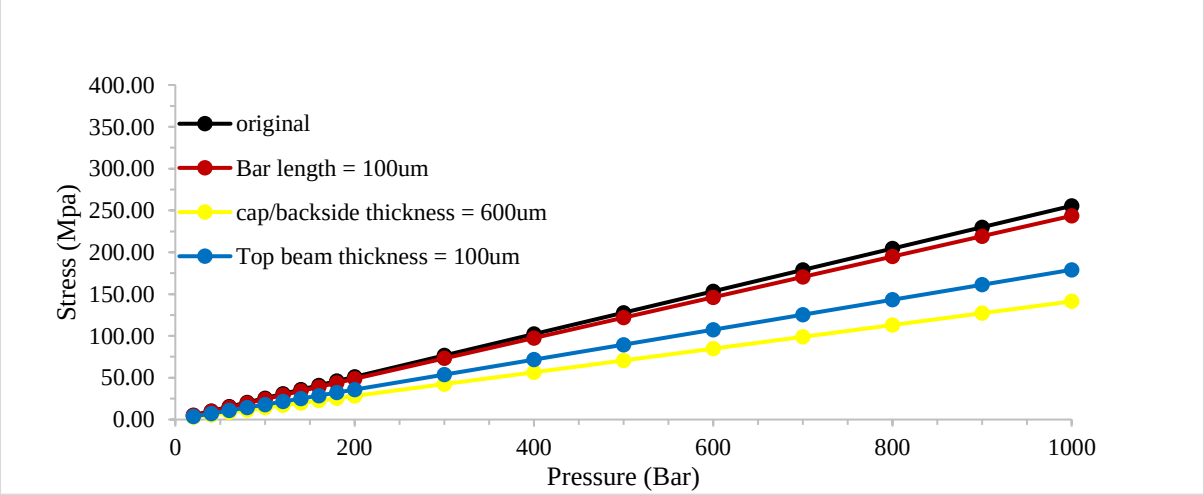

Figure 5.11: double-mass tensile stress against applied pressure for transmission bar structure

One advantage of the remodified bar transmission design is removal of the bulky spring structure. Therefore, the overall volume of the packaging solution is reduced by 14% from 3.84 m^3 to 3.36 m^3. The backside displacement of the robust bar design is significantly lower than its spring counterpart as I compare fig. 5.6 and fig.5.10. Therefore, the bar design is favourable for downhole application. Considering the variations of the two structures, there are similarities in performance. The most influential factor to the backside displacement is the backside thickness in both designs. However, the outcomes of these deformations are distinctive. Due to the transmission bar structure that directly applied the pressure to the double-mass, tensile stress is transduced on the resonator structure, which is preferable to compressive stress.

5.4 Fabrication

This section illustrates the fabrication process of a lateral stress-induced structure. The process is based on the process for the double-mass structure in chapter 4 with modifications. These modifications are in term of changing the structure design in the photolithographic mask and removing the dopant diffusion process. Since a high proportion of the process is repeated, a reduced fabrication flow is presented.

5.4.1 Photomask design with vertical comb-arm integration

In chapter 3, I have discussed the advantages of vertical comb-arm in MEMS application. Due to the identified disadvantages of the piezoresistive detection mechanism, the vertical comb-arm used for both detection and excitation is employed in this design. For flexibility, the comb-arm is separated into an array consisted of 4 bases. Each base comprises one or two comb arms depending on the available space.

The critical step in fabrication is the integration of the electrical connection, drive and detection mechanisms into the photomask design. In the transmission spring, 4 sets of stationary comb and 3 sets of movable combs for each mass are implemented as seen in fig.5.12. This comb designs are connected to 4 conductive pads, which can be flexibly used for drive or detection.

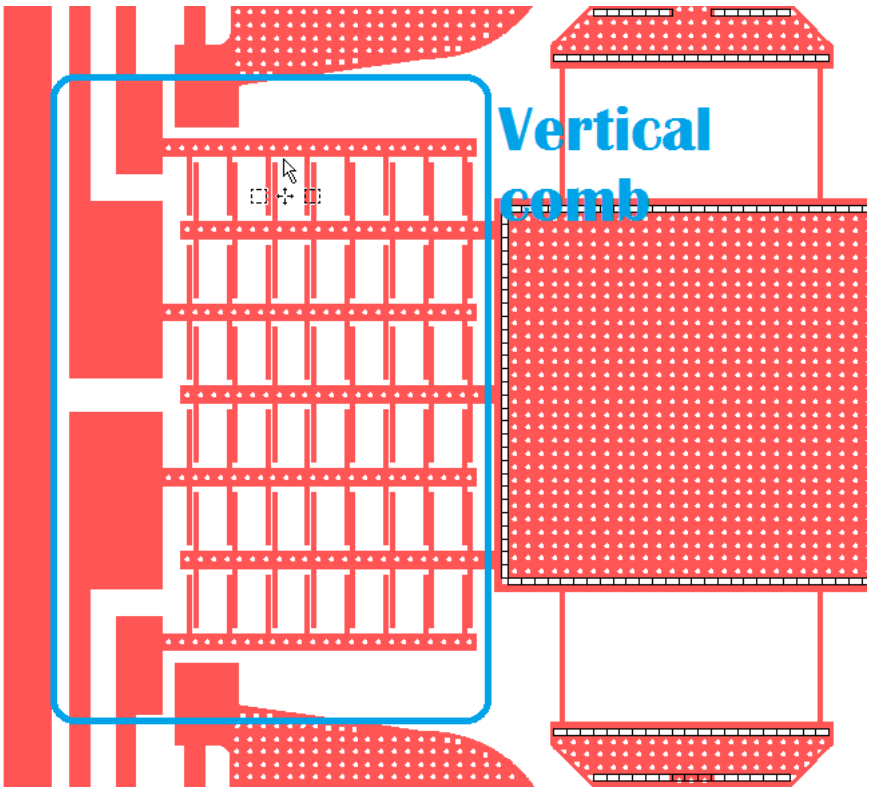

Figure 5.12: Integration of comb-arm arrays into transmission spring design

In the transmission bar structure, the spring design is replaced with the bar design. Thus, I have additional space to integrate for comb fingers. 6 sets of stationary combs

and 5 sets of movable combs for each mass are connected to 4 conductive pads as seen in fig.5.13.

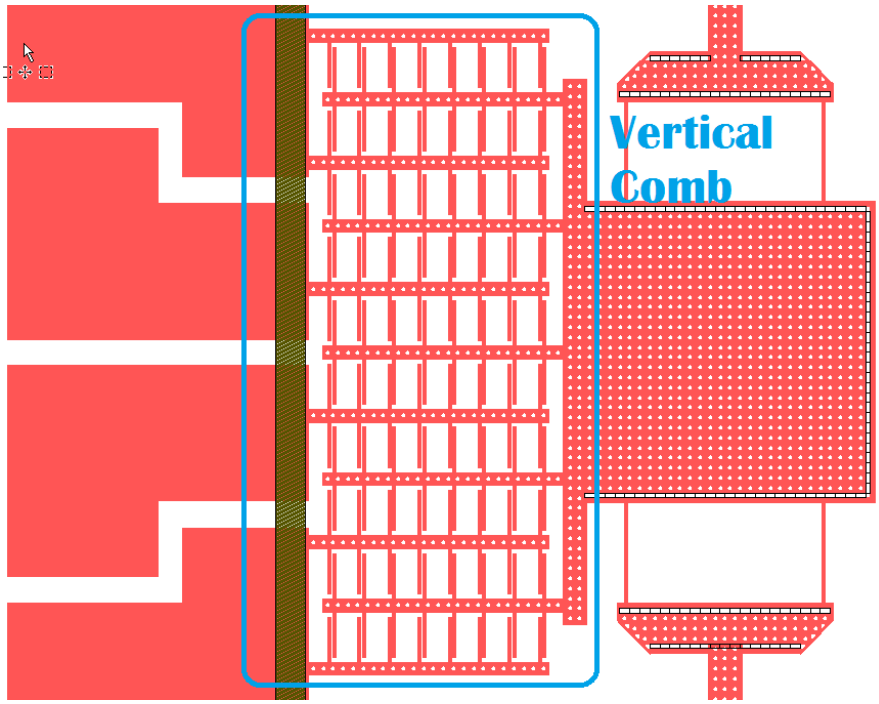

Figure 5.13:Intergration of comb-arm array into transmission bar design

5.4.2 Fabrication flow

The lateral stress-induced structure was fabricated using a double mask silicon on insulator (SOI) process with a structural layer of 25 µm thickness. The process flow comprises four main steps:

1. Pattern transfer for the device layer
2. Alignment and pattern transfer for the backside layer
3. Deep reactive ion etch (DRIE) to define the device layer and the backside layer
4. Release suspended resonator structure using HF vapour

5.4.2.1 Patterning the resonator

The pattern transfer process allows the device features in the mask to be precisely relocated onto the SOI wafer. The patterning material in this process is Silicon dioxide, which firstly is deposited on top of the SOI layer via PECVD. Next, a regular photolithography process is implemented. In this process, S1813 is chosen as the positive resist due to its high resolution for small features such as the comb-finger and suspension beam. Once the exposed resist is removed, the pattern is etched into the oxide layer via ICP. The summary of the process is shown in table 5.4.

Table 5.4 Processing steps for patterning device layer

No	Step	Material	Method	Thickness	Time	Mask
1	Deposit	Oxide	Use PECVD (SiH_4, N_2, N_20)	1um	15 min	
2	Deposit	Positive resist S1813	Spin-coating at 5000 rpm	1.5 um	1 min	
3	Removal	Positive resist S1813	- Expose to UV light under the photo-mask in a mask aligner - Develop in developer MF-319	1.5um	2s 45s	Device layer
4	Removal	Oxide	Etch using ICP (C_4F_8/O_2)	1um	5 min	
5	Removal	Positive resist S1813	Use oxygen plasma	1.5um	10 min	
6	Deposit	Positive resist S1813	Spin-coating at 5000 rpm	1um	60 s	

5.4.2.2 Alignment and backside pattern transfer

Double-sided alignment is a critical step that allows patterning features in both layers transfer with precision. The aligner's double-cross mode was used to mark the location of device layer features. Then, using this location, the backside feature are transferred to the wafer. Similar to the device layer patterning process, Silicon dioxide is using at the patterning material. However, the positive resist is switched from S1813 to AZ9260 in anticipation of backside layer's deep etching process. AZ9260 provides a thickness of 6 µm compared to 1 µm of S1813. Therefore, the pattern can be transferred onto the 5 µm oxide layer, which is required for the etching of 600 µm thick backside silicon. The summary of the process can be founded in table 5.5

Table 5.5 Processing steps for patterning the back-side layer

No	Step	Material	Method	Thickness	Time	Mask
1	Deposit	Oxide	Use PECVD (SiH_4, N_2, N_20)	4.5um	60 min	
2	Deposit	Positive resist AZ9260	Spin-coating at 3500 rpm	6um	2 min	
3	Removal	Positive resist AZ9260	- Expose to UV light under the photo-mask in a mask aligner - Develop in developer AZ400K	6um	10s 6 min	Backside
4	Removal	Oxide	Etched using ICP (C_4F_8/O_2)	4.5um	23 min	
5	Removal	Positive resist AZ9260	Use oxygen plasma	6um	15 min	

5.4.2.3 Deep reactive ion etch (DRIE) for both layers

The final step is to transfer the pattern from the oxide layer to the SOI wafer. Silicon dioxide has high etch resistance (~20-30:1) during deep reactive silicon etching

(DRIE). In addition, DRIE also provide a high resolution feature, deep penetration as well as vertical trenches. So, it is the preferred method.

Table 5.6 Processing steps for etching and releasing device structure

No	Step	Material	Method	Thickness	Time	Mask
1	Etching (removal)	SOI layer	DRIE with DSE	25um	5 min	
3	Etching (removal)	Backside layer	DRIE with DSE	625um	120 min	

The device layer thickness is 25 µm. The etch finishes once the device layer feature is defined and the BOX layers can be observed under a microscope.

The backside etch is more challenging due to the significant increase in thickness of this layer compared to the device layer. Since the deep etch requires a constant increase in penetration power to break the silicon bond, adjustable bias voltage is introduced. The bias voltage increases exponentially in order to release an increasing ion bombardment of the deep silicon trenches. The trench width in this design is raised from 50 to 60 µm, which accelerate the etch process slightly. A customised recipe that increases the bias voltage from 400 to 600V over 120 minutes is used. The process stopped prematurely during the last cycle because the centre trenches finished, and ion particles start bombarding the wafer holder underneath. The helium cooling system raised its temperature, which lead to a systematic pause. The details of backside etching can be found in table 5.7.

Table 5.7 Backside etch for SOI wafer using the customised recipe with bias voltage ramping from 400 to 600 V

Time	Voltage	Centre trenches	Edge trenches
30 min	400 - 426V	241 µm	215 µm
60 min	426 - 457 V	410 µm	365 µm
90 min	457 - 499 V	560 µm	500 µm
100 min	500 – 530 V	600 µm	580 µm

5.4.2.4 Structural release using HF vapour

The incorporation of HF vapour step allows the structural device to be released and suspended as well as avoiding any stiction as occurs with a standard HF solution. The HF only reacts with the Oxide material, leaving the silicon untouched. The etch starts with the deposited oxide layer then moves to the deeper BOX layer. Both oxide layers are removed by the end of the process. When the BOX layer is removed, the devices are suspended via 2 anchors located on each side of the resonator. Due to different etch rates across the wafer, the observed release times vary. A few devices are released after 90 minutes but most of them are released after 100 and 120 minutes. An SEM image of the released device is shown in fig. 5.14.

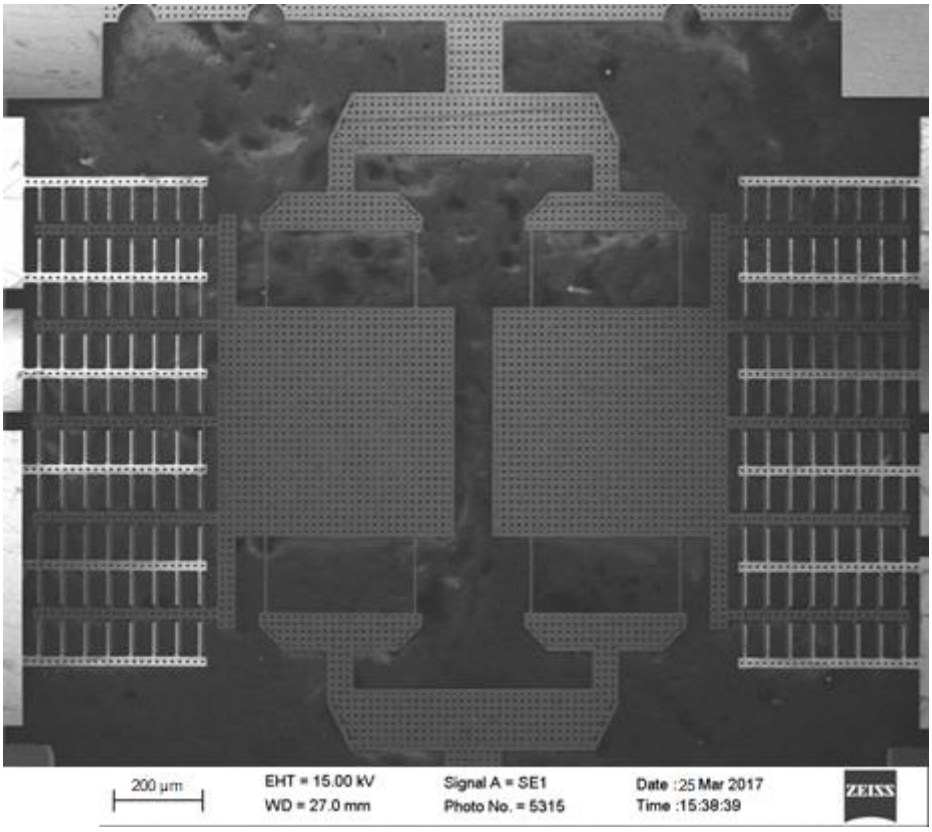

Figure 5.14: SEM image of bar transmission device

5.5 Experimental testing of the devices

5.5.1 Methodology

The Q factor of a resonator can be measured using two approaches being frequency spectrum sweep and ringdown-time. A frequency sweep was used in the double-mass experiment for the lower Q resonator. As the Q increases, the sweep range become narrower, so the resolution of the spectrum analyser is unable to provide sufficient detail on the half power points for Q factor of 100000 and higher. Instead of acquiring an expensive state-of-the-art spectrum analyser, the ringdown-time method can be implemented to minimize the cost.

The ringdown-time method measures Q factor using the undriven time of the resonator. Upon turning off the excitation force, the resonator behaviour can be modelled as an underdamped oscillator. Its vibration amplitude is given by:

$$x = A_0 e^{-\zeta \omega_n t} sin(\omega t + \varepsilon)$$

Where A_0 is the initial amplitude, ζ is the damping coefficient, ω_n is the natural frequency, $\omega = \omega_n\sqrt{1-\zeta^2}$ is the damped frequency, ε is the initial phase and t is the decay time. The waveform can be seen in fig.5.15.

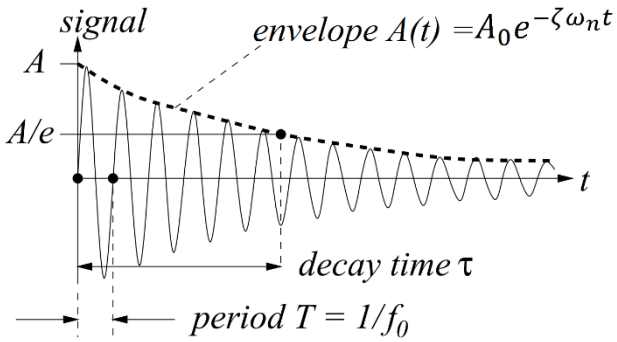

Figure 5.15: Ringdown behaviour of an underdamped resonator after turning off the excitation force

The damping coefficient is inversely proportional to the Q factor as $\zeta = 1/2Q$. Since the term $sin(\omega t + \varepsilon)$ fluctuate between 1 and -1, the peak amplitude can be calculated from the term $e^{-\zeta\omega_n t}$. If τ is the time needed for the amplitude reach a value of A_0/e. Hence, the Q factor can be calculated from:

$$Q = \frac{\omega_n \tau}{2}$$

Thus, the first step in calculating the Q factor is to obtain the natural frequency of the resonator. The natural peak of vibration can be obtained from spectrum analyser and confirmed visually using Scanning electron microscope (SEM). Then, the excitation force is switched off and the decay waveform is observed on a digital oscilloscope.

5.5.2 Experimental setup

The bar-transmission resonator structure is integrated into the test set-up as seen in fig.5.16. The resonator is located inside the SEM chamber, which is kept under vacuum. All electrical connections are made via a system of feedthrough cables with a micrometre-tip probe. The signal generator is connected to both side of the drive comb-base. Thus, a spontaneous pull or push force is generated onto the resonator to drive it into the out-of-phase mode when excited. A DC bias is connected to the main body of the resonator while the vibration is detected via the detection comb-base. The signal is amplified and then fed to oscilloscope and/or spectrum analyser for observation. The vibration can be visually observed via an SEM.

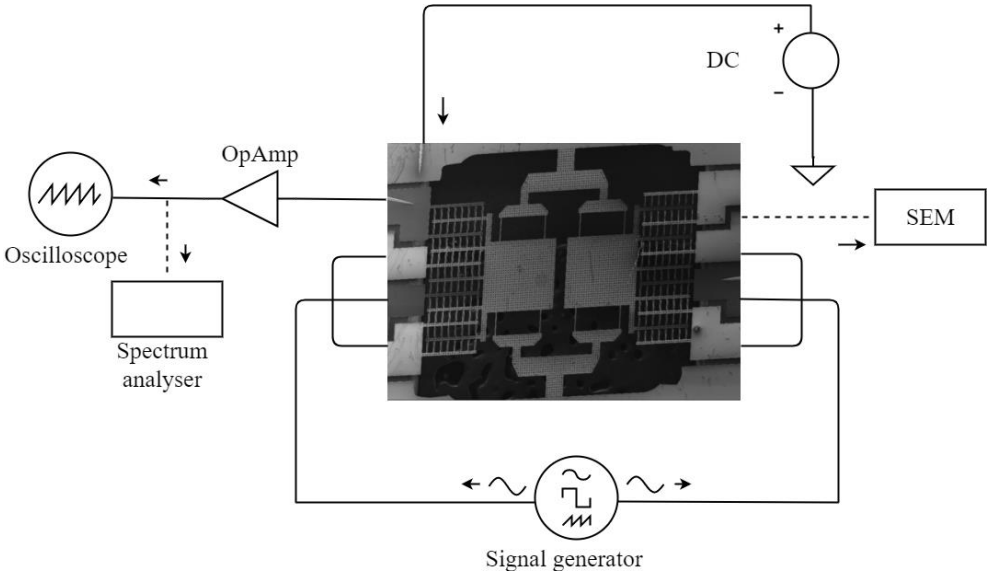

Figure 5.16: Experimental configuration of the bar-transmission resonator structure for resonant frequency and Q factor measurement

5.5.3 Circuit board design

The electrical signal from the resonator is picked up using a two-stage low input current amplifier (LICA) as show in fig.5.17. The LCIA has an input impedance which is inversely proportional to its open loop gain so is negligible. This is ideal for detecting the bar-transmission resonator signal since the resonator has a very low impedance. When connecting signal from a low impedance source to a higher impedance op amp, the op amp adds significant noise into the amplified signal. In addition, the LICA typically has a low bias input current, hence avoiding an offset current in output signal. The amplifiers used in the experiment are AD8065s made by Analog Device ltd, which amplify nano ampere current (nA) levels to micro voltage (μV) levels. The first stage of the op-amp system employs feedback consisting 2 resistors in series. Each resistor is in parallel with a small value capacitor to prevent the LICA circuit from self-oscillating. A large value of resistance is preferred for higher gain. The calculated gain of the first stage is 6.6 MegV/A. The second stage is an inverting amplifier to further increase the gain of the whole circuit. The value for the input and feedback resistors are 100 Ω and 100 kΩ respectively.

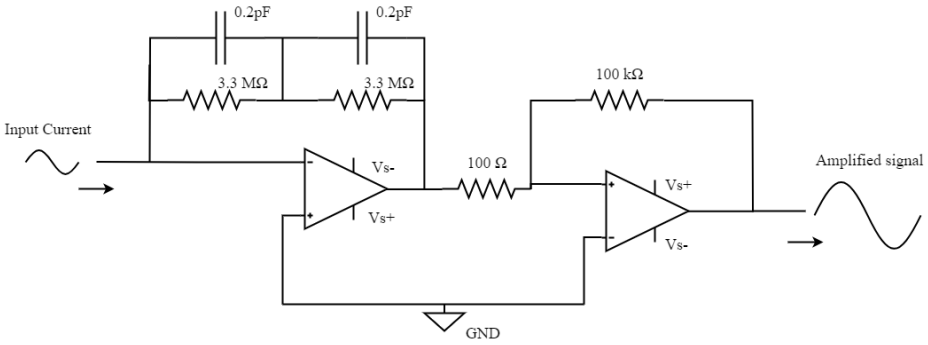

Figure 5.17 Detail schematic of two stage low input current amplifier.

The board receives a signal from the resonator via the feedthrough cable and header-pin while transmits the amplified output to an oscilloscope and/or spectrum analyser via D-sub connectors.

5.5.4 Experimental results

In this section, the measurements from the bar-transmission resonator devices are presented and analysed. First, the peak resonant frequency of 9 different devices is shown and discussed. Then the Q factor of is calculated using the ringdown method.

5.5.4.1 Frequency measurement

The frequency testing of a series of bar-transmission devices identifies the repeatability of fabrication. The simulated unstressed resonant frequency of a bar-transmission device is 22.568 kHz. The resonant frequencies found in total of 9 devices are presented in table 5.8. Five working samples have resonant frequencies from 23.034 to 25.966 kHz. There are 4 samples which do not provide the resonant frequency. Two out of four samples are identified to be affected by pull-in voltage. Uniformity level in successful fabrication, which can be calculated by divided minimum frequency over maximum frequency of measured resonator, is 88.7% with the difference between smallest and largest frequency is 2.33 kHz.

Table 5.8 out-of-phase resonant frequency for 9 bar-transmission samples with two settings i.e. bias voltage of 4V and 9V. Excitation voltage is 300 mV p-p

	Dev. 1	**Dev.2**	**Dev.3**	**Dev.4**	**Dev.5**	**Dev.6**	**Dev.7**	**Dev.8**	**Dev.9**
V_{DC}=4V, V_{AC}=300mV	23.636	fail	23.428	23.272	Pull in	fail	24.886	25.966	Pull in
V_{DC}=9V, V_{AC}=300mV	23.565	fail	23.267	23.034	x	fail	24.561	25.41	x

The vibration for different amplitudes was recorded using an SEM. The approach is to on a specific comb finger. During the excitation process, multiple images of the comb finger were taken as shown in fig 5.18. These images represent the amplitude hence indirectly show the Q factor of bar-transmission structure. The blurrier the movable comb is, the higher the Q factor is. The distance between the movable and static comb finger is 5µm. On low amplitude mode, the movable comb vibrates slightly side to

side. The image of resonator starts to get blurry as seen in fig 5.17(a). Then, when the comb vibrates with larger amplitude, the released holes' edges overlap to generate oval shapes in the centre of the holes as shown in fig.5.17(b). When the amplitude increases to approximately 5µm, the shape of the released holes is extremely blurry. The combs' edges overlaps creating a cloud in the vibrating area as shown in fig.5.17(c). The amplitude is at limit as this point, any increase results in a pull-in effect and the vibration stops.

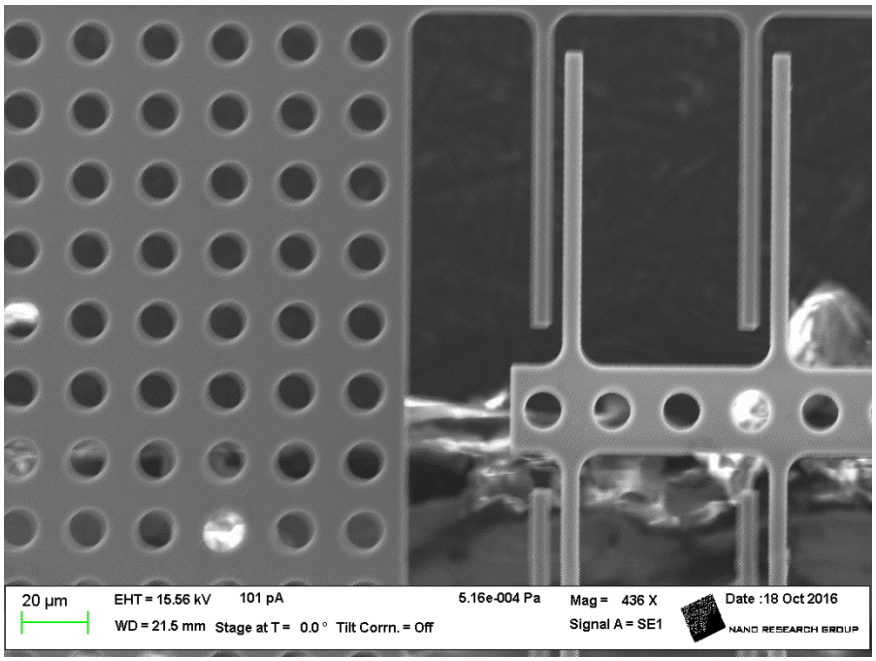

(a)

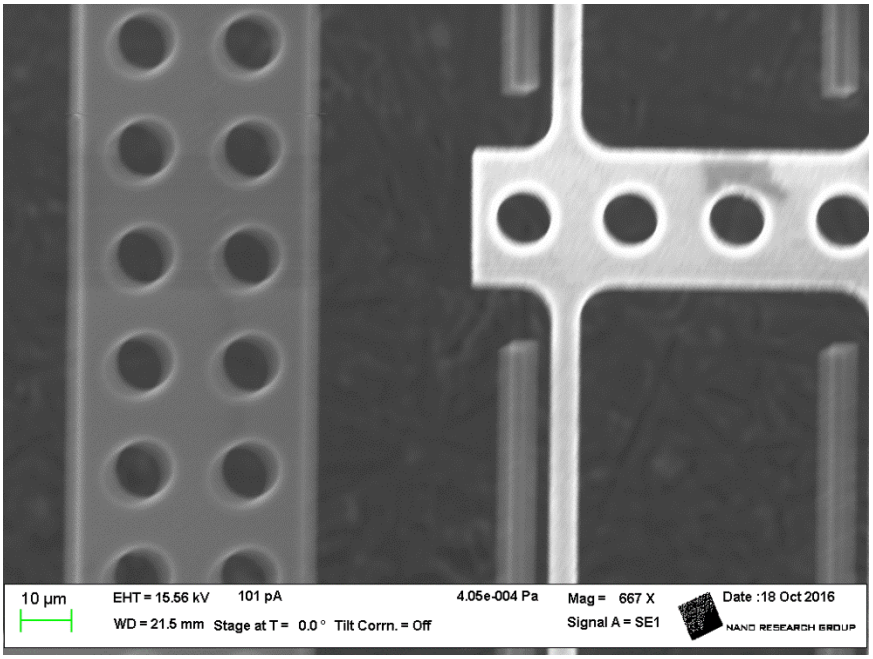

(b)

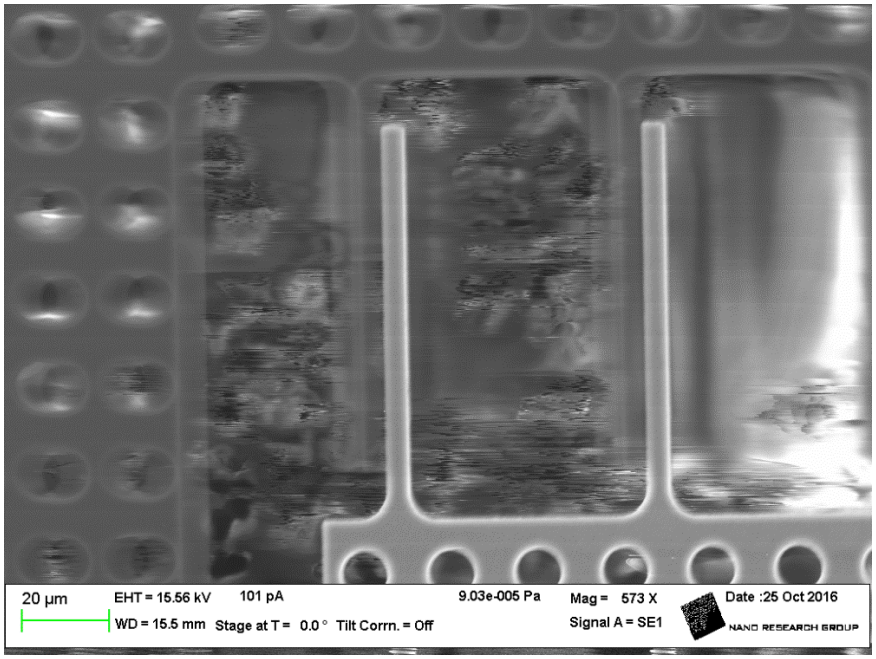

(c)

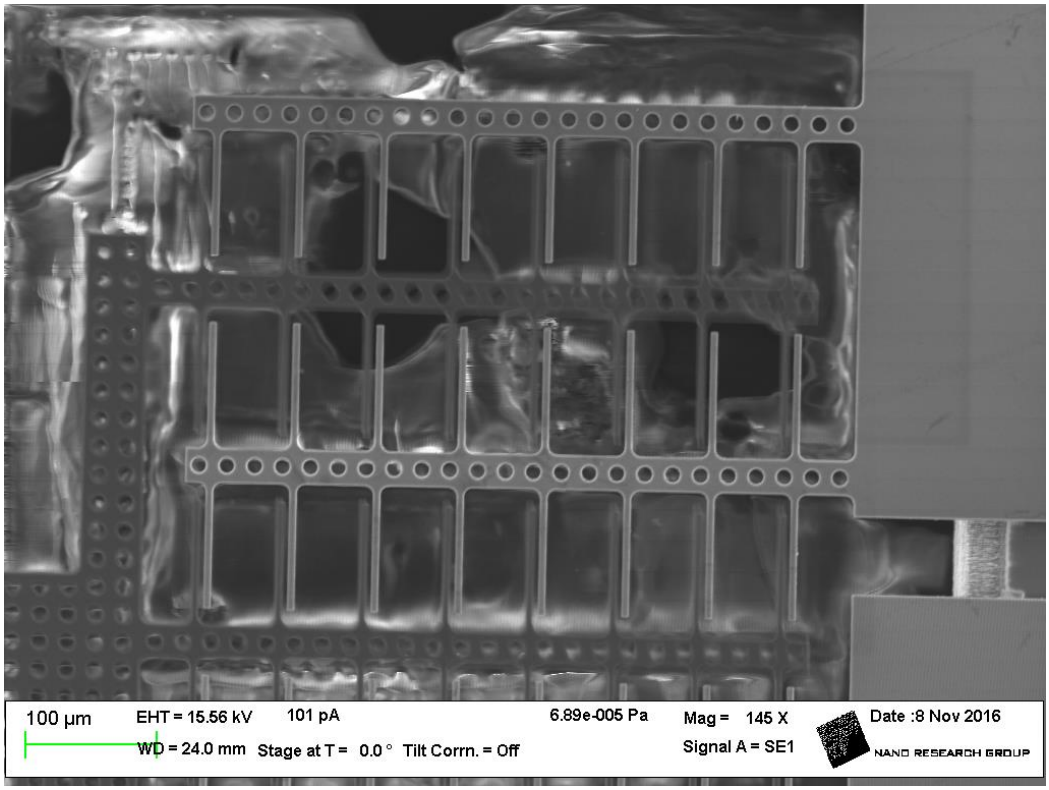

(d)

Figure 5.18 Resonator vibration at peak out-of-phase resonant frequency with (a) low amplitude (b) moderate amplitude (c) high amplitude and (d) a whole comp structure.

A repeated problem with the experiment is the pull-in effect. In static mode, the pull-in voltage of a pair of electrostatic plates can be calculated by formula [104]

$$U_p = \sqrt{\frac{8}{27}\frac{kd^3}{\varepsilon A_{el}}} \quad (5.2)$$

Where k is the spring constant, d is the gap and A_{el} is the overlapping area between two plates. The pull-in voltage is typically large for a rigid material such as silicon. However, the vibration during resonance significantly reduces the required voltage for electrostatic plates to move them closer. When oscillating in high amplitude, defects on the comb fingers causes them to touch and pull-in effect occurs as seen in fig.5.19.

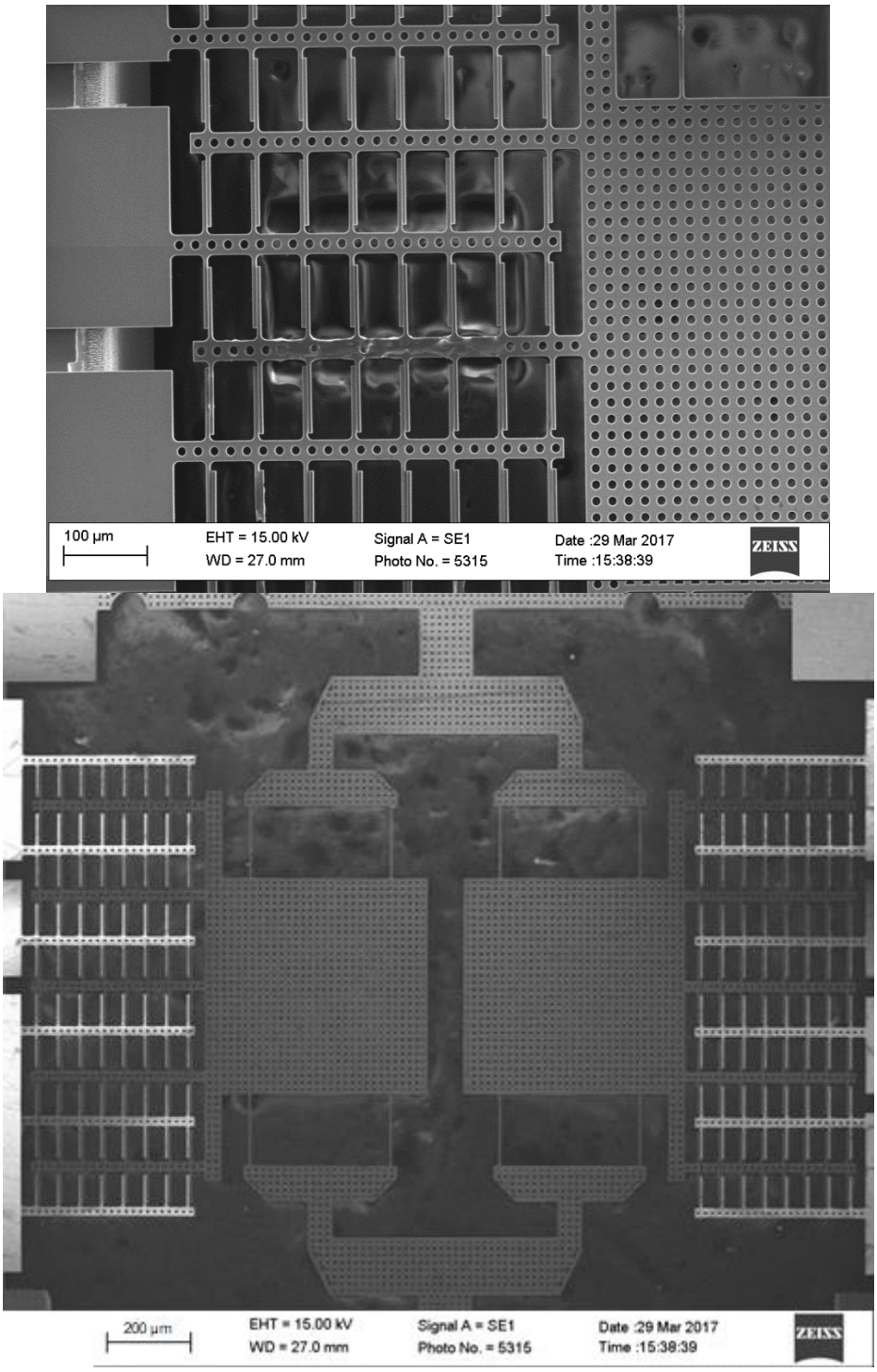

Figure 5.19 Pull-in effect as results of high amplitude vibration

Once the opposite comb fingers are in contact, the electrical excitation signal passes directly from the drive electrode to the resonator. Hence, the vibration stops. To disengage the two structures, high positive DC voltages are applied to the resonator and the static comb to create a repulsive force where the comb is not stuck. This approach is partly successful in removing the adhesion but damages the flexure beam structures as seen in fig.5.20. Due to low its low resistance, the resonator experiences large current when a high value voltage applied. This current generated a large heat output that eventually melts the thin structures in the resonator i.e. flexure beams and comb fingers. The melting happened when a voltage of 20V was applied.

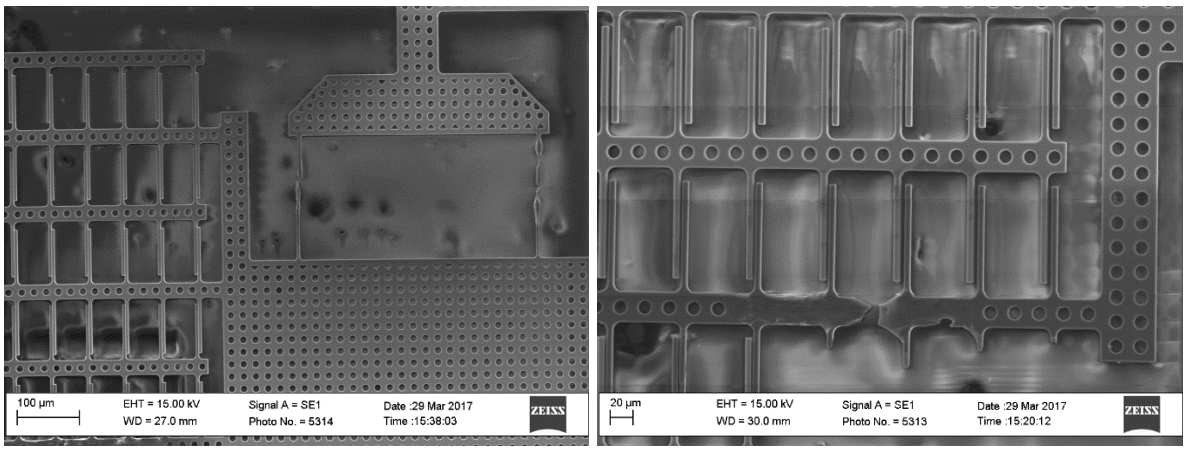

(a) (b)

Figure 5.20 High DC current flow damage small structures in the resonator device: (a) flexure beam and (b) comb finger

5.5.4.2 Q factor measurement

A frequency sweep measurement using the spectrum analyser is used to identify the dynamic range of the bar-transmission structure. A typical frequency response fat 4V DC bias is shown in fig5.21. The peak out-of-phase mode's frequency is observed as 23636.12 Hz without observing the in-phase mode. The resonant peak is sharp, which leads to difficulty in measuring an accurate Q-factor using the half-power bandwidth method. Thus, the ring-down time method is preferable to measure the Q-factor.

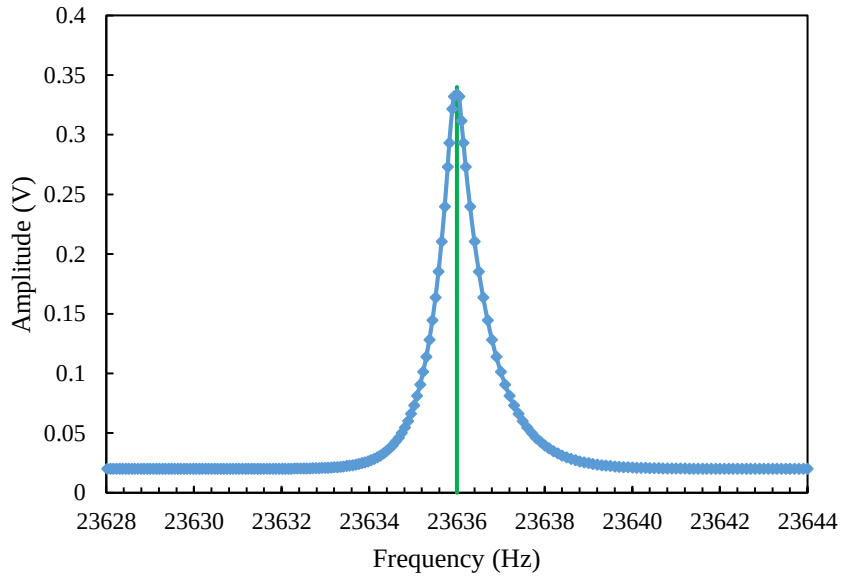

Figure 5.21 frequency response of device 1 using resolution of 10 samples/Hz

To calculate the Q-factor value, I measure the decay time (τ), at which amplitude is equal to the initial amplitude over e (A_0/e). For various devices, the initial decay amplitude varies as shown in fig.5.22. Five working samples were used to measure the decay times. Results for the decay times and Q factor are provided in table 5.10. The 5 samples show a Q factor ranging from 100k to 170k. These results suggest that low resistance crystal silicon remove the internal friction issue and thus improve the Q factor. The thermal loss of energy is reduced significantly compared with high resistance silicon, which in turn lead to 10000 increases in Q factor compared to first prototype. A Q factor of over 100k is suitable for long-term operation with minimal energy loss and material degradation i.e. downhole pressure measurement.

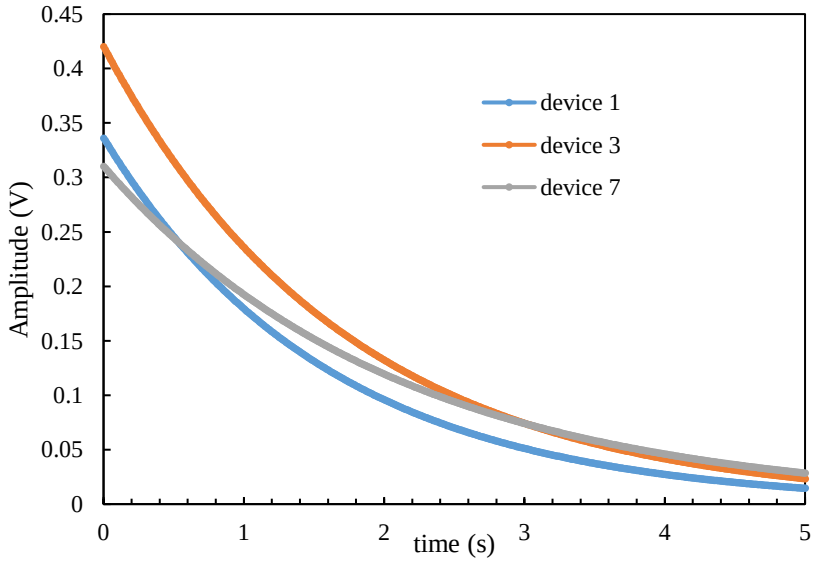

Figure 5.22 Excitation-free decay of amplitude with time for 3 different devices

Table 5.9 decay time and Q factor for tested devices

Device	τ(s)	Q factor
1	1.8	133658.4
3	1.95	143522.4
4	1.41	103086.7
7	2.12	165745.2
8	1.67	136229.6

5.5.5 Discussion

The experimental results have partially demonstrated the viability of bar-transmission resonator structure in downhole application with its high Q factor. The measured resonant frequency is slightly larger than the simulated data. The widest recorded difference is 3.398 kHz, which represents a for 15.05% increase compared with the simulated frequency. The Q factor improved significantly from 6.9 in the piezoresistive detection resonator to 133000 in the capacitive detection resonator. Thus, a combination of a double-mass silicon resonator and capacitive detection offers an ideal platform, on which to develop the resonant pressure sensor.

5.6 Dual double-mass design consideration for temperature compensation

As mentioned in chapter one, the targeted application of double-mass resonator is down-hole pressure measurement. The environment in oil reservoir is typically high pressure and high temperature. The effect of high pressure environment has been covered intensively in this work. However, relationship between change in temperature and resonant frequency of double-mass structure is also critical for the operation of the resonator. It is well-documented in both theoretical[105] and experimental[106] work that young's modulus of silicon decreases as the temperature increases. The temperature (T) dependence of the Young's modulus is formulized as

$$E = E_0 \exp\left(\frac{Q}{k_B T}\right) \quad (5.3)$$

Where Q is the activation energy and k_B is the Boltzmann's constant. As previously discussed in chapter 2, the change in stiffness of the structure ultimately leads to the change in resonant frequency of said structure. Thus, the high temperature in down hole environment certainly alters the resonant frequency of the double-mass structure. This characteristic adds noise to the pressure measurement process in significant magnitude. An increase of 150°C in temperature can lead to a drop of 1.3% in <100> silicon's stiffness[105]. There are several available methods to counter this problem such as temperature compensation via degenerate doping[107] or mechanically temperature-compensated[108] via added support structures. These approaches have

limited success in negating the temperature dependency but haven't removed the effect of temperature completely.

In this work, I consider a new approach called dual double-mass design to the problem. The idea is instead of trying to mechanically compensate the effect of temperature on resonator, the resonant frequency that is temperature-depended is measured separately from un-filtered frequency. Then, by comparing the two signals, I can isolate the resonant frequency shift that is sorely induced from applied pressure.

The approach is to fabricate two identical resonator structures in proximity. The two resonators need to be located close to each other to minimize the difference in temperature fluctuation. One resonator is exposed to applied pressure while the other is completely sealed from outside pressure. Once the dual resonator structure is put to work, the pressure-exposed resonator starts measure the change in both pressure and temperature while the sealed resonator only records the change in temperature. Contracting two information, I obtain both pressure and temperature measurement in down hole environment. The dual double-mass structure, then is developed from bar-transmission double-mass structure and can be seen in fig.5.23. The pressure (P) is applied to one end of the structure, which is mechanically coupled with one resonator. The whole structure is designed to be relatively small i.e. under 3000 µm wide and 7000 µm long. Thus, heat (T) can penetrate the structure instantly from every direction and affect both resonator equally. The other end of the structure is clamped for support. Top and bottom of the resonator structure are capped with two silicon layers to encapsulate the resonator in vacuum.

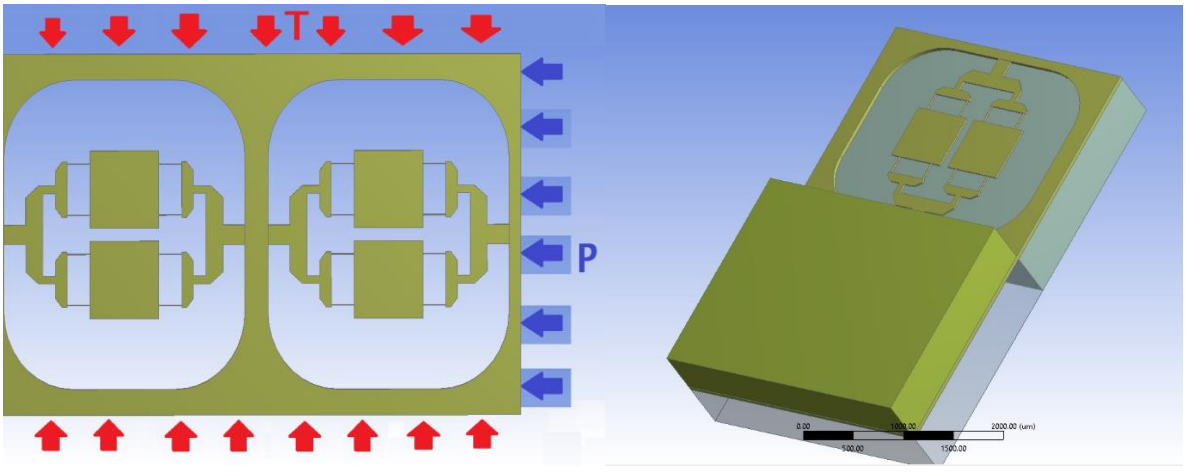

(a) (b)

Figure 5.23 Dual double-mass structure (a) with applied pressure and heat (b) cross-section view with capped layers

It is worth considering the effect that external pressure has on the sealed resonator. The distance and coupling mechanism between two resonators need to be optimized. Thus, in the next section, I will investigate the response of the dual resonator structure

to applied pressure. The frequency response of the resonator for different applied heat will also be discussed.

5.6.1 Dual double-mass structure simulation

In this section, first, I simulate effect of temperature on resonant frequency of bar-transmission resonator. Then, the complete bar-transmission model with packaging solution is simulated for three cases of external force, i.e. isolated pressure, isolated temperature and combined pressure and temperature. Finally, the dual double-mass structure is optimized to remove any residue stress on the sealed resonator as well as maximize the frequency response versus applied pressure.

From theoretical perspective, the raising temperature introduce additional thermal energy into the mechanical structure, which in turn increase the kinetic energy of the structure's molecules. The structure body typically expand to cope with this change in internal energy lead to the increase in body side. However, as the number of molecules doesn't increase, their bonds become weaker and hence, reduce the overall stiffness of the structure. In complex structure, these expansions introduce stress into the system, particularly in region with low stiffness. To simulate this theory, a uniform thermal force is applied unto the resonator structure. The temperature, then, is increased steadily from 0°C to 200°C to resemble the condition in down oil environment. The induced tensile stress and resonant frequency can be calculated via multi-physic modelling. Three different thickness of flexure beam is used in the simulation. The flexure beam dimension is the deciding factor for the resonator initial stiffness. Thus, the effect of thermal force on different stiffness can be observed. The resultant stress and resonant frequency can be seen in fig.5.24.

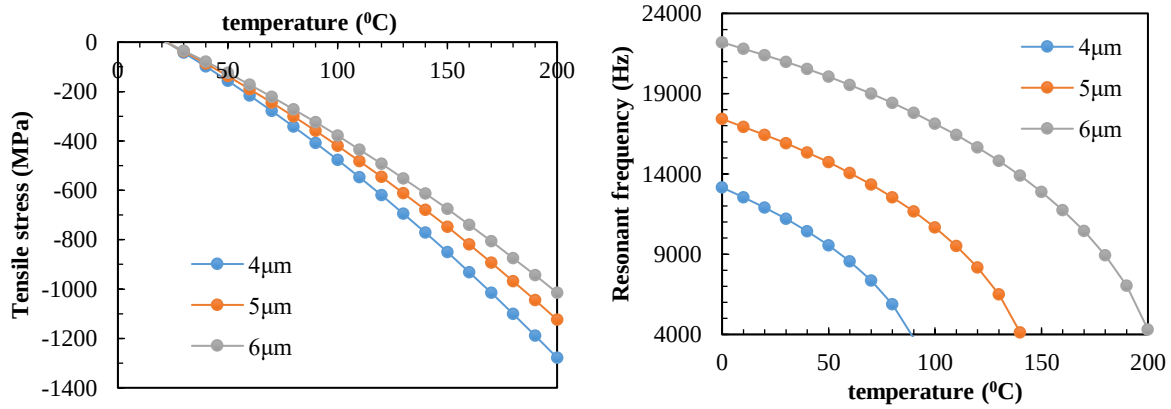

Figure 5.24 temperature fluctuation trigger change in resonator's (a) tensile stress and (b) resonant frequency for bar-transmission structure with different flexure beam thickness

The resonator expanding under heat generates large stress onto the low stiffness part of its body, i.e. the flexure beam. The thinner the beam, the larger the generated tensile stress. This stress lead to considerable shift in resonant frequency. The shift is more vigorous for thinner flexure beam design. Increasing temperature from 0 to

100°C, I observe a decrease of 10.1 kHz in 4 µm beam design while a reduction of 4.2 kHz is shown in 6µm design for the same applied condition. This result agrees with the literature on the dependency of mechanical structure and its resonant frequency on temperature fluctuation.

Second simulation is to explore the effects of both pressure and temperature have on the resonator structure together. To understand these effects entirely, I switch from using the resonator model in fig.5.23 (a) to using the completed package model with encapsulation layer shown in fig 5.23 (b). There are two approaches to simulate this idea being simultaneous or isolated simulation. The former is to simultaneously apply pressure and temperature condition to the structure and measure the response in induced tensile stress. This approach provides the more accurate dataset of the shift in induced stress, which in turn can be used to calculate the change in resonant frequency. It is worth noting that the drawback of the method is an increasing number of simulation needed to acquire data. The second approach is to simulate the effect on pressure and temperature separately. Then, I can calculate the shift in induced from the two acquired results. Using the second approach, I only need a set of data on pure pressure and an another on pure temperature condition. Fig.5.25 shows the induced stress from simultaneous simulation and the difference in percentage between the two approaches.

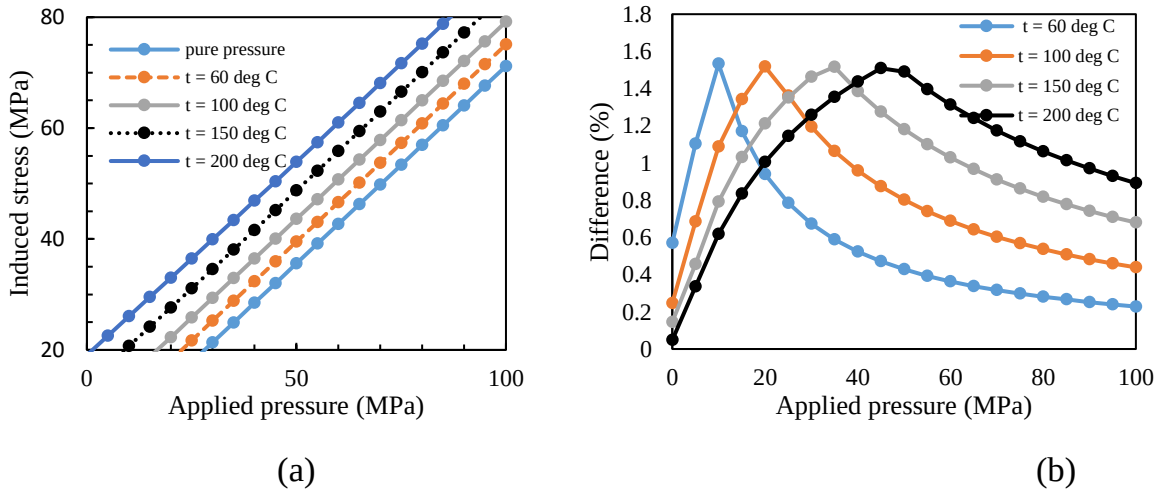

Figure 5.25 (a) induced stress vs applied pressure for a range of temperature and (b) difference in percentage from simultaneous and separated approach

As observed, increases in temperature leads to a linear raise in induced stress. The added stress from temperature only increase the stress by a constant number through the range of the simulation suggesting a positively-sloped linear relationship between induced stress and temperature. This behavior seems contradict to the analysis on decreasing stiffness with temperature. However, I need to take into consideration that the simulated mechanical body has been switch from only resonator structure to the resonator and complete package one. The added layers of encapsulated silicon expand in under increased temperature as well. This expansion imposes additional stress onto

the resonator layer. Since the outer layers are much thicker by design, their effects on the resonator layer restrict the resonator expansion in-plane only. Hence, resulting in larger tensile on the flexure beam. This mechanism is similar with the effect on pressure have on the bar-transmission structure as previously discussed.

The calculated stress from separated temperature and pressure simulation shows a small variation between the two datasets. The difference for each temperature condition is varied but shares the common trend of sharply raising from 0 to around 1.6% then gradually reducing to lower than 1%. This data indicates that two approaching method share very similar outcome. The separated simulation significantly reduces the simulation time to only two set of data without introducing a large margin of error, thus making it a preferable method for future simulation on pressure and temperature induced-stress.

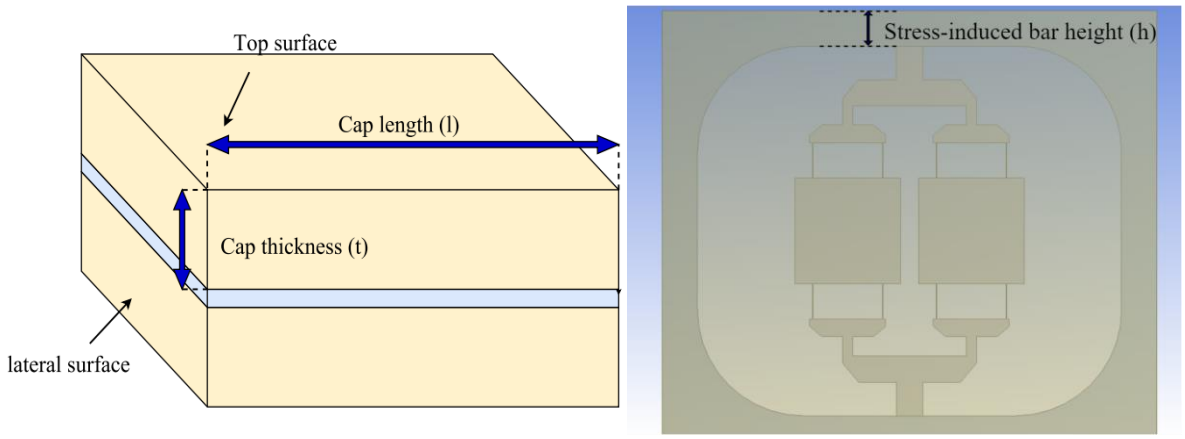

Figure 5.26 Dual double mass resonators' dimensions (a) Encapsulation layer thickness(t) and length(l) and (b) Height of stress-induced bar (h)

The third simulation aims to optimize the stress-induced mechanism as well as eliminate the pressure-induced stress on the isolated resonator structure. As discussed in earlier in this chapter, the size of encapsulation layer is critical to the induced tensile stress on bar-transmission structure. The pressure is uniformly applied to all device surface. Thus, the larger the top-surface area and smaller the lateral-surface area, the larger the top-surface force in compared to lateral-surface one. There are two dimensions deciding the exposed area of top-surface and lateral-surface namely cap length (l) and cap thickness (t) as seen in fig.5.26 (a). Cap length and cap thickness are the length and the thickness of the silicon encapsulation layer respectively. It is worth noting that the cap width (w) is not considered for the simulation. The cap width (w) is the share dimension of both said surface. Thus, any change in its value affects both surface area equally. The cap length (l) is a sum of stress-induced bar height (h), length of the resonator (l_r) and the gap (g) between exposed resonator and isolated resonator. In this simulation, I avoid complicating the design of the resonator, thus,

the change in cap length (l) can be implemented via alternating the stress-induced bar height (h) as shown in fig 5.26 (b). The gap (g) between resonator will be used in the second part of the simulation, where I look for a method to eliminate the pressure-induced stress on the isolated resonator.

To simulate the induced stress for various cap thickness and pressure-induced bar height efficient, I set the cap thickness constant and fluctuate the length (h) and measure the induced stress. The whole structure is under 100 MPa. The simulation can be repeated with different value of cap thickness until I obtain enough data in the range of interest. The same approach is used for pressure-induced bar height (h). The result for both sets of simulation is shown in fig.5.27. The increase in pressure-induced bar height (h) initially lead to a significant raise in induced stress. However, as the height value approach 1100 μm, the induced stress dip in value and then come to a stall. This behavior can be explained through stiffness change of the structure. Early fast raising on induced stress is introduced from additional top-surface area. As the top-surface area expand, the newly generated area contribution is becoming less and less in compared to pre-existing one. While the contribution from new exposed area reduced, the increase in size of the bar-transmission structure lead to its increase in stiffness. The stiffness of bar-transmission structure reduces its elasticity and deformation under stress as the result. The induced stress is mainly depended on the deformation of the bar-transmission structure. Combined both factors, I experience a stall in induced stress with larger height (h) value.

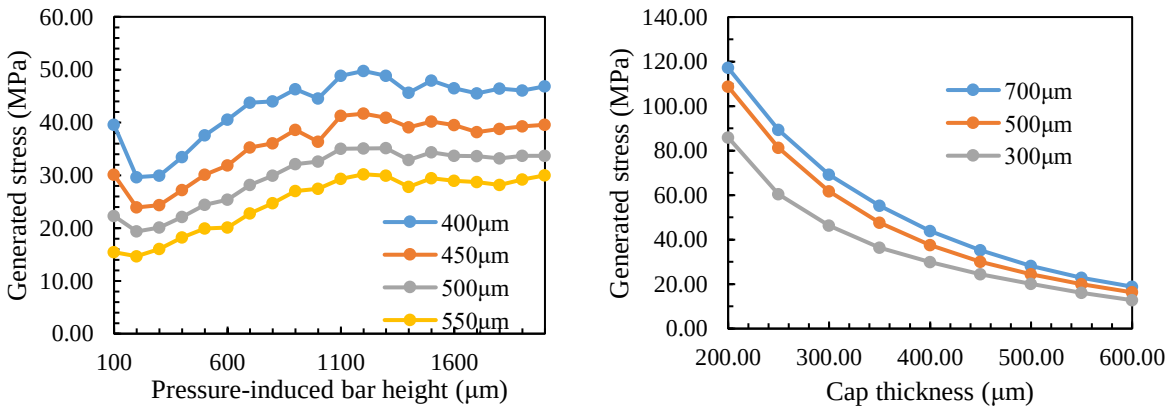

Figure 5.27 Exposed resonator performance varies with (a) a set of different cap thickness and (b) a set of different pressure-induced bar length

On the other hand, the increase in cap thickness (t) lead to a significant reduction of induced stress. The data suggests that as the induced stress reduces in a fast pace with low cap thickness and miniature pace for higher cap thickness. This behavior can be expanded in a similar argument with the pressure-induced bar height case. The larger the cap thickness, the less impact the newly added area has on the induced stress.

Another aim of this simulation is to eliminate the pressure-induced stress on isolated resonator. The Resonators' gap as shown in fig.5.28 separates the two resonator structures. The larger the gap, the higher the stiffness of mid-bar structure. The induced stress can diverge into this area, hence, reduce its impact on the isolated resonator structure. The gap is varied for different set of top cap thicknesses to diversify the dataset. For each data point, I simulate the generated stress on the isolated resonator, then calculate the stress ratio between the two resonators.

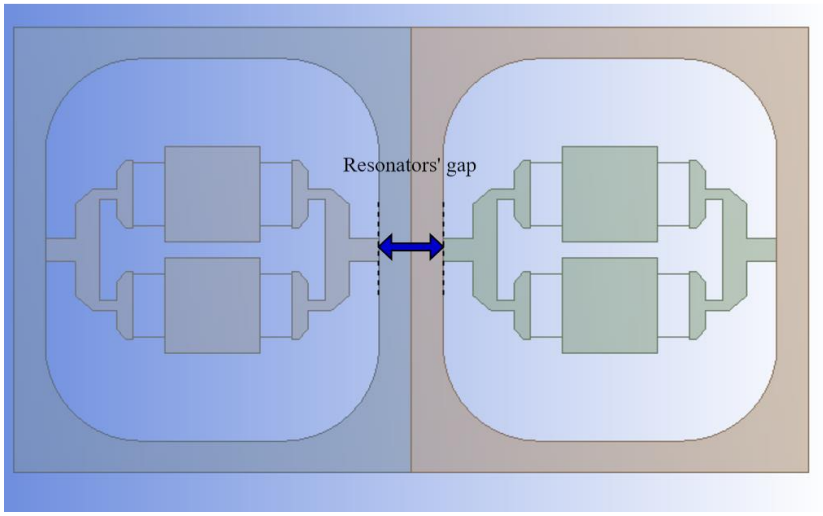

Figure 5.28 Dual double-mass structure with resonators' gap

As shown in fig.5.29, the induced stress is remarkably high at low gap value. However, the stress value sharply reduces as the gap widens. The induced stress is almost neglectable when the gap value approaches 500 μm. The result is slightly different for the stress ratio calculation. In general, all datasets sharply decrease its calculated ratio as the gap value increases. However, the initial ratios at 100 μm gap are significantly varied for different cap layer thickness. The higher the cap layer thickness, the larger the ratio value. The ratio value is the division of isolated resonator's stress over exposed one. As the cap thickness increases, the exposed resonator's stress reduces while the isolated resonator's stress remains intact, which in turn lead to previous observed phenomenon.

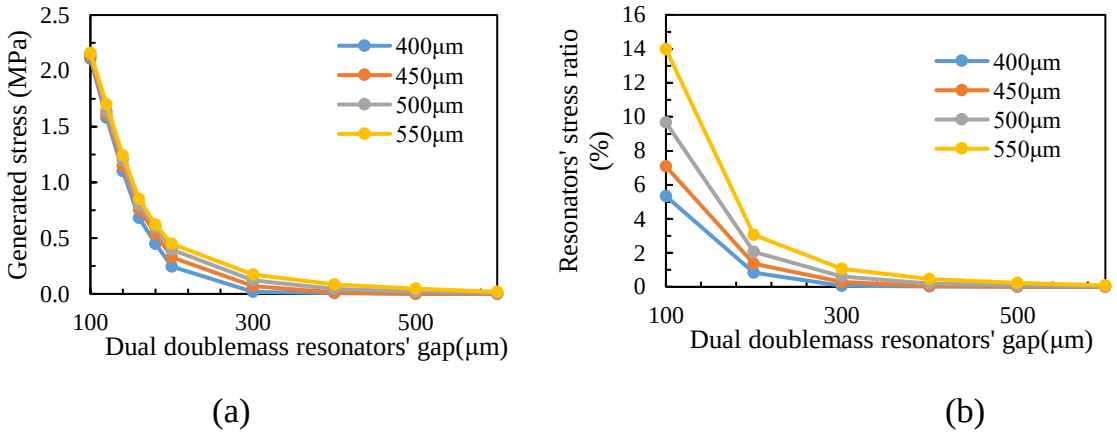

(a) (b)

Figure 5.29 Isolated resonator's (a) induced stress vs resonators' gap and (b) ratio of resonators' stress for the range of resonators' gap

5.6.2 Discussion

High temperature in down hole environment has created an opportunity for novelty in pressure sensor designing process. In this chapter, I have proposed dual double-mass resonator-based sensor and proven its viability using multi-physic simulation. Four sets of simulation are created to investigate as well as optimise the dual double-mass structure for desired working environment. Temperature vs induced stress proved the softening effect that high temperature has on single layer silicon device. When adding top and bottom layer into the simulation, the effect reverses and stiffness of the device layer increases. In addition, the temperature and pressure have a compound effect on structural stress of the resonator. Both simulated datasets have shown two consistent linear relationships of temperature and pressure with induced stress but with different proportion. Another simulation is to optimise the dual double-mass structure to maximise the structural stress caused by pressure input. Encapsulation layer thickness and length decide the area of top-surface and lateral-surface, which are shown to significantly affect the induced structural stress. Two datasets on cap length and cap thickness present the behaviour of induced stress for various data points. Finally, the structure is optimised to eliminate the induced stress on the isolated resonator. Both structural stress and stress ratio dataset suggest that the isolated resonator stress is insignificant as the gap value approach 500 µm. It is worth considering that other structures can be used to reduce the gap between two resonators without increasing the structural stress.

5.7 Conclusion

In this chapter, I have performed a throughout investigation on the lateral stress induced resonator. During a compression motion, the structure is under two type of stress i.e. compressive stress and tensile stress. The typical diaphragm structure can only employ the tensile stress without engaging the compressive stress into strain generating process. To understand the issue, I have to investigate the position of the

diaphragm relative to the resonator structure. It is widely implemented that the diaphragm is located underneath the resonator. When pressure applied, the diaphragm compresses inward generating both compressive stress and shear stress. Since resonator structure is typically symmetrical, the compressive stress induces the same inward force into both anchor point of the resonator. As the result, no internal tensile stress is generated from the induced compressive stress. The lateral stress induced structure (LSIS) changes the approach of engaging the stress by alter the position of the pressure sensitive structure to the resonator. The LSIS is located on the same plane with the resonator. Under applied pressure, the LSIS compresses induce a compressive stress onto the inner structure. To engage this compressive stress, the spring-transmission structure (STS) is developed. The STS has its anchor located in the centre of the LSIS to maximise the transferred stress. the other end is connected to top of the resonator structure. When the LSIS compress, the two STSs on two side of the resonator move inward, generating a tensile stress onto the resonator in the middle.

Simulation on the packaging solution of STS revealed the addition stress causing by the added top and bottom silicon layer. The newly introduced stress caused the STS to move outward, hence inducing compressive stress onto the resonator. Since compressive stress can cause fatigue in long and thin structures i.e. the flexure beams. The STS is not viable for keeping the device pristine in high pressure environment. The bar transmission structure (BTS) is introduced as the replacement mechanism. The BTS employs outward motion generated by the extra layer of silicon and transfer the stress directly onto the resonator structure. The resultant stress is in form of tensile and increase the effective stiffness of the resonator. the simulation results confirm the effectiveness of the BTS in transfer the generated stress to the resonator. A process of optimising the structure was discussed in detail. The fabrication process on the resonator with BTS is optimised from previous attempt on double-mass resonator. the released devices were tested for resonant frequency and Q factor. Out of ten tested samples, five provides the resonant frequency in the range of interest while the other five fails to present a specific resonant peak. The reason for each failed case was discussed as well.

State-of-the-art dual double-mass resonator then is proposed. The structure consists of two identical resonator structures, one being exposed to pressure while the other is isolated to prevent pressure-induced stress from happening. The isolated resonator frequency shift is accounted for the thermal expansion and its source, down hole high temperature environment. The data from the isolated resonator is used for compensation in the exposed one. Subtracting the frequency shift from thermal expansion, I obtained the sensitivity caused by applied pressure. The optimisation process for the device was simulated and result was discussed.

Chapter 6 **Conclusions and future work**

6.1 **Conclusions**

In section 1.2, I have presented a list of research objectives. At the end of the research, I have mainly achieved following result:

- Objective 1: Find an effective way to improve the sensitivity and capacity of pressure coupled resonator sensor via simulation model.

  Achievement 1: propose a novel structure that is able to improve the sensitivity and range of operating pressure via simulation effectively. The coupled double-mass resonator with modified anchor points can improve the sensitivity from 35 Hz/Bar in quartz sensor to 48 Hz/Bar while maintaining the operational range of 1000 Bar. In term of mode crossover, the minimum gap between in-phase and out-of-phase frequency is 5.7 kHz across the operational range.

  The key to improve the sensitivity for the double-mass structure is to move the contact points between resonator and diaphragm closer to centre of the diaphragm, while increasing the stiffness of the anchor beam proportionally. In this way, a high level of induced stress is transferred to the resonator structure while the frequency gap between mode is kept intact.

- Objective 2: Develop a fabrication process and investigate the frequency response and Q factor on the fabricated sensors

  Achievement 2: In this work, I have developed a fabrication flows for SOI wafer based on Sari's publication. Modifications are included to adjust the fabrication for the smaller devices as well as introducing the diffusion process. In addition, I have implemented a trans-impedance circuit to detect the piezoresistive signal from the resonator. the gap between measured and simulated frequency peak of the resonator is 6.42 kHz, accounting for 10.8% of the measured frequency. The measured Q factor is at magnitude of 5.9. The internal damping of single crystal silicon is reduced due to the generated heat of piezoresistor-on-chip system.

- Objective 3: Analyse the stress-induced structures and find an alternative solution to traditional diaphragm

  Achievement 3: the stress induction mechanism was investigated. The expression for diaphragm stress and deflection caused by applied pressure are given by Eqn. 3.18. From the expression, it is worth noting that the area, which is close to the centre of the diaphragm, has the high concentration of stress and deflection. In addition, the diaphragm structure typically only uses the shear element of the stress. The state-of-the-art lateral stress induced structure (LSIS)

has shown to utilise the compressive element of the stress. LSIS is able to acquire sensitivity of 48 Hz/Bar, which is similar to diaphragm structure, as seen in fig.5.3.

- Objective 4: Investigate the state-of-the-art LSIS structure frequency response and Q factor, then compare with the first prototype.

  Achievement 4: in section 5.4 and 5.5, I have presented the fabrication and experiment of the LSIS structure for its resonant frequency and Q factor. The structure has shown a significant improvement in Q factor. The capacitive detection mechanism has eliminated the risk of overheat in the resonator structure. In addition, the resonant frequencies match with simulation results. The widest gap between two results is 3.398 kHz.

- Objective 5: Investigate a solution for high temperature compensation for downhole resonant pressure sensor via simulation.

  Achievement 5: in section 5.6, I have presented the problem of high temperature in downhole application. Thus, I proposed a state-of-the-art dual double-mass structure that is able to compensate for the frequency shift in thermal expansion. The structure utilised two encapsulation layers to isolate one of its two resonators from applied pressure. The isolated device then provided a signal that response to the change in only temperature. Simulation result suggest that the isolated device has neglectable effect from applied pressure, hence making it ideal for temperature compensation mechanism.

However, there are other problems that need to be addressed for double-mass resonator for downhole application. Firstly, the structure proved its effectiveness with sensitivity in simulation. However, the experimental test only showed the resonant frequency and Q factor. A stress induced mechanism needed to develop to test these devices response to stress. Secondly, the piezoresistor-on-chip system has significantly reduced the Q factor of the device. Piezoresistor should be fabricated separately and adhere to the resonator to eliminate the problem. Finally, both diaphragm and lateral stress induced structure only engage either shear or compressive stress in their induction mechanism. None of them exploit the full potential of stresses generated from applied pressure. These issues lead to proposed future work beyond the scope of the thesis.

6.2 **Future work**

This section outlines the plan for future task that aim to fulfil the potential of this research.

6.2.1 Optimisation of the device design

As stated multiple times in this thesis, the design of the device parameter is not optimal. Hence, the optimisation of parameters should be focused in the scope of

future work. Ad discussed in structural design sections throughout this thesis, trade-offs exists in a few parameters. Therefore, in the future, I should consider specific design requirement to balance the trade-offs. Currently, the focus of optimisation is the sensitivity of the sensor. As discussed in the thesis, sensitivity is controlled by the generated stress via induction mechanism. It is crucial to expand the range of simulated dimension of induction structure to find the most optimal set of parameters.

6.2.2 Combined stress induction mechanism optimisation

In this thesis, I discussed the benefit of using both lateral stress inducing structure (LSIS) and diaphragm. Thus, the aspect of combing both structures into a single induction mechanism is viable. Since the diaphragm's shear stress and the LSIS compressive stress work in coherent. The sum of two stresses theoretically is larger than each individual. It is important to optimise the device structure for maximum efficiency.

6.2.3 Fabrication process development

The resonator has proved to be useful in pressure sensing application via simulation. The fabricated device shows high Q factor and expected resonant frequency. To develop a complete sensory package, I need an encapsulation process that put the resonator under vacuum without the use of vacuum chamber. The complete device then can be tested for its response against applied pressure. Our approach could be using the epitaxial silicon deposition as first cap layer while employing the backside handle layer in SOI wafer as second cap layer.

Appendix A

Photomask for double-mass with diaphragm design

Photo mask design contains four different layers that are used for various purposes including alignment mark etching, dopant diffusion, front-side device and backside trench. All layers share the same sizes: 7 inches × 7 inches square. These masks accommodate the patterns that are transferred to 6 inches silicon wafer as shown in fig. A.1.

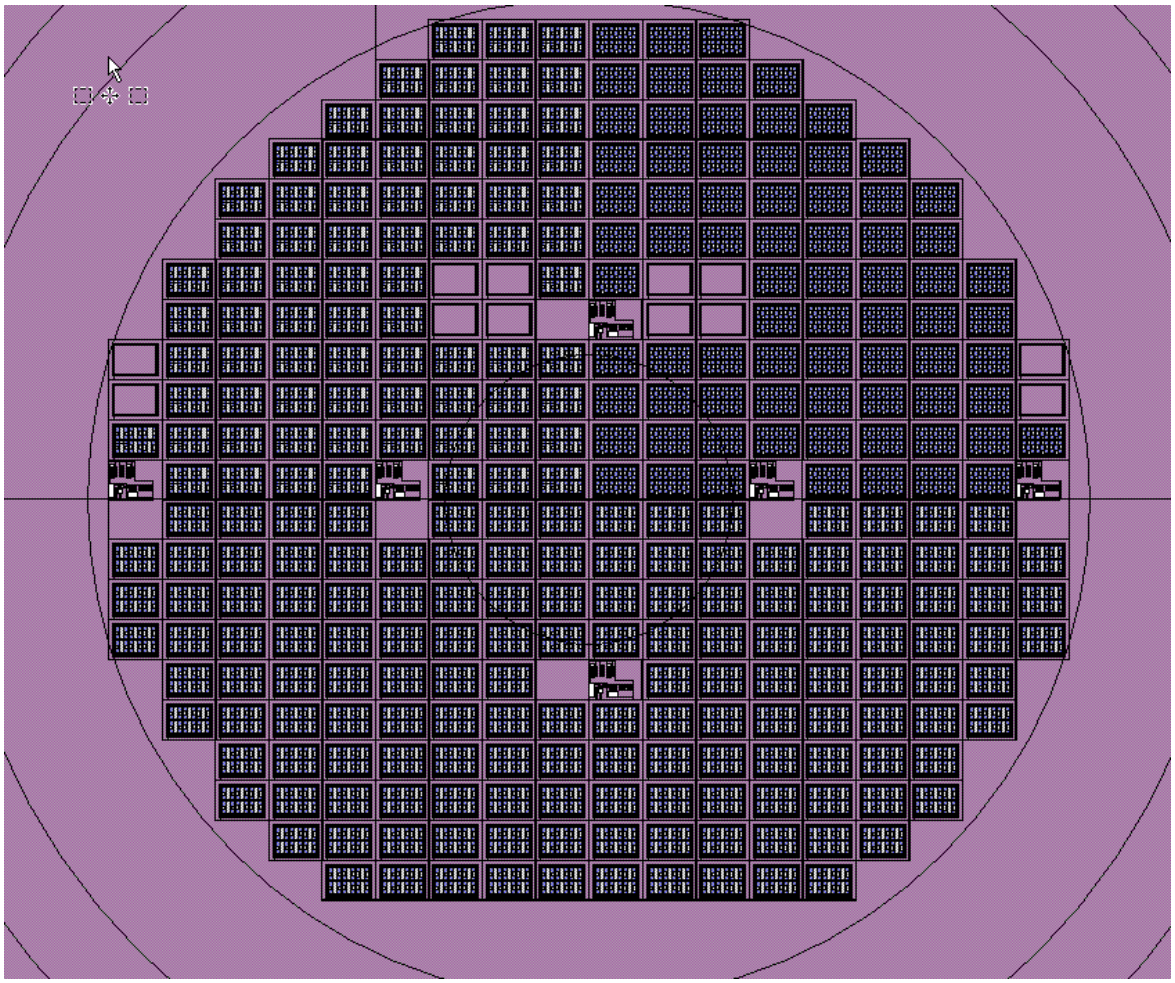

Figure A.0.1 Overall design of 4 photomask layer overlapping

Alignment mark etching mask have six-mark designs in total. Four-mark designs are located along the horizontal diameter line of the mask while the other two is place along the vertical diameter line. The mark contains a precision mark area for critical dimension test. The mark area design is shown in fig.A.2.

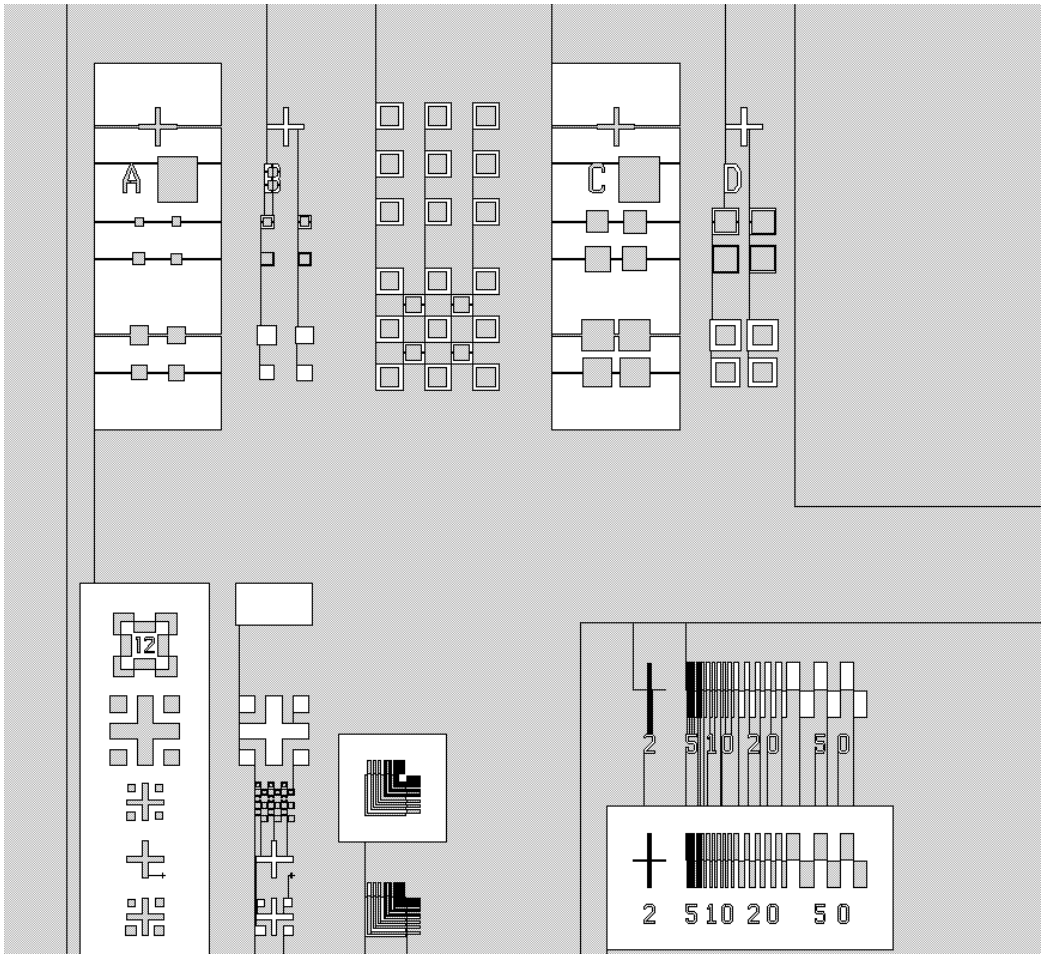

Figure A.0.2 Alignment mark design including the precision mark

The remaining three masks are chip structure oriented. The total of 300 chip designs are located in the three masks. Each chip contains 6 different resonators structures. The mask for dopant diffusion consists of 4 rectangular shape that is used to expose the contact area for doping. Thus, there are 24 shapes per chip as shown in fig.A.3. This mask also includes the aligment mark in the same position with the first mask for aligment purpose.

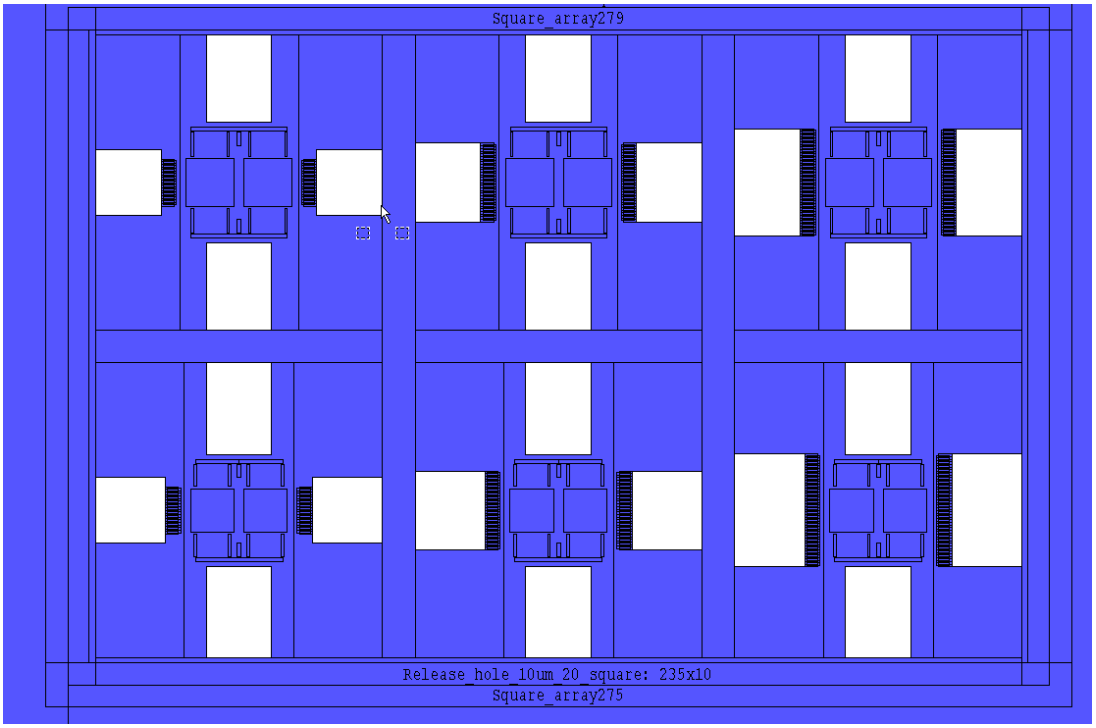

Figure A.0.3 Dopant diffusion mark design for a single chip

The front-side device mask for a single is illustrated in fig.A.4. Each resonator structure is separated by 25µm trenches running across the chip. The chip border is pattern with a bank of 10µm release holes. These holes support the BOX etch process during HF vapour step.

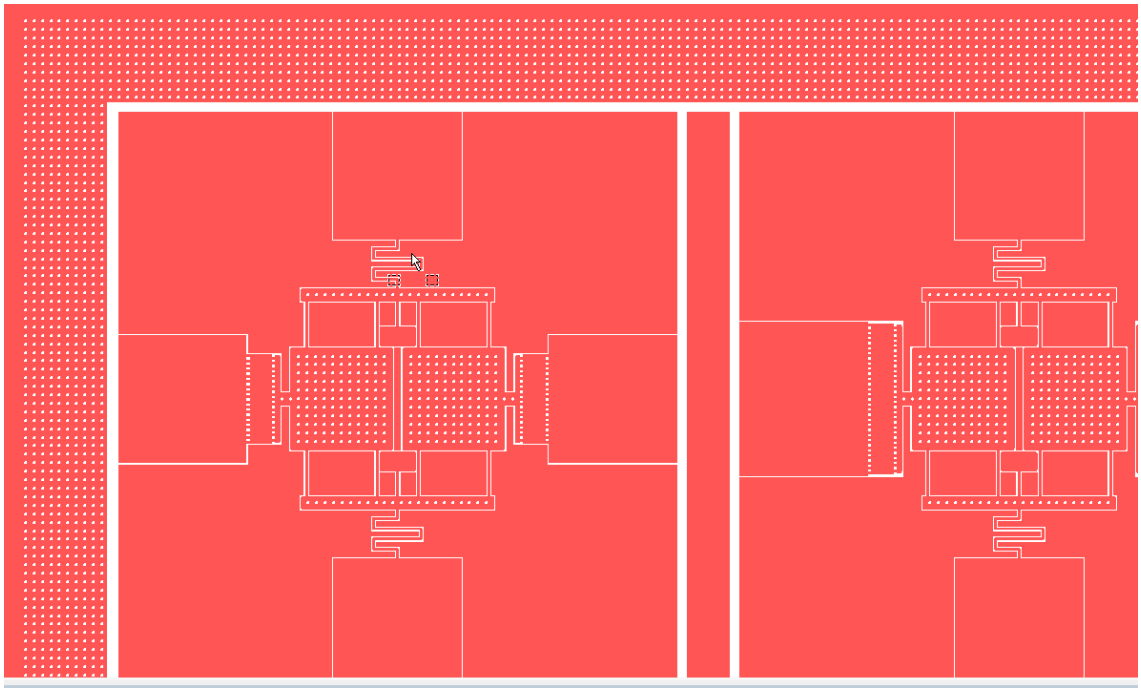

Figure A.0.4 Front-side device mask with separation trenches and banks of release hole

The backside trenches mask is used to pattern the handle wafer for chip separation. The trenches enclose the chip structure. Thus, after DRIE etch, each individual chip is released. The backside mask employs the backside alignment mask, which is used to align the trenches with front-side structure. Overlapping structure of backside trenches and front-side pattern is shown in fig. A.5.The backside trenches are represented in brown.

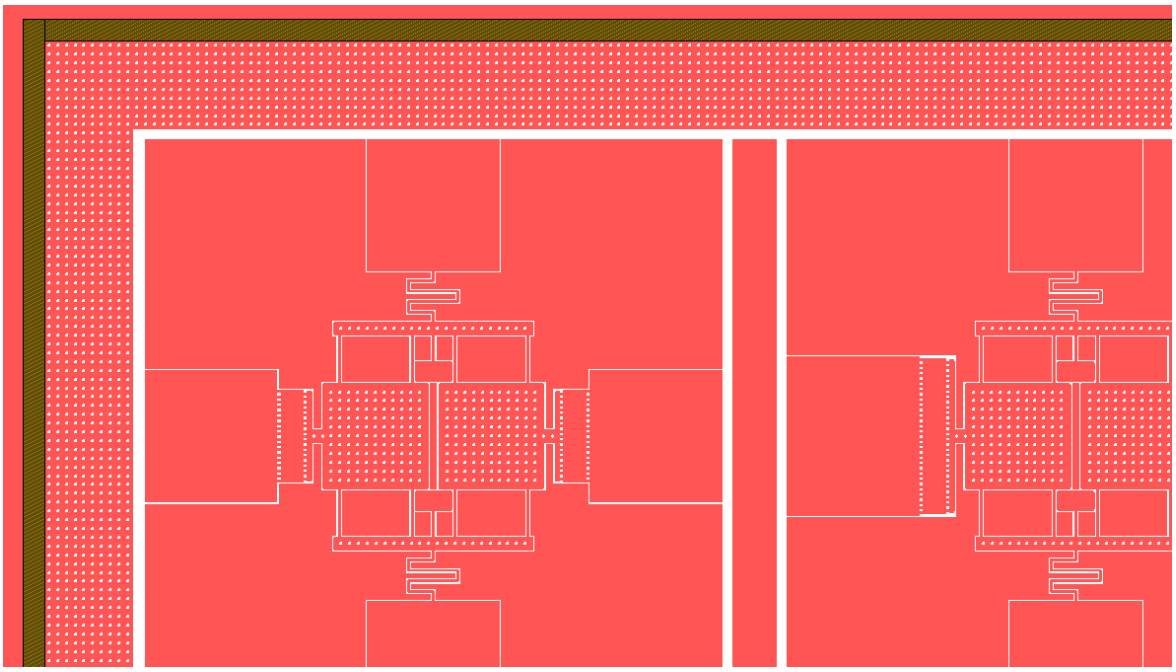

Figure A.0.5 Backside trenches in align with front-side device mask

Appendix B

Vacuum chamber and test circuit component

Testing the operation of strain gauge resonator requires a vacuum condition to maximize the resonator's Q factor. Vacuum chamber provides an encapsulated area from which air is removed by a vacuum pump to create a very low-pressure environment close to vacuum condition. In this project, I place both resonator device and its test circuit board inside the vacuum chamber. The input and output signals are connected with outer circuits and equipment via vacuum chamber electrical feedthroughs. The vacuum chamber design consists of three main parts including mechanical components, electrical connections, vacuum seals and clamps.

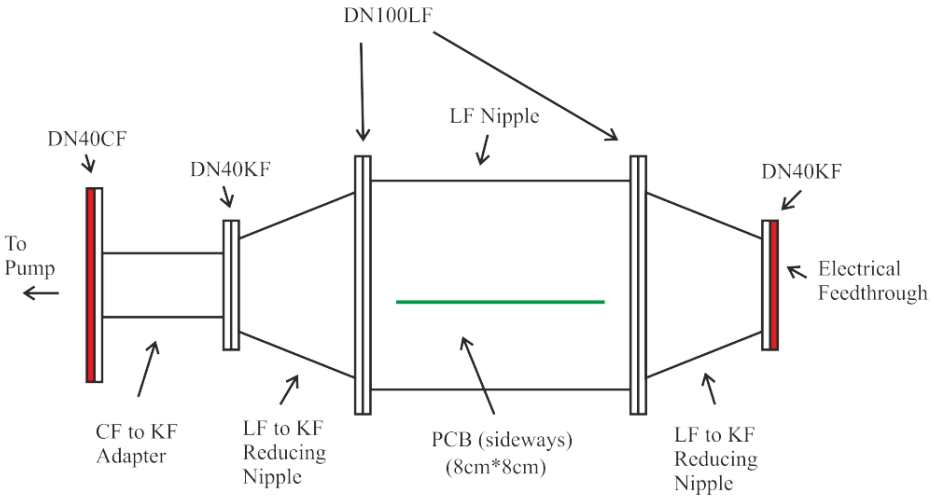

Figure B.0.1 Schematic drawing of the customized vacuum chamber

The body of the chamber is made from stainless steel to maintain vacuum condition. The main parts contain a 10x10 cm hollow cylinder interfacing two conical adapters. One adapter is used to connect the vacuum pump while the other is employed to hold the electrical feedthrough as seen in fig. 5.1 (a). Vacuum seals are inserted in to fill the gap between all interfaces to prevent air from leaking into the chamber.

(a) Front view (b) Inside the chamber

Figure B.0.2 Vacuum chamber view from (a) front side and (b) inside

As the test circuit is placed inside the chamber, I need to maximise the number of electrical connection in order to deliver all the input signals and obtain sufficient data from output ports. 9 pin D type electrical feedthrough and ribbon cable (supplied by Lewvac Components Ltd.) are suitable to work in near vacuum condition down to 10^{-8} Torr [1]. The feedthrough is connected to outer circuit via male connector while the ribbon cable uses female connector to interface with test circuit as seen in fig. 5.1 (b).

List of vacuum chamber's components

No	Component	Quantity
1	DN100LF full nipple L=100mm	1
2	DN100LF to 40KF conical reducer L = 63mm	2
3	DN40KF hinged clamp	2
4	DN63LF-DN100LF double claw clamp	8
5	DN100LF ST-ST centring ring	2
6	D9 F/T on DN40KF	1
7	Ribbon cable 9-way female	1

[1] From Lewvac catalogue, can be found at http://www.lewvac.co.uk/index_files/section%201.1.pdf

Appendix C

MATLAB code for solving deflection and inphane stress for rectangular plate

The following MATLAB code is used for solving the deflection and inphane stress for rectangular plate with vertical pressure applied from backside. The value used in this code are the same as illustrated in section 3.4. The Maltab code for other cases can be easily derived from this code. It is worth noting that this may not be the optimum code for this purpose.

```
a  = 0.800;
b  = 0.800;
H  = 0.18;
h  = H/2;
E  = 220e9;
v  = 0.22;
q0 = 100e6;
D  =E*H^3/(12*(1-v^2));
w  = 0;
Oxx_t = 0;
Oxx_m = 0;
Oxx_b = 0;
Oyy_t = 0;
Oyy_m = 0;
Oyy_b = 0;
x  = 0:a/200:a;
y  = 0:b/200:b;

for m =1:10
    for n = 1:10
        amp  = 16*q0/((2*m-1)*(2*n-1)*pi^4)*(((2*m-1)/a)^2+((2*n-1)/b)^2)^-
2;
        agr  = sin((2*m-1)*pi/2)*sin((2*n-1)*pi*y/b);
        w = w + amp*agr/(pi^2*D);
        Oxx_b = Oxx_b + amp*agr*(((2*m-1)/a)^2+v*((2*n-1)/b)^2)*3*(-
h)/(2*h^3);
        Oxx_m = Oxx_m + amp*agr*(((2*m-1)/a)^2+v*((2*n-
1)/b)^2)*3*0/(2*h^3);
        Oxx_t = Oxx_t + amp*agr*(((2*m-1)/a)^2+v*((2*n-
1)/b)^2)*3*h/(2*h^3);
        Oyy_b = Oyy_b + amp*agr*(((2*n-1)/b)^2+v*((2*m-1)/a)^2)*3*(-
h)/(2*h^3);
        Oyy_m = Oyy_m + amp*agr*(((2*n-1)/b)^2+v*((2*m-
1)/a)^2)*3*0/(2*h^3);
        Oyy_t = Oyy_t + amp*agr*(((2*n-1)/b)^2+v*((2*m-
1)/a)^2)*3*h/(2*h^3);
    end
end

figure %new firgure
ax1 = subplot(1,3,1);
ax2 = subplot(1,3,2);
```

```
ax3 = subplot(1,3,3);
plot(ax1,y,w)
xlabel (ax1,'y(mm)')         % x-axis label
ylabel (ax1,'{\omega}_{(x,y)} (mm)')  % y-axis label
plot(ax2,y,Oxx_b/10^6,y,Oxx_m/10^6,y,Oxx_t/10^6)
xlabel (ax2,'y(mm)')         % x-axis label
ylabel (ax2,'{\sigma}_{xx} (MPa)')  % y-axis label
plot(ax3,y,Oyy_b/10^6,y,Oyy_m/10^6,y,Oyy_t/10^6)
xlabel (ax3,'y(mm)')         % x-axis label
```

Appendix D

Photomask for double-mass with bar-transmission structure

Photo mask design contains two separated layers that are used for patterning transferring. The front-side mask is for device details while backside mask is for released trenches. Both layers share the same sizes: 7 inches × 7 inches square. These masks accommodate the patterns that are transferred to 6 inches silicon wafer as shown in fig. D.1.

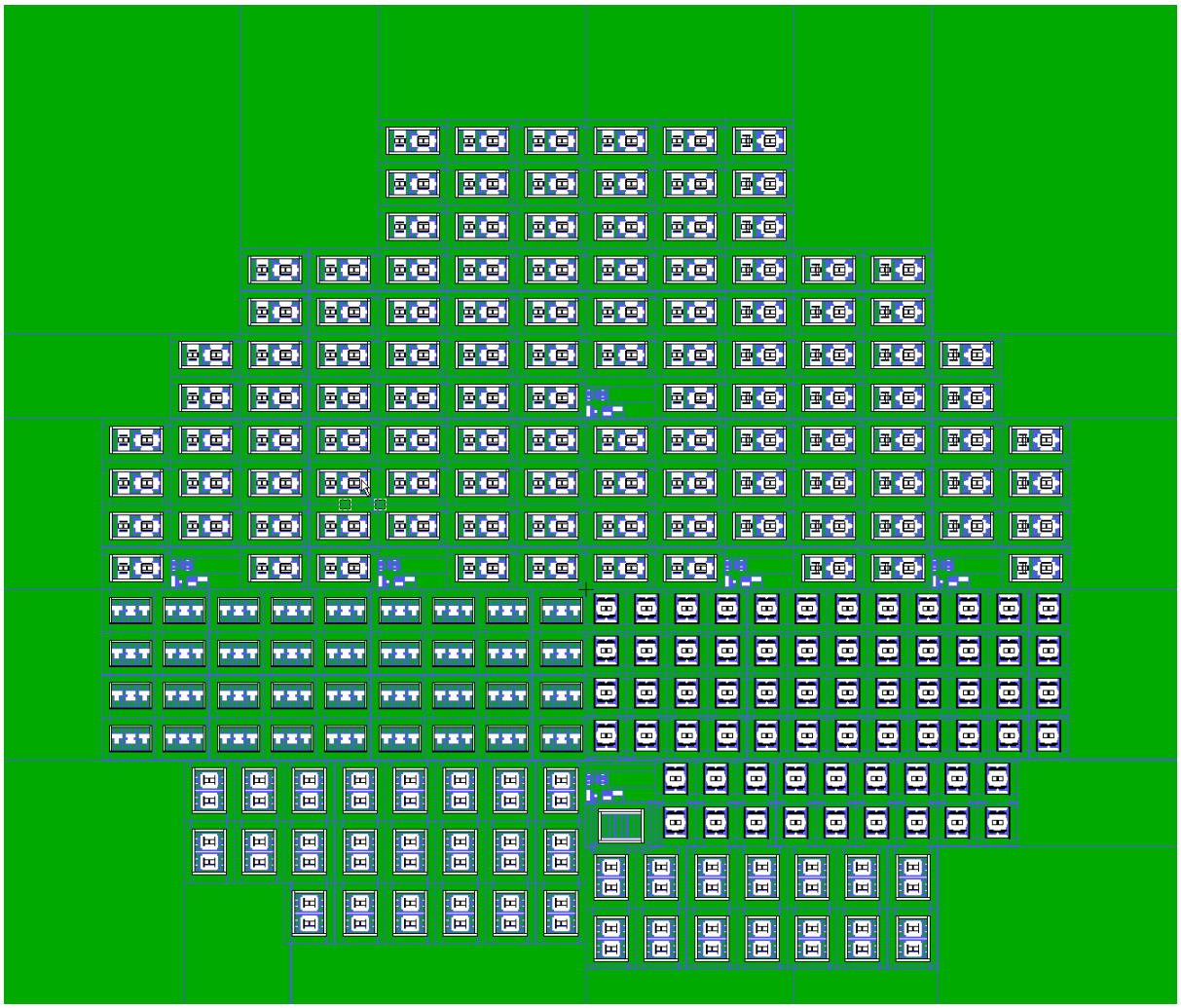

Figure D.0.1: Wafer size mask layout for bar-transmission and spring transmission design

The front-side device mask for a single is illustrated in fig.D.2. Each resonator structure is separated by 60 µm trenches running across the chip. The chip border is pattern with a bank of release holes, whose diameter are 20µm. These holes support the BOX etch process during HF vapour step.

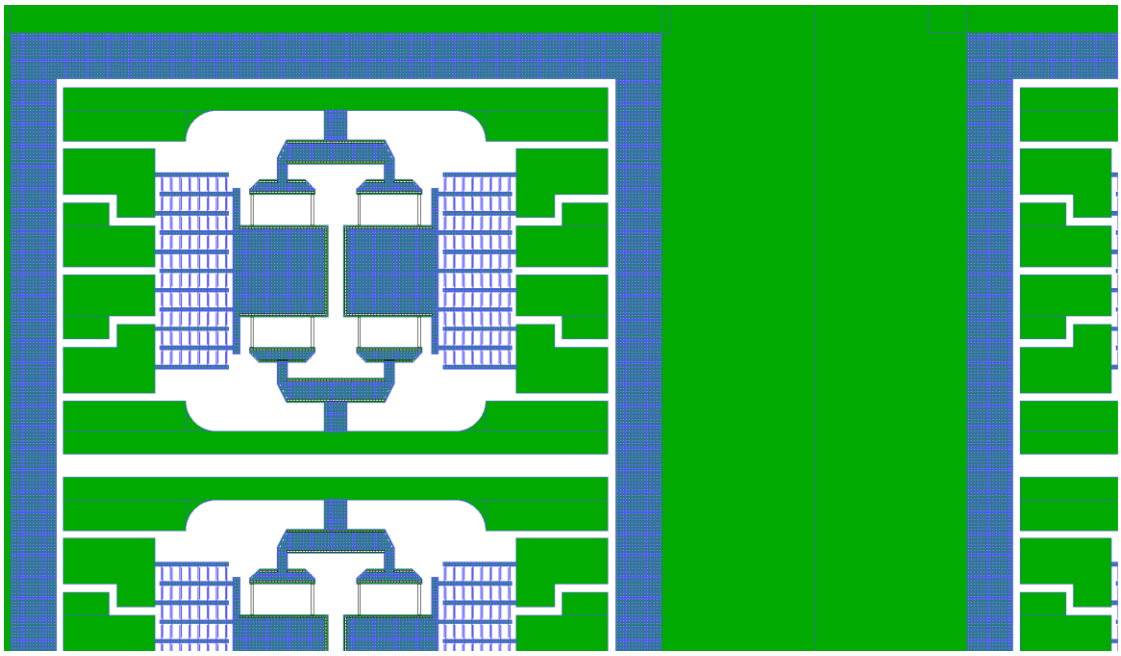

Figure D.0.2: Bar transmission device layer mask with details

The backside trenches mask is used to pattern the handle wafer for chip separation. The trenches enclose the chip structure. Thus, after DRIE etch, each individual chip is released. The backside mask employs the backside alignment mask, which is used to align the trenches with front-side structure. Overlapping structure of backside trenches and front-side pattern is shown in fig. A.5.The backside trenches are represented in brown.

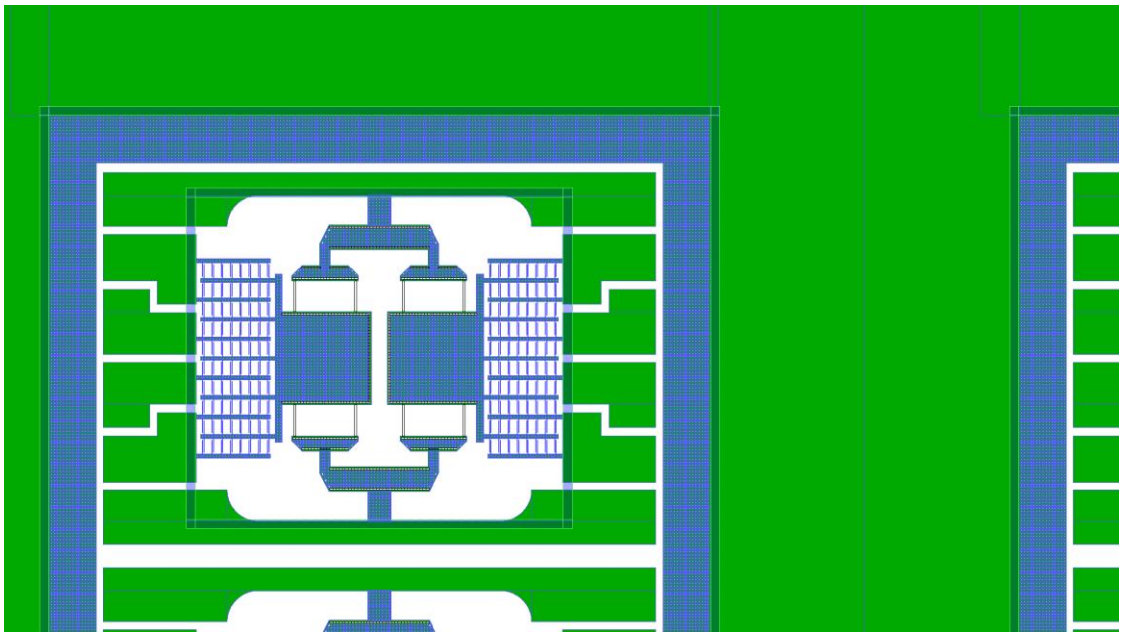

Figure D.0.3: Bar transmission backside layer mask is aligned underneath the device layer mask

Reference

[1] S. Li, Y. Lin, Y. Xie, Z. Ren, and C. T. Nguyen, "MICROMECHANICAL 'HOLLOW-DISK' RING RESONATORS," in *IEEE int. Micro Electro Mechanical Systems*, 2004, pp. 821–824.

[2] W.-T. Hsu and C. T.-C. Nguyen, "Stiffness-compensated temperature-insensitive micromechanical resonators," in *IEEE Int. Micro Electro Mechanical Systems Conferenace*, 2002, vol. 2, pp. 2–5.

[3] B. Kim and R. N. Candler, "Frequency stability of wafer-scale encapsulated MEMS resonators," *Solid-State Sensors, Actuators, Microsystems Work.*, vol. 2, pp. 1965–1968, 2005.

[4] L. Xu, J. Xu, F. Dong, and T. Zhang, "On fluctuation of the dynamic differential pressure signal of Venturi meter for wet gas metering," *Flow Meas. Instrum.*, vol. 14, no. 4–5, pp. 211–217, Aug. 2003.

[5] S. Beeby and G. Ensell, "Micromachined silicon resonant strain gauges fabricated using SOI wafer technology," *J. Microelectromechanical Syst.*, vol. 9, no. 1, pp. 104–111, 2000.

[6] E. Stemme and G. Stemme, "A balanced resonant pressure sensor," *Sensors Actuators A Phys.*, vol. 23, pp. 336–341, 1990.

[7] Norsok Standard, "NORSOK Standard Drilling facilities," 2012. [Online]. Available: https://www.standard.no/en/sectors/energi-og-klima/petroleum/norsok-standard-categories/d-drilling/d-0012/.

[8] T. R. Albrecht, P. Grutter, D. Horne, and D. Rugar, "Frequency modulation detection using high-Q cantilevers for enhanced force microscope sensitivity," *J. Appl. Phys.*, vol. 69, no. 2, pp. 668–673, 1991.

[9] U. Durig, J. K. Gimzewski, and D. W. Pohl, "Experimental Observation of Forces Acting during Scanning Tunneling Microscopy," *Phys. Rev. Lett.*, vol. 57, no. 19, pp. 2403–2407, 1986.

[10] T. a. Roessig, R. T. Howe, a. P. Pisano, and J. H. Smith, "Surface-micromachined resonant accelerometer," *Proc. Int. Solid State Sensors Actuators Conf. (Transducers '97)*, vol. 2, pp. 1–4, 1997.

[11] A. A. Seshia, M. Palaniapan, T. A. Roessig, R. T. Howe, R. W. Gooch, T. R. Schimert, and S. Montague, "A vacuum packaged surface micromachined resonant accelerometer," *J. Microelectromechanical Syst.*, vol. 11, no. 6, pp. 784–793, 2002.

[12] R. Sunier, T. Vancura, Y. Li, K. U. Kirstein, H. Baltes, and O. Brand, “Resonant Magnetic Field Sensor With Frequency Output,” *J. Microelectromechanical Syst.*, vol. 15, no. 5, pp. 1098–1107, 2006.

[13] B. Bahreyni and C. Shafai, “A resonant micromachined magnetic field sensor,” *IEEE Sens. J.*, vol. 7, no. 9, pp. 1326–1334, 2007.

[14] R. Azevedo and D. Jones, “A SiC MEMS resonant strain sensor for harsh environment applications,” *Sensors Journal, IEEE*, vol. 7, no. 4, pp. 568–576, 2007.

[15] P. Thiruvenkatanathan, J. Woodhouse, J. Yan, and A. A. Seshia, “Limits to mode-localized sensing using micro- and nanomechanical resonator arrays,” *J. Appl. Phys.*, vol. 109, no. 10, pp. 1–11, 2011.

[16] N. H. Saad, C. J. Anthony, and R. Al-Dadah, “Exploitation of multiple sensor arrays in electronic nose,” *IEEE Sensors*, pp. 1575–1579, 2009.

[17] M. Spletzer, A. Raman, A. Q. Wu, X. Xu, and R. Reifenberger, “Ultrasensitive mass sensing using mode localization in coupled microcantilevers,” *Appl. Phys. Lett.*, vol. 88, no. 25, pp. 10–13, 2006.

[18] E. Gil-Santos, D. Ramos, A. Jana, M. Calleja, A. Raman, and J. Tarnayo, “Mass sensing based on deterministic and stochastic responses of elastically coupled nanocantilevers,” *Nano Lett.*, vol. 9, no. 12, pp. 4122–4127, 2009.

[19] K. Y. Yasumura, T. D. Stowe, E. M. Chow, T. Pfafman, T. W. Kenny, B. C. Stipe, and D. Rugar, “Quality factors in micron- and submicron-thick cantilevers,” *J. Microelectromechanical Syst.*, vol. 9, no. 1, pp. 117–125, 2000.

[20] Y. Martin, C. C. Williams, and H. K. Wickramasinghe, “Atomic force microscope-force mapping and profiling on a sub 100 um scale,” *J. Appl. Phys.*, vol. 61, no. 10, pp. 4723–4729, 1987.

[21] G. Stemme, “Resonant silicon sensors,” *J. Micromechanics Microengineering*, vol. 1, no. 2, pp. 113–125, Jun. 1991.

[22] S. Ren, W. Yuan, D. Qiao, J. Deng, and X. Sun, “A micromachined pressure sensor with integrated resonator operating at atmospheric pressure.,” *Sensors (Basel).*, vol. 13, no. 12, pp. 17006–24, Jan. 2013.

[23] C. J. Welham, J. Greenwood, and M. M. Bertioli, “A high accuracy resonant pressure sensor by fusion bonding and trench etching,” *Sensors Actuators A Phys.*, vol. 76, no. 1–3, pp. 298–304, Aug. 1999.

[24] S. Beeby, G. Ensell, M. Kraft, and N. White, *MEMS mechanical sensors*. Norwood, MA: Artechhouse, 2004.

[25] O. N. Tufte, P. W. Chapman, and D. Long, “Silicon Diffused-Element Piezoresistive Diaphragms,” *J. Appl. Phys.*, vol. 33, no. 11, p. 3322, 1962.

[26] S. Franssila, “Silicon,” in *Introduction to microfabrication*, 1st ed., Wiley, 2004, p. 35.

[27] C. Smith, “Piezoresistance effect in germanium and silicon,” *Phys. Rev.*, vol. 919, 1954.

[28] S. . Clark and K. D. Wise, “Pressure sensitivity in anisotropically etched thin-diaphragm pressure sensors,” *IEEE Trans. Electron Devices*, vol. 26, no. 12, 1979.

[29] H. Takao, Y. Matsumoto, and M. Ishida, “Stress-sensitive differential amplifiers using piezoresistive effects of MOSFETs and their application to three-axial accelerometers,” *Sensors Actuators A Phys.*, vol. 65, pp. 61–68, 1998.

[30] GE Measurement & Control, “Trench Etched Resonant Pressure Sensor,” 2009.

[31] C. S. Sander, J. W. Knutti, and J. D. Meindl, “A monolithic capacitive pressure sensor with pulse-period output,” *IEEE Trans. Electron Devices*, vol. 27, no. 5, pp. 927–930, May 1980.

[32] F. Rudolf and H. De Lambilly, “Low-cost pressure sensor microsystem,” *Microsyst. Technol.*, no. 1995, 1995.

[33] W. Eaton and J. Smith, “Micromachined pressure sensors: review and recent developments,” *Smart Mater. Struct.*, vol. 530, 1997.

[34] H. Kim, Y. Jeong, and K. Chun, “Improvement of the linearity of a capacitive pressure sensor using an interdigitated electrode structure,” *Sensors Actuators A Phys.*, vol. 62, pp. 586–590, 1997.

[35] P. Pons, G. Blasquez, and R. Behocaray, “Feasibility of capacitive pressure sensors without compensation circuits,” *Sensors Actuators A Phys.*, vol. 37–38, pp. 112–115, Jun. 1993.

[36] J. C. Greenwood, “Silicon in mechanical sensors,” *J. Phys. E.*, vol. 22, no. 3, pp. 191–191, 2002.

[37] R. Buser and N. De Rooij, “Very high Q-factor resonators in monocrystalline silicon,” *Sensors Actuators A Phys.*, vol. 23, pp. 323–327, 1990.

[38] J.-Q. Zhang, S.-W. Yu, and X.-Q. Feng, “Theoretical analysis of resonance frequency change induced by adsorption,” *J. Phys. D. Appl. Phys.*, vol. 41, no. 12, p. 125306, Jun. 2008.

[39] N. V. Lavrik, M. J. Sepaniak, and P. G. Datskos, “Cantilever transducers as a platform for chemical and biological sensors,” *Rev. Sci. Instrum.*, vol. 75, no. 7, p. 2229, 2004.

[40] J. S. Rao, *Advanced theory of vibration*. New York: Wiley, 1992.

[41] M. a Hopcroft, W. D. Nix, and T. W. Kenny, “What is the Young ’ s Modulus of Silicon ?,” *J. Microelctromechanical Syst.*, vol. 19, no. 2, pp. 229–238, 2010.

[42] A. W. McFarland, M. A. Poggi, M. J. Doyle, L. A. Bottomley, and J. S. Colton, “Influence of surface stress on the resonance behavior of microcantilevers,” *Appl. Phys. Lett.*, vol. 87, no. 5, pp. 1–4, 2005.

[43] P. D. Mitcheson, S. Member, T. C. Green, S. Member, E. M. Yeatman, and A. S. Holmes, “Architectures for Vibration-Driven Micropower Generators,” vol. 13, no. 3, pp. 429–440, 2004.

[44] M. Tudor, M. Andres, K. Foulds, and J. Naden, “Silicon resonator sensors:

interrogation techniques and characteristics," in *IEE Proceedings D (Control Theory and Applications)*, 1988, vol. 135, no. 5.

[45] M. Christen, "Air and gas damping of quartz tuning forks," *Sensors and Actuators*, vol. 4, no. 1983, pp. 555–564, 1983.

[46] R. HoI and R. Muller, "Resonant-microbridge vapor sensor," in *IEEE Transactions on Electron Devices*, 1986, no. 4, pp. 499–506.

[47] J. Zook, D. Burns, and H. Guckel, "Characteristics of polysilicon resonant microbeams," *Sensors Actuators A Phys.*, vol. 35, pp. 51–59, 1992.

[48] S. Beeby and M. Tudor, "Modelling and optimization of micromachined silicon resonators," *J. Micromechanics Microengineering*, vol. 103, pp. 7–10, 1995.

[49] R. N. Kleiman, G. K. Kaminsky, J. D. Reppy, R. Pindak, and D. J. Bishop, "Single-crystal silicon high-Q torsional oscillators," *Rev. Sci. Instrum.*, vol. 56, no. 11, p. 2088, 1985.

[50] J. Greenwood, "Etched silicon vibrating sensor," *J. Phys. E.*, vol. 650, pp. 8–11, 1984.

[51] V. Kaajakari, T. Mattila, A. Oja, and H. Seppä, "Nonlinear limits for single-crystal silicon microresonators," *J. Microelectromechanical Syst.*, vol. 13, no. 5, pp. 715–724, 2004.

[52] A. Tocchio, C. Comi, G. Langfelder, A. Corigliano, and A. Longoni, "Enhancing the linear range of MEMS resonators for sensing applications," *IEEE Sens. J.*, vol. 11, no. 12, pp. 3202–3210, 2011.

[53] W. Tang, "Laterally driven polysilicon resonant microstructures," *Sensors and actuators*, vol. 20, no. 2, pp. 25–32, 1989.

[54] A. V. Gluhov, V. P. Dragunov, V. U. Dorgiev, and I. V. Knjazev, "Features of pull-in effect in one-capacitor MEMS," *12th Int. Conf. APEIE*, p. 34006, 2014.

[55] G. Fedder, C. Hierold, J. Korvink, and O. Tabata, *Resonant MEMS: Fundamentals, Implementation, and Application*. Weinheim, Germany: Wiley, 2015.

[56] D. DeVoe, "Piezoelectric thin film micromechanical beam resonators," *Sensors Actuators A Phys.*, vol. 88, no. 3, pp. 263–272, 2001.

[57] M. Bau, V. Ferrari, and D. Maroli, "Contactless excitation of MEMS resonant sensors by electromagnetic driving," in *Proceedings of the COMSOL Conference*, 2009.

[58] D. Burns, J. Zook, and R. Horning, "Sealed-cavity resonant microbeam pressure sensor," *Sensors Actuators A Phys.*, vol. 48, no. 3, pp. 179–186, 1995.

[59] S. Bianco, M. Cocuzza, and I. Ferrante, "Silicon microcantilevers with different actuation-readout schemes for absolute pressure measurement," *J. Phys. Conf. Ser.*, vol. 100, no. 9, 2008.

[60] M. a. Fonseca, J. M. English, M. von Arx, and M. G. Allen, "Wireless micromachined ceramic pressure sensor for high-temperature applications," *J. Microelectromechanical Syst.*, vol. 11, no. 4, pp. 337–343, Aug. 2002.

[61] A. Baldi, W. Choi, and B. Ziaie, "A self-resonant frequency-modulated micromachined passive pressure transensor," *Sensors Journal, IEEE*, vol. 3, no. 6, pp. 728–733, 2003.

[62] C. Welham, J. Gardner, and J. Greenwood, "A laterally driven micromachined resonant pressure sensor," *Sensors Actuators A Phys.*, vol. 52, no. 1–3, pp. 86–91, 1996.

[63] T. Corman, P. Enoksson, and G. Stemme, "Gas damping of electrostatically excited resonators," *Sensors Actuators A Phys.*, vol. 61, no. 1–3, pp. 249–255, Jun. 1997.

[64] D. R. Southworth, H. G. Craighead, and J. M. Parpia, "Pressure dependent resonant frequency of micromechanical drumhead resonators," *Appl. Phys. Lett.*, vol. 94, no. 21, 2009.

[65] E. Defay, C. Millon, C. Malhaire, and D. Barbier, "PZT thin films integration for the realisation of a high sensitivity pressure microsensor based on a vibrating membrane," *Sensors Actuators A Phys.*, vol. 99, no. 1–2, pp. 64–67, Apr. 2002.

[66] Z. Luo, D. Chen, J. Wang, and J. Chen, "A differential resonant barometric pressure sensor using SOI-MEMS technology," in *2013 Ieee Sensors*, 2013, pp. 1–4.

[67] K. Ikeda and H. Kuwayama, "Three-dimensional micromachining of silicon pressure sensor integrating resonant strain gauge on diaphragm," *Sensors Actuators A Phys.*, vol. 23, no. 1–3, pp. 1007–1010, 1990.

[68] K. Wojciechowski, "A MEMS resonant strain sensor operated in air," in *Micro Electro Mechanical Systems*, 2004.

[69] J. C. Greenwood, "Microsensor with resonator structure," US 6389898 B1, 2003.

[70] P. K. Kinnell and R. Craddock, "Advances in Silicon Resonant Pressure Transducers," *Procedia Chem.*, vol. 1, no. 1, pp. 104–107, Sep. 2009.

[71] GE, "No Title." [Online]. Available: http://www.ge-mcs.com/en/pressure-and-level/transducerstransmitters/rps-dps-8000.html. [Accessed: 01-Jan-2016].

[72] GE Measurement & Control, "No Title." [Online]. Available: http://www.ge-mcs.com/download/pressure-level/TERPS_video.swf. [Accessed: 01-Jan-2016].

[73] P. K. Kinnell, "Sensor," GB2470398, 2010.

[74] A. a. Kosterev, F. K. Tittel, D. V. Serebryakov, A. L. Malinovsky, and I. V. Morozov, "Applications of quartz tuning forks in spectroscopic gas sensing," *Rev. Sci. Instrum.*, vol. 76, no. 4, p. 043105, 2005.

[75] E. P. Eernisse and R. B. Wiggins, "Review of thickness-shear mode quartz resonator sensors for temperature and pressure," *IEEE Sens. J.*, vol. 1, no. 1, pp. 79–87, 2001.

[76] E. P. Eernisse, R. W. Ward, and R. B. Wiggins, "Survey of Quartz Bulk Resonator Sensor Technologies," *IEEE Trans. Ultrason. Ferroelectr. Freq. Control*, vol. 35, no. 3, pp. 323–330, 1988.

[77] Parosscientific, "Digiquartz pressure intrumentation." [Online]. Available:

http://paroscientific.com/pdf/400 Resonant Quartz Crystal Technology.pdf. [Accessed: 01-Jan-2017].

[78] J. Paros, "precision digital pressure transducer," *ISA Trans.*, vol. 12, pp. 173–179, 1973.

[79] T. Ueda, F. Kohsaka, and E. Ogita, "Precision force transducers using mechanical resonators," *Measurement*, vol. 3, no. 2, pp. 89–94, 1985.

[80] A. D. Ballato, "Effects of Initial Stress on Quartz Plates Vibrating in Thickness Modes," *14th Annu. Symp. Freq. Control*, no. 1, pp. 89–114, 1960.

[81] J. M. Ratajski, "Force frequency coefficient of Singly Rotated Vibrating Quartz Crystals," *IBM J. Res. Dev.*, vol. 12, no. 1, pp. 92–99, 1968.

[82] C. R. Dauwalter, "The temperature dependence of the force sensitivity of AT-cut quartz crystals," *J. Photochem. Photobiol. A Chem.*, vol. 69, no. June, pp. 1–5, 1992.

[83] H. E. Karrer and J. Leach, "Quartz Resonator Pressure Transducer," *IEEE Trans. Ind. Electron. Control Instrum.*, vol. 16, no. 1, pp. 44–50, 1969.

[84] R. J. Besson, J. J. Boy, and B. Glotin, "A Dual-Mode Thickness-Shear Quartz Pressure Sensor," *IEEE Trans. Ultrason. Ferroelectr. Freq. Control*, vol. 40, no. 5, pp. 584–590, 1993.

[85] E. . EerNiesse, "Theoretical modeling of quartz resonator pressure transducers," in *41st Annual frequency control symposium*, 1987, pp. 339–343.

[86] Quartzdyne, "Transient performance," 2003. [Online]. Available: www.quartzdyne.com.

[87] A. A. S. Mohammed, W. A. Moussa, and E. Lou, "High-performance piezoresistive MEMS strain sensor with low thermal sensitivity," *Sensors*, vol. 11, no. 2, pp. 1819–1846, 2011.

[88] Kistler, "Piezoresitive high-pressure sensor." [Online]. Available: http://www.sensorsportal.com/HTML/DIGEST/june_07/Presure_sensors.htm. [Accessed: 01-Jan-2017].

[89] GE Measurement & Control, "UNIK 5000 Silicon pressure sensor." [Online]. Available: https://www.gemeasurement.com/sensors-probes-transducers/pressure-transducers-and-transmitters/unik-5000-silicon-pressure-sensor. [Accessed: 01-Jan-2017].

[90] A. A. Seshia and R. T. Howe, "Integrated micromechanical resonant sensors for inertial measurement systems," UC Berkeley, 2002.

[91] L. E. Picolet, "Vibration problems in engineering," *J. Franklin Inst.*, vol. 207, no. 2, pp. 286–287, 1929.

[92] V. Kaajakari, *Pratical MEMS*, 1st ed. Las Vegas: Small Gear Publishing, 2009.

[93] C. Zhao, "A MEMS sensor for stiffness change sensing applications based on three weakly coupled resonators," University of Southampton, 2014.

[94] E. . Smith, *Mechanical Engineer's Reference Book*, 12th Editi. Butterworth-Heinemann, 2013.

[95] R. D. Cook, D. S. Malkus, and M. . Plesha, *Concepts and Applications of Finite Element Analysis*, Fourth edi. John Wiley and Sons, 1989.

[96] S. Timoshenko, *Theory of plates and shells*, 2nd ed. New york: McGraw-Hill Book Company, 1987.

[97] T. Mattila, J. Kiihamaki, T. Lamminmaki, O. Jaakkola, P. Rantakari, A. Oja, H. Seppa, H. Kattelus, and I. Tittonen, "A 12 MHz micromechanical bulk acoustic mode oscillator," *Sensors Actuators, A Phys.*, vol. 101, no. 1–2, pp. 1–9, 2002.

[98] T. Namazu, Y. Isono, and T. Tanaka, "Evaluation of size effect on mechanical properties of single crystal silicon by nanoscale bending test using AFM," *J. Microelectromechanical Syst.*, vol. 9, no. 4, pp. 450–459, Dec. 2000.

[99] I. Sari, I. Zeimpekis, and M. Kraft, "A dicing free SOI process for MEMS devices," *Microelectron. Eng.*, vol. 95, pp. 121–129, Jul. 2012.

[100] H. Sandmaier and K. Kuhl, "A square-diaphragm piezoresistive pressure sensor with a rectangular central boss for low-pressure ranges," *Electron Devices, IEEE Trans.*, vol. 40, no. October, pp. 1754–1759, 1993.

[101] R. Khakpour, "Analytical comparison for square, rectangular and circular diaphragms in MEMS applications," in *International Conference on Electronic Devices, Systems and Applications*, 2010, no. Icedsa201 0, pp. 297–299.

[102] S. Y. Huang, H. L. Lin, C. G. Chao, and T. F. Liu, "Effect of compressive stress on nickel-induced lateral crystallization of amorphous silicon thin films," *Thin Solid Films*, vol. 520, no. 7, pp. 2984–2988, 2012.

[103] N. a. Fleck, C. S. Shin, and R. a. Smith, "Fatigue crack growth under compressive loading," *Engineering Fracture Mechanics*, vol. 21, no. 1. pp. 173–185, 1985.

[104] N. Anadkat and J. S. Rangachar, "Simulation based Analysis of Capacitive Pressure Sensor with COMSOL Multiphysics," *Int. J. Eng. Res. Technol. (IJERT）*, vol. 4, no. 04, pp. 848–852, 2015.

[105] K. Shirai, "Temperature Dependence of Young's Modulus of Silicon," *Jpn. J. Appl. Phys.*, vol. 52, no. 83, pp. 1129–1138, 2013.

[106] C.-H. Cho, "Characterization of Young's modulus of silicon versus temperature using a 'beam deflection' method with a four-point bending fixture," *Curr. Appl. Phys.*, vol. 9, no. 2, pp. 538–545, Mar. 2009.

[107] A. K. Samarao and F. Ayazi, "Temperature compensation of silicon resonators via degenerate doping," *IEEE Trans. Electron Devices*, vol. 59, no. 1, pp. 87–93, 2012.

[108] J. R. Clark and C. T.-C. Nguyen, "Mechanically temperature-compensated flexural-mode micromechanical resonators," in *International Electron Devices Meeting 2000. Technical Digest. IEDM (Cat. No.00CH37138)*, 2000, pp. 399–402.